INVESTIGATION OF THERMO-ELECTROMAGNETIC MATERIALS IMPLEMENTED IN HARVESTING OF THERMOELECTRIC ENERGY IN ELECTRICAL MACHINES

by

Muhammid Hamid Al-Baghdadi

A thesis submitted to Cardiff University in candidature for
the degree of Doctor of Philosophy

Wolfson Centre for Magnetics
College of Physical Sciences and Engineering
Cardiff University
Wales, United Kingdom

July 2016

DECLARATION

The work has not previously been accepted in substance for any degree and is not being concurrently submitted in candidature for any degree.

Signed ……..…… (Muhammid Hamid Husein Al-Baghdadi)

Date ……

STATEMENT 1

This thesis is being submitted in partial fulfilment of the requirements for the degree of PhD.

Signed: ……. (Muhammid Hamid Husein Al-Baghdadi)

Date: ……..

STATEMENT 2

This thesis is the result of my own investigations, except where otherwise stated. Other sources are acknowledged by the provision of explicit references.

Signed ……..…… (Muhammid Hamid Husein Al-Baghdadi)

Date ……

STATEMENT 3

I hereby give consent for my thesis, if accepted, to be available for photocopying and for inter-library loan, and for the title and summary to be made available to outside organisations.

Signed ……..…… (Muhammid Hamid Husein Al-Baghdadi)

Date ……

ACKNOWLEDGME

This work was carried out at the Wolfson Centre for Magnetics, School of Engineering, Cardiff University and financially supported by the Iraqi Ministry of Higher Education and Scientific Research Scholarship. I would like to express my highest gratitude and appreciation to them for providing the opportunity to attain the PhD, financial support and resources required in my study to complete this project.

First of all, I am deeply grateful to my academic supervisors, Dr Fatih Anayi and Dr. Gao Min for their excellent guidance, encouragement, care, patience, constructive criticism and insight during this project.

Similarly, I would like to express my special thanks to Dr. J. J. Bomphrey, Dr. Jorge Garcia Canadas, and Dr. Phil Buckle, Cardiff School of Physics, for their encouragement and invaluable guidance and continual support. I wish thank the other members of the Wolfson Centre, Dr. Jeremy Hall, Dr Turgut Meydan, and Dr Yevgen Melikhov for their advice and comments at all levels of my research. Special thanks go to all the members of the thermoelectric group at Cardiff University for their friendship and making my study life a memorable one.

I would also like to acknowledge Dr. Mike Harbottle, Dr. Richard Marsh, and Anthony Oldroyd, members of the research office, electronic workshop, and mechanical workshop, for taking time out from their busy schedule to help and support my project during my study in Cardiff University.

My greatest thanks are reserved for my family: especially my mother and father for their unconditional love, support and encouragement throughout my life, and to my wife for her constant care, love, support and standing beside me during happy and sad moments and to my sons and daughter who have suffered the most during my absence at their most needed times.

ABSTRACT

Many researchers have tried to exploit waste heat to generate electrical power. There are two phenomena that are related to the conversion of heat into electrical power: thermoelectric (TE) and thermomagnetic (TM) phenomena. In this work the latter (TM phenomenon) deals with the conversion of waste heat to generate electrical power. TM effect began in the 1960s due to the difficulties in induction of a strong magnetic field in the past.

The work presented in this thesis focuses on the preparation of polycrystalline indium antimonide (InSb) bulk materials and investigation of their TM properties. The research was motivated by their anticipated application in technologically important regions of reducing energy losses and in operating conditions of electro-magnetic machines, such as motors, generators and transformers, by incorporating such energy conversion devices into the machines at carefully chosen locations.

When a thermomagnetic sample is subjected to both temperature gradient and magnetic flux density concurrently, it will produce electrical output. A high electrical power output will be produced when the sample has similar numbers of both charge carriers, and, in addition, when the sample is subject to high temperature difference and high magnetic flux density across it.

A new technique has been developed in this work to make undoped and doped InSb polycrystalline bulk materials with tellurium Te, based on open quartz tube instead of the traditional method requiring sealing of the quartz tube. A modification in the raw materials ratio was adjusted to obtain pure InSb sample. The X-ray diffraction (XRD) and the inter-planar spacing analysis were carried out to check the structure of the samples and the result confirmed that the material was pure InSb.

Measurements were taken under direct magnetic field, which was produced from direct current (DC) supply, and alternative magnetic field, which was induced from alternative current (AC). The design procedure involved determining the longitudinal, transverse and hybrid transverse voltages. Modifications in design of the measurement

system have been made to minimise the effect of AC magnetic field on these parts, such as the heat sink being made of copper plate and K-type thermocouples. In addition, magnetic shielding was used for wires in the vicinity to minimise the induced voltage that affects measurements of transverse voltage. The induced voltage was still higher than the transverse voltage, even with the use of magnetic shielding. For this reason, the research performed in this work relating to the thermomagnetic parameters under AC magnetic field did not obtain appropriately good results.

The thermomagnetic parameters of samples under DC magnetic field have been improved by doping them with Te at different levels of 0.1% and 0.25%. The resistivity and Seebeck coefficient of the doped InSb with 0.25% Te was lower than those for undoped InSb single crystalline, which was used as a reference sample. The resistivity was lower, around 24% and 38% at the magnetic flux density 0 T and 1 T respectively, and the Seebeck coefficient was about 8% lower for various magnetic flux densities. In contrast, the Nernst, Righi-Leduc voltages and thermomagnetic power of the doped InSb with 0.25% Te were higher than those for undoped InSb single crystalline. The Nernst voltage was around 2% and 0.5% for the magnetic flux density of 1 T and temperature difference 30 °C and 80 °C respectively, while the Righi-Leduc voltage was higher, around 2.6% and 0.9%, and thermomagnetic power was higher around, 2.9% and 1% respectively for the same magnetic field and temperature differences.

LIST OF ABBREVIATIONS AND NOMENCLATURES

Abbreviations:

TE	Thermoelectric phenomena
TM	Thermomagnetic phenomena
InSb	Indium antimonied
Te	Tellurium element
XRD	X-ray diffraction
DC	Direct current
AC	Alternating current
TME	Thermo-magneto electric phenomena
n-type	Negative type semiconductor (the majority carriers are negative charge)
C	Carbon element
Ge	Germanium element
In	Indium element
Sb	Antimony element
O_2	Oxygen molecular
In_2O_3	Indium trioxide
P-type	Positive type semiconductor (the majority carriers are positive charge)
III-V	Three-five semiconductor group
LPE	Liquid phase epitaxy process
MBE	Molecular beam epitaxy process
MOVPE	Metal-organic vapour phase epitaxy process
MOCVD	Metal-organic chemical vapour epitaxy process
THM	Travelling heater method
VDS	Vertical directional solidification process
FZM	Floating zone melting
TSM	Traveling solvent method
HgSe	Mercuric selenide
BiSb	Bismuth antimonied
CdAs	Cadmium arsenide
Bi	Bismuth
e.m.f	Electro motive force
CdTe	Cadmium tellurium
ZT	Dimensionless figure of merit
InAs	Indium arsenide
GMT	Geometrical magneto-thermo power
Ni	Nickel element
Ag	Silver element
HgTe	Mercuric tellurium
(hkl)	Lattice plane
CP4	Etching solution
PCB	printed circuit board
K-type	Thermocouple type K (magnetic materials)

EM	Electromagnetic
IH	Induction heating
T-type	Thermocouple type T (non-magnetic materials)
r.m.s	The root means square of voltage

Nomenclatures:

μ_e	Mobility of charge carriers
B	Magnetic flux density
m*	Density of states effective mass
κ	Thermal conductivity
δ	Seebeck coefficient
ΔV	Voltage difference
ΔT	Temperature difference
Q	Generated heat
$\prod$	Peltier coefficient
I	Electrical current
β	Thomson coefficient
$\mathcal{J}$	current density
∇T	Temperature gradient
N	Nernst coefficient
dT/dy	Temperature gradient in y-axis
E	Electrical field
S	Righi-Leduc coefficient
dT/dx	Temperature gradient in x-axis
$_h\mathrm{L}_e$	Longitudinal potential difference coefficient
H	Magnetic field strength
x	The distance between two points
Q	The heat transfer rate
A	Area
$\dot{q}$	Distance derivative of heat flux
W	Width
$\mathbb{E}$	The energy
h	Thermal convection
ρ	Resistivity
$\mathbb{E}_g$	Band gap energy
K_B	Boltzmann's constant
n	The electron density
p	The hole density
n_i	Intrinsic carriers density
λ	The wave length of X-ray
$\mathbb{N}$	Diffraction order
d	Lattice inter-planar spacing
θ	The angle between the plane wave and lattice plane
V	The voltage

R	The resistance
$\mathbb{A}$	The cross-section area
L	Length
$\mathbb{m}$	The turn density for the winding
τ	The thermal time constant
v	The sample volume
c	The specific heat capacity
A_s	The sample area that attached to the media
L_c	The ratio of the solid's volume to surface area
F	The Lorenz force
ϑ	The charge carrier velocity
m_e	The electron mass
φ	The flux linkage
$\mathcal{N}$	The number of turns
ω	The angular frequency
f	The frequency
μ_0	The permeability of the free space
g	The air gap length

TABLE OF CONTENTS

Chapter 1: Introduction

Chapter 2: Theory

Chapter 3: Literature Review

Chapter 4: Material Preparation and Characterisation

Chapter 5: Measuring Systems

Chapter 6: Result and Discussion

Chapter 7: Conclusion and future plan

LIST OF FIGURES CHAPTURES

Chapter 2

Chapter 3

Chapter 4

Chapter 5

Chapter 6

LIST OF TABLES CHAPTURES

Chapter 3

Chapter 5

Chapter 6

CHAPTER 1

Introduction

1.1: Introduction

Global concern regarding the environment and contaminants that are emitted from energy generators has become a critical current issue. The build-up of contaminants in the atmosphere leads to an increasingly negative impact on the environment. [1.1].

Over the past 200 years, the proportion of energy consumption throughout the world has increased. This has led to an energy crisis in that there is a continual depletion of energy sources weighted against a predicted increase in energy demands over time. This situation is exacerbated by the fact that fossil fuels are non-renewable and will eventually be exhausted. Furthermore, the burning of fossil fuels generates greenhouse gases, which increase global warming [1.2]. Therefore, dependence on fossil fuels for energy generation is no longer tenable. Scientists have been trying to develop a technology that can provide an alternative energy conversion and then transition to green environmental fuel. One of these technologies is the conversion of waste heat into electrical power (with and without an applied magnetic field). This would provide a basic function in the challenge to develop a technology that reduces dependence on fossil fuels and greenhouse gas emissions [1.1, 1.3]. The concept is the conversion of waste heat into electricity. It

could potentially convert waste heat into electrical energy in several different applications, including industrial processes, automotive exhaust and home heating [1.2].

The raising of the temperature in rotary electrical machines or large electronic devices leads to damage of these machines and devices [1.4]. A device is needed to utilise waste thermal energy and supply an auxiliary device (e.g. a fan) or use it for cooling purposes.

1.2: Thermomagnetic effect

The TM phenomena are also known as Thermo-magneto electric (TME) effect. Thermomagnetic materials can transform a temperature gradient into electrical power when they are subjected to a magnetic field perpendicular to the temperature gradient and the electrical field. The field of TM was studied in the 1960s [1.5, 1.6]. In those days, induction of a strong magnetic field resulted in considerable loss of energy. This loss of energy is the main reason why the TM effect was not studied during the interim period. Nowadays, improvement in superconducting magnet provides higher efficiency of induction of a strong magnetic field. Several years ago, researchers developed a system for measuring transport coefficients under a strong magnetic field to estimate the efficiency of thermomagnetic materials [1.6].

Thermomagnetic generators are solid-state devices with no moving parts, no maintenance (increase in system life), silent, reliable and scalable, making these devices ideal for small distributed power generation [1.1]. Recent studies have shown that the transverse TM effects have particular preferences over the TE effects, when used in energy conversion [1.7-1.11]. One fact is that they employ single elements rather than thermocouples (thermoelectric module). Also, thermomagnetic devices, such as infrared radiation detectors, direct-current transformers and heat-flow

meters, have much shorter response times than the corresponding thermoelectric devices [1.7].

Indium antimonide (InSb) bulk semiconductor material is made of the indium element In and antimony element Sb and is one of the promising Nernst materials.

1.3: Research objectives

The objectives of the research work presented in this thesis are as follows:

- Produce undoped polycrystalline InSb semiconductor by using a new technique based on open quartz tube inside a niobium container. In this method, the raw materials ratio was taken into consideration to make pure samples but of stoichiometric composition. Also, produce doped polycrystalline InSb n-type with Te, with different doping levels.
- Separate the three components (Nernst, Righi-Leduc and misalignment voltages) of the total transverse voltage. This can be achieved by quickly changing the polarity of the magnetic field.
- Calculate the transport coefficients for single crystal InSb as a reference, as well as for undoped polycrystalline InSb, then make a comparison between them.
- Investigate the transport coefficients for doped InSb n-type semiconductor with Te for different doping levels, and compare with undoped single crystal and polycrystalline material.
- Investigate minimising the Righi-Leduc effect for undoped and doped InSb n-type semiconductors under AC magnetic field, then compare transport coefficient with DC magnetic field.

1.4: Research methodology

To achieve the above objectives, research was undertaken in four stages:

- First, produce the polycrystalline InSb sample by using the new technique. The ratio of the raw materials weight was controlled to obtain pure InSb. In addition, produce doped InSb with Te for different doping levels (1% and 0.25%).
- Second, separate the three components (Nernst, Righi-Leduc and misalignment voltages) of the total transverse voltage by changing the polarity of the magnetic field using a switch to reverse the direction of the current.
- Third, compare transport coefficients among undoped and doped InSb samples.
- Fourth, investigate the effect of AC magnetic field on the transport coefficients for InSb samples (undoped single crystal, undoped polycrystalline, doped with 0.1% Te and 0.25% Te).

1.5: Aims of the work

This work suffered from a shortage of published works in its field (thermomagnetic generator). Most authors recommended InSb semiconductor as the more effective thermomagnetic generator material, due to its properties. Unfortunately, all previous research papers that have been published used single commercial InSb crystalline doped with Te, carbon C, germanium Ge [1.12, 1.13], whereas there has been no published research using undoped InSb. Therefore, this work investigates, for the first time, the effect of TM effect on undoped InSb bulk material.

The traditional way to produce InSb samples is sealing the quartz tube. The facility of the sealing quartz tube is not available at Cardiff University. This project is the first work to design and construct a unique sample reaction chamber consisting of an open-end quartz tube sealed inside a niobium container in order to produce doped and undoped InSb samples by using growth from melting method.

The total transverse voltage consists of three components which are: Nernst, Righi-Leduc and misalignment voltages. There is only one published paper explaining the method to separate these three components [1.14]. In that paper, a plot between Nernst voltage and magnetic field made no mention of the Righi-Leduc or misalignment voltages. This current thesis is the first work to give the amount of all three of the components mentioned above for undoped and doped InSb bulk material.

Ebnalwaled [1.15, 1.16] covered preparation of P-type polycrystalline undoped InSb bulk materials with off-stoichiometric composition. The material produced has a Seebeck coefficient less than 100 μV/°C from 290-400 K. The Seebeck coefficient result confirmed that the conductivity is more than that for undoped single crystal, due to the increase in the charge carriers. These papers [1.14, 1.15] support and provide the motive to produce InSb off-stoichiometry rather than the stoichiometric composition. Furthermore, polycrystalline films for InSb have potentially important applications in thermomagnetic devices [1.17].

The synthesis off-stoichiometry composition to prepare InSb semiconductor creates vacancies [1.15]. The type of vacancies depends on the ratio of In/Sb; indium In enriched produces anion vacancies and antimony Sb enriched produces cation vacancies. The existence of two types of charge carriers with charge concentrations closer to equal can obtain higher thermal conductivity and Nernst effects than those materials that have one type of carrier [1.18, 1.19]. In this work, the holes are created due to the non-perfect stoichiometric composition and the reaction of InSb melt with the contaminants. The oxygen atoms inside the furnace react with InSb melt to

produce indium trioxide (In_2O_3). The vacancies appear due to the difference between the numbers of antimony and indium atoms; the vacancies are cation vacancies due to Sb enriched. In addition, the doping with Te leads to substitute Te atoms instead of Sb atoms position. This process increases the number of electrons due to the number of electrons in the external shell and also increases cation vacancies due to Sb enriched. In other words, the process increases both negative and positive charge carriers.

The Righi-Leduc voltage is opposite to the Nernst voltage polarity, which leads to minimising the output voltage. A proposed technique to minimise the Righi-Leduc voltage is by using an AC magnetic field. This work is the first work to attempt to maximise output voltage by minimising Righi-Leduc voltage using AC magnetic field.

All the information above created the motivation to start utilizing TM effects on undoped and doped bulk polycrystalline InSb materials with various doping levels; then, to try to enhance the thermomagnetic power and Nernst voltage by changing the doping level. Some applications, such as motors, generators and transformers, might benefit from the TM effects. This benefit can occur by incorporating such energy conversion devices into machines at carefully chosen locations.

1.6: Outline of the thesis

This thesis is organised into seven chapters, followed by appendices. Each chapter is further divided into sections and sub-sections to make the presentation more clarity. A brief overview of each chapter follows:

Chapter 1 (Introduction) provides a brief introduction to the background of this study. Research objectives and research methodology are explained to provide brief clarification of how the work was conducted. This is followed by the aims and outline of the work.

Chapter 2 (Theory) reviews the theory of this study. It contains a brief explanation for TE and TM phenomena and the effects that belong to them. The heat transfer and two types of point defects in the solid state are demonstrated. The ambipolar effect, thermal conductivity and the effect of magnetic field on InSb are explained due to the significant impact on thermomagnetic transport coefficients. The required properties to obtain good generation materials are illustrated to help in choosing an appropriate candidate for TM effect materials. The x-ray powder diffraction and crystal growth are explained. The EDx analysis is also illustrated.

Chapter 3 (Literature Review) presents a literature review for producing and measuring TE and TM effect. It is divided into three essential parts:

- The production of the single crystal InSb bulk materials, polycrystalline InSb bulk materials and thin films.
- The previous studies related to some TE effects for materials other than InSb.
- The studies of InSb materials.

The structure of InSb and some properties of this material are presented.

Chapter 4 (Characterization and Production of InSb Material) presents the methodology that has been utilized to prepare undoped and doped polycrystalline InSb with Te. The experimental conditions are illustrated. The design of a chamber with its components that was used to maintain the raw materials is also covered. X-ray diffraction is illustrated to help in analysing the XRD pattern. The reason for choosing Te element to be doped in InSb rather than other elements is demonstrated. The optimum sample shape, extracting, polishing and etching for InSb sample are clarified. Determining how to produce undoped and doping polycrystalline InSb by using a new technique based on the growth from melt method is explained. The X-ray patterns are presented for undoped and doped polycrystalline with Te.

Chapter 5 (Measuring System) presents the setup that was designed to be suitable for measuring and calculating thermomagnetic transport coefficients. It is divided into two parts: 1- under DC magnetic field. 2- under AC magnetic field.

The areas covered in this chapter are:

- The setup that was designed with all components explained. The device used for making and measuring the magnetic field and calculating the Seebeck coefficient and the resistivity is demonstrated. The setup used for measuring the thermomagnetic coefficient and resistivity that was designed in this work is illustrated.
- The setup designed with all components is explained. The device used for making and measuring the magnetic field is illustrated. The magnetic shielding and its properties are explained. The properties of the transverse voltage that was obtained in this work are also explained.

Chapter 6 (Results and Discussions) presents the results of the undoped single and polycrystalline InSb and doped polycrystalline InSb with Te at the various doping levels. The chapter opens with an introduction containing a brief summary that explains how the results were obtained. It is divided into three parts: material production, thermomagnetic transport coefficient under the DC magnetic field, and thermomagnetic transport coefficient under the AC magnetic field:

- Part one: discussing the X-ray analysis for undoped and doped polycrystalline with Te. In addition, the inter-planar spacing of the sample to proof the structure of the sample is demonstrated.
- Part two: determining the magnetic flux density of the DC magnetic field. In this part five samples have been investigated. The Seebeck coefficient and its repeatability are calculated with and without the applied magnetic field. The Seebeck, total transverse, and hybrid voltages are measured. Changing the polarity of the magnetic field is used to measure the Nernst and Righi-Leduc voltages. The Nernst coefficient,

thermomagnetic power and resistivity are also calculated for five samples.

- Part three: determining the magnetic flux density of the AC magnetic field. In this section the same previous five samples have been investigated. The Seebeck coefficient and its repeatability are calculated under the magnetic field. The Seebeck and transverse voltages are measured for all samples.

Chapter 7 (Conclusions and Future Work) presents the conclusions that are drawn on the main results of this work and recommendations are offered for further research.

References

[1.1] D. Kim, "Thermoelectric properties of InSb- and $CoSb_3$-based compounds," Osaka University, 2013.

[1.2] J. Snyder and E. S. Toberer, "Complex thermoelectric materials.," *Nat. Mater.*, vol. 7, no. 2, pp. 105–114, 2008.

[1.3] T. M. Tritt and M. A. Subramanian, "Thermoelectric Materials, Phenomena, and Applications: A Bird's Eye View," *MRS Bull.*, vol. 31, no. 03, pp. 188–198, Mar. 2006.

[1.4] A. Banerjee, A. Tiwari, J. Vico, and C. Wester, "Motor protection principles," *2008 61st Annu. Conf. Prot. Relay Eng.*, pp. 215–231, 2008.

[1.5] H. Nakamura, K. Ikeda, and S. Yamaguchi, "Transport coefficients of InSb in a strong magnetic field," *XVI ICT "97. Proc. ICT"97. 16th Int. Conf. Thermoelectr. (Cat. No.97TH8291)*, no. 1, pp. 1–6, 1997.

[1.6] H. Nakamura, K. Ikeda, and S. Yamaguchi, "Physical model of Nernst element," *in Seventeenth International Conference on Thermoelectrics. Proceedings ICT98 (Cat. No.98TH8365)*, no. 7, pp. 97–100, 1998.

[1.7] C. Uher and H. J. Goldsmid, "A comparison of thermomagnetic materials for use at room temperature," *J. Phys. D. Appl. Phys.*, vol. 5, no. 8, pp. 1478–1488, 2002.

[1.8] H. Nakamura, K. Ikeda, and S. Yamaguchi, "Transport coefficients of InSb in a strong magnetic field," *in XVI ICT "97. Proceedings ICT"97. 16th International C`onference on Thermoelectrics (Cat. No.97TH8291)*, pp. 142–146, 1997.

[1.9] M. Hamabe, S. Yamamoto, S. Yamaguchi, H. Takahashi, H. Okumura, I. Yonenaga, T. Sasaki, and K. Watanabe, "Magnetic field effect for improvement of thermoelectric conversion: A proposal for Nernst-Seebeck element," *Proc. ICT'03. 22nd Int. Conf. Thermoelectr. (IEEE Cat. No.03TH8726)*, pp. 567–570, 2003.

[1.10] W. M. Yim and A. Amith, "Bi-Sb alloys for magneto-thermoelectric and thermomagnetic cooling," *Solid. State. Electron.*, vol. 15, no. 10, pp. 1141–1165, Oct. 1972.

[1.11] E. H. Putley, "Thermoelectric and Galvanomagnetic effects in Lead Selenide and Telluride," *Proc. Phys. Soc. Sect. B*, vol. 68, no. 1, pp. 35–42, 2002.

[1.12] J. Heremans, C. Thrush, and D. Morelli, "Geometrical magnetothermopower in n- and p-type InSb," *Phys. Rev. B*, vol. 65, no. 3, pp. 1–8, 2001.

[1.13] J. P. Heremans, C. M. Thrush, and D. T. Morelli, "Geometrical magneto-thermopower in semiconductors," *Phys. Rev. Lett.*, vol. 86, no. 10, pp. 2098–2101, 2001.

[1.14] M. R. El-Saden and F. W. Thomas, "Nernst effect in indium antimonide," *J. Appl. Phys.*, vol. 36, no. 1, pp. 181–183, 1965.

[1.15] A. A. Ebnalwaled, "Evolution of growth and enhancement in power factor of InSb bulk crystal," *J. Cryst. Growth*, vol. 311, no. 19, pp. 4385–4390, 2009.

[1.16] A. Ebnalwaled, "Hopping conduction and dielectric properties of InSb bulk crystal," *Ijens.Org*, vol. 11, no. 6, pp. 194–207, 2011.

[1.17] H. H. Wieder, *Intermetallic Semiconducting Films*, First edit. London: Pergamon Press Ltd., 1970.

[1.18] R. T. Delves, "Thermomagnetic effects in semiconductors and semimetals," *Reports Prog. Phys.*, vol. 28, no. 1, pp. 249–289, 1965.

[1.19] C. M. Orovets, "Search for Resonant Impurities in Bismuth and Bismuth-Antimony Alloys: Lithium, Magnesium, and Sodium," The Ohio State University, 2012.

CHAPTER 2

Theory

2.1: Introduction

This chapter illustrates the two types of phenomena that can turn heat into electricity, TE and TM phenomena. A brief explanation is presented for each phenomenon type and its conditions. Conduction heat transfer and heat distribution inside the sample are also demonstrated. Some properties that are important to improve and enhance the thermomagnetic coefficient are presented. The effects of magnetic field on material and requirements for useful materials as thermomagnetic generators are listed.

2.2: Thermoelectric phenomenon

TE phenomenon converts temperature differences into electrical voltage and vice versa. There are three effects that are related to TE phenomenon: the Seebeck, Peltier, and Thomson effects.

Seebeck reported in 1823 that the connection between two dissimilar electrically conductive metals with different temperature junctions would deflect a needle of magnet [2.1]. This is because a current is generated that passes through

the circuit and produces a magnetic field. He observed that this effect produces thermoelectric power generation (as shown in Figure 2-1(a)). A thermocouple is one of the devices that is based on the Seebeck effect. It is used widely for measuring temperature according to the following relationship:

$$\delta = \frac{\Delta V}{\Delta T} \quad \text{……(2.1)}$$

where: δ is the Seebeck coefficient, ΔV and ΔT are the voltage and temperature difference between hot and cool sides respectively.

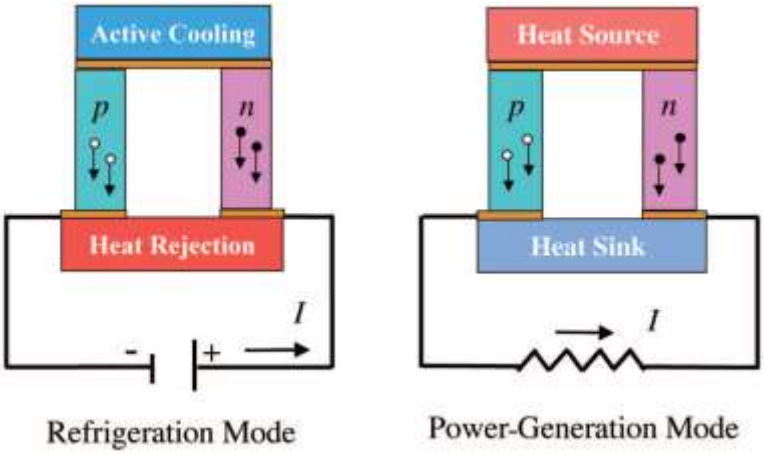

a: Power generation **b: Refrigeration**

Figure 2- 1: Schematic diagram illustrates, (a): thermoelectric module for Power generation (the Seebeck effect) and (b): refrigeration (the Peltier effect) [2.2].

In 1834, Peltier observed that when two dissimilar electrically conductive metals are connected together at one end to create a junction and electrical current is passed through this junction, heat is absorbed or rejected at / from the junction, depending on the direction of the current [2.2]. Figure 2-1 (b) illustrates the Peltier effect. The Peltier effect is the opposite of the Seebeck effect. It can be written as:

$$Q = \prod \mathrm{I} \quad \text{……(2.2)}$$

where: $\prod$ is the Peltier coefficient; Q is the heat which is generated at the junction and I is the electrical current pass through the junction.

Thermoelectric module is a device that consists of many thermoelectric couples, of n and p-type semiconductors. It is connected electrically in series and thermally in parallel. The cooling or heating ability of the whole unit is proportional to the number of thermoelectric couples in it, as illustrated in Figure 2-2.

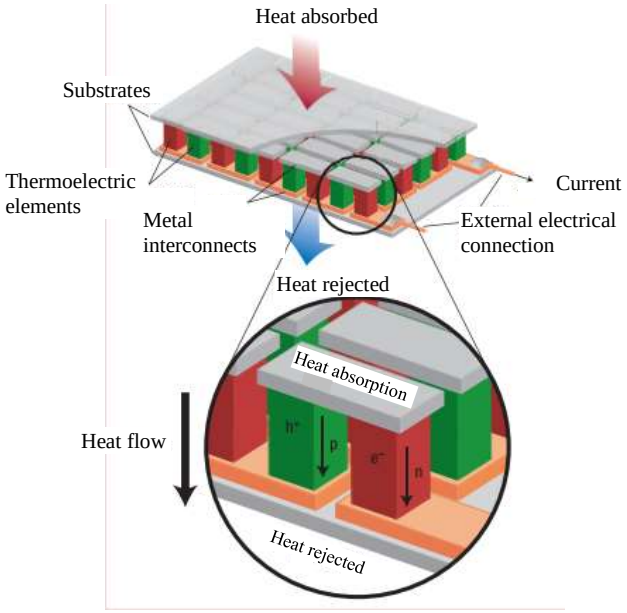

Figure 2- 2: Schematic illustrates of a thermoelectric module [2.3].

William Thomson (later Lord Kelvin) issued a comprehensive explanation of the Seebeck and Peltier effects in 1851. He also described their interrelationship (known as the Kelvin relations) [2.4]. The thermodynamic derivation led Thomson to predict the third thermoelectric effect, now known as the Thomson effect. Heat is absorbed or produced when a current flows through a material with a temperature gradient. The heat is proportional to both the electric current and the temperature gradient.

Thomson showed that the net energy accumulation per unit volume in a bar of material with a current through it can be written as:

$$\mathcal{Q} = -\beta \mathcal{J} \,.\nabla T \quad \text{……..(2.3)}$$

where: β is The Thomson coefficient; $\mathcal{J}$ is the current density and ∇T is the temperature gradient.

2.3: Thermomagnetic phenomenon

TM phenomenon converts temperature differences with a magnetic field to electrical voltage or vice versa.

In 1886, Albert von Ettingshausen and his PhD student Walther Nernst were studying the Hall effect in Bi. They found that when the temperature of one side of the sample was increased under a magnetic field, unexpected currents flow perpendicular to each other. Conversely, when applying a current (along the y-axis) and a perpendicular magnetic field (along the z-axis) a temperature gradient appears along the x-axis, as shown in Figure 2-3 [2.5].

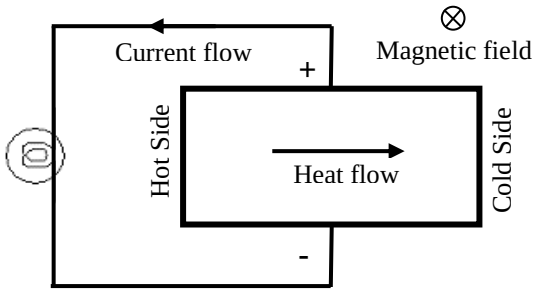

Figure 2- 3: Schematic diagram illustrates the Ettingshausen effect [2.5].

Thermomagnetic effects are caused by the action of a magnetic field on moving particles that carry electric charges (electrons and holes) in semiconductors. There are four types of effects associated with thermomagnetics: two transverse and two longitudinal effects [2.6]:

The thermomagnetic effects are:

1- A transverse potential difference (the Nernst effect).

2- A transverse temperature difference (the Righi-Leduc effect).

3- A longitudinal potential difference (the Seebeck effect under magnetic field (magneto-thermoelectric effect)).
4- A longitudinal temperature difference (change in thermal conductivity).

The distortion of the electrical and thermal flow makes the transverse thermomagnetic device complicated. This is obtained by the presence of the contacts on the ends and sides of the sample [2.7]. The three following sub-sections provide an explanation of some thermomagnetic effects.

2.3.1: Nernst effect

The Nernst effect (first Nernst–Ettingshausen effect) is observed when a sample is subjected to a temperature gradient in the y-direction and a magnetic field in the z-direction. An electromotive force e.m.f. (the Nernst voltage) in the x-direction will be produced. This e.m.f. is due to the Nernst effect, which is analogous to the Hall effect. The Nernst coefficient is usually defined, as shown in Figure 2-4. This effect is proportional to the magnetic field strength, longitudinal temperature gradient and the width of the plate, but independent of the thickness [2.8].

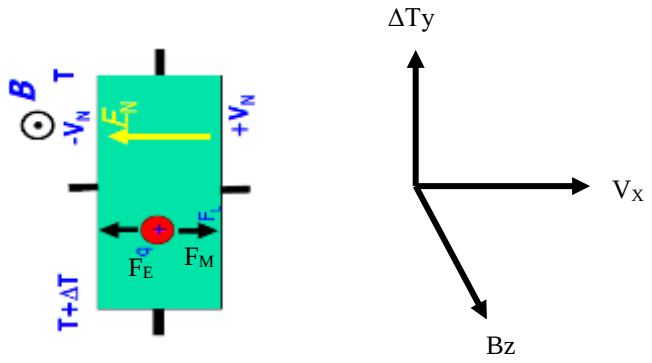

Figure 2- 4: Schematic diagram illustrates the Nernst effect [2.9].

$$|N| = \frac{E_x/B_z}{dT/dy} \quad \text{.....(2.4)}$$

where: N is the Nernst coefficient; E_x is the x-component of the electrical field; B_z is the z-component of the magnetic field and dT/dy is the temperature gradient on y-axis.

The Nernst effect is negative (Bismuth), when the direction of the heat current is not in the same direction as the electrical current in the electromagnet device and vice versa (Iron), as shown in Figure 2-5. The sign of the Nernst voltage changes with the direction of the magnetic field and also with the direction of the heat current in sample [2.6].

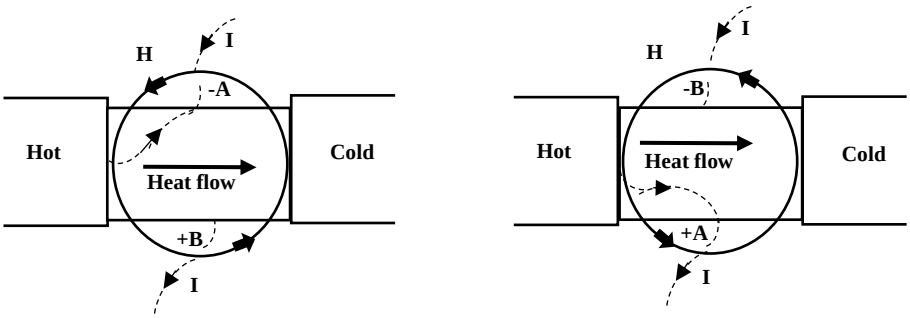

A – negative Nernst effect (Bismuth). B- positive Nernst effect (Iron).

Figure 2- 5: Schematic diagram illustrates the Nernst effect sign [2.6].

2.3.2: Righi-Leduc effect

The Righi-Leduc effect (the thermal Hall effect), which is the thermal analogous of the Ettingshausen effect, was discovered almost simultaneously in 1887 by the Italian physicist A. Righi and the French physicist S. Leduc. This effect is observed when a conductor, under which a temperature gradient and a heat flow are maintained, is placed in a constant magnetic flux density B. There is an established difference in temperature in the direction perpendicular to the primary heat flow and the magnetic field. Like the Hall effect, it is due to the curvature of thermal electrons under the magnetic field, as shown in Figure 2-6. It is proportional to the magnetic field strength, temperature gradient, but independent of the dimensions of the plate [2.5].

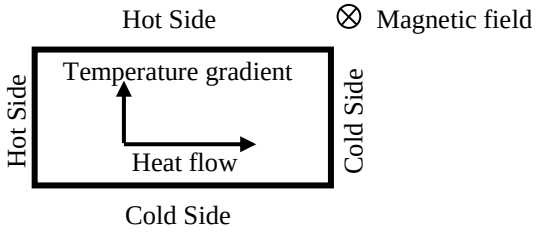

Figure 2- 6: Schematic diagram illustrates the Righi-Leduc effect [2.5].

$$|S| = \frac{dT/dy}{B_z\, dT/dx} \quad \text{……..(2.5)}$$

where: S is the Righi-Leduc coefficient and dT/dx is the temperature gradient on the y-axis.

The Righi-Leduc effect is negative (Bismuth), when the heat current is in the opposite direction to the current in the electromagnet and vice versa, as shown in Figure 2-7. The direction of the temperature difference changes with the direction of the magnetic field and heat current in sample [2.6].

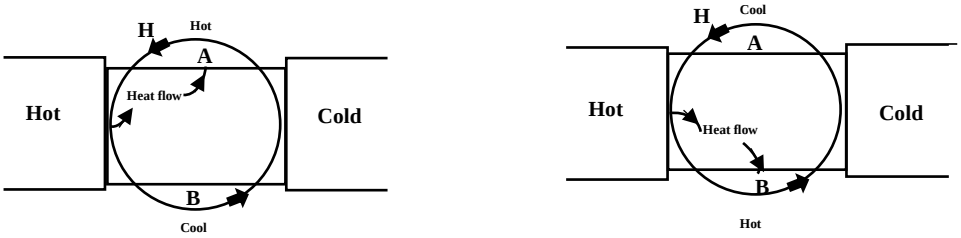

A- Negative Righi-Leduc effect (Bismuth). B- Positive Righi-Leduc effect (Iron).

Figure 2- 7: Schematic diagram illustrates the Righi-Leduc effect sign [2.6].

The Righi-Leduc effect is the least among all thermomagnetic effects: the lattice thermal conductivity was shorted out in the Righi-Leduc effect, and the latter can be neglected in a shallow doped semiconductor. It is still small, even in the case of a heavily doped semiconductor, because it is proportional to the mobility of the electrons [2.8].

2.3.3: Longitudinal potential difference

Ettingshausen and Nernst reported in 1886 that the transverse magnetic field set up longitudinal electromotive force in a sample with temperature gradient. The effect is proportional to the magnetic field strength and temperature gradient, but independent of the dimensions of the plate [2.6], as shown in Figure 2-8.

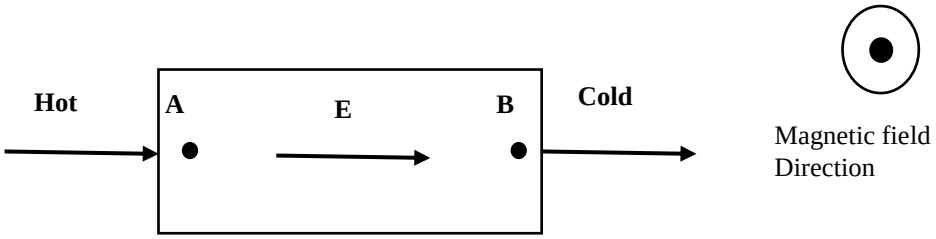

Figure 2- 8: Schematic diagram illustrates thermomagnetic longitudinal potential difference [3.6].

The longitudinal potential difference coefficient is given by:

$$ {}_hL_e = \pm \frac{\Delta E}{H^2.x.\frac{dT}{dx}} = \frac{\Delta E}{H^2(T_2 - T_1)} \quad \text{.....(2.6)} $$

where: x is the distance between the points (A & B); T_2 and T_1 are temperatures at (A & B) points and H is the magnetic field strength.

The Longitudinal potential difference effect is negative if the longitudinal e.m.f sends an electric current in the opposite direction to the heat current.

In 1887, Grimaldi discovered that the longitudinal thermomagnetic potential difference was due to the change in thermal conductivity and thermoelectric power of a sample in the magnetic field. The change of temperature at the two ends of a sample results in the change in thermal conductivity, and a difference in thermo-electro-motive force would follow [2.6].

2.4: Conduction heat transfer

If a body is exposed to a temperature gradient, energy is transferred from the high temperature toward the low temperature. This transfer of energy from hot side (more energetic) to the other side (less energetic) is due to the interactions between the particles inside the materials.

The modern view for conduction heat transfer is due to the lattice waves produced by atomic motion (atomic activity in the form of lattice vibrations) [2.10]. In insulating materials (non-conductor) the transfer is via lattice waves, while in conducting materials it is via the free electrons as well as through lattice waves. The electrons will transport thermal energy from the high-temperature region to the low temperature region as they transport electrical charges. Vibration energy in the lattice structure of the material will also transfer energy, but this energy transfer is less than electron transport. Therefore, good heat conductors are obtained by good electrical energy [2.11].

The appropriate rate equations can be used to quantify heat transfer processes. It is possible to compute the amount of energy being transferred per unit of time by using these equations. The rate equation is known as Fourier's law. For a one dimensional plane wall it has a temperature distribution $T_{(x)}$, as shown in Figure 2-9. The rate equation is:

$$Q_x = \frac{d\bar{\bar{q}}_x}{dt} = -A\kappa\frac{dT}{dx} = -A\kappa\frac{T_2-T_1}{W} = -A\kappa\frac{\Delta T}{W} \quad \text{.....(2.7)}$$

where: Q_x is the heat transfer rate in the x direction; $\bar{\bar{q}}_x$ is the heat transfer in the direction x; A is the area of the plane wall and W is the width of the wall.

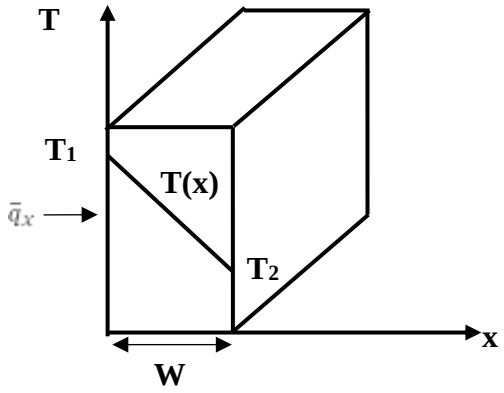

Figure 2- 9: One-dimensional heat transfer by conduction (diffusion of energy) [2.10].

2.5: Heat distribution inside plane wall with thermal energy generation

There is an additional effect on the temperature distribution of processes which may occur in the medium. The extra thermal energy is being generated due to the conversion from some other energy form, such as electrical energy and chemically reacting systems.

For a plane wall which has uniform energy generation per unit volume ($\dot{q}\ is\ constant$) and the surface temperature is maintained at $T_{s,1}$ and $T_{s,2}$, as shown in Figure 2-10, the heat equation form can be shown as:

$$\frac{d^2T}{dx^2} + \frac{\dot{q}}{\kappa} = 0 \quad \text{.....(2.8)}$$

where: $\dot{q}$ is the distance derivative of heat flux, the general solution for the above equation is :

$$T = -\frac{\dot{q}}{2\kappa}x^2 + C_1x + C_2 \quad \text{.....(2.9)}$$

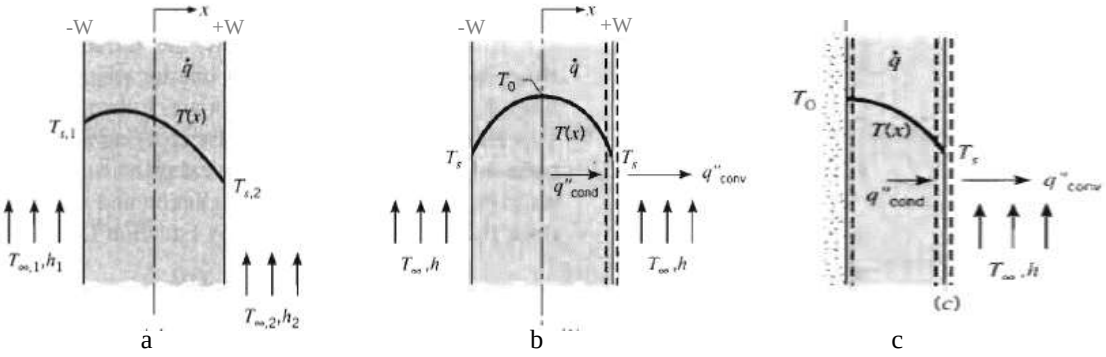

Figure 2- 10: Conduction in a plane wall with uniform heat generation, a: asymmetrical boundary conditions; b: symmetrical boundary conditions and c: adiabatic surface at mid-plane [2.10].

where: C_1 and C_2 are constants. The boundary condition is:

$$T(-W) = T_{s,1} \quad and \quad T(W) = T_{s,2} \qquad \text{.....(2.10)}$$

where: W is the width of the plane wall. The constants can be evaluated as:

$$C_1 = \frac{T_{s,2} - T_{s,1}}{2W} \quad and \quad C_2 = \frac{\dot{q}}{2\kappa} W^2 + \frac{T_{s,1} + T_{s,2}}{2} \qquad \text{.....(2.11)}$$

$$T(x) = \frac{\dot{q}W^2}{2\kappa}\left(1 - \frac{x^2}{W^2}\right) + \frac{T_{s,2} - T_{s,1}}{2}\, x + \frac{T_{s,1} + T_{s,2}}{2} \qquad \text{.....(2.12)}$$

The equation above represents the heat flux at any point on the wall. However, the heat flux will no longer be independent of (x) when it involves the heat generation. In the case of both surfaces being maintained at the same temperature $T_{s,1} \equiv T_{s,2} \equiv T_s$, the temperature distribution will be symmetrical about the mid-plane,

$$T(x) = \frac{\dot{q}W^2}{2\kappa}\left(1 - \frac{x^2}{W^2}\right) + T_s \qquad \text{.....(2.13)}$$

The maximum temperature at the mid-plane is [2.10] :

$$T(0) \equiv T_0 = \frac{\dot{q}W^2}{2\kappa} + T_s \qquad \text{.....(2.14)}$$

Eq. (2.13) represents the heat flux flow inside the sample as a second order equation. The maximum temperature distribution is in the middle of the curve, as shown in Figure 2-10.

2.6: Crystal defects

In nature, real materials are not perfect crystal structures. Atoms in real materials have been arranged in patterns that do not follow perfect crystal patterns. It is difficult to eliminate the imperfections during the growth process of crystals. For perfect materials, their properties would be predicted only by their composition and crystal structure. The crystal defects are the most important features for real imperfect materials. These defects can be manipulated to control the behaviour of material. This chapter focuses on point defects.

A point defect disturbs the crystal pattern at an isolated site. There are two types of these defects: intrinsic and extrinsic defects. They appear in a pure material and impurity atoms, respectively [2.12].

2.6.1: Point defect (intrinsic)

An Intrinsic defect requires no impurities and is a thermally activated process. An intrinsic defect, as shown in Figure 2-11, occurs when:

1- An atom is missing from a position in the crystal, which must be filled; in this position it will create a vacancy.
2- An atom occupies an interstitial site, which must have no existing atom, causing an interstitially.

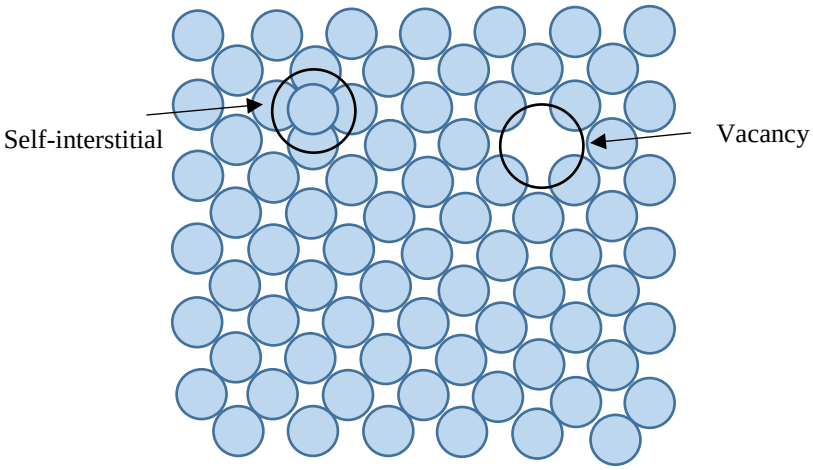

Figure 2- 11: The two types of intrinsic point defects (Vacancies, Interstitials) in crystal structure [2.13].

This work is concerned with intrinsic defects due to the Schottky defect (when an atom leaves its position to create a vacancy).

There are two types of vacancies, anion and cation vacancies [2.14]:

- Anion vacancies have a negative effective charge. They are created when an atom, which accepts electrons, is removed.
- Cation vacancies have a positive effective charge. They are created when an atom, which donates electrons, is removed, as illustrated in Figure 2-12.

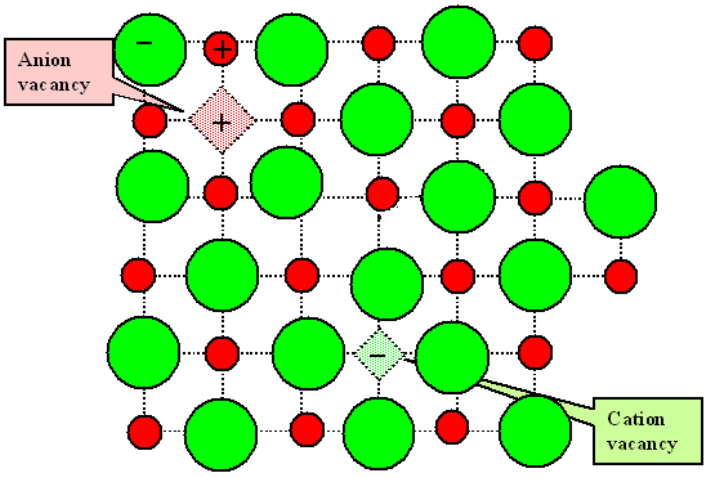

Figure 2- 12: The two types of electronic Vacancies [2.14].

2.6.2: Point defect (extrinsic)

An extrinsic defect comprises odd atoms. These atoms are called solute when added intentionally to the materials and impurities if unintended. If the odd atoms occupy a lattice site, it is called a substitutional solute; however, it is called an interstitial solute if the odd atoms occupy an interstitial site. This is because the size of interstitial sites is relatively small. The small solute atoms often fill interstitial sites. However, larger atoms will substitute a lattice site [2.12].

2.7: Ambipolar effect

Ambipolar effects appear significantly at high temperatures (dependent on the type of material). The high temperature excites charge carriers to form electron-hole pairs. These carriers will be in excess of their equilibrium concentration. If a temperature gradient is maintained in a semiconductor, the concentrations of charge carriers (electrons and holes) will increase more than equilibrium concentration. The concentration gradient of each charge carrier is in the direction of the temperature gradient. Therefore, the diffusion of charge carriers will cause a flux (electron and hole fluxes) towards the temperature gradient. These fluxes cannot be predicted to be equal; in other words, there is a net electrical current. In the presence of an electrical field, the net current will reduce to zero. The two fluxes will be very close to each other. The large one has been decreased and the second component increased, owing to the field. This effect is called an ambipolar effect. The flow due to the ambipolar effect is particularly interesting because it contributes extra terms [2.15].

When a material is subjected to a temperature gradient, there are many electron-hole pairs that are excited thermally at the hot end. These carriers will diffuse towards the cool side (T cool), and then the electron-hole pairs recombine and release heat. The overall thermal conductivity will increase as well as the Nernst

effect, while thermopower is decreased due to the ambipolar effect [2.8, 2.16]. The beginning of ambipolar thermal conduction occurs at almost the same temperature of the peak value of the Seebeck and electrical resistivity. This is due to the ambipolar effects [2.3].

2.8: The intrinsic regime

An intrinsic regime is a regime in which the ambipolar effect happens. In this regime both carrier charges (electrons and holes) are present in equal numbers. At special temperatures, when the thermal-generated carrier densities in both the conduction and valence bands are much larger than the background doping densities, the semiconductor behaves as an intrinsic semiconductor (in the intrinsic regime). The carrier densities are given as [2.17]:

$$n = p = n_i \quad \text{……..(2.15)}$$

where: n , p are the numbers of electron and hole densities inside the material at T temperature respectively and n_i is the number of carrier densities in material during the intrinsic regime.

When a sample is in the intrinsic regime, the Seebeck and Righi-Leduc effects tend to be zero. This is due to the contribution of electrons and holes cancelling each other. In contrast, in the Nernst effect, thermal and electrical conductivity tend to be additive due to the contribution of electrons and holes being added to each other [2.8].

2.9: The thermal conductivity

In physics, thermal conductivity κ is the property of material to conduct heat, or how well a material can conduct heat. However, heat transfer by

conduction involves the transfer of energy within a material without any motion of the material as a whole.

The contribution towards thermal conductivity of an electronic conductor can be divided into two parts. The first part of the heat flux is carried by the electrons, or the holes, or by both κe (electronic); the other, κ_l (lattice) is that part carried by the lattice vibrations, usually the acoustic phonons. These contributions are not always independent and are often difficult to separate experimentally.

$$\kappa = \kappa_e + \kappa_l \quad \text{.....(2.16)}$$

If a semiconductor is pure (or very lightly doped) the κ_e will be negligible compared with the lattice part κ_l. If a semiconductor is moderately heavily doped with $l0^{l8}$ to 10^{20} electrons/cm^3, the electronic and lattice parts can be comparable in magnitude. If we apply a magnetic field, we change κ_e, leaving κ_l unchanged. The change in κ_e is related to the scattering mechanism, mobility and degree of degeneracy of the material.

where: κ_e is the electrical thermal conductivity and κ_l is the lattice thermal conductivity. Also, we can define electronic thermal conductivity related to the two types of charge carries (electron and holes):

$$\kappa_e = \kappa_e^e + \kappa_e^h + \kappa_a \quad \text{.....(2.17)}$$

where: κ_e^e and κ_e^h are electrical thermal conductivity related to electrons and holes respectively and κ_a is the electronic thermal conductivity due to ambipolar effect.

Many researchers have attempted to minimize the thermal conductivity (because electrical conductivity κ_e is fixed to the material at a fixed temperature). This happens when the phonons have an average free path equal to the interatomic spacing between the atoms of thermoelectric materials [2.1].

2.10: Effects of magnetic field on thermoelectric materials

The effect of a magnetic field would change the direction of the motion and the mean energy of the electrons [2.18, 2.19]. It thereby acts as a sort of scattering agent, this scattering being always to one side for a given field and type of carrier [2.7].

1) Sometimes it enhances the Seebeck coefficient more than 50%, and otherwise, it changes the sign of the Seebeck coefficient [2.20].
2) Increase of the electrical resistivity ρ.
3) Reduction of the thermal conductivity κ.

The decrease in the electronic thermal conductivity is somewhat faster than in the electric conductivity [2.21]. This is due to the lower electron velocity of thermal energy than that of the electrical field.

The impact of the magnetic field on the thermal conductivity increases due to the effect on electronic thermal conductivity κ_e. The effect of the magnetic field on thermal conductivity for thermoelectric and thermomagnetic semiconductor samples is small. This is because most of the heat is conducted by phonons (lattice vibration) κ_l [2.22].

2.11: Properties requirement for useful thermomagnetic materials

The materials that are used as power generators should have [2.21, 2.23]:

1- Intrinsic or lightly doping single crystal materials which exhibit intrinsic behaviour at a specific temperature.

2-

- Large electron mobility and mobility ratio (electrons mobility divided by holes mobility).

- The value $\mu_e B \geq 10^4$ T.cm^2.V^{-1}.Sec^{-1}.
- Small thermal conductivity and electrical resistivity.
- Narrow band gap $\mathbb{E}_g$ of the order of $K_B T$.
  where: (K_B) is the Boltzmann's constant.
- Large effective mass.

In other words, it is useful to make the magnitude $\frac{(m^*)^{3/2}\ \mu_e}{\kappa_L}$ as large as possible. Excellent thermo-magnetic materials require a perfect combination of values of all the above parameters [2.21].

2.12: X-ray powder diffraction

X-ray diffraction is one of the scientific techniques that use X-ray to obtain information about the structural characterization of crystal materials. This is conducted by incident X-ray of powder or microcrystal of the specimen.

Sample identification was carried out by using the X-ray diffraction (XRD) technique. Consider a set of lattice planes (hkl) with equidistant spacing between them, d(hkl). The wave vector of an incident plane wave is $\overrightarrow{K_o}$, and the incident angle between the plane wave and lattice plane is θ. Any point of one lattice plane (hkl) is scattering waves in phase in a direction $\vec{K}$ corresponding to the reflection law. In particular, the optical path between O and $\acute{O}$ follows directly [2.24], as shown in Figure 2-13:

$$\delta = HO + OK = 2d(hkl)sin\theta \quad \text{.....(2.18)}$$

where δ is the optical path between O and $\acute{O}$.

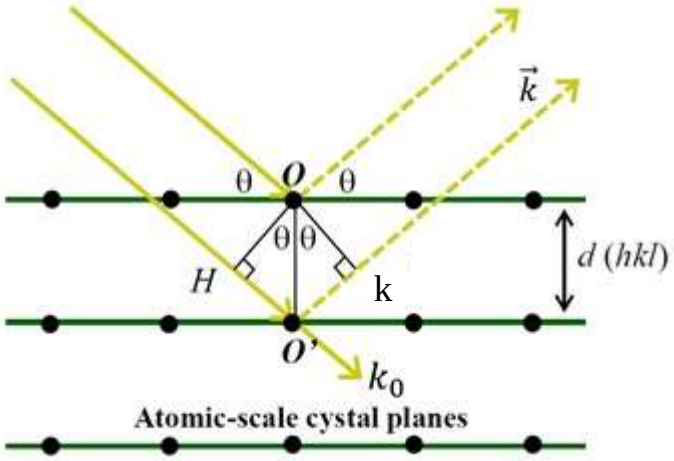

Figure 2-13: Scattering of x-rays from successive planes in phase [4.44].

The condition of this equation is that the optical path difference between the Incident and scattered waves is equal to an integer number of wavelengths. This equation is known as Bragg's equation or Bragg's law [2.24], and the condition which must be met to materialise this equation is called Bragg's condition.

$$2d(hkl)sin\theta = n\lambda \qquad Bragg's\ equation \quad \text{.....(2.19)}$$

$$\lambda \leq 2d \qquad Bragg's\ condition \quad \text{.....(2.20)}$$

where: λ is the wavelength, and n is an integer value known as the diffraction order, d is the lattice inter-planar spacing of the crystal. A single compound will have a set of d-spaces which represent the planes where an x-ray beam can pass through the atoms. Each set of planes has a specific angle for diffracted X-rays due to the difference in the distance between these sets. The structure of any compound is understood by making a comparison between the sets of d-spaces obtained and the standard sets of compounds. The peaks in diffraction pattern refer to the X-rays that reflect at special angles based on the spaces between the atomic planes in the crystal structure. A powder has different orientation planes through the structure due to the random orientation of the powder material, as shown in figure 2-14.

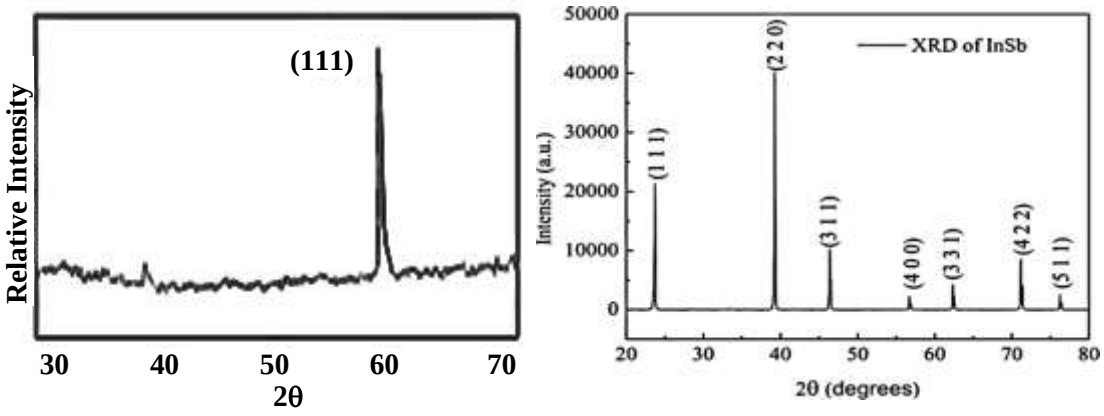

Figure 2-14: XRD pattern for InSb: (a) bulk single crystal [4.25] and (b) powder single crystal [4.26].

2.13: Crystal growth

The growth methods can be classified as solution, vapour and melt growth [2.27]. The first two methods are used to prepare films. Preparation of epitaxial films can be achieved by implementing the following processes: liquid phase epitaxy (LPE) [2.28], molecular beam epitaxy (MBE) [2.29] and metal-organic vapour phase epitaxy (MOVPE) or metal-organic chemical vapour deposition (MOCVD) [2.30, 2.31]. The third method is used to prepare InSb bulk crystals using one of the techniques such as: Czochralski [2.32], Bridgman [2.33], travelling heater [2.34] and zone melting [2.35].

This work is concerned with the production of bulk sample methods, since the sample used in this research was bulk. Hence, a brief description on mean methods used to produce a single crystal is presented, although none of these methods was used in this research work:

1- Czochralski method [2.36]: the raw material is melted in a crucible, which is normally made of quartz, under inert atmosphere. A seed crystal is mounted on a rod. The rod is dipped into the melt, then pulled upwards with rotation at the same time. The control of temperature gradient, rate of pulling, and

speed of rotation can produce a large, cylindrical single-crystal, as shown in Figure 2-15.

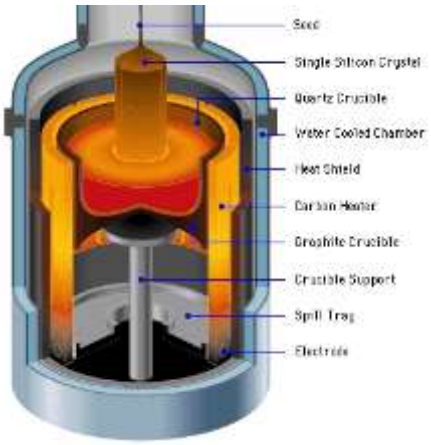

Figure 2-15: Schematic diagram illustrates Czochralski method [2.36].

2- Bridgman method [2.37]: the polycrystalline materials are heated up above their melting point in a container; the container is a sealed quartz tube. Then, by slowly cooling the tube from the seed crystal end, a single crystal is grown on. The seed is formed along the tube length, as depicted in Figure 2-16. The crystallographic orientation of the single crystal produced is the same as that of the seed crystallographic orientation. The produced crystal in this method has striations, ridges and voids. The Bridgman method can be performed in two different ways: horizontal and vertical geometries. This method is easier to implement than the Czochralski method.

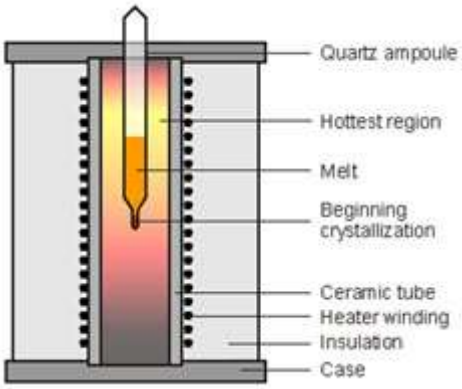

Figure 2-16: Schematic diagram illustrates Bridgman method [2.36].

3- Travelling heater method [2.38]: this method is based on using a melt of another material as a solvent e.g. Te for the dissolution, transport and growth of the crystal purposes. This process (vertical growth) occurs inside a sealed quartz tube. The movement of either heater or the sealed ampule leads to obtaining a molten zone and then growing the crystal sample, as shown in Figure 2-17.

Figure 2-17: Photo illustrates Travelling heater method [2.36].

4- Zone melting method [2.39]: this method is used to produce ultra-pure metal with low defect density. The polycrystalline rod sample is placed in a tubular furnace. The heater has the ability to move very slowly in one direction. As the heater moves along the tube, the material crystalizes, as shown in Figure 2-18.

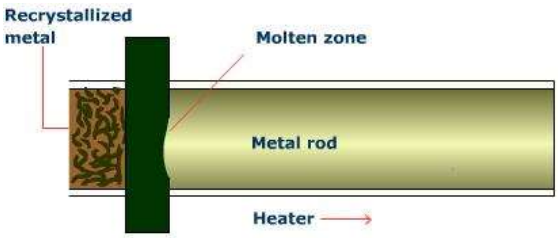

Figure 2-18: Schematic diagram illustrates Zone melting method [2.36].

The best material among the III-V semiconductors for fabrication is InSb [2.27]. As a result of the relatively low melting point for InSb (527 °C) and the small saturation vapour pressure, the ability to produce bulk InSb by more than one

method is feasible. Scientists began to fabricate single crystal InSb bulk materials in 1962 [2.27]. In 1959, the polycrystalline InSb was an easily obtainable material [2.40].

2.14: EDX analysis

Energy dispersive X-ray spectroscopy (EDX) is a chemical microanalysis technique implemented with scanning electron microscopy (SEM). The principle of the EDX technique is to detect X-rays which are emitted from a sample through bombardment by an electron beam. The emitted X-rays are implemented to characterize the elemental composition of the sample [2.41].

The sample is bombarded with an electron beam which is emitted from the scanning electron microscope. The incident electrons collide with the sample atoms that have electrons; in the process some of them are knocked. The vacated position in the inner shell electron is occupied by a higher-energy electron that came from an outer shell. An X-ray is emitted in this process [2.41].

The transferring electron releases an amount of energy that is dependent on the shell that the electron was transferred from, as well as the shell that the electron is transferring to. Furthermore, each element atom releases X-rays with individual amounts of energy through the transference process. Thus, the identity of the atom can be established by measuring the energy presented in the X-rays that are released by the sample through electron beam bombardment [2.42].

Counting photons is used to measure X-ray intensities and the statistical error limits the precision obtained. The precision for most elements is typically lower than ± 1%, the accuracy is generally nearer ± 2%, due to other factors such as uncertainties in the composition of the standards and errors in the different corrections which need to be stratified to the raw data [2.43].

References

[2.1] A. F. Loffe, *Semiconductor thermoelements, and thermoelectric cooling*, Revised. Infosearch, Ltd., 1957, 1957.

[2.2] T. M. Tritt and M. A. Subramanian, "Thermoelectric Materials, Phenomena, and Applications: A Bird's Eye View," *MRS Bull.*, vol. 31, no. 03, pp. 188–198, Mar. 2006.

[2.3] G. J. Snyder and E. S. Toberer, "Complex thermoelectric materials.," *Nat. Mater.*, vol. 7, no. 2, pp. 105–114, 2008.

[2.4] http://thermoelectrics.matsci.northwestern.edu/thermoelectrics/history.html

[2.5] G. S. Nolas, J. Sharp, and H. J. Goldsmid, *Thermoelectrics*, vol. 45. Berlin, Heidelberg: Springer Berlin Heidelberg, 2001.

[2.6] L. L. Campbell, *Galvanomagnetic and thermomagnetic effects*, J. J. Thom. London ; New York [etc.] : Longmans, Green and co., 1923.

[2.7] D. M. Rowe, *CRC Handbook of thermoelectrics*. 1995.

[2.8] R. T. Delves, "Thermomagnetic effects in semiconductors and semimetals," *Reports Prog. Phys.*, vol. 28, no. 1, pp. 249–289, 1965.

[2.9] Makariy A. Tanatar November 21, 2008, http://canfield.physics.iastate.edu/course/EM_35.pdf

[2.10] F. P. Incropera, D. P. DeWitt, T. L. Bergman, and A. S. Lavine, *Fundamentals of Heat and Mass Transfer*, Sixth Edit. John Wiley & Sons, 2007.

[2.11] J. P. Holman, *Heat Transfer*, Sixth Edit. McGraw-Hill, 1986.

[2.12] http://www.mse.berkeley.edu/groups/morris/MSE205/Extras/defects.pdf

[2.13] http://www.slideshare.net/adhiprimartomo/mme-323-materials-science-week-5-imperfection-in-solids

[2.14] http://www.tf.uni-kiel.de/matwis/amat/def_en/kap_2/illustr/t2_1_2.html

[2.15] P. J. Price, "CXXXV. Ambipolar thermodiffusion of electrons and holes in semiconductors," *Philos. Mag. Ser. 7*, vol. 46, no. 382, pp. 1252–1260, Nov. 1955.

[2.16] C. M. Orovets, "Search for Resonant Impurities in Bismuth and Bismuth-Antimony Alloys: Lithium, Magnesium, and Sodium," The Ohio State University, 2012.

[2.17] S. S. Li, *Semiconductor Physical Electronics*. New York, NY: Springer New York, 2006.

[2.18] R. T. Delves, "The prospects for Ettingshausen and Peltier cooling at low temperatures," *Br. J. Appl. Phys.*, vol. 13, no. 9, pp. 440–445, Sep. 1962.

[2.19] M. E. Ertl, G. R. Pfister, and H. J. Goldsmid, "Size dependence of the magneto-Seebeck effect in bismuth-antimony alloys," *British Journal of Applied Physics*, vol. 14, no. 3. Ertl2002, pp. 161–162, 2002.

[2.20] S. Tanuma, "Thermoelectricity, thinking of the past and tomorrow," *Seventeenth Int. Conf. Thermoelectr. Proc. ICT98 (Cat. No.98TH8365)*, pp. 33–36, 1998.

[2.21] R. W. . J. Ure, "Theory of materials for thermoelectric and thermomagnetic devices," *Proc. IEEE*, vol. 51, no. 5, 1963.

[2.22] C M Bhandari; David Michael Rowe, *Thermal conduction in semiconductors*. New York : Wiley, 1988.

[2.23] S. W. Angrist, "A Nernst Effect Power Generator," *J. Heat Transfer*, vol. 85, no. 1, p. 41, 1963.

[2.24] C. Kittel, *Introduction to Solid State Physics*, vol. 8th edition. John Wiley & Sons, Inc., 1995.

[2.25] M. K. Khalaf, G. H. Mohammed, and F. Y. Hadi, "Growth Techniques and Some Physical Properties of InSb Single Crystal Abstract : Introduction :," vol. 8, no. 1, 2011.

[2.26] X. Cai and J. Wei, "Temperature dependence of the thermal properties of InSb materials used in data storage," *J. Appl. Phys.*, vol. 114, no. 8, pp. 1–8, 2013.

[2.27] V. Tetyorkin, A. Sukach, and A. Tkachuk, "Infrared Photodiodes on II-VI and III-V Narrow-Gap Semiconductors," in *Infrared Photodiodes on II-VI ans III-V Narrow-Gap Semiconductors, Photodiodes - From Fundamentals to Applications*, I. Yun, Ed. InTech, 2012.

[2.28] V. K. Dixit, B. V. Rodrigues, H. L. Bhat, R. Venkataraghavan, K. S. Chandrasekaran, and B. M. Arora, "Growth of InSb epitaxial layers on GaAs (0 0 1) substrates by LPE and their characterizations," *J. Cryst. Growth*, vol. 235, no. 1–4, pp. 154–160, 2002.

[2.29] R. Tessler, C. Saguy, O. Klin, S. Greenberg, E. Weiss, R. Akhvlediani, R. Edrei, and a. Hoffman, "Oxide-free InSb (100) surfaces by molecular hydrogen cleaning," *Appl. Phys. Lett.*, vol. 88, no. 3, pp. 1–3, 2006.

[2.30] P. Caroff, M. E. Messing, B. Mattias Borg, K. a Dick, K. Deppert, and L.-E. Wernersson, "InSb heterostructure nanowires: MOVPE growth under extreme lattice mismatch.," *Nanotechnology*, vol. 20, no. 49, p. 495606, 2009.

[2.31] O. Sugiura, H. Kameda, K. Shiina, and M. Matsumura, "Low-temperature growth of InSb by vacuum MOCVD using TEln and SbH3," *J. Electron. Mater.*, vol. 17, no. 1, pp. 11–14, Jan. 1988.

[2.32] G. N. Kozhemyakin, "Influence of ultrasonic vibrations on the growth of semiconductor single crystals," *Ultrasonics*, vol. 35, no. 8, pp. 599–604, 1998.

[2.33] A. A. Ebnalwaled, "Evolution of growth and enhancement in power factor of InSb bulk crystal," *J. Cryst. Growth*, vol. 311, no. 19, pp. 4385–4390, 2009.

[2.34] K. W. Benz and G. Müller, “GaSb and InSb crystals grown by vertical and horizontal travelling heater method,” *J. Cryst. Growth*, vol. 46, no. 1, pp. 35–42, Jan. 1979.

[2.35] D. R. Mason and J. S. Cook, “Zone Leveling and Crystal Growth of Paratectic Compounds,” *J. Appl. Phys.*, vol. 32, no. 3, p. 3, 1961.

[2.36] http://www.tf.uni-kiel.de/matwis/amat/elmat_en/kap_6/illustr/i6_1_1.html

[2.37] https://www.mtixtl.com/xtlflyers/bridgman.doc

[2.38] http://rmdinc.com/traveling-heater/

[2.39] http://www.britannica.com/science/zone-melting

[2.40] R. Bowers, R. W. Ure, J. E. Bauerle, and A. J. Cornish, “InAs and InSb as thermoelectric materials,” *J. Appl. Phys.*, vol. 30, no. 6, pp. 930–934, 1959.

[2.41]http://www.surfacesciencewestern.com/analytical-services/scanning-electron-microscopy-coupled-with-energy-dispersive-x-ray-semedx-spectroscopy/

[2.42] http://www.eag.com/mc/energy-dispersive-x-ray-spectroscopy.html

[2.43] University of California, “Introduction to Energy Dispersive X-ray Spectrometry (EDS),” 2015.

CHAPTER 3

Literature Review

3.1: Introduction

Various methods have been investigated for growing III-V semiconductor crystals. As a result of the relatively low melting point for InSb (527 °C) and the small saturation vapour pressure, it is possible to produce bulk InSb by more than one method. The best material among the III-V semiconductors for fabrication is InSb [3.1].

Scientists began to make single crystal InSb bulk materials in 1962 [3.1], having discovered three years earlier that polycrystalline InSb was an easily obtainable material [3.2].

3.2: The production of the single crystal InSb bulk material

In 1979, Benz et al. [3.3] succeeded in producing single crystals of GaAs and InSb. These materials were grown using the travelling heater method (THM) that employed vertical and horizontal systems. The effect of ultrasonic vibrations on striations in InSb crystals grown that have the orientation (111) was investigated by

Kozhemyakin (1998) [3.4]. A modification was made to the Czochralski method by employing ultrasonic vibrations, which led to minimising the striations in the central part of the grown crystals.

Meanwhile, Gadkari et al. (1998) [3.5] were studying the vertical directional solidification (VDS) technique. They successfully grew high electron mobility undoped and doped single crystals InSb with Te. The XRD pattern of InSb from the open ampoule was of poor quality crystal structure and it was polycrystalline. However, the sealed ampoule under vacuum 10^{-5} Torr, showed better quality and prominent reflection for (220) orientation, while the sealed ampoule with inert gas showed the best quality and prominent (220) orientation. The XRD data for the last sealed ampoule method showed an excellent agreement with the standard data for XRD pattern. The undoped crystal exhibited as p-type behaviours, while doped crystal doped with tellurium exhibited as n-type.

In a further study, Gadkari et al. (2000) [3.6] utilised the VDS technique to grow undoped InSb and doped with Te; the former was p-type and the latter n-type. The mobility of undoped InSb was 3.4×10^{3} $cm^{2}.V^{-1}.Sec^{-1}$ at 20 k and 3×10^{4} $cm^{2}.V^{-1}.Sec^{-1}$ at 20 K for doped single crystals InSb with Te. The XRD pattern of InSb showed good quality crystal structure and was in full agreement with the standard data. It was observed that a good quality crystal structure of single crystals InSb could be grown reliably by VDS methods.

Later studies included an experiment (Boguslavskii et al., 2004) [3.7], that used floating zone melting (FZM) to obtain indium antimonide monocrystal doped with Te and an investigation (Khalaf et al., 2011) [3.8] utilizing vertical growth in a two-zone furnace from the pure melt to obtain single crystals of InSb. The XRD for bulk materials observed that the crystallographic direction was fully oriented within the (220) plane. The intensity of this plane was increased near to the stoichiometry of the compound. The XRD patterns were in full agreement with standard data for InSb compound. However, the thin film sample had a polycrystalline structure. It was

grown highly oriented with (220), (200) and (111) directions. The optical energy gap values at room temperature were 0.16 and 0.17 eV.

Finally Gadkari (2012) [3.9], extended earlier studies (1998; 2000) by employing the VDS technique to obtain uncoated bulk single crystals without a seed and with no contact to the ampoule wall, in the absence of any external pressure application. The furnace used in this method was designed and fabricated for stable axial and radial temperature gradients. This technique led to detached growth, relatively low dislocation density and higher carrier mobility. The XRD analysis showed that the samples were monocrystalline and the single peak occurs at 2θ with (220) direction. The study's conclusion was that the VDS technique appeared to be a more commercial method.

3.3: The production of the polycrystalline InSb bulk material

During the same period, a number of studies were investigating various methods for the production of Polycrystalline InSb bulk material. Ebnalwaled (2009; 2011) [3.10, 3.11] employed the vertical Bridgman technique (modified traveling solvent method (TSM) technique). The study obtained low-defect InSb crystals from stoichiometric melts. The XRD pattern showed that the sample was polycrystalline material, with prominent peaks from (111), (220), (311), (400), (331), (422), and (511). It was observed that the structural parameters for InSb crystal obtained were in full agreement with the standard values. It was also reported that the sample exhibited as p-type semiconductor properties related to the Seebeck coefficient measurement.

The Bridgman method was also used by Se-Hwan et al. (2011) [3.12] to grow InSb crystal at various crystal growth speeds. The Bridgeman furnace used had three heating zones. The research team studied dependency of the crystal growth speed on the crystal quality structure. The obtained crystals were not singly oriented and the transmittance of the crystal increased with decreasing growth speed.

All the above methods prepared bulk single crystal or polycrystalline InSb based on the use of a sealed quartz tube to obtain good quality crystal structure. By contrast, Gadkari et al. (1998) [3.11] had obtained poor quality crystal structure when using open quartz tube. Furthermore, studies by Ebnalwaled (2009; 2011) [3.10, 3.11] obtained polycrystalline samples that had a Seebeck coefficient 35 folds lower than a single crystal due to the increase of charge carriers (electrons and holes).

Table 3-1 explains the differences among all the above methods.

Table 3-1: provides a critical comparison on different methods performed by researchers and their achieved results.

	Author	crystallinity	method	Doped element
1.	K. W. Benz et al. [3.3]	single crystals	TH	undoped
2.	G.N. Kozhemyakin [3.4]	single crystals	Czochralski	Te
3.	D. B. Gadkari et al. [3.5]	Polycrystalline (open tube) single crystals (sealed tube under vacuum) single crystals (sealed tube under inert gas)	VDS	Undoped, Te
4.	A. A. Boguslavskii et al. [3.7]	single crystals	FZM	Te
5.	M. K. Khalaf et al. [3.8]	single crystals (sealed tube under vacuum)	two-zone furnace	undoped
6.	D. B. Gadkari [3.9]	single crystals	VDS with some modoification	undoped
7.	A. A. Ebnalwaled [3.10, 3.11]	Polycrystalline (sealed tube under vacuum)	vertical Bridgman technique	undoped
8.	Se-Hwan et al. [3.12]	Polycrystalline (sealed tube under vacuum)	Bridgman	undoped

3.4: The production of the polycrystalline InSb thin films

The production of polycrystalline InSb thin films has been explored in two key studies. In the first (Senthilkumar, et al., 2005) [3.13], InSb thin film was prepared on

glass substrates by vacuum evaporation. The glass substrates were well-cleaned at different substrate temperatures (303, 473 and 523 K). The elemental composition of the samples was examined and found to be 24% In and 76% Sb. The samples were polycrystalline InSb thin films according to the XRD patterns, with preferential orientation along (111) plane. The Hall measurements indicated that the films were p-type, with carrier concentration $\approx 10^{16}$ cm^{-3} and electron mobility 1.1-6.5$\times 10^{3}$ $cm^{2}.V^{-1}.S^{-1}$.

The second study (Vishwakarma, et al., 2012) [3.14] presented n-type InSb thin films. The thin films were deposited on a substrate made of glass with a thickness of 300 nm under vacuum levels of $\sim 10^{-5}$ Torr. The thin films were deposited from starting materials that were prepared by using 5N purity from indium and antimony metal powders as raw materials with different non-stoichiometric compositions as $In_{1-x}Sb_x$ ($0.2<x<0.4$). The XRD pattern for both starting materials and thin films confirm the samples were polycrystalline with orientation along (111) and (220).

Both studies described above used off-stoichiometric composition to obtain either n-type or p-type, depending on the mixing ratio of raw materials. The obtained sample behaves as n-type when In is enriched and p-type for enriched Sb.

Table 3-2 explains the differences between the two above methods.

Table 3-2: provides a comparison between different methods performed by researchers and their obtained results.

	Author	crystallinity	Semiconductor type	Doping ratio
1.	V. Senthilkumar, et al. [3.13]	Polycrystalline	p-type	24% In and 76% Sb
2.	S. R. Vishwakarma, et al. [3.14]	Polycrystalline	n-type	In1-xSbx ($0.2<x<0.4$)

3.5: Previous studies related to some thermomagnetic effects on different materials

There has been extensive research into thermomagnetic effects on different materials within recent decades. Prior to that, as mentioned in Chapter One, research was more limited due to the fact that induction of a strong magnetic field resulted in considerable loss of energy. Consequently, despite initial interest in the TM effect during the 1960s, research into the topic largely waned until more recent developments occurred in the higher efficiency of magnetic conduction.

Previous key research has tended to investigate thermomagnetic effects in relation to one or other of the four TMEs detailed in Chapter Two (Nernst effect; Righi-Leduc effect; Seebeck effect; and change in thermal conductivity) as well as making comparisons between them in some cases. A summary of the main research studies conducted since the late 1950s follows.

Herring et al. (1958) [3.16], reported that thermoelectric power and Nernst field depend on a magnetic field. Their factors were measured for a single-crystal n-type sample of high purity n-type Ge with various orientations. The measurements were under a magnetic field up to 0.18 T. The temperature was maintained between liquid hydrogen and the onset intrinsic conduction. They observed that Nernst coefficient and thermoelectric power near liquid air temperature are elevated. This is due to diffusion of the electrons and from their anisotropic scattering by the phonons, which is moved from hot to cold side.

Both the Nernst and Ettingshausen effects for a single crystal of Ge were investigated by Mette et al. (1959). The samples had different types of conductivity and various impurity densities. The samples were subjected to temperatures from 300-750 K and magnetic fields of 0.9 and 0.21 T. A comparison between the experimental results and theoretical expressions for the Nernst and Ettingshausen coefficients was made, and a very good qualitative agreement was observed, as shown in Figures 3-1, 3-2.

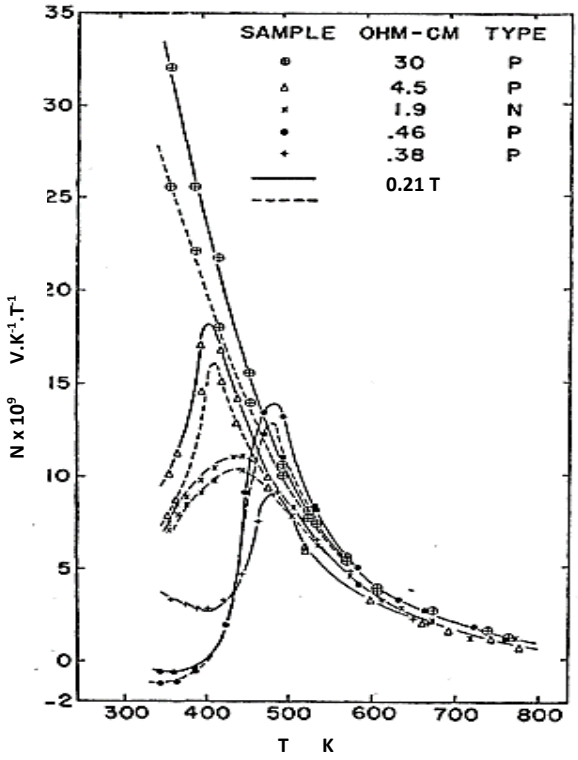

Figure 3- 1: The experimental Nernst coefficient in n- and p-type germanium as a function of temperature between 300-750 K under 0.9 T magnetic field [3.17].

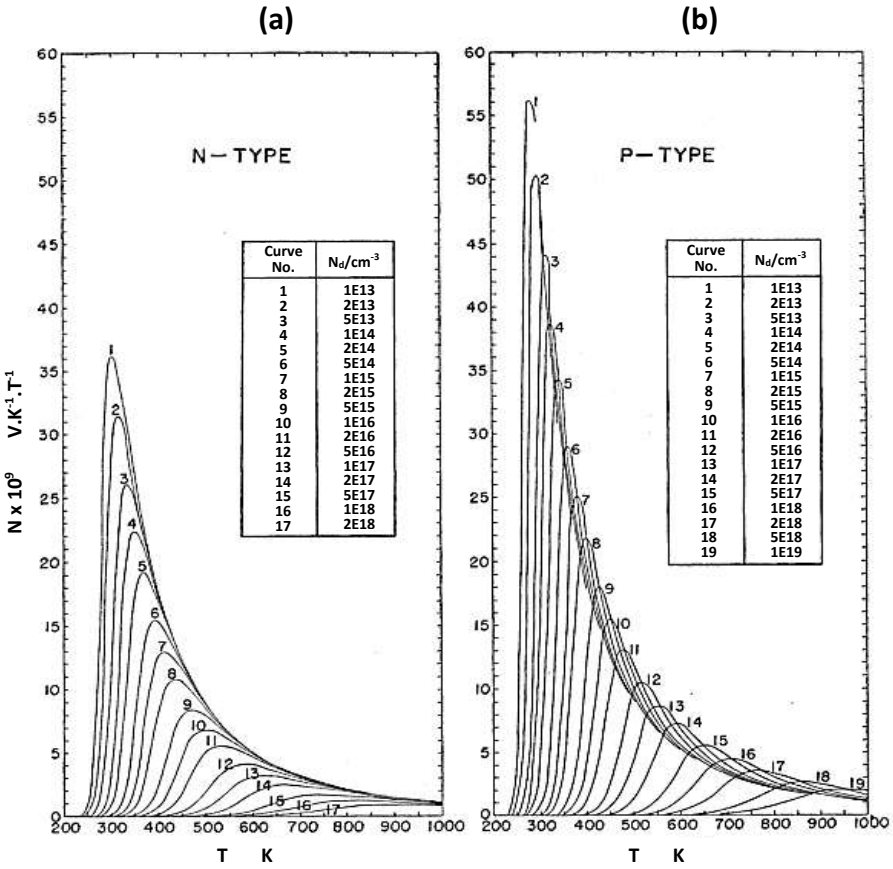

Figure 3- 2: The dependence of temperature on theoretical Nernst coefficient in, (a): n-type and (b): p-type germanium between 200-1000 K, under 0.9 T magnetic field [3.17].

By comparison, the Righi-Leduc effect was studied (Whitsett, 1961) [3.18] in mercuric selenide (HgSe) samples, which is a thermal analogy of the Hall effect where the temperature plays the role of the voltage and heat flow instead of electrical current. It was reported that the Righi-Leduc effect was particularly large. The results show the Righi-Leduc coefficient as a function of temperature, magnetic field and electrons concentration. The study found that for one carrier material, the Righi-Leduc coefficient was $S \cong (\kappa_E/\kappa)\mu$, where: κ_E is the electronic thermal conductivity, κ is the total thermal conductivity and μ is the electron mobility. This expression for the Righi-Leduc coefficient is in agreement with the experimental results. The experimental results showed that at room temperature the Righi-Leduc coefficient was between 0.27 and 0.34 $m^2.V^{-1}.Sec^{-1}$ for a sample that had carrier concentration between 55×10^{17} and 5.6×10^{17} cm^{-3} respectively, as shown in Figure 3-3.

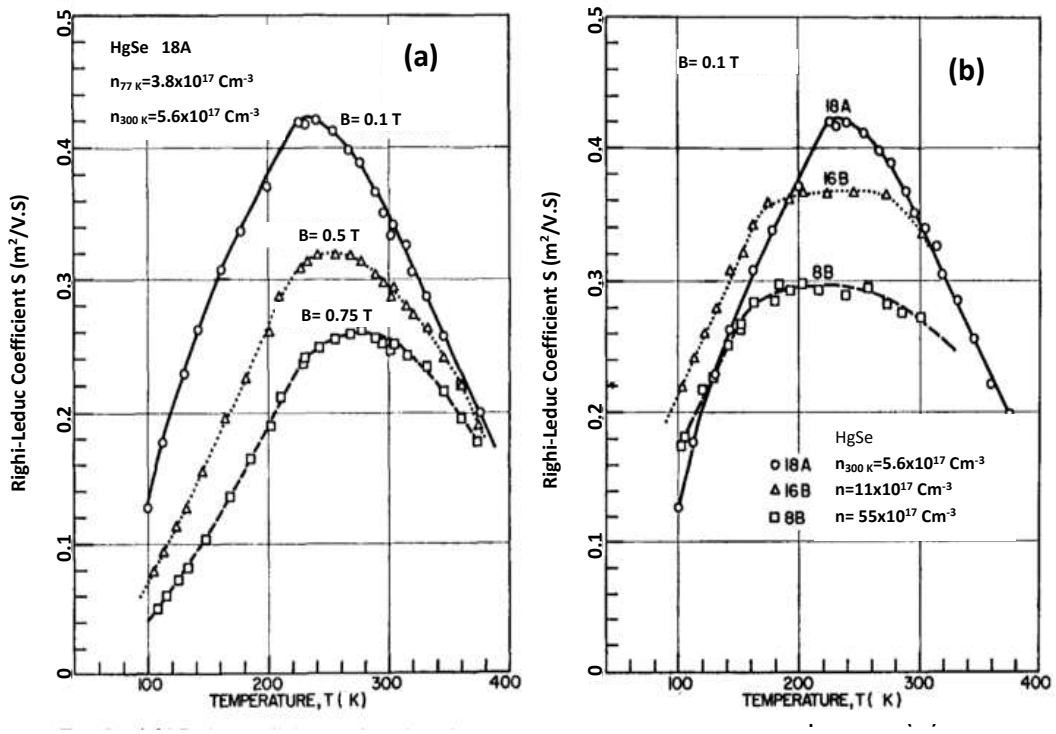

Figure 3- 3: The Righi-Leduc coefficient for HgSe as a function of temperature in, (a): different field for 5.6 x 10^{17} cm^3 electron concentration and (b): different electron concentrations under 0.1 T [3.18].

The effect of a magnetic field on the Seebeck coefficient, the resistivity, thermal conductivity and figure of merit under temperatures from 78-295 K and magnetic field up to 1352.8 kA/m for $Bi_{88}Sb_{12}$ samples were examined by Wolfe and

Smith (1962) [3.19]. The change in the direction of the magnetic field (rotate) in the plane perpendicular to the threefold axis will change the measured properties. The highest change will occur when the magnetic field is parallel to a bisectrix axis (y-axis). The figure of merit at room temperature was increased from 1.2×10^{-3} K^{-1} up to $2.9x10^{-3}$ K^{-1} under magnetic field of 1352.8 kA/m. It was 8.6×10^{-3} K^{-1} at 100 K under 79.5 kA/m, as shown in Figure 3-4.

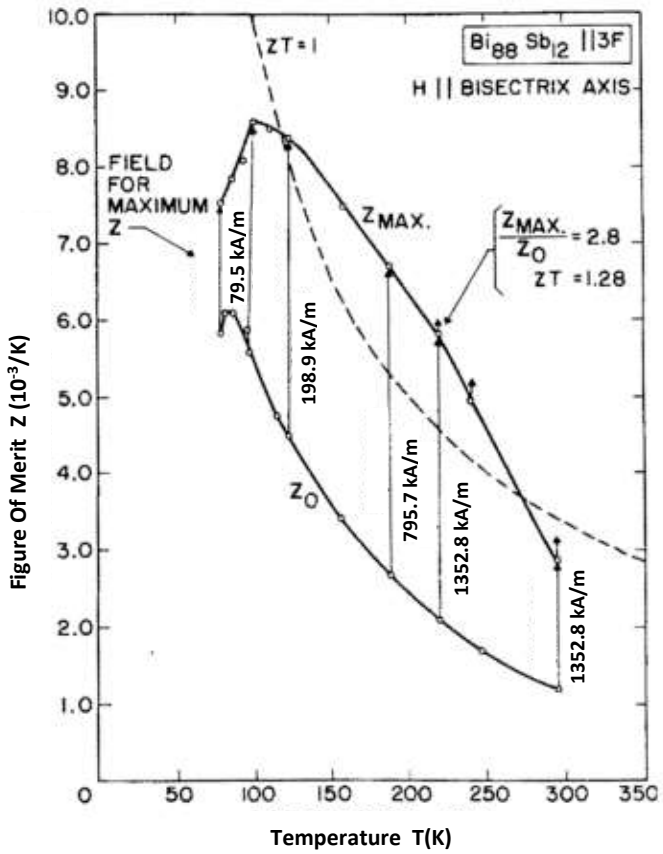

Figure 3- 4: The variation of thermoelectric properties with magnetic field for $Bi_{88}Sb_{12}$ sample [3.19].

The magneto-Seebeck coefficient was investigated (Ertl et al. 1963) [3.20] for bismuth antimonide (BiSb) alloys at 80 K under magnetic field; the length was reduced between each experiment to study the effect of sample geometry on magneto-Seebeck coefficient. The temperature gradient was subjected on the sample along the trigonal axis in all measurements. The experimental result for an alloy of 93% Bi-7% Sb showed that the maximum difference between the Seebeck coefficient under 397.8 kA/m for the greatest and shortest lengths was not more than 36 µV/°C. The size-dependence of thermoelectric power for 95% Bi -5% Sb was

measured. The expected change in thermoelectric power was calculated for the sample with a minimum length to width, as shown in Figure 3-5. It is preferable to utilize long thermoelements rather than short. This case would lead to obtaining higher Seebeck and Nernst coefficients. Also, it showed a difference in the sign of the Nernst coefficient with increasing magnetic field (from negative to positive values).

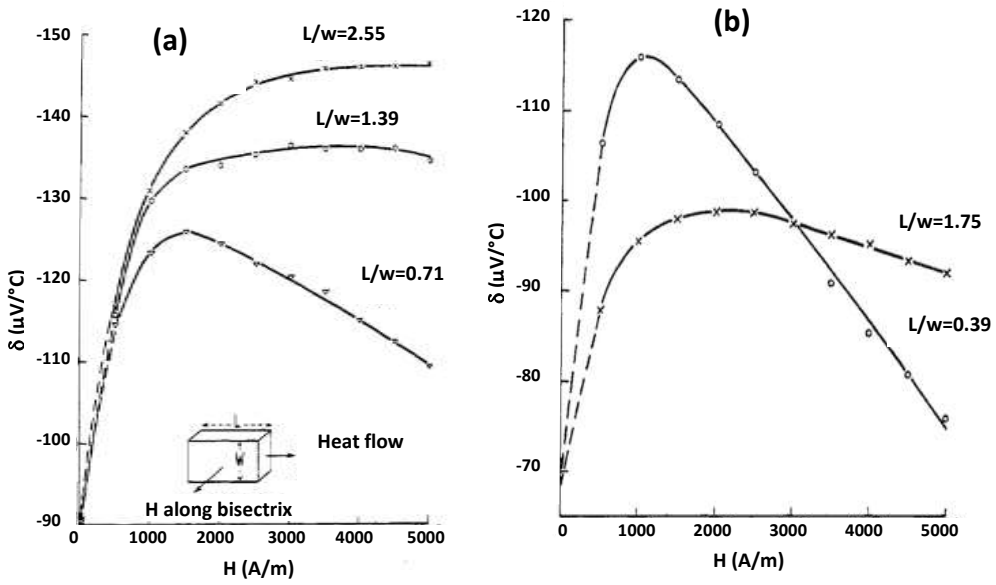

Figure 3- 5: The dependence of magnetic field strength on magneto Seebeck effect for, (a): 93% Bi – 7% Sb and (b): 95% Bi – 5% Sb samples [3.20].

Ure (1963) [3.21], reported that the figure of merit, which is dependent on Seebeck coefficient, for isotropic materials and parabolic bands will increase under magnetic field. This will happen when the dominant scatter is acoustic scattering. The study concluded that the device materials, which are based on thermomagnetic effects (has high Nernst figure of merit), should have:

1- The value of $\mu B >> 10^4$ $T.cm^2.V^{-1}.Sec^{-1}$.

where: μ is the mobility of charge carrier (depend on type of material p or n-type) and B is the magnetic field density.

2- The energy gap is less than K_BT.

3- The mobility of electrons and holes are similar.

where: K_B is Boltzmann's constant and T is the temperature degree.

4- Degenerate sample (sample doped with high level). In this case, the Nernst figure of merit was more than ten times smaller than Seebeck figure of merit.

5- The value of $(m^*)^{3/2}\,\mu/\kappa$ should be large.

where: m* is the effective mass of charge carrier (depend on type of material p or n-type) and κ is the thermal conductivity.

The comparison between Nernst and Seebeck devices was made, as shown in Figure 3-6.

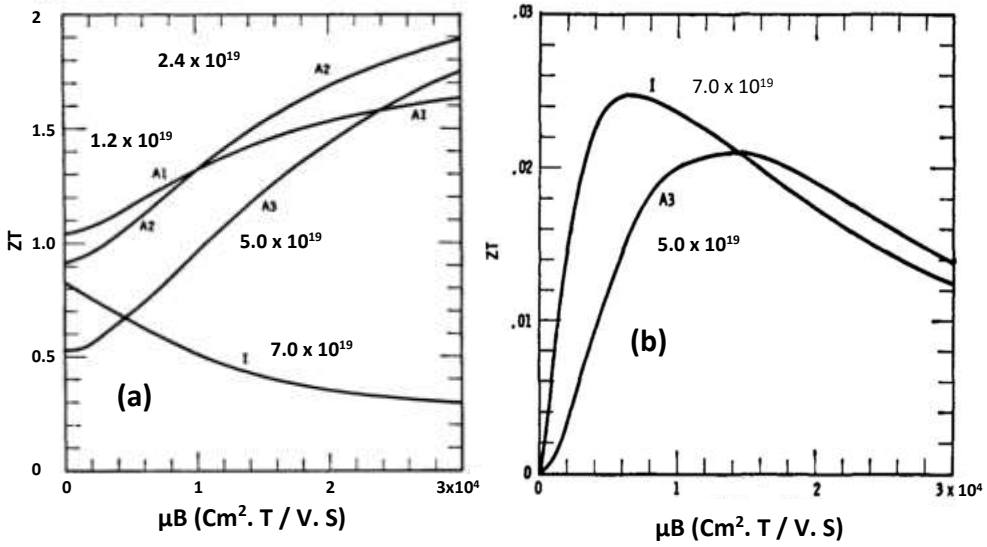

Figure 3- 6: The dependence of magnetic field on, (a): Seebeck figure of merit and (b): Nernst figure of merit for extrinsic semiconductor with different carrier concentrations [3.21].

Research into the Righi-Leduc effect on cadmium arsenide (CdAs) sample (Lovett et al., 2002) [3.22] exhibited a large Righi-Leduc effect. Measurements were taken under a temperature range of 300-64 K and magnetic field 39.7- 954.9 kA/m. It was observed that the results were in good agreement with expected values for a degenerate semiconductor. The experimental results were obtained that showed the Righi-Leduc coefficient was 0.66×10^4 $cm^2.V^{-1}.S^{-1}$ at room temperature and 1.4×10^4 $cm^2.V^{-1}.S^{-1}$ at 85 K. The Righi-Leduc coefficient was approximately independent at the low magnetic field, but it was dependent as B^{-2} with the high magnetic field, as would be expected, as shown in Figures 3-7, 3-8.

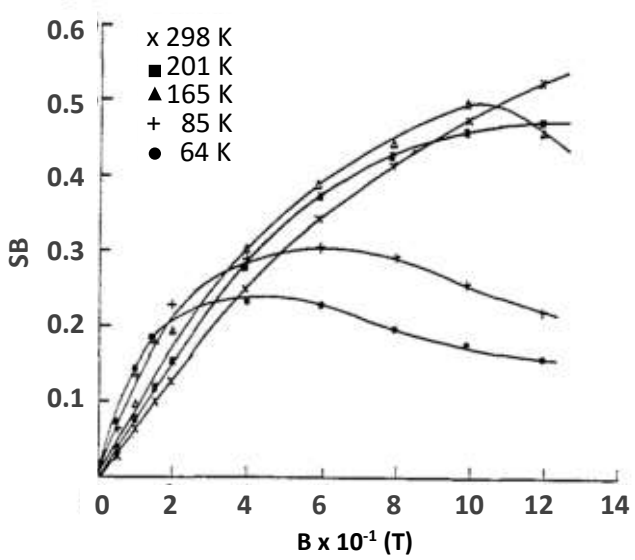

Figure 3- 7: The variation of dimensionless Righi-Leduc coefficient as a function of magnetic field for CdAs sample [3.22].

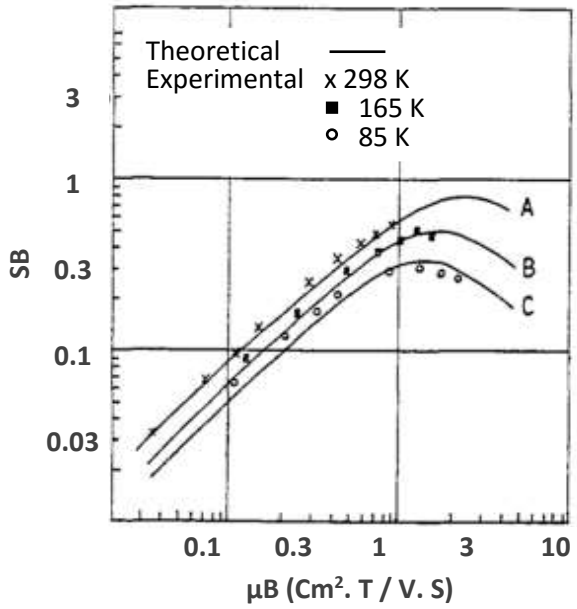

Figure 3- 8: The comparison of theoretical and experimental values of dimensionless Righi-Leduc coefficient as a function of magnetic field for CdAs sample [2.22].

Research into a thermal radiation detector (Washwell et al., 1970) [3.23], based on the Nernst effect, observed the ability to operate a thermal radiation detector possessing a relatively high-speed operation without loss of its responsivity. The experimental results showed that the material that had the optimum properties was Bi. It was found that bismuth Bi could operate at room temperature and $Bi_{97}Sb_3$ at a lower temperature.

Highly homogeneous undoped single crystal BiSb alloys were utilised (Yim and Amith, 1971) [3.24] to measure thermoelectric and thermomagnetic effects. This was conducted at temperatures from 77-300 K and under magnetic field of 0- 596.8 kA/m of n-type BiSb alloys. Thermoelectric and thermomagnetic effects were reported to be dependent on temperature difference, magnetic field level and crystallographic direction (parallel or perpendicular to the trigonal axis). The experimental results showed the largest thermoelectric figure of merit for n-type $Bi_{85}Sb_{15}$ (11×10^{-3} deg^{-1} at 100 and 80 K under 238.73 and 103.45 kA/m). The experimental results also showed the largest thermoelectric figure of merit for n-type $Bi_{99}Sb_1$ (4.1×10^{-1} deg^{-1} at 100 K under 596.8 kA/m). The figure of merit for p-type $Bi_{88}Sb_{12}$ doped with Sn was 2.3×10^{-3} deg^{-1} at 85 K under 596.8 kA/m. The hybrid cooling of Peltier plus magneto-Peltier effects in Te, Bi-Sb alloys were continued to cool from room temperature down to 128 K.

Tausch & Newrock (1977) [3.25] investigated the effect of the strong magnetic field on the Righi-Leduc coefficient of potassium polycrystalline samples. The temperature range was measured from 2 to 9 K under a maximum magnetic field of 9 T. It was observed that the lattice thermal conductivity led to a low-temperature Righi-Leduc coefficient dependent on the magnetic field. The Righi-Leduc coefficient was close to the theoretical predictions, after correcting the measuring Righi-Leduc coefficient due to the lattice contribution. The Righi-Leduc coefficient of potassium sample was relatively large due to the very large change in electronic thermal resistivity.

Grabov and Uryupin (1997) [3.26] prepared single crystals $Bi_{1-x}Sb_x$ ($0<x<0.15$) and measured electrical resistivity and thermal conductivity for $Bi_{1-x}Sb_x$ crystals for temperatures from 77-300 K and magnetic field up to 2 T. These parameters were dependent on alloy composition, doping, crystallographic orientation, temperature gradient and magnetic field. The experimental results investigated the magneto-thermoelectric figure of merit for n-type $Bi_{0.93}Sb_{0.07}$ crystals at temperature 180 K. The sample had a magneto-thermoelectric figure of merit 2.79×10^{-3} K^{-1} at B=0 T and 4.95×10^{-3} K^{-1} at B=0.5 T. The change of transport coefficient and figure of merit

caused by the magnetic field due to the reduction of energy, are shown in Figure 3-9. The highest magneto-thermoelectric figure of merit was obtained by doping with donor or acceptor impurity.

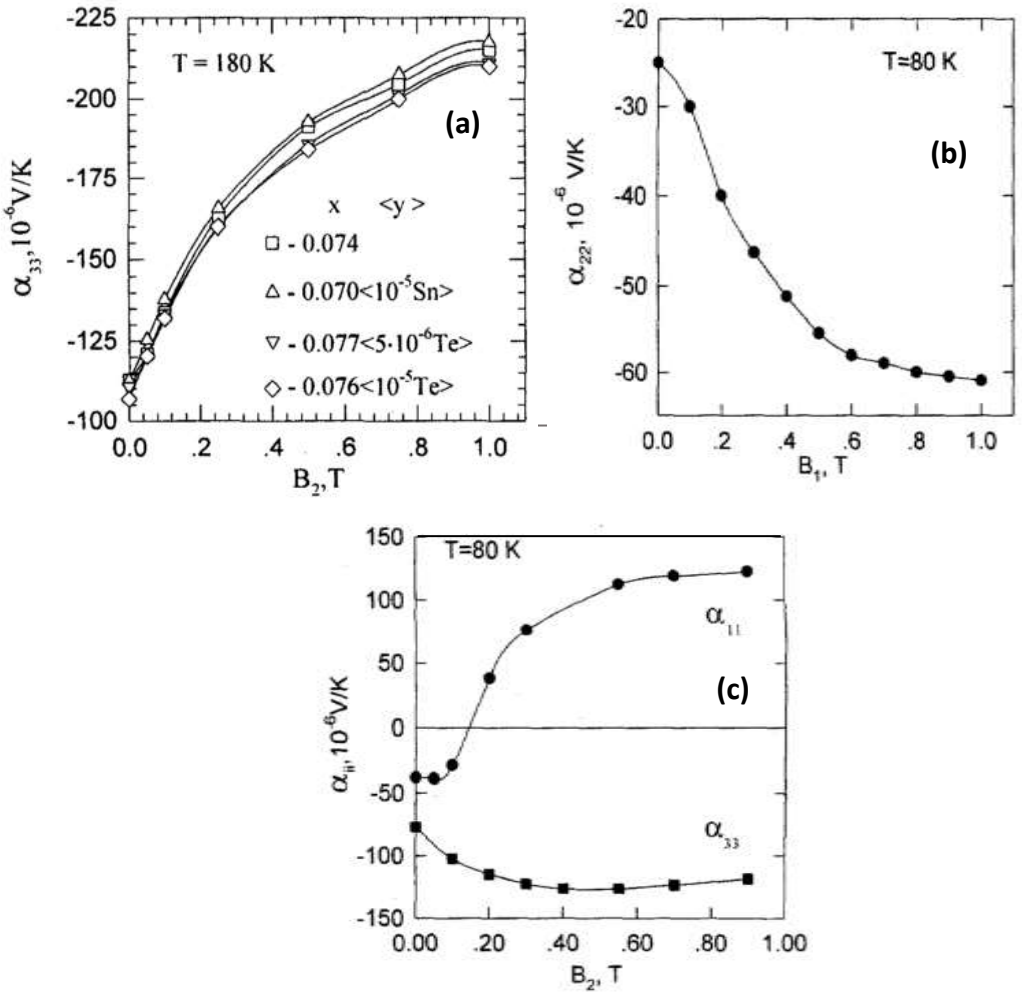

Figure 3- 9: The dependence of magnetic field on Seebeck coefficient for, (a): $Bi_{1-x}Sb_x$, (b): Bi<Te $_{0.05\ at\%}$> and (c): Bi single crystal samples [3.26].

Galvanomagnetic and thermomagnetic effects were investigated (Sakurai et al.1997) [3.27] to exploit the energy conversion by researching the ability to improve the clear changes in the Seebeck electromotive force (e.m.f) (longitudinal Nernst-Ettingshausen effect) and Petier cooling (Nernst effect) under the magnetic field. A temperature difference of 23 K at the environmental temperature of 100 K results from the Ettingshausen effect on the BiSb sample. The width was 10 mm, the magnetic flux density was 1 T, and the current density was 1 A/mm^2. The Nernst

temperature difference was 15.4 K under the above conditions, as shown in Figure 3-10.

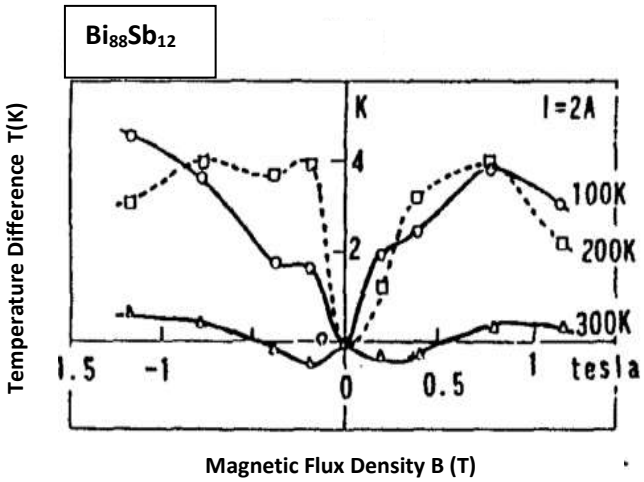

Figure 3- 10: The dependence of magnetic field on Nernst temperature difference for $Bi_{88}Sb_{12}$ sample [2.27].

Research undertaken by Ikeda et al. (1998) [3.28], showed that there was qualitative agreement between experimental and theoretical results using the parabolic two band model. They used Ge samples under magnetic field 0-4 T and temperature gradient between two sides was maintained at 10 K and the temperature average at the hot side was between 250-350 K. The experimental results showed that there was a temperature dependence on both Seebeck and Nernst coefficients. The samples were changed from the extrinsic state to the intrinsic at room temperature, as shown in Figure 3-11.

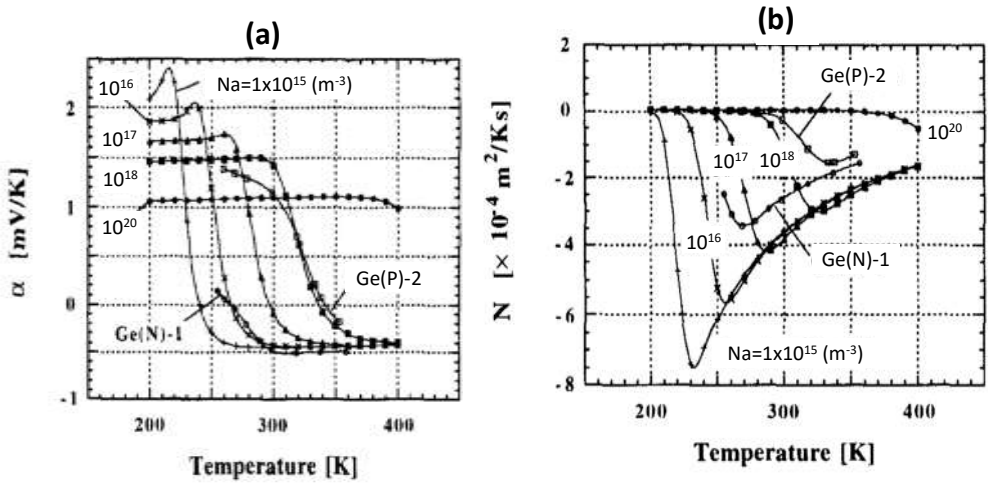

Figure 3- 11: The dependence of temperature on, (a): Seebeck coefficient and (b): Nernst coefficient for various carrier concentration for Ge sample [3.28].

Bi and BiSb thin film were grown on cadmium arsenide (CdTe) substrates with an oblique angle on (211) in a 1999 study (Cho et al.) [3.29] to examine the Seebeck and magneto-Seebeck coefficients under magnetic field up to $\pm$0.7 T and temperature up to 300 K. Results showed that there was a strong relationship between the crystal axis and the magnetic field direction. The experimental results showed that the magneto-Seebeck coefficients for the sample grown along the tilted axis were larger than the untitled sample. In addition, the oblique films from the substrate normal had better thermoelectric properties than the typical films.

Cho et al. (1999) [3.30] also suggested a new method of achieving a large figure of merit ZT materials through preparation of different Bi/Sb periods from 7.7 to 55 Å (artificially ordered alloy structures). XRD was used to confirm the formation of samples. The power factor (square Seebeck coefficient time conductivity $\delta^2\sigma$) was comparable to that of the random alloy. A lower thermal conductivity was expected owing to the increase in phonon scattering from the layers, which might result in a higher figure of merit over a random alloy. It was shown that Bi-rich $Bi_{1-x}Sb_x$ alloys could be used as n-type thermoelement, which was operating at around 80 K. The study achieved ZT of 1.2 of ZT be at 80 K under 0.13 T magnetic field.

Okumura et al. (1999) [3.31], introduced theoretical and computational approaches to calculate thermoelectric and thermomagnetic coefficients for $Bi_{88}Sb_{12}$ semiconductors, then linked them with experimental results. They reported that for finite-geometry samples, there was a strong coupling between thermoelectric and thermomagnetic effects. This coupling can make the measured profile of the magnetic field effect quite different from that of bare value (theoretical value of thermoelectric and thermomagnetic effects (raw sample)), as shown in Figure 3-12.

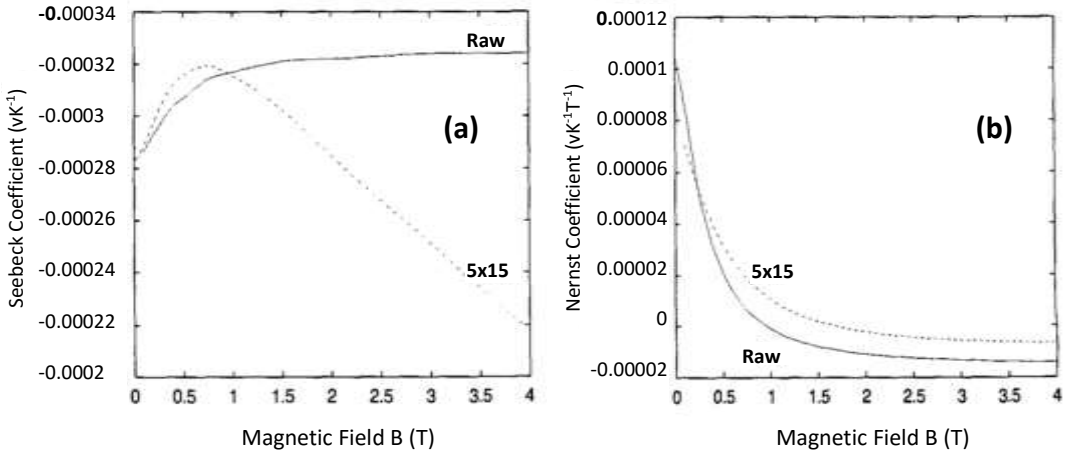

Figure 3- 12: The dependence of magnetic field of, (a): Seebeck coefficient and (b): Nernst coefficient for $Bi_{88}Sb_{12}$ sample [3.31].

The influence of magnetic field levels on thermoelectric properties to enhance a thermoelectric power generator was investigated (Hamabe et al., 2003)[3.32] using Bi polycrystalline samples under magnetic field to measure the thermoelectric properties under temperatures at 200 K and 290 K. The thermoelectric power and figure of merit were enhanced owing to the Nernst plus Seebeck hybrid effects. The maximum figure of merit obtained from Nernst + Seebeck effect was around 4 times higher than that for each of Seebeck and Nernst effect separately. There was 10~12 % enhancement in the conversion efficiency in the square geometry compared to the standard Seebeck element, as shown in Figure 3-13.

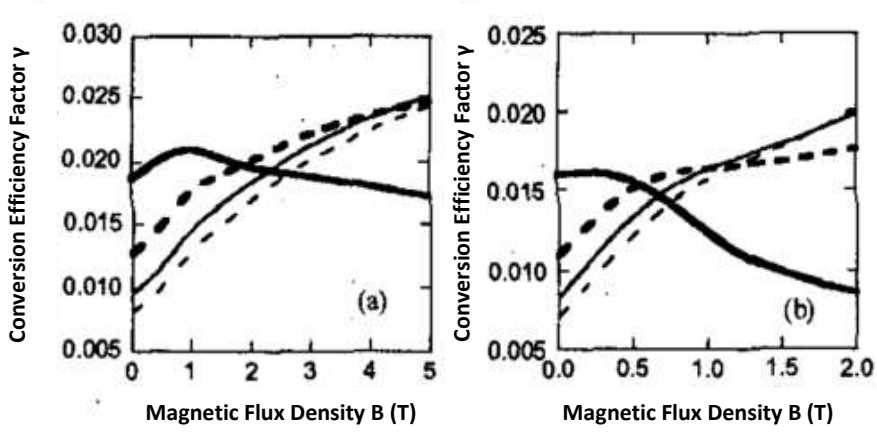

Figure 3- 13: The dependence of magnetic field on conversion efficiency factor at the maximum generated power at, (a): T_H=300 K and T_L =290 K and (b): T_H=200 K and T_L =190 K. Thick solid line for 1/1 width electrode, thick broken line for ½ width, thin solid line for 1/3 width, and thin broken line for ¼ width for Bi polycrystalline sample [3.32].

Teramoto et al. (2008) [3.33] calculated the magneto-Seebeck coefficient along the trigonal axis (z-axis)under magnetic field along the bisectrix axis (y-axis) direction of BiSb alloys at 100 K. Two and three band models were used to estimate the effect of band structure on the magneto-Seebeck coefficient. They found that the Seebeck coefficient was increased when the band overlap decreased but the increase was small for the magneto-Seebeck coefficient. The magneto-Seebeck coefficient was effectively enhanced under low magnetic field and increased as the effective electron mass decreased.

Measurement of the Nernst - Ettingshausen effect for pure polycrystalline bismuth under high-temperature 275 K (de Sande and Guerrs, 1992) [3.34] observed good agreement in the comparison between the experimental results with a simple theoretical approach. The study found that the Nernst – Ettingshausen coefficient for single crystals and for polycrystalline Bi was fully different. It was also in full agreement with the Nernst – Ettingshausen coefficient calculated experimental, with each type (single crystal and polycrystalline sample), as shown in Figure 3-14.

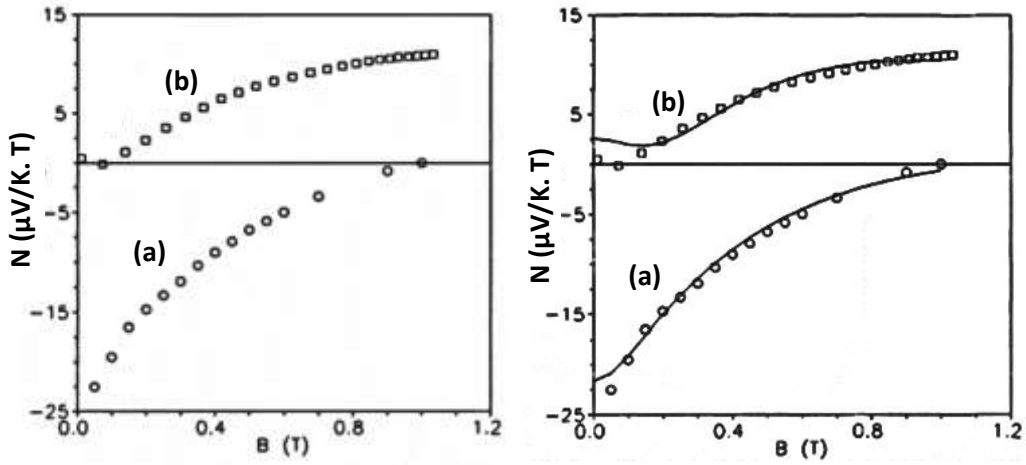

Figure 3- 14: The dependence of magnetic field on Nernst-Ettingshausen coefficient for Bi sample, (a): single crystal and (b): polycrystalline, solid lines represent theoretical values for the case [3.34].

Research undertaken by Putley (2002) [3.15], measured thermoelectric and thermomagnetic coefficient for PbSe and PbTe. The study reported that the behaviour of these effects was in full agreement with the expected theoretical value. Those coefficients were also calculated from known values of conductivity and Hall

coefficient. Good agreement was shown when they were compared with the experimental measurements and theoretical galvanomagnetic coefficients.

All the publications outlined above covered the thermomagnetic effects on different materials. They reported that measuring values of thermomagnetic effects were in full agreement with expected theoretical values. The change of the magnetic field direction relating to the crystal axis will change the measured properties of thermomagnetic effects for BiSb sample. In addition, BiSb is a good thermomagnetic candidate for cooling purposes, because the maximum values of thermomagnetic effects were obtained under low temperature ≤ 100 K. The maximum figure of merit could be obtained from Nernst + Seebeck effects.

3.6: Studies of InSb materials

3.6.1 Research investigating the thermoelectric effects on InSb

The following studies explored the use of waste heat to generate electrical power:

Bowers et al. (1959) [3.2], measured the electrical conductivity, thermal conductivity and Seebeck coefficient of InSb and indium arsenide (InAs) at high temperatures. They observed that the thermoelectric figure of merit for InSb was $0.42\times10^{-3}\ K^{-1}$ at a temperature range from 100 to 500 °C. Also, it was $0.44\times10^{-3}\ K^{-1}$ for InAs sample from 500 to 750 °C. They suggested use of these materials at a high temperature would provide higher efficiency due to the larger temperature difference that could be used. They also reported that the thermal conductivity results required further discussion due to the lack of literature concerning the temperature dependence of InSb.

An examination of the effect of the temperature on the thermoelectric coefficient of bulk single crystal InSb doped with Te (Yamaguchi et al., 2005) [3.35]

found that the scattering by optical phonons for temperatures higher than 50 K was dominant due to the small band gap value. The temperature was within 10 to 723 K. The ZT (dimensionless figure of merit) had a maximum value of 0.6 at 673 K. The open output voltage was 28 mV and the highest output power was 216 µW at 195 K.

3.6.2 Research examining the thermomagnetic effects on InSb

The following outline traces the range of studies exploring both heat and magnetic field to generate electricity:

Mette (1963) [3.36] researched the Righi-Leduc effect of n-type InSb crystals with different mobilities. He reported that an increase in Righi-Leduc effect with temperature indicated that the contribution of the unipolar part (one charge carrier type) is dominant over the bipolar part (two charge carrier types existing together). The Righi-Leduc coefficient was determined as a function of magnetic field. Comparison was made between the theoretical and experimental values of Righi-Leduc effect under a magnetic field and the results agreed remarkably. The strong decrease in Righi-Leduc effect was explained as being due to the magnetoresistance term due to the dependence of the thermomagnetic effects on the charge carrier mobility, as shown in Figure 3-15.

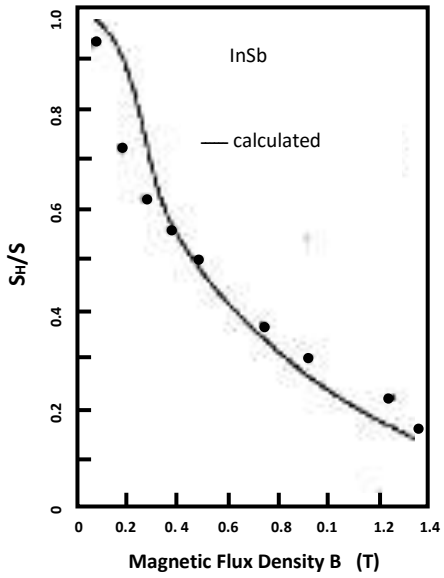

Figure 3- 15: The relative change of Righi-Leduc coefficient as a function of magnetic field for n-type InSb sample [2.36].

The conversion of heat to electricity under magnetic field (Angrist, 1963) [3.37] was clearly shown in InSb semiconductors. This was due to having large electron mobility, large mobility ratio (the ratio between electrons to holes mobilities) and relatively small energy gap. It was shown in theory that indium antimonide had the best performance so far. The study found that in the case of applied temperature difference of 300 K and under the magnetic field of 1 T, theoretically the thermal efficiency of about 1.6% and a power density of 10 $W.cm^{-3}$ can be achieved for length ratio (width to length) equal 0.25, as shown in Figure 3-16, 3-17.

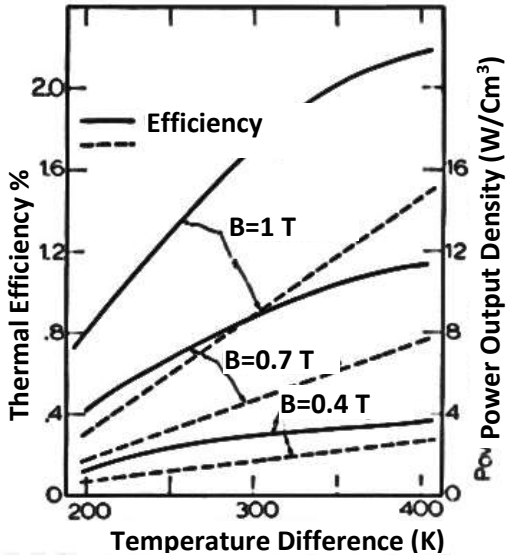

Figure 3- 16: The thermal efficiency and power output density as a function of temperature difference for different magnetic flux densities for InSb sample [3.37].

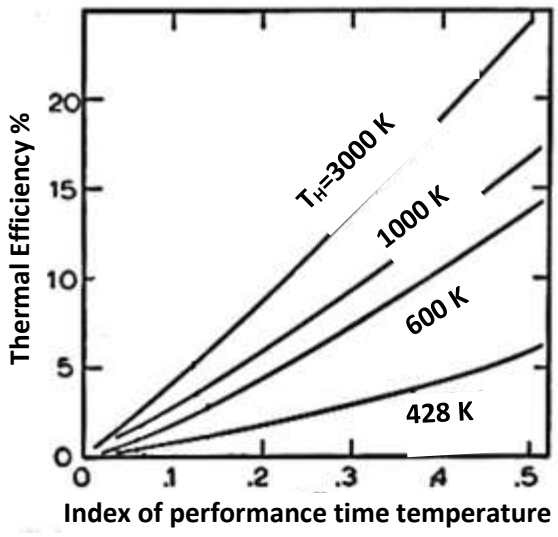

Figure 3- 17: The efficiency of Nernst generator as a function of index of performance for InSb sample [3.37].

El-Saden et.al. (1965) [3.38] measured the Nernst coefficient of n-type InSb under magnetic field between 0.4-1.2 T, and temperature gradient between 260-340 K. For InSb sample, they reported there was an ability to eliminate the difference between the adiabatic and isothermal Nernst coefficient due to its negligibility. The method used to measure Nernst voltage was identical to that for Hall voltage. The research team separated the three components that produce the transverse voltage. These parameters applied: Nernst; Righi-Leduc and potential difference due to misalignment contact points. The experimental results showed that the maximum value of Nernst coefficient was under a magnetic field within 1.2 T and at temperature from 310 to 320 K, as shown in Figure 3-18.

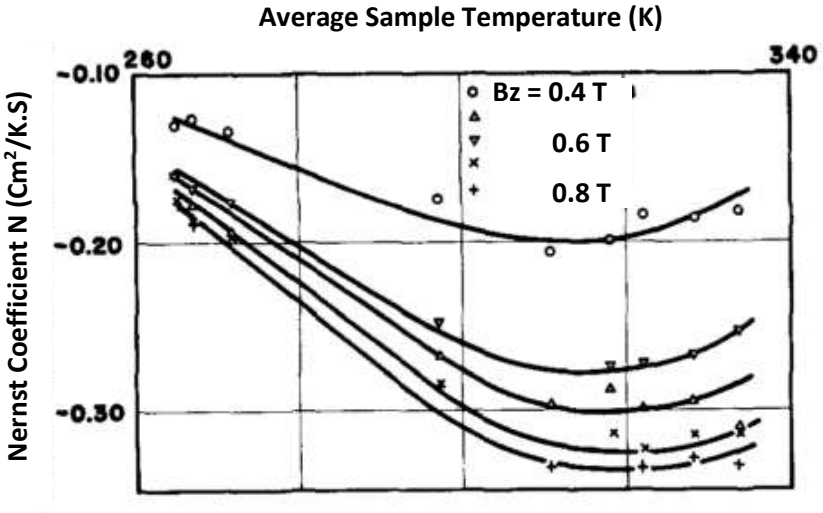

Figure 3- 18: The variation of Nernst coefficient with temperature and magnetic field for n-type InSb sample [3.38].

Materials that had a good figure of merit were investigated. under Nernst effect (Nakamura et al. 1996) [3.39]. InSb was suggested as a candidate for thermomagnetic material due to its properties. The Boltzmann equation of parabolic two-band model gave the transport coefficients under temperature range from 100 to 400 K. The temperature dependence on conductivity, Hall coefficient and thermoelectric power were observed. The dominant process in this case was acoustic-phonon scattering process. The Nernst coefficient obtained by the Boltzmann equation under the same conditions did not match with the result of the experiment, as shown in Figure 3-19.

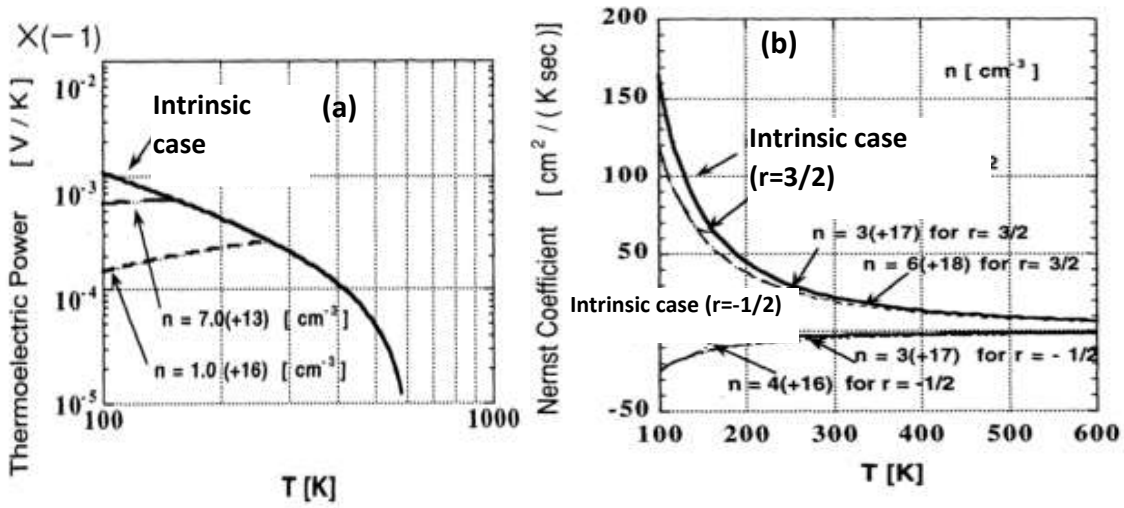

Figure 3- 19: The dependence of temperature on, (a): thermoelectric power and (b): thermomagnetic power for InSb sample, solid line represent the theoretical values and dish line represent measured values [3.39].

Another study (Ikeda et al., 1996) [3.40] applying the Nernst effect on semiconductors (Nernst elements) reported that InSb was a suitable candidate for Nernst element. The efficiency of the energy conversion depended on the transport coefficients. It was found that the Nernst voltage was about 3 mV under a magnetic field of 4 T and a temperature gradient of 100 K per 17 mm for n-InSb doped with Te, as shown in Figure 3-20.

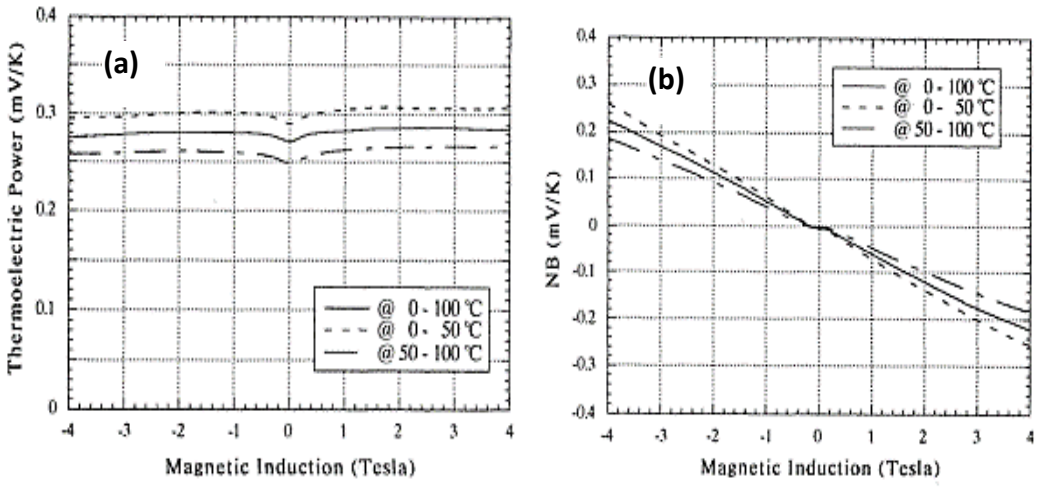

Figure 3- 20: The dependence of magnetic field for InSb doped with Te sample on, (a): thermoelectric power and (b): thermomagnetic power for various temperature difference [3.40].

The experimental results of a further study by Nakamura et al. (1997) [3.41] showed the temperature gradient and magnetic field levels' dependence of both thermoelectric power and Nernst coefficient for InSb sample. The study utilized two different samples InSb A: $n=2.1\times10^{22}$ m^{-3} and sample B: $n=2.9\times10^{21}$ m^{-3} at 77 K. The thermopower and Nernst coefficient under magnetic field B range -4 – 4 T, temperature T_H=373 K and T_L=263 K were measured. It was reported that sample B was in the intrinsic region near room temperature. Both thermopower and Nernst coefficient for sample A were lower than those of sample B. The Nernst coefficient for both samples was proportional to the Nakamura et al. (1997) [3.41]magnetic field. These findings did not agree with the theoretical result, as shown in Figure 3-21.

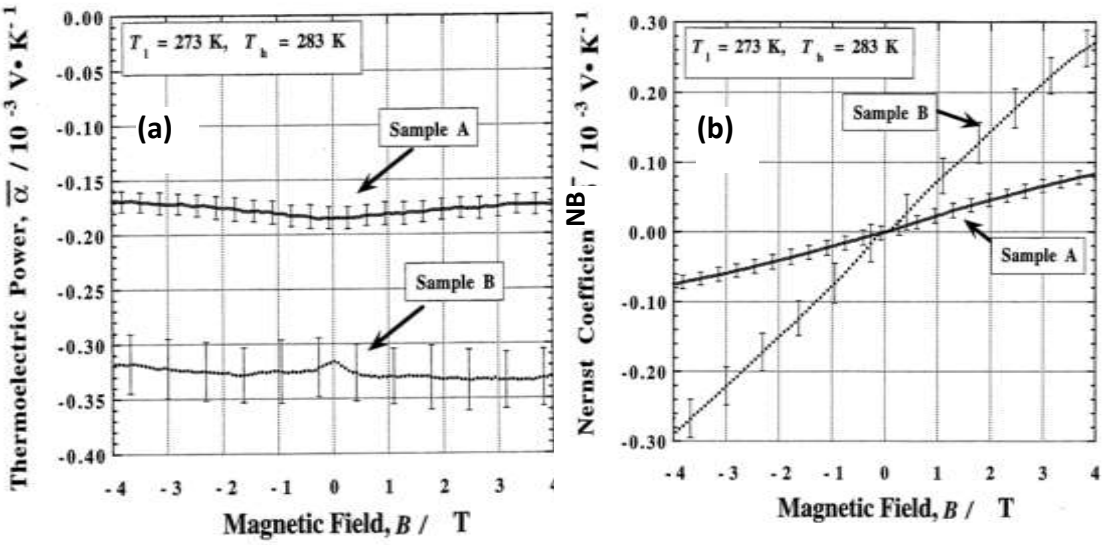

Figure 3- 21: The dependence of magnetic field on, (a): thermoelectric power and (b): thermomagnetic power at T_L=273 K and T_H=373 K for n-type InSb sample [3.41].

An investigation into the effect of the geometrical shape of pure n-type InSb (Ikeda et al., 1997) [3.42], made two different shapes (Bridge, and Fat-Bridge); the former was one fifth of the width of the latter, as shown in Figure 3-22. Two different temperature conditions were operated between the two ends: first, 10 °C and the temperature of the cold side was raised from 0–80 °C by 10 °C; second, 100 °C and the temperature of the cold side was fixed at 0 °C, under magnetic field from 0 up to 4 T. The study observed that Nernst coefficient under magnetic field at 4 T of Bridge shape was 12% larger than of Fat-Bridge shape. In addition, the

thermoelectric power for the former was greater than that for the latter within 1-8%. The thermoelectric power was asymmetric to the direction of the magnetic induction, as shown in Figures 3-22, 3-23, 3-24.

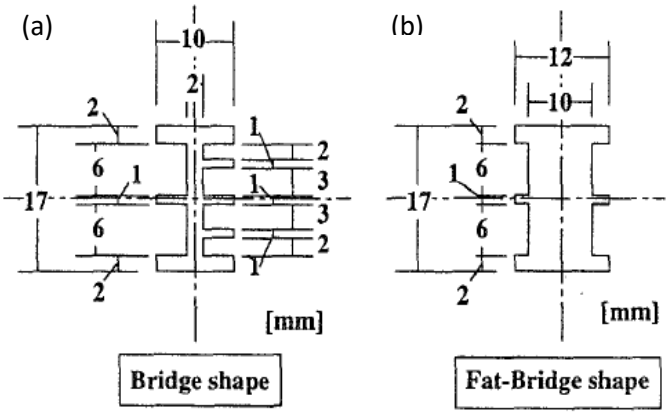

Figure 3- 22: The shape of samples, (a): bridge and (b): fat-bridge shapes for InSb sample [3.42].

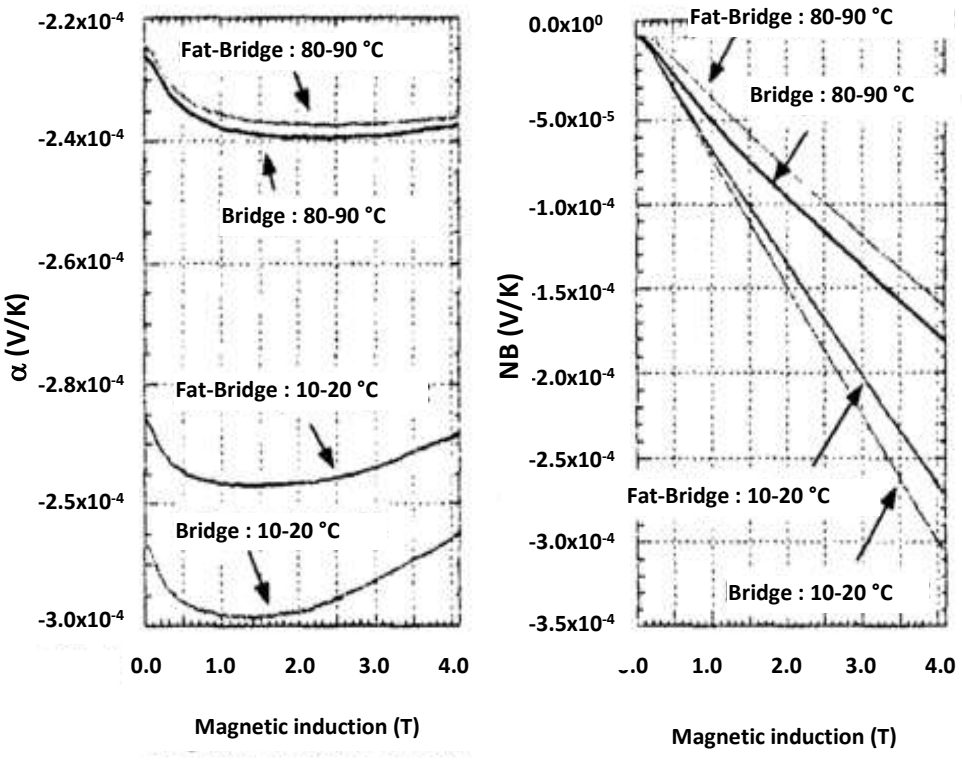

Figure 3- 23: The dependence of magnetic field on, (a): thermoelectric power and (b): thermomagnetic power for bridge and fat-bridge shapes for n-type InSb sample [3.42].

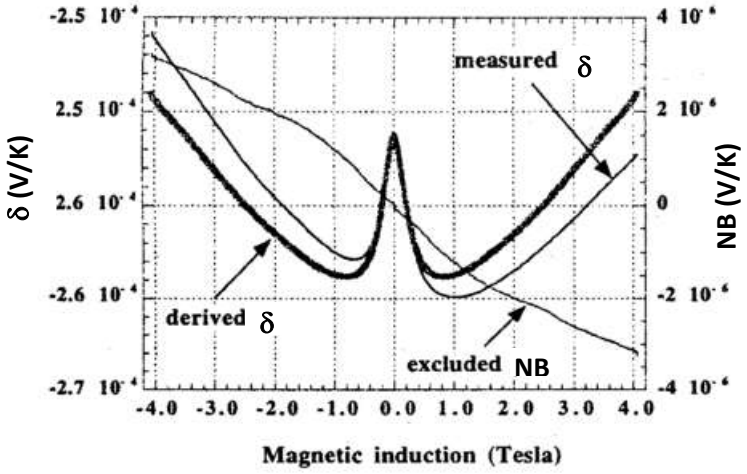

Figure 3- 24: The thermoelectric power: measured and analytically derived, and excluded thermomagnetic power as a function of magnetic field for n-type InSb sample [3.42].

An investigation carried out by Nakamura et al., (1997) [3.43] measured transport coefficients of the first candidate of Nernst element InSb. The samples used to measure thermoelectric power and Nernst coefficient had a bridge shape. The temperature difference was within 10-100 K under a magnetic field up to 4 T. The thermoelectric power change was reported to be less than the change in thermomagnetic coefficient under the magnetic field. It was found that the Hall coefficient and the thermoelectric power matched with the values theoretically expected. However, the theoretical Nernst coefficient was 10 times higher than the experimental values under the weak magnetic field, as shown in Figures 3-25, 3-26.

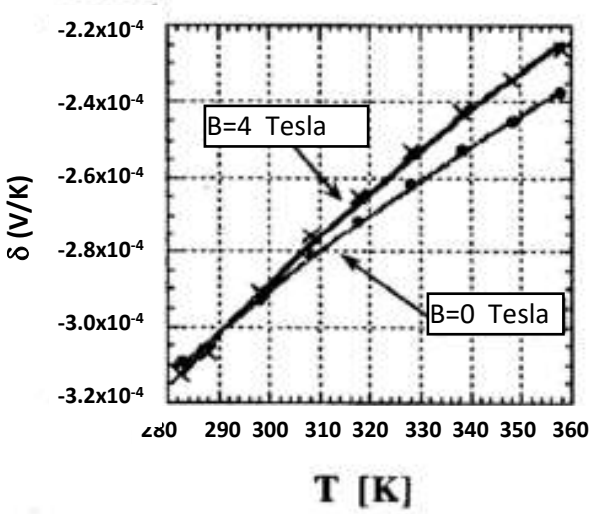

Figure 3- 25: The thermoelectric power as a function of temperature for InSb under 0,4 T [2.43].

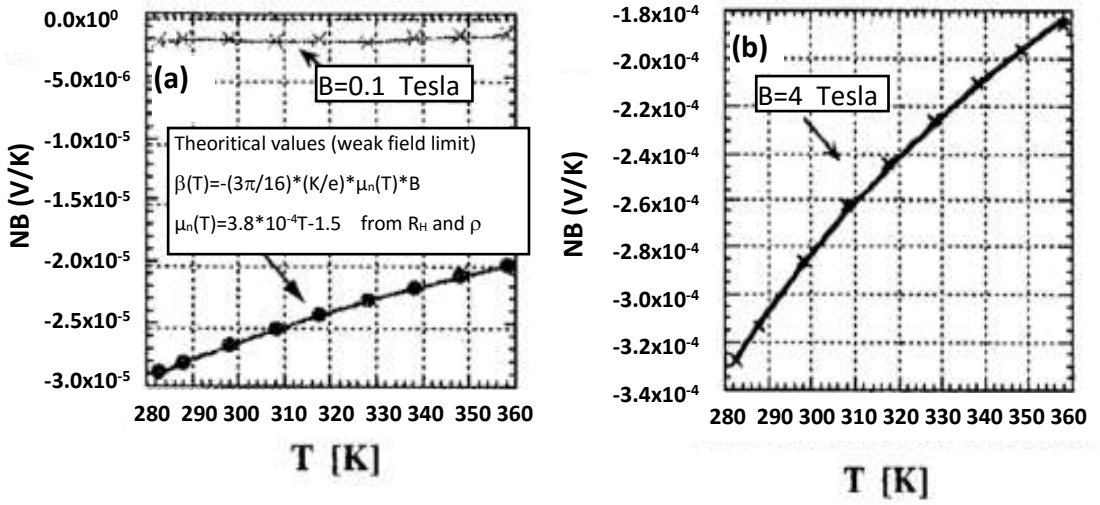

Figure 3- 26: The dependence of temperature on thermomagnetic power for InSb under, (a): 0.1 T and (b): 4 T. The crosses indicated the experimental results, the filled circles for theoretical results [3.43].

Experimental and theoretical studies of semiconductor transport properties (Yamaguchi et al., 1998) [3.44] suggested a Nernst element to convert the heat (thermal energy) in a fusion reactor. The study used n-type InSb bridge shape samples under magnetic field from -4 – 4 T. The Nernst coefficient was reported to be dependent on the carrier mobility (electrons and holes), temperature gradient and magnetic flux density. It was also observed that the electrical resistivity increased with the magnitude of the magnetic field, as shown in Figures 3-27, 3-28.

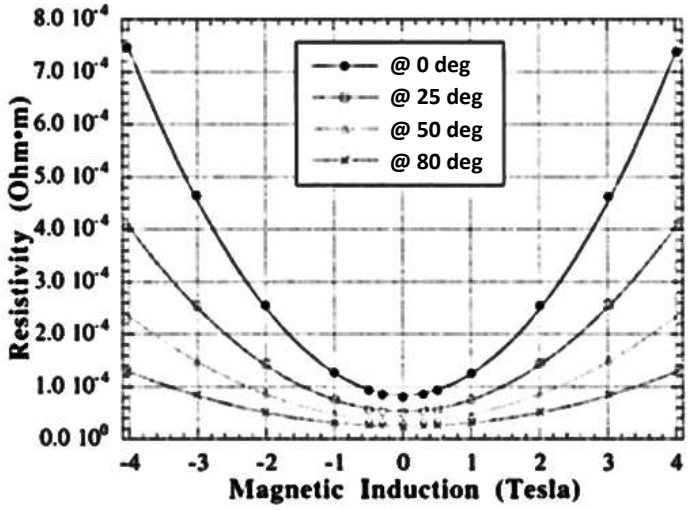

Figure 3- 27: The electrical resistivity versus magnetic field for InSb doped with Te sample [3.44].

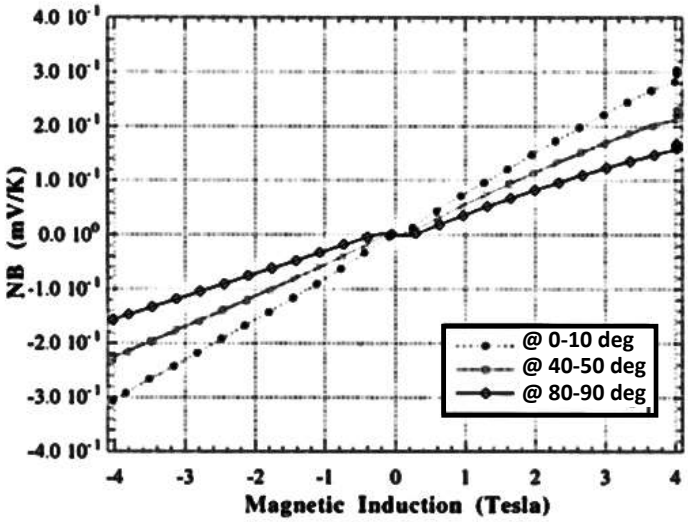

Figure 3- 28: The thermomagnetic power versus magnetic field for InSb doped with Te [3.44].

A numerical simulation was developed, together with a numerical algorithm for TE and TM effects of two-dimensional of intrinsic InSb (Okumura et al., 1998) [3.45]. The results for Seebeck and Nernst coefficient were compared with experimental results of various sample geometries. It was reported that the Seebeck effect was not sensitive to the geometry of current leads if it was narrow enough, but it was degraded if the current leads had the same sample width. In addition, the Nernst effect was sensitive to geometry of current leads. It was found that the best way to generate potential energy was to measure the voltage between the bottom left and the top right corners, as shown in Figure 3-29 for sample under magnetic field 4 T and temperatures of T_H=373 K and T_L=272 K.

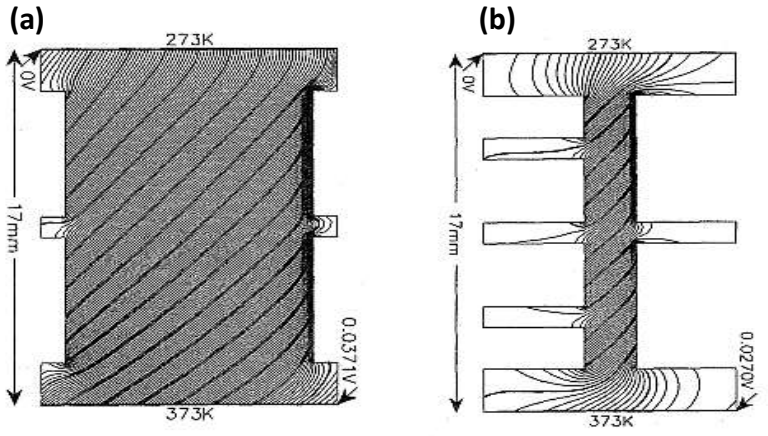

Figure 3- 29: The Contour map of calculated potential energy distribution for, (a): fat-bridge and (b): bridge shape for intrinsic InSb sample [3.45].

A study by Nakamura et al. (1998) [3.46], tried to find Nernst elements with a high thermomagnetic figure of merit. They designed a physical model to describe the transport phenomena (assumed a parabolic two-band model in classical statistics) and nominated InSb as a good candidate. They measured the transport coefficients of InSb under magnetic field up to 4 T and temperature region from 270 to 330 K. Two different samples were utilised: InSb-X: $n=6.6\times10^{20}$ m^{-3} and sample InSb-B: $n=2.1\times10^{22}$ m^{-3} at 77 K; the former was doped by Te lighter than the latter. It was observed that the theoretical and experimental values were coincident in a strong magnetic field, as shown in Figure 3-30.

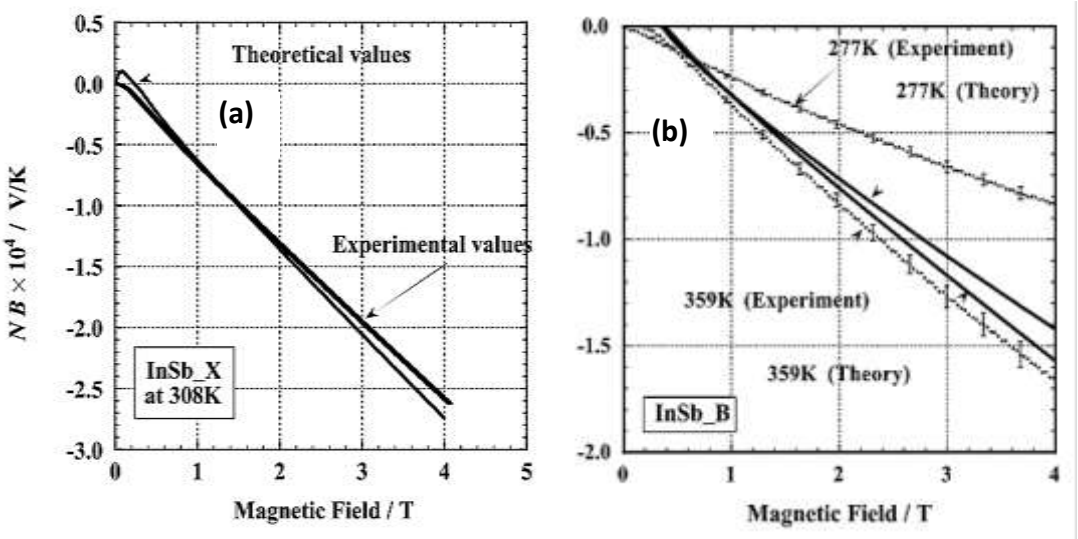

Figure 3- 30: The dependence of magnetic field on thermomagnetic power for InSb doped with Te, (a): X sample at 308 K and (b): B sample at 273 K and 353 K [3.46].

Further research undertaken by Nakamura et al. (1999) [3.47], investigated the transport coefficient of InSb under a temperature gradient and magnetic field numerically. The model for a parabolic two-band in classical statistics was used in this work. A comparison was made between their theoretical results and experimental results. The measurement was under a magnetic field up to 4 T and temperature from 271-358 K. They utilized InSb-X: $n=6.6\times10^{20}$ m^{-3}. The results of both theoretical and experiment were almost in full agreement, apart from the values of Nernst coefficient when the magnetic field was below 0.1 T. It was assumed that the criterion condition to estimate the power factor of the Nernst materials was the parabolic two-band model. The study suggested inclusion of the optical scattering

process, as well as the acoustic branch, when calculating the transport coefficients. This inclusion would reduce the difference between the theoretical calculations and the experimental results, as shown in Figure 3-31.

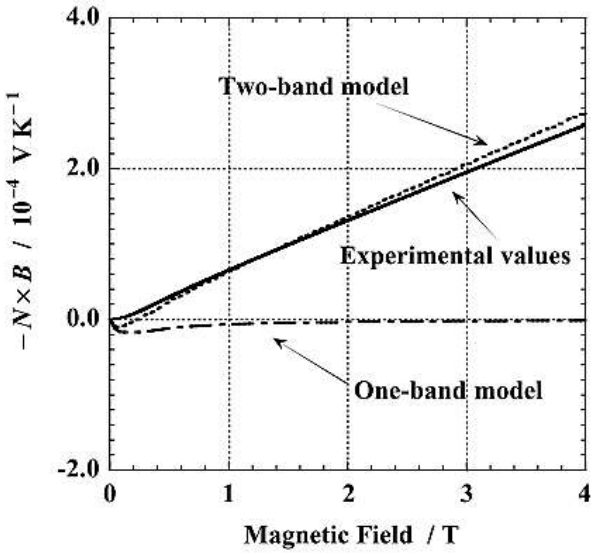

Figure 3- 31: The thermomagnetic power versus magnetic field for InSb doped with Te sample at 308 K: Solid curve for experimental values, dashed curve for the theoretical results which were calculated by the two-band model, dash-dot curve for one model which were gave the calculated results for InSb sample [3.47].

An important experiment (Heremans et al., 2001) [3.48] investigated the effect of the geometrical semiconductor samples on thermoelectric power. The design created a significant change in which thermoelectric power under a magnetic field of InSb wafer sample doped with Ge was examined. This effect appears to be similar to the effect of the sample geometry on the magnetoresistance. It was reported that the geometrical magneto-thermopower GMT of p-type InSb semiconductor was dependent on the geometry of sample and type of charge carrier to obtain total thermopower. This was due to freezing out the contribution of the minority carriers. The GMT effect can enhance the figure of merit of semiconductor InSb by factor 1.8, as shown in Figure 3-32.

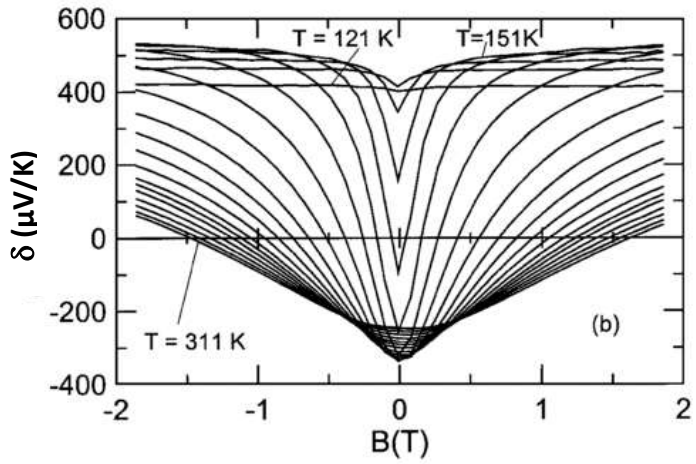

Figure 3- 32: The thermoelectric power against magnetic field direction and temperature for p-type InSb sample [2.48].

Further investigation by Heremans et al. (2001) [3.49] researched the GMT in n-type InSb doped with Te. They reported that the thermo-power changed its dependence on the type of charge carriers under a magnetic field. The change occurred from high mobility carriers (electrons) under zero magnetic field to low mobility carriers (holes) under a high magnetic field, even though the latter are the minority carriers (holes). The GMT effect is symmetric with the magnetic field direction even in asymmetric geometries. It was predicted that GMT could increase thermoelectric power factor, as well as figure of merit, by more than 80%. It was concluded that semiconductors that have two types of carriers with different mobilities could create large variations under the magnetic field. This is true for geometrical shapes that have length to width ratios much greater than one, as shown in Figure 3-33

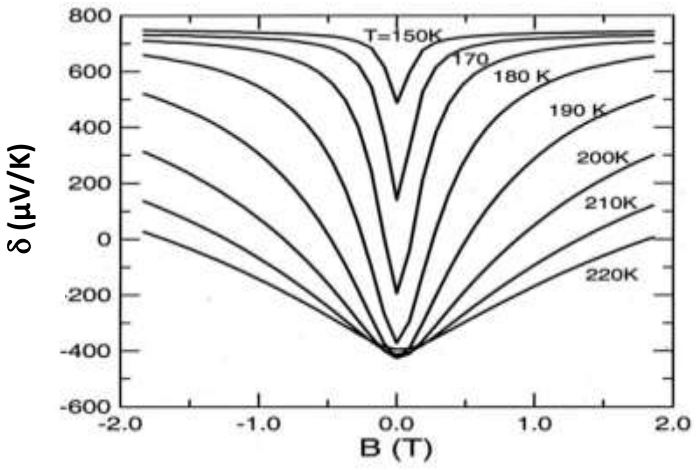

Figure 3- 33: The thermoelectric power against magnetic field direction and temperature for n- type InSb sample [3.49].

Uher and Goldsmid (2002) [3.50], investigated the properties of some promising thermomagnetic materials, based on the hybrid DC thermoelectric and thermomagnetic transformers, and conducted a comparison among these materials. The comparison was determined for various devices under room temperature and magnetic field within 1.5 T. It was suggested that the InSb-NiSb was a good material to utilise as heat-flow meter, as shown in Figure 3-34.

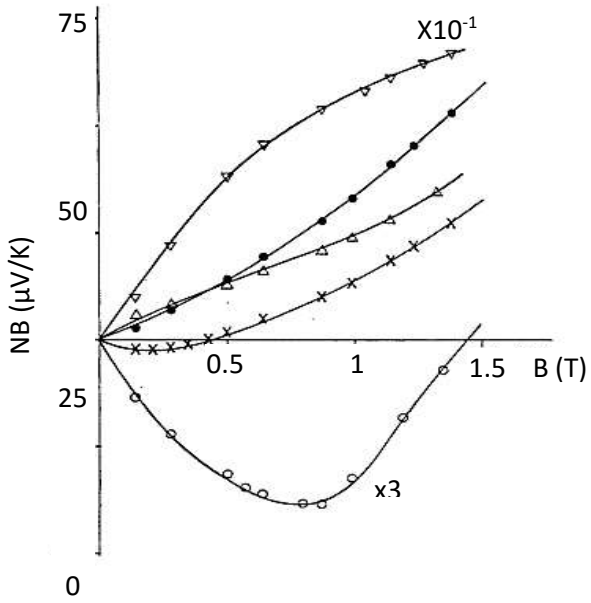

Figure 3- 34: The thermomagnetic power against magnetic field: ● Bi , X $Bi_{95}Sb_5$, △ Bi-Ag , ○ Cd_3As_2-NiAs , ▽ InSb-NiSb samples [2.50].

More recently, Gadjialiev et.al. (2014) [3.51] have examined the thermoelectric power of InSb with carrier concentration of 2×10^{14} cm^{-3} under a magnetic field up to 557 kA/m and temperature between 4.8 to 120 K. They observed that the thermoelectric power was independent of the magnetic field at a temperature close to 56 K.

All the research outlined above has covered the thermomagnetic effects on InSb material doped with Te, Ge, or C. It has been reported that InSb is a good thermomagnetic candidate at room temperature because it is operated in intrinsic region at this temperature. In addition, the best way to generate potential energy is to measure the voltage between the bottom left and the top right corners of a sample, due to the doubled effects of Nernst and Seebeck.

Table 3-3 demonstrates a comparison among all the above studies.

Table 3-3 demonstrates a critical comparison on different studies performed by researchers that highlights their achieved results.

	Author	Crystallinity of InSb sample	Thermomagnetic Coefficients
1.	R. Bowers et al. [3.2]	Polycrystalline	δ decreased with increasing temperature differences; it was 280 μV/°C at 100 °C and 130 μV/°C at 500 °C. The ZT changed with increasing temperature differences; it was 0.17 at 100 °C and maximum value 0.5 at 400 °C.
2.	S. Yamaguchi et al. [3.35]	Single crystal doped with Te	The InSb bulk material operated in intrinsic regime at temperature over 150 K. The σ and δ changed with increasing temperature. The thermoelectric ZT increased with increasing temperature. It was 5×10^{-6} at 10 K and 0.6 at 673 K.
3.	H. Mette [3.36]	Single crystal	The relative Righi-Leduc coefficient decreased with increasing magnetic flux density; it was 0.93 at 0.1 T and 0.18 at 1.4 T.
4.	S. W. Angrist [3.37]	Single crystal	The thermal efficiency, power output density and Nernst voltage increased with increasing temperature difference and magnetic flux density.
5.	M. R. El-Saden et.al. [3.38]	Single crystal doped with Te	σ increased with increasing temperature from 225 $\Omega^{-1}cm^{-1}$ at 270 K to 380 $\Omega^{-1}cm^{-1}$ at 330 K. N changed with increasing magnetic field, the maximum values at temperature difference 310 K; it was -0.2 $cm^2/K.s$ at 0.4 T to -0.385 $cm^2/K.s$ at 1.2 T.
6.	H. Nakamura et al. [3.39]	Single crystal doped with Te	σ, δ and N for extrinsic semiconductors have high carrier concentration need higher temperature to operate under intrinsic regime than that for low carrier concentration (same charge carrier types). For σ the sample has carrier concentration $p=4\times10^{15}$ cm^{-3} operates around 240 K but for $p=2\times10^{17}$ cm^{-3} operates around 430 K. For δ the sample has carrier concentration $n=1\times10^{16}$ cm^{-3} operates around 260 K but for $n=7\times10^{13}$ cm^{-3} operates around 60 K. For N the sample has carrier concentration $n=6\times10^{18}$ cm^{-3} operates around 340 K but for $n=4\times10^{16}$ cm^{-3} operates around 160 K.

7.	K. Ikeda et al. [3.40]	Single crystal doped with Te	δ changed with increasing magnetic field but decreased with increasing temperature differences; it was -2.5×10^{-4} V/K at 0 T to -2.75×10^{-4} V/K at -4 T but -2.85×10^{-4} V/K at 4 T for temperature difference sides 0-100 °C and -2.92×10^{-4} V/K at 0 T to -2.97×10^{-4} V/K at -4 T but -3.1×10^{-4} V/K at 4 T under temperature difference sides 0-50 °C. NB increased with increasing magnetic field and deceased with increasing temperature differences, it was0 V/K at 0 T to -2.1×10^{-4} V/K at -4 T but2.15×10^{-4} V/K at 4 T for temperature difference sides 0-100 °C and 0 V/K at 0 T to -2.7×10^{-4} V/K at -4 T but -2.58×10^{-4} V/K at 4 T under temperature difference sides 0-50 °C. δ and NB were asymmetric with magnetic field directions.
8.	H. Nakamura et al. [3.41]	Single crystal doped with Te	δ and NB for samples carrier concentration (sample B) $n=2.9\times10^{21}$ m^{-3} were higher than those for carrier concentration (sample A) 2.1×10^{22} m^{-3}. δ changed with increasing magnetic field, it was -1.85×10^{-4} V/K at 0 T to -1.71×10^{-4} V/K at -4 T but -1.73×10^{-4} V/K at 4 T for sample A and -3.13×10^{-4} V/K at 0 T to -3.2×10^{-4} V/K at -4 T but -3.3×10^{-4} V/K at 4 T under temperature difference 273-373 K. NB increased with increasing magnetic field; it was 0 V/K at 0 T to -0.75×10^{-4} V/K at -4 T but 0.8×10^{-4} V/K at 4 T for sample A and 0 V/K at 0 T to -2.9×10^{-4} V/K at -4 T but -2.7×10^{-4} V/K at 4 T under temperature difference sides 273-373 K. δ and NB were asymmetric with magnetic field directions.
9.	K. Ikeda et al. [3.42]	Single crystal doped with Te	δ and NB for Bridge shape was higher than that for Fat-Bridge shape. δ changed with increasing magnetic field and temperatures of both sides (hot and cool sides), it was -2.57×10^{-4} V/K at 0 T to -2.54×10^{-4} V/K at 4 T for Fat-Bridge shape and -2.6×10^{-4} V/K at 0 T to -2.67×10^{-4} V/K at 4 T for Bridge shape at temperature difference 0-100 K. It was for Bridge shape -3.07×10^{-4} V/K at 0 T to -3.05×10^{-4} V/K under magnetic flux density 4 T and at temperature differences 10-20 K but -2.27×10^{-4} V/K at 0 T to -2.37×10^{-4} V/K under magnetic flux density 4 T at temperature difference 80-90 K. δ was asymmetric with magnetic field directions. NB

			increased with increasing magnetic field but decreased with increasing temperature differences, it was 0 V/K at 0 T and -2.1×10^{-4} V/K for Fat-ridge shape and 0 V/K at 0 T to -2.4×10^{-4} V/K at 4 T for Bridge shape under temperature difference sides 0-100 K. It was for Bridge shape 0 V/K at 0 T to -3.05×10^{-4} V/K under magnetic flux density 4 T and at temperature differences sides 10-20 K but 0 V/K at 0 T to -1.8×10^{-4} V/K under magnetic flux density 4 T at temperature difference sides 80-90 K.
10	H. Nakamura et al. [3.43]	Single crystal doped with Te	ρ decreased with increasing temperature from 7.6×10^{-5} Ω.m at 270 K to 2.2×10^{-5} Ω.m at 355 K. δ decreased with increasing both magnetic field and temperature differences; it was -3.1×10^{-4} V/K at 283 K to -2.37×10^{-4} V/K at 358 K under 0 T and -3.15×10^{-4} V/K at 283 K to -2.27×10^{-4} V/K at 358 K under 4 T. NB increased with increasing magnetic field but decreased with increasing temperature differences, it was -3.27×10^{-4} V/K at 283 K to -1.85×10^{-4} V/K at 358 K under 4 T and -2×10^{-6} V/K at 283 K to -1.5×10^{-6} V/K at 358 K under 0 T.
11	S. Yamaguchi et al. [3.44]	Single crystal doped with Te	The resistivity increased with increasing magnetic field but decreased with increasing temperature; it was 0.55×10^{-4} Ω.m at 25 deg and 0 T and 4.1×10^{-4} Ω.m at 25 deg and 4 T. NB increased with increasing of magnetic field for same temperature differences. The maximum values were for temperature sides 0-10 deg; it was 0 V/K at 0 T and 3×10^{-4} V/K at 4 T.
12	H. Okumura et al. [3.45]	Single crystal doped with Te	The relative magnetoresistance for Samples that have length greater than width was lower. δ was not sensitive to the width of leads when it was narrow enough. In contrast, N was sensitive even when with narrow leads. The largest output voltages under magnetic field could be obtained from the bottom left to the top right edges.
13	H. Nakamura et al. [3.46]	Single crystal doped with Te	σ decreased with increasing magnetic field but increased with increasing temperature; it was 3.1×10^{4} $\Omega^{-1}m^{-1}$ to 1.1×10^{4} $\Omega^{-1}m^{-1}$ at 273 K and 5.7×10^{4} $\Omega^{-1}m^{-1}$ to 1.5×10^{4} $\Omega^{-1}m^{-1}$ at 353 K. δ decreased with increasing both magnetic field and temperature differences over RM; it was

			-2.6×10^{-4} V/K to -2.75×10^{-4} V/K at 277 K and -1.8×10^{-4} V/K to -1.73×10^{-4} V/K at 359 K. NB increased with increasing both of magnetic field and temperature differences; it was 0 V/K to -0.8×10^{-4} V/K at 277 K and 0 V/K to -1.65×10^{-4} V/K at 359 K. All above results were at magnetic flux density from 0 T to 4 T. All these results for sample which has carrier concentration n=2.1× 10^{22} m^{-3}; this sample has lower values of δ and NB for sample carrier concentration n=6.6×10^{20} m^{-3}.
14	H. Nakamura et al. [3.47]	Single crystal doped with Te	σ decreased with increasing magnetic field but increased with increasing temperature; it was 1.3×10^{4} Ω^{-1}m^{-1} to 4.7×10^{4} Ω^{-1}m^{-1} at 0 T and 0.3×10^{4} Ω^{-1}m^{-1} to 0.8×10^{4} Ω^{-1}m^{-1} at 4 T. δ decreased with increasing both magnetic field and temperature differences over RM; it was -3.4×10^{-4} V/K to -2.3×10^{-4} V/K at 0 T and -3.3×10^{-4} V/K to -2.4×10^{-4} V/K at 4 T. N increased with increasing magnetic field but decreased with increasing temperature; it was -0.8×10^{-4} m^{2}K^{-1}s^{-1} to -0.5×10^{-4} m^{2}K^{-1}s^{-1} at 4 T, but was not coincident at magnetic flux density below 0.1 T. All above results were at temperature difference from 270 K o 355 K.
15	J. P. Heremans et al. [3.48]	Single crystal doped with Te	δ was -340 μV/K but 60 μV/K at 311 K and -2 T and 40 μV/K at 311 K and -2 T.
16	Joseph P. Heremans et al. [3.49]	Single crystal doped with Ge	δ was -420 μV/K but 25 μV/K at 220 K and -2 T and 10 μV/K at 311 K and -2 T.
17	C. Uher and H. J. Goldsmid [3.50]	Eutectic	NB was 6.6 μV/K at 1.5 T. κ was 15.2 Wm^{-1}K^{-1} at 0 T and saturation stated above 0.5 T; it was 14.7 Wm^{-1}K^{-1} at 1.5 T. ρ was 4.52×10^{-3}Ω.m at 0 T and 90.85×10^{-3} Ω.m.
18	M. M. Gadjialiev et.al. [3.51]	Single crystal	δ at temperature close to 56 K was independent on magnetic field.

3.7: Why InSb

Current trends have seen many electronic devices being taken out of commission due to their relatively high power consumption, with attention

shifting toward devices with lower power requirements [3.35]. InSb is the most suitable candidate material for such devices because the operation voltage for devices utilising InSb is predicted to be low. Thus, InSb is a vital material from the viewpoint of both the active use of heat and the reduction of heat from devices [3.35].

Additionally, InSb has been identified as a promising Nernst material (the best candidate) as it possesses very large carrier mobility, a narrow band gap and a high mobility ratio (the ratio of electron mobility to the hole mobility) [3.35, 3.37, 3.44, 3.52, 3.53].

The concept of using a semiconductor in an intrinsic region is a promising approach for developing high performance thermomagnetic materials, in which the semiconductor at an appropriate temperature plays a crucial role in achieving high thermomagnetic performance. There is mounting evidence that InSb is a favourable thermomagnetic material because it transits from the extrinsic region to the intrinsic region at temperatures close to room temperature [3.46, 3.47, 3.41, 3.53]. The intrinsic thermomagnetic and its other properties of InSb distinguish it from other candidates of Nernst materials, such as Ge [3.28], Bi [3.24, 3.32, 3.54], BiSb [3.23-3.24, 3.31-3.32, 3.54-3.56], HgTe and HgSe [3.57, 3.58].

Finally, the simplicity of synthesising InSb makes it feasible to produce doped and undoped polycrystalline versions of the material.

3.8: Structure and phase diagram of InSb

Indium antimonide has a simple Zincblende crystal structure [3.59], as shown in Figure 3-35. InSb has a simple binary phase diagram [3.60, 3.61], as shown in Figure 3-36. InSb crystals can be readily formed by slow cooling [3.62].

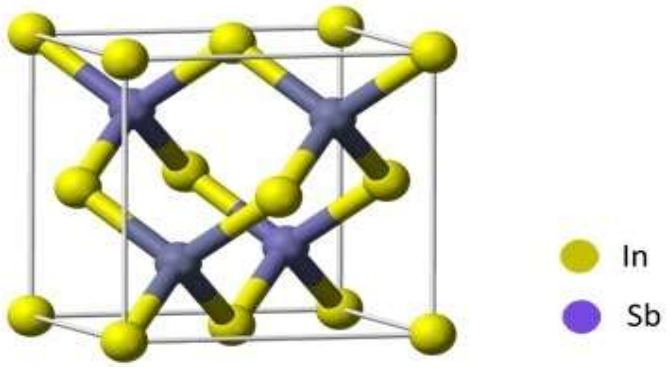

Figure 3-35: The Zincblende crystal structure of InSb [3.59].

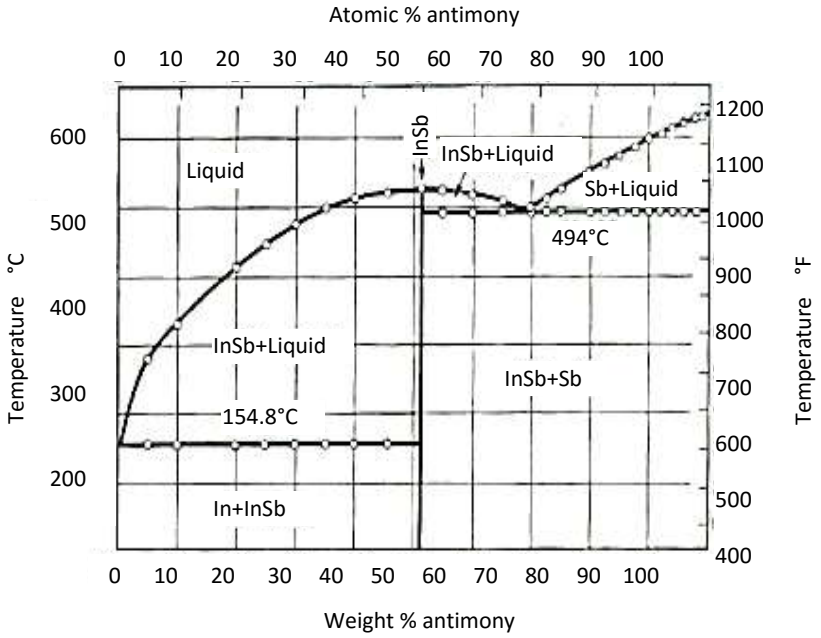

Figure 3-36: The binary phase diagram of InSb elements [3.60, 3.61].

3.9: Physical properties of InSb

InSb is a III-V semiconductor, which has a narrow band gap of about 0.17 eV (direct gap) as shown in Figure 3-37 [3.63]. The highest electron mobility ($\mu_e \leq 77000\ cm^2V^{-1}S^{-1}$) is comparable with other materials from this group. Table 3-4 contains lists of some properties of single crystal InSb at room temperature [3.74]. Figure 3-38 shows the relationship between energy gap and lattice thermal

conductivity for various semiconductors [3.64], while Figure 3-39 shows the relationship between effective mass and band gap [3.65].

InSb has important applications in infrared, optical, microwave, and millimetre-wave devices, high mobility transistors, thermo-photovoltaic cells, high-speed devices and magnetic sensors [3.65-3.73].

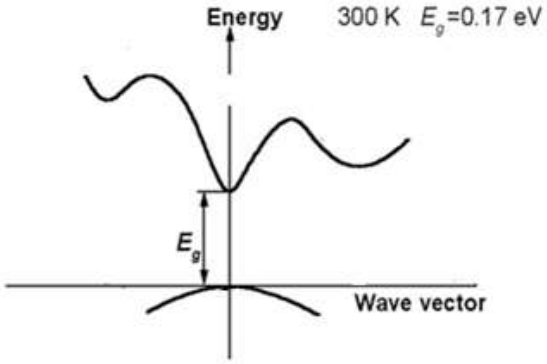

Figure 3-37: The band structure of InSb with Eg ≈0.17 eV at 300 K [3.63].

Table 3-4: Some properties of single crystal InSb at 300 K [3.63].

Mat.		Band gap Eg (eV)	μe ($cm^2V^{-1}S^{-1}$)	μp ($cm^2V^{-1}S^{-1}$)	Melting point (°C)	Thermal conductivity ($WCm^{-1}K^{-1}$)	Intrinsic carrier density (cm^{-3})
1.	InSb	0.170	≤ 77000	≤ 850	527	0.18	2×10^{16}
2.	InAs	0.354	≤ 40000	≤ 500	942	0.27	1×10^{15}
3.	InP	1.344	≤ 5400	≤ 200	1060	0.68	1.3×10^{7}
4.	GaSb	0.726	≤ 3000	≤ 1000	712	0.32	1.5×10^{12}
5.	GaAs	1.424	≤ 8500	≤ 400	1240	0.55	2.1×10^{6}
6.	GaP	2.260	≤ 250	≤ 150	1457	1.10	2

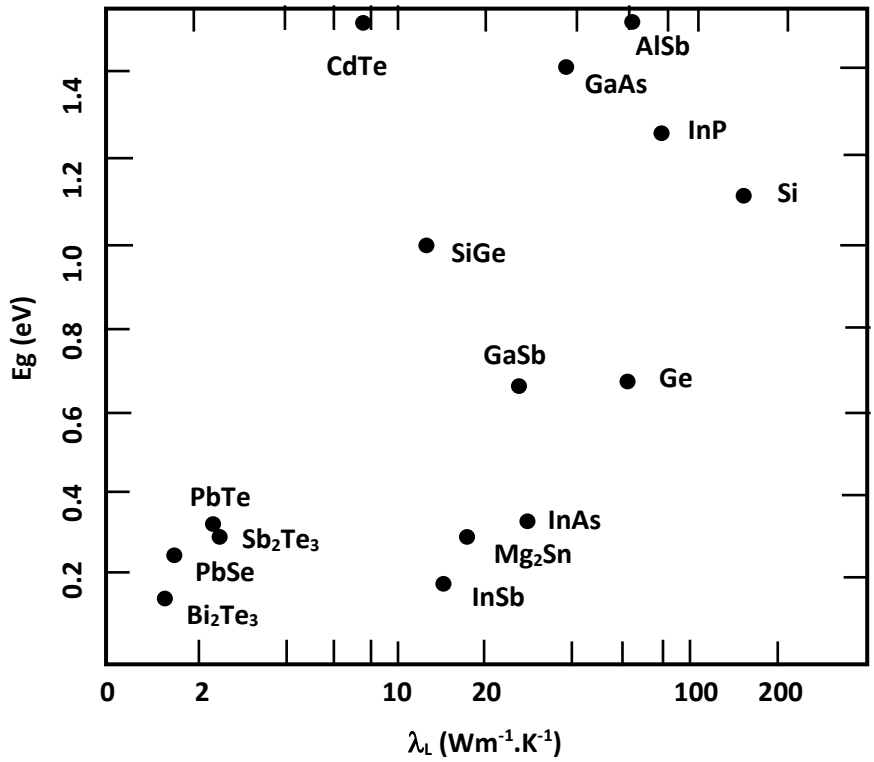

Figure 3-38: The energy gap as a function of lattice thermal conductivity for various semiconductors [3.64].

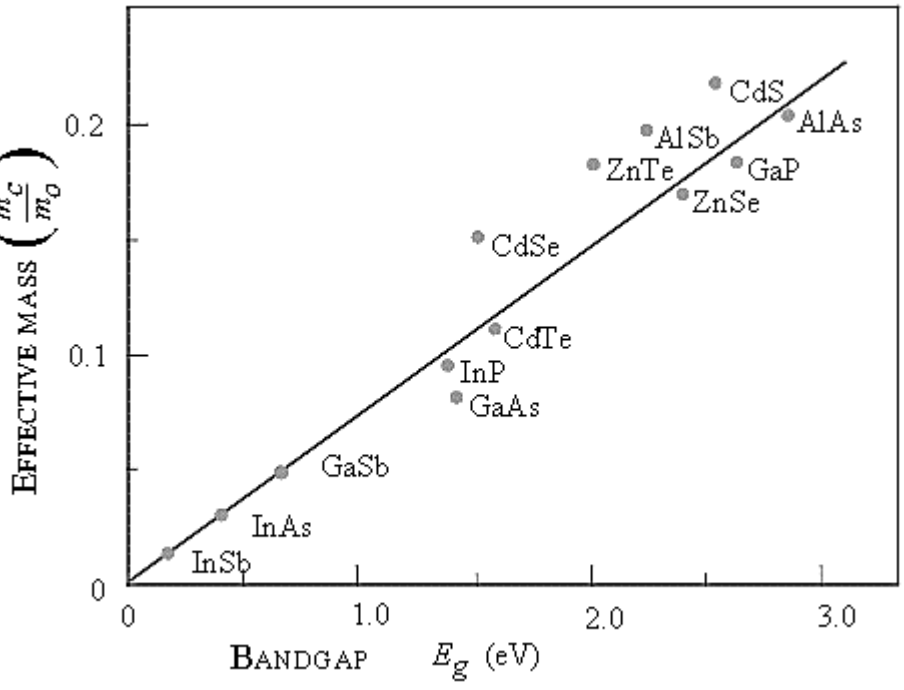

Figure 3-39: The effective mass as a function of band gap for various semiconductors [3.65].

It is worth noting that the carrier mobility changes with temperature. Rode [3.74] reported that InSb possesses high carrier mobility, as shown in Figure 3-40,

which presents the measured mobility data as a function to the temperature. The theoretical model calculations match the measured Hall mobility reasonably well.

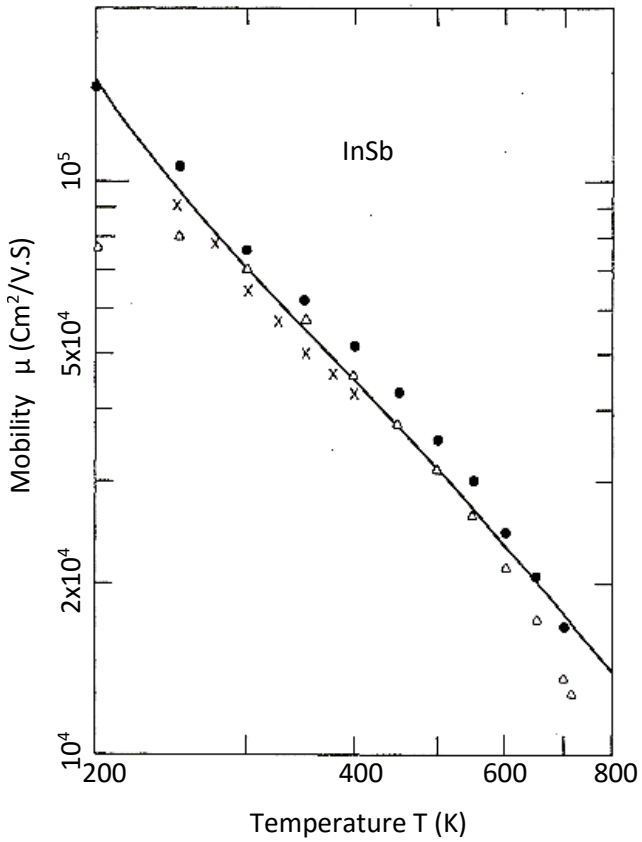

Figure 3-40: The temperature dependence of carrier mobility of InSb. The solid line is the theoretical calculation and the data points are the measured Hall mobility [3.74].

The thermoelectric parameters of polycrystalline InSb at 500 K have also been investigated. Typical data are listed in Table 3-5 [3.2].

Table 3-5: Typical thermoelectric parameters of polycrystalline InSb at 500 K [3.2].

Material	Seebeck Coefficient μV/K	Electrical Conductivity S/m	Thermal conductivity W/m.K	ZT
InSb	~200	~1.7×10^4	~10	~0.25

Figure 3-41 shows the index of performance as a function of temperature under a magnetic field of 1 T [3.37]. The performance Index provides information about the actual manner of how the materials are reacting to stimuli such as temperature gradient and magnetic field. Table 3-6 gives some material properties for thermomagnetic materials.

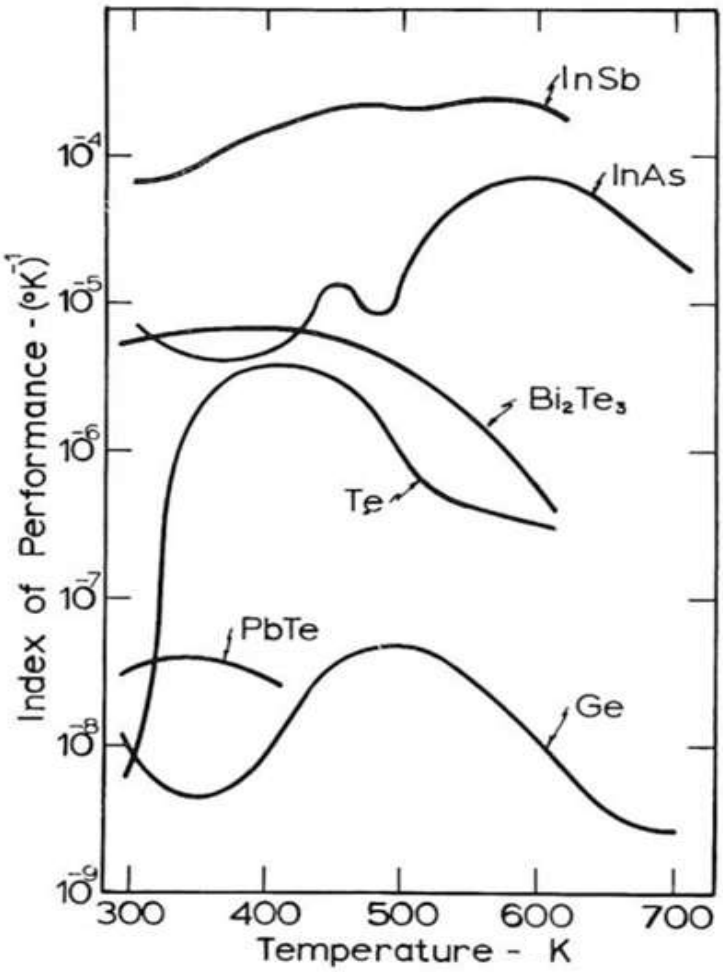

Figure 3-41: The index of performance as a function of temperature for several different semiconductors at a magnetic flux density of 1 T [3.37].

Figure 3-41 shows that the index of performance depends on temperature difference at fixed magnetic field. It is non-linear behaviour, because the index of performance depends on thermal conductivity, resistivity and Nernst coefficient for each material, which is dependent on temperature and magnetic flux density.

$$\theta = \frac{(\mathrm{NB})^2}{\rho\kappa} \quad \text{.....(3.1)}$$

where: N is the Nernst coefficient; B is the magnetic flux density, ρ is the resistivity and λ is the thermal conductivity.

Table 3-6: Some material properties for thermomagnetic generators [3.37].

	Material	Mobility Ratio	Index of Performance At 400 K
1.	Silicon	2.8	1.56×10^{-11}
2.	Germanium	2.0	84.00×10^{-9}
3.	Tellurium	2.1	4.00×10^{-8}
4.	Lead Selenide	1.6	2.00×10^{-8}
5.	Lead Telluride	1.4	2.00×10^{-8}
6.	Bismuth Telluride	1.2	6.70×10^{-6}
7.	Indium Arsenide	70.0	4.10×10^{-6}
8.	Indium Antimonide	80.0	1.60×10^{-4}

Non-stoichiometric InSb can be either n-type or p-type. It may exhibit as an n-type semiconductor due to anion vacancies, which are caused by excess indium. On the other hand, it could exhibit as a p-type semiconductor due to cation vacancies, which are caused by excess antimony [3.13, 3.14]. This means that the type of semiconductor depends on the sign of the total charge carrying: electrons and holes.

In view of the synthesis of InSb for thermomagnetic applications, a strategy of preparing undoped polycrystalline InSb and doped with tellurium (Te) by small amount of dopant to improve the Nernst effect. In the following sections, the facilities, products and techniques developed/employed for sample preparation and characterisation are presented.

All of the properties detailed above justify InSb being deemed the best candidate for thermomagnetic materials. The literature survey undertaken in this chapter indicates that, despite the wide range of previous research conducted into thermomagnetic effects the effect of an AC magnetic field on the thermomagnetic coefficient for thermomagnetic materials has not been previously studied. This present research is therefore intended to occupy this research gap.

References

[3.1] V. Tetyorkin, A. Sukach, and A. Tkachuk, “Infrared Photodiodes on II-VI and III-V Narrow-Gap Semiconductors,” in *Infrared Photodiodes on II-VI ans III-V Narrow-Gap Semiconductors, Photodiodes - From Fundamentals to Applications*, I. Yun, Ed. InTech, 2012.

[3.2] R. Bowers, R. W. Ure, J. E. Bauerle, and A. J. Cornish, “InAs and InSb as thermoelectric materials,” *J. Appl. Phys.*, vol. 30, no. 6, pp. 930–934, 1959.

[3.3] K. W. Benz and G. Müller, “GaSb and InSb crystals grown by vertical and horizontal travelling heater method,” *J. Cryst. Growth*, vol. 46, no. 1, pp. 35–42, Jan. 1979.

[3.4] G. N. Kozhemyakin, “Influence of ultrasonic vibrations on the growth of semiconductor single crystals,” *Ultrasonics*, vol. 35, no. 8, pp. 599–604, 1998.

[3.5] D. B. Gadkari, K. B. Lal, and B. M. Arora, “Growth of undoped and Te doped InSb crystals by vertical directional solidification technique,” *Bull. Mater. Sci.*, vol. 21, no. 2, pp. 127–131, Apr. 1998.

[3.6] D. B. Gadkari and B. M. Arora, “Characterization of p and n-type bulk InSb crystals grown by vertical directional solidification technique,” *Indian J. Pure Appl. Phys.*, vol. 38, no. 4, pp. 237–242, 2000.

[3.7] A. A. Boguslavskii, V. V Sazonov, S. M. Sokolov, V. S. Zemskov, M. R. Raukhman, and V. P. Shalimov, “Influence of Microaccelerations on the Impurity Distribution in the InSb:Te Crystals Grown in Orbital Flights by the Method of Floating Zone Melting,” *Cosm. Res.*, vol. 42, no. 2, pp. 148–154, 2004.

[3.8] M. K. Khalaf, G. H. Mohammed, and F. Y. Hadi, “Growth Techniques and Some Physical Properties of InSb Single Crystal Abstract : Introduction :,” vol. 8, no. 1, 2011.

[3.9] D. B. Gadkari, “Advances of the Vertical Directional Solidification Technique for the Growth of High Quality GaSb Bulk Crystals,” vol. 6, pp. 65–73, 2012.

[3.10] A. A. Ebnalwaled, “Evolution of growth and enhancement in power factor of InSb bulk crystal,” *J. Cryst. Growth*, vol. 311, no. 19, pp. 4385–4390, 2009.

[3.11] A. A. Ebnalwaled, “Hopping conduction and dielectric properties of InSb bulk crystal,” *Ijens.Org*, vol. 11, no. 6, pp. 194–207, 2011.

[3.12] P. Se-Hwan, S. K. Han, S. Hee-Sung, K. Ho-Dong, C. Yun-Ho, and K. K. Yong, “Development of InSb Semiconductor Detector for High Resolution Radiation Measurement,” *J. Korean Phys. Soc.*, vol. 58, no. 6, p. 1577, Jun. 2011.

[3.13] V. Senthilkumar, M. Thamilselvan, K. Premnazeer, S. K. Narayandass, D. Mangalaraj, B. Karunagaran, K. Kim, and J. Yi, “Characterization of p-type In-

Sb thin films prepared by vacuum evaporation," *Vacuum*, vol. 79, no. 3–4, pp. 163–170, 2005.

[3.14] S. R. Vishwakarma, a. K. Verma, R. S. N. Tripathi, S. Das, and Rahul, "Study of structural property of n-type indium antimonide thin films," *Indian J. Pure Appl. Phys.*, vol. 50, no. 5, pp. 339–346, 2012.

[3.15] E. H. Putley, "Thermoelectric and Galvanomagnetic effects in Lead Selenide and Telluride," *Proc. Phys. Soc. Sect. B*, vol. 68, no. 1, pp. 35–42, 2002.

[3.16] C. Herring, T. H. Geballe, and J. E. Kunzler, "Phonon-Drag Thermomagnetic Effects in n-Type Germanium. I. General Survey," *Phys. Rev.*, vol. 111, no. 1, pp. 36–57, Jul. 1958.

[3.17] H. Mette, W. W. Gärtner, and C. Loscoe, "Nernst and Ettingshausen Effects in Germanium between 300 and 750°K," *Phys. Rev.*, vol. 115, no. 3, pp. 537–542, Aug. 1959.

[3.18] C. R. Whitsett, "Righi-Leduc Effect in Mercuric Selenide," *J. Appl. Phys.*, vol. 32, no. 10, p. 2257, 1961.

[3.19] R. Wolfe and G. E. Smith, "Effects of a magnetic field on the thermoelectric properties of a bismuth-antimony alloy," *Appl. Phys. Lett.*, vol. 1, no. 1, pp. 5–7, 1962.

[3.20] M. E. Ertl, G. R. Pfister, and H. J. Goldsmid, "Size dependence of the magneto-Seebeck effect in bismuth-antimony alloys," *Br. J. Appl. Phys.*, vol. 14, no. 3, pp. 161–162, Mar. 1963.

[3.21] R. W. . J. Ure, "Theory of materials for thermoelectric and thermomagnetic devices," *Proc. IEEE*, vol. 51, no. 5, 1963.

[3.22] D. R. Lovett and D. W. G. Ballentyne, "The Righi - Leduc effect in cadmium arsenide," *British Journal of Applied Physics*, vol. 18, no. 10. pp. 1399–1402, 2002.

[3.23] E. R. Washwell, "THE NERNST DETECTOR: FAST THERMAL RADIATION DETECTION," *Appl. Phys. Lett.*, vol. 17, no. 4, p. 164, 1970.

[3.24] W. M. Yim and A. Amith, "Bi□Sb alloys for magneto-thermoelectric and thermomagnetic cooling," *Solid. State. Electron.*, vol. 15, no. 10, pp. 1141–1165, Oct. 1972.

[3.25] P. J. Tausch and R. S. Newrock, "High-field Righi-Leduc effect and lattice thermal conductivity of potassium," *Phys. Rev. B*, vol. 16, no. 12, pp. 5381–5389, Dec. 1977.

[3.26] V. M. Grabov and O. N. Uryupin, "Magneto-thermoelectric properties of undoped and doped Bi-Sb single crystals," *XVI ICT "97. Proc. ICT"97. 16th Int. Conf. Thermoelectr. (Cat. No.97TH8291)*, pp. 176–179, 1997.

[3.27] S. T. and I. Y. M.Sakurai, N.Satoh, "Energy Conversion by galvanomagnetic and thermomagnetic effects with the use of BiSb alloys," *in IEEE*, pp. 1–10, 1997.

[3.28] K. Ikeda, H. Nakamura, I. Yanenaga, and S. Yamaguchi, "Transport coefficients of Ge in magnetic fields," *Seventeenth Int. Conf. Thermoelectr. Proc. ICT98 (Cat. No.98TH8365)*, no. 1 998, pp. 277–279, 1998.

[3.29] S. C. S. Cho, Y. K. Y. Kim, a. DiVenere, G. K. Wong, J. B. Ketterson, and J. R. Meyer, "Anisotropic Seebeck and magneto-Seebeck coefficients of Bi and BiSballoy thin films," *Eighteenth Int. Conf. Thermoelectr. Proceedings, ICT'99 (Cat. No.99TH8407)*, vol. 808, no. 2000, pp. 1–6, 1999.

[3.30] S. C. S. Cho, Y. K. Y. Kim, a. DiVenere, G. K. L. Wong, a. J. Freeman, J. B. Ketterson, L. J. Olafsen, I. Vurgaftman, J. R. Meyer, and C. a. Hoffman, "Artificially ordered BiSb alloys: growth and transport properties," *Eighteenth Int. Conf. Thermoelectr. Proceedings, ICT'99 (Cat. No.99TH8407)*, pp. 16–19, 1999.

[3.31] H. Okumura, Y. Hasegawa, H. Nakamura, and S. Yamaguchi, "A computational model of thermoelectric and thermomagnetic semiconductors," *in Eighteenth International Conference on Thermoelectrics. Proceedings, ICT'99 (Cat. No.99TH8407)*, vol. 2, no. 1 999, pp. 209–212, 1999.

[3.32] M. Hamabe, S. Yamamoto, S. Yamaguchi, H. Takahashi, H. Okumura, I. Yonenaga, T. Sasaki, and K. Watanabe, "Magnetic field effect for improvement of thermoelectric conversion: A proposal for Nernst-Seebeck element," *Proc. ICT'03. 22nd Int. Conf. Thermoelectr. (IEEE Cat. No.03TH8726)*, pp. 567–570, 2003.

[3.33] T. Teramoto, T. Komine, S. Yamamoto, M. Kuraishi, R. Sugita, Y. Hasegawa, and H. Nakamura, "Influence of the band structure of BiSb alloy on the magneto-Seebeck coefficient," *J. Appl. Phys.*, vol. 104, no. 5, 2008.

[3.34] J. C. G. de Sande and J. M. Guerra, "Nernst-Ettingshausen effect in polycrystalline bismuth at high temperature," *Phys. Rev. B*, vol. 45, no. 20, pp. 469–473, 1992.

[3.35] S. Yamaguchi, T. Matsumoto, J. Yamazaki, N. Kaiwa, and A. Yamamoto, "Thermoelectric properties and figure of merit of a Te-doped InSb bulk single crystal," *Appl. Phys. Lett.*, vol. 87, no. 20, p. 201902, 2005.

[3.36] H. Mette, "Righi-Leduc Effect in InSb between 250C and 300oC," *Zeitschrift Phys.*, vol. 176, no. 4, pp. 329–335, Dec. 1963.

[3.37] S. W. Angrist, "A Nernst Effect Power Generator," *J. Heat Transfer*, vol. 85, no. 1, p. 41, 1963.

[3.38] M. R. El-Saden and F. W. Thomas, "Nernst effect in indium antimonide," *J. Appl. Phys.*, vol. 36, no. 1, pp. 181–183, 1965.

[3.39] H. NAKAMURA, K. IKEDA, S. YAMAGUCHI, and K. KURODA, "Transport coefficients of thermoelectric semiconductor InSb-a candidate for the Nernst element.," *Journal of Advanced Science*, vol. 8, no. 3/4. pp. 153–157, 1996.

[3.40] K. IKEDA, H. NAKAMURA, S. YAMAGUCHI, and K. KURODA, "Measurement of transport properties of thermoelectric materials in the magnetic field.," *Journal of Advanced Science*, vol. 8, no. 3/4. pp. 147–152, 1996.

[3.41] H. Nakamura, K. Ikeda, and S. Yamaguchi, "Transport property and energy conversion of nernst elements in strong magnetic field," *Nippon Kinzoku Gakkaishi/Journal Japan Inst. Met.*, vol. 61, no. 12, pp. 1318–1325, 1997.

[3.42] K. Ikeda, H. Nakamura, and S. Yamaguchi, "Geometric contribution to the measurement of thermoelectric power and Nernst coefficient in a strong magnetic field," *in XVI ICT "97. Proceedings ICT"97. 16th International Conference on Thermoelectrics (Cat. No.97TH8291)*, no. 6, pp. 155–158, 1997.

[3.43] H. Nakamura, K. Ikeda, and S. Yamaguchi, "Transport coefficients of InSb in a strong magnetic field," *XVI ICT "97. Proc. ICT"97. 16th Int. Conf. Thermoelectr. (Cat. No.97TH8291)*, no. 1, pp. 1–6, 1997.

[3.44] S. Yamaguchi, K. Ikeda, H. Nakamura, K. Kuroda, and O. Motojima, "A fusion study of thermoelectric conversion in magnetic fields," *Fusion Eng. Des.*, vol. 41, no. 1–4, pp. 555–559, 1998.

[3.45] H. Okumura, S. Yamaguchi, H. Nakamura, K. Ikeda, and K. Sawada, "Numerical computation of thermoelectric and thermomagnetic effects," *in Seventeenth International Conference on Thermoelectrics. Proceedings ICT98 (Cat. No.98TH8365)*, pp. 10–13, 1998.

[3.46] H. Nakamura, K. Ikeda, and S. Yamaguchi, "Physical model of Nernst element," *in Seventeenth International Conference on Thermoelectrics. Proceedings ICT98 (Cat. No.98TH8365)*, no. 7, pp. 97–100, 1998.

[3.47] H. Nakamura, K. Ikeda, and S. Yamaguchi, "Transport Coefficients of Indium Antimonide in a Magnetic Field," *Jpn. J. Appl. Phys.*, vol. 38, no. Part 1, No. 10, pp. 5745–5749, Oct. 1999.

[3.48] J. P. Heremans, C. M. Thrush, and D. T. Morelli, "Geometrical magnetothermopower in semiconductors," *Phys. Rev. Lett.*, vol. 86, no. 10, pp. 2098–2101, 2001.

[3.49] J. Heremans, C. Thrush, and D. Morelli, "Geometrical magnetothermopower in n- and p-type InSb," *Phys. Rev. B*, vol. 65, no. 3, pp. 1–8, 2001.

[3.50] C. Uher and H. J. Goldsmid, "A comparison of thermomagnetic materials for use at room temperature," *J. Phys. D. Appl. Phys.*, vol. 5, no. 8, pp. 1478–1488, 2002.

[3.51] M. M. Gadjialiev, Z. S. Pirmagomedov, and T. N. Efendieva, "Temperature and

magnetic-field dependences of the thermoelectric power of electronic indium antimonide," *Semiconductors*, vol. 48, no. 9, pp. 1139–1140, Sep. 2014.

[3.52] S. Zhu, "Thermoelectric Study of Insb Secondary Phase Based Nano," Clemson University, 2013.

[3.53] H. Nakamura, K. Ikeda, and S. Yamaguchi, "Transport coefficients of InSb in a strong magnetic field," *in XVI ICT "97. Proceedings ICT"97. 16th International Conference on Thermoelectrics (Cat. No.97TH8291)*, 1997, pp. 142–146.

[3.54] K. F. Cuff, R. B. Horst, J. L. Weaver, S. R. Hawkins, C. F. Kooi, and G. M. Enslow, "THE THERMOMAGNETIC FIGURE OF MERIT AND ETTINGSHAUSEN COOLING IN Bi[Single Bond]Sb ALLOYS," *Appl. Phys. Lett.*, vol. 2, no. 8, p. 145, 1963.

[3.55] C. F. Kooi, R. B. Horst, K. F. Cuff, and S. R. Hawkins, "Theory of the Longitudinally Isothermal Ettingshausen Cooler," *J. Appl. Phys.*, vol. 34, no. 6, pp. 1735–1742, 1963.

[3.56] O. Yamashita and S. Tomiyoshi, "Effect of geometrical shape on magneto-Peltier and Ettingshausen cooling in Bi and Bi 0.88Sb 0.12 polycrystals," *J. Appl. Phys.*, vol. 92, no. 7, pp. 3794–3802, 2002.

[3.57] R. T. Delves, "The prospects for Ettingshausen and Peltier cooling at low temperatures," *Br. J. Appl. Phys.*, vol. 13, no. 9, pp. 440–445, Sep. 1962.

[3.58] T. C. Harman and J. M. Honig, "Theory of Galvano-Thermomagnetic Energy Conversion Devices. I. Generators," *J. Appl. Phys.*, vol. 33, no. 11, p. 3178, 1962.

[3.59] https://en.wikipedia.org/wiki/Indium_antimonide.

[3.60] http://www.crct.polymtl.ca/fact/documentation/SGTE/SGTE_Figs.htm.

[3.61] K. F. Hulme and J. B. Mullin, "Indium antimonide—A review of its preparation, properties and device applications," *Solid. State. Electron.*, vol. 5, no. 4, pp. 211–IN10, Jul. 1962.

[3.62] D. G. Avery, D. W. Goodwin, W. D. Lawson, and T. S. Moss, "Optical and Photo-Electrical Properties of Indium Antimonide," *Proc. Phys. Soc. Sect. B*, vol. 67, no. 10, pp. 761–767, 2002.

[3.63] http://www.ioffe.ru/SVA/NSM/Semicond/.

[3.64] D. M. Rowe, *CRC Handbook of thermoelectrics*. 1995.

[3.65] J. Singh, *Electronic and optoelectronic properties of semiconductor structures*. New York: Cambridge University Press, 2003.

[3.66] M. A. Kinch, "infrared Detector Matrials", *J., of Electronic Materials*, vol. 29, Issue 6, June 2000.

[3.67] N. K. Udayashankar and H. L. Bhat, "Growth and characterization of indium

antimonide and gallium antimonide crystals," *Bull. Mater. Sci.*, vol. 24, no. 5, pp. 445–453, Oct. 2001.

[3.68] T. Thundat, "Experimental and theoretical investigation of chemisorbed Ga on Si(111)," *J. Vac. Sci. Technol. A Vacuum, Surfaces, Film.*, vol. 6, no. 3, p. 681, May 1988.

[3.69] T. D. Mishima and M. B. Santos, "Effect of buffer layer on InSb quantum wells grown on GaAs (001) substrates," *J. Vac. Sci. Technol. B Microelectron. Nanom. Struct.*, vol. 22, no. 3, p. 1472, 2004.

[3.70] R. G. van Welzenis and B. K. Ridley, "On the properties of InSb quantum wells," *Solid. State. Electron.*, vol. 27, no. 2, pp. 113–120, Feb. 1984.

[3.71] V. K. Dixit, B. V. Rodrigues, H. L. Bhat, R. Kumar, R. Venkataraghavan, K. S. Chandrasekaran, and B. M. Arora, "Effect of lithium ion irradiation on the transport and optical properties of Bridgman grown n-type InSb single crystals," *J. Appl. Phys.*, vol. 90, no. 4, p. 1750, 2001.

[3.72] V. K. Dixit, B. V. Rodrigues, H. L. Bhat, R. Venkataraghavan, K. S. Chandrasekaran, and B. M. Arora, "Growth of InSb epitaxial layers on GaAs (0 0 1) substrates by LPE and their characterizations," *J. Cryst. Growth*, vol. 235, no. 1–4, pp. 154–160, 2002.

[3.73] T. Zhang, S. K. Clowes, M. Debnath, a. Bennett, C. Roberts, J. J. Harris, R. a. Stradling, L. F. Cohen, T. Lyford, and P. F. Fewster, "High-mobility thin InSb films grown by molecular beam epitaxy," *Appl. Phys. Lett.*, vol. 84, no. 22, pp. 4463–4465, 2004.

[3.74] D. L. Rode, "Electron Transport in InSb, InAs, and InP," *Phys. Rev. B*, vol. 3, no. 10, pp. 3287–3299, May 1971.

CHAPTER 4

Material Preparation and Characterisation

4.1: Introduction

In this chapter, the structure and physical properties of InSb were summarised. Then it is followed by a description of the experimental technique developed to produce InSb bulk samples, including the amount of the raw materials, environmental conditions and the design and construction of a unique sample reaction chamber consisting of an open-end quartz tube sealed inside a niobium container.

The procedures for preparing specific sample geometry by cutting, polish and etching were also presented.

4.2: Material preparation

There are many techniques used to grow crystal materials, each of them has its own advantages and disadvantages. The method generally employed for the bulk growth of group III-V materials is the Czochralski technique [4.1-4.2]. The main disadvantage of this technique is that it is difficult to balance the axial and radial thermal gradients [4.3, 4.4].

Horizontal and vertical travelling heater methods are also employed to grow InSb crystals [4.5], as is vertical directional solidification [4.6]. The principal difficulty experienced in these methods is the extremely slow growth rate [4.7, 4.8]. High-quality crystals can also be grown using the Bridgman technique [4.9, 4.10].

InSb crystals can be readily formed by slow cooling from a melt with a stoichiometric amount of In and Sb [4.11]. The III-V InSb compounds melt congruently, which means a liquid and solid having identical compositions are in equilibrium at the melting point. Thus, InSb can be grown directly from the melt [4.12].

The vertical Bridgeman method was also suggested for preparation doped and undoped polycrystalline InSb bulk samples. Ebnalwaled [4.9, 4.13] employed vertical Bridgman method to produce low-defect crystals, and a p-type polycrystalline was obtained. In Bridgeman method the quartz tube must be sealed under a vacuum condition (to prevent contamination during synthesis, handling and crystal growth). However, as this facility is not available at Cardiff University, a new technique based on the growth by melt method was used to prepare the InSb.

4.3: Experimental setup

4.3.1: The rig design

The technique used to prepare InSb in this study is by melting the raw materials together and then leaving the melt to cool under vacuum conditions. The rig that was designed and tested in this study is shown in Figure 4-1, which contains:

1- A furnace. 2- Vacuum pump. 3- Vacuum gauge.
4- Valve. 5- Thermometer. 6- Temperature controller.

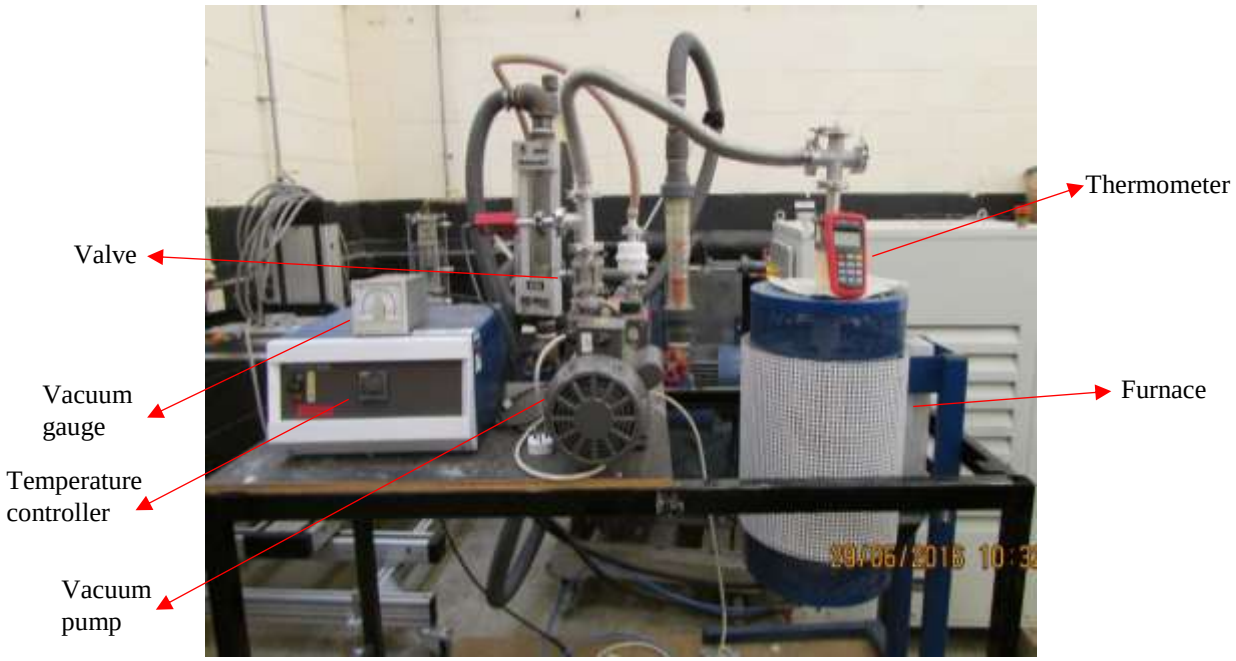

Figure 4-1: The rig that was designed to prepare InSb.

4.3.1.1: Furnace

A furnace manufactured by the company "Lenton" (Type 15/50/180) was used for melting the raw materials to form InSb compounds.

The furnace contains a central ceramic tube surrounded by heaters which raise the temperature to 1500 °C. The heaters are governed by a controller system located beside the furnace. The ceramic tube has a ring clip at each end, which consists of four bolts. These bolts hold a stainless steel plate (with a stainless steel seal) which is fixed in place by four wingnuts. The stainless steel seals makes the ceramic tube gas tight and allow the specimens to be tested under vacuum or flowing gas conditions.

A 'Viton' washer, supplied by Alliance & Heatshield Engineering Company was inserted between the tube and the stainless steel seals. The purpose of using this washer is to prevent any leakage inside the tube, which helps to improve the vacuum level.

The lower end of the tube is attached to a gas nozzle on the stainless steel seal as either a vacuum or gas flow outlet. The top end has a KF-25 designation outlet which fixed on the stainless steel seal to connect the furnace tube to a vacuum pump.

Two radiation shields (or insulating plugs) were used to prevent the radiation of heat from reaching the two ends of tube, as shown in Figure 4-2. This radiation may otherwise cause damage to the Viton washer and consequently reduce the vacuum level.

4.3.1.2: Vacuum

The production of polycrystalline InSb by growth from melting needsa good vacuum to minimise possible oxidation during the melting and cooling processes. This requirement can be achieved by a two-stage system.

A pump made by the Edwards company E2M 18 was used to evacuate the tube from the top end. It can reach a vacuum level of 5×10^{-2} mbar within 10 minutes

and maintain the level over the whole period of operation, which is usually longer than 8 hours.

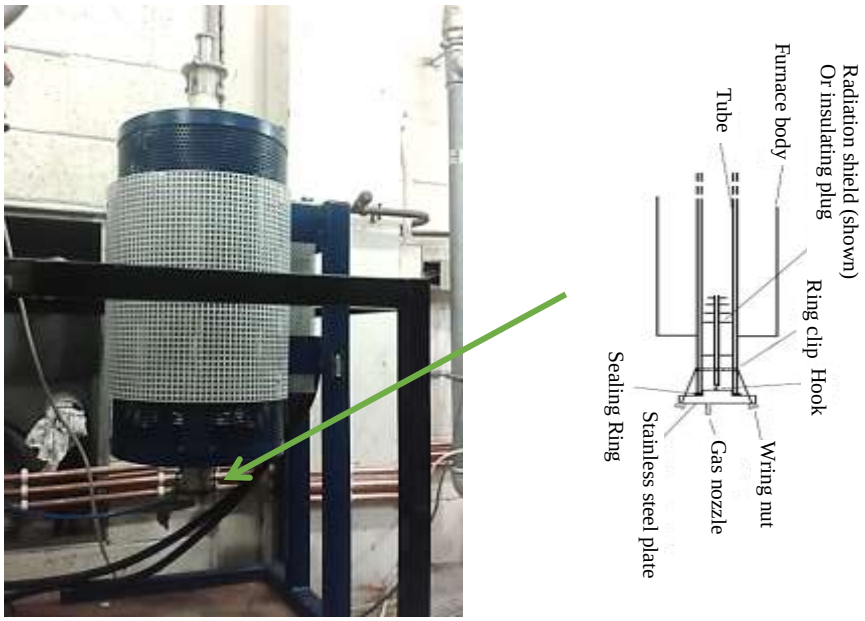

Figure 4-2: The furnace that was used to prepare InSb.

4.4: Experimental conditions

4.4.1: Raw materials

The oxidation of raw materials will form oxides in InSb, affecting the purity of materials, which is not desired. The minimising of oxidation before, during and after melting is important to obtain a pure InSb phase.

The antimony Sb oxidizes when heated in air. Although this occurs very slowly, it will react at ambient temperatures with water to forming trioxide antimony (III) Sb_2O_3. For this reason, all experiments were carried out under a vacuum to prevent this as much as possible.

4.4.2: Sample melting chamber design

A novel sample holder was designed instead of the sealed quartz tube which were used by most researchers. It is a closed container that maintains the raw materials In and Sb under inert gas atmosphere. This arrangement force holding the quartz tube vertically inside the furnace.

4.4.2.1: Quartz test tube

The raw materials In and Sb must put inside a container, which may be either ceramic or metal (crucible) or quartz tube. This holds them vertically inside the furnace. Initially a quartz tube was chosen to melt the In and Sb components (raw materials) together. The container subjected to temperatures up to 750 °C to ensure that a homogeneous distribution of the materials in the melt could be obtained. The quartz tube is preferred for these reasons:

1- It has high-temperature melting point. The highest temperature it can withstand is 1250 °C, so the materials inside the tube will melt without mixing with the tube substances.
2- A crucible is more expensive than quartz and it is more difficult to extract InSb from it without it breaking. For these reasons a quartz tube was considered to be the best choice of melting container for the raw materials.

In other hand, crucible is more expensive than quartz and it is more difficult to extract InSb from it without it breaking. For these reasons a quartz tube was considered to be the best choice of melting container for the raw materials.

The quartz tube that was used supplied by H Baumbach & Co Ltd. The quartz tube dimension is 9 mm outer diameter, 7 mm inner diameter and 40 mm long with one rounded end.

4.4.2.2: Niobium container

If the raw materials inside the quartz tube is subjected to air when left inside the furnace, the raw materials will become oxidised. Therefore, it is very important to maintain the raw materials under inert gas atmosphere to minimise the oxidation of the raw materials.

In this work the niobium container, made from cylindrical niobium rod was used to make sure the raw materials In and Sb were maintained under an argon atmosphere. The reason for using the Niobium container is the higher melting point, which is 2468 °C, than the melting point of both raw materials (for In is 156.6 °C and Sb is 630.63 °C respectively) and that of the quartz tube 1250 °C.

A cylindrical rod of Niobium, of 19 mm diameter and 10 cm length, was supplied by the Alfa Aesar company.

In the initial design, The Niobium rod was cut into two pieces, one was machined into a container and the other as a lid. The lid and container have threads so that they can be tightly joined together, as demonstrated in Figure 4-3 below. This is to minimise the oxidation that might otherwise befall the raw materials. To check if the container can operate at temperatures up to 800 °C, the container was placed inside the furnace and the temperature was increased gradually from 25 °C to 800 °C. In a test, when the temperature increased from 25 °C to 600 °C, no problems occurred and the lid was opened easily. Unfortunately, when the container was tested at temperatures between 600-650 °C, it was impossible to open the lid afterward as the threads had melted and bended together. For this reason, the design was changed to a lid without the threads and the opposite end of the container was cut to make into a new lid.

A stainless steel washer with thicknesses of 0.17 cm was put between the lid and container, which can withstand high temperatures (the melting points of stainless steel range between 1325 °C and 1530 °C). This prevented any adhesion between the lid and the container. Figure 4-4 shows the niobium container after modification.

The photographs of the niobium container before and after modification are shown in Figure 4-5.

It is obvious that the first design did not meet the requirement of installing the quartz tube vertically. A modification was made to add a hook and attached it to a chamber to fulfil the design requirement.

4.4.2.3: Chamber and its holder

The chamber was designed to ensure the raw materials and quartz tube was sealed inside the container under an argon atmosphere. The chamber consists of two stainless steel circular plates and three stainless steel bolts. They sandwich the niobium container in the middle and tightened using the 3 bolts and nuts as shown in Figure 4-6. A photograph of the chamber holder assembly is shown in Figure 4-7.

The chamber holder was designed also to keep the niobium container, lid and quartz tube vertically positioned inside the furnace. A hook is used as the chamber holder and is made from iron. It is fixed in the middle of the top stainless steel plate for hanging the chamber inside the furnace. A Ni-Cr wire is used to hang the chamber from the hook to the top stainless steel seal of the furnace tube, as shown in Figure 4-7. The Ni-Cr is chosen because it can withstand high temperatures (melting point is about 1400 °C).

A K-type mineral insulated thermocouple supplied by Labfacility Ltd. was used to monitor the temperature of the Niobium container inside the furnace. It is passed through a blank flange then through the chamber to make contact with the Niobium container. The blank flange is closed the top way of a 3-way tee over the top stainless steel seal. A Nickel wire is used to attach the thermocouple tip and niobium container together as shown in Figure 4-8.

A high temperature silicate supplied by Technicqll.pl was used to seal the point where the thermocouple passed through the vacuum system.

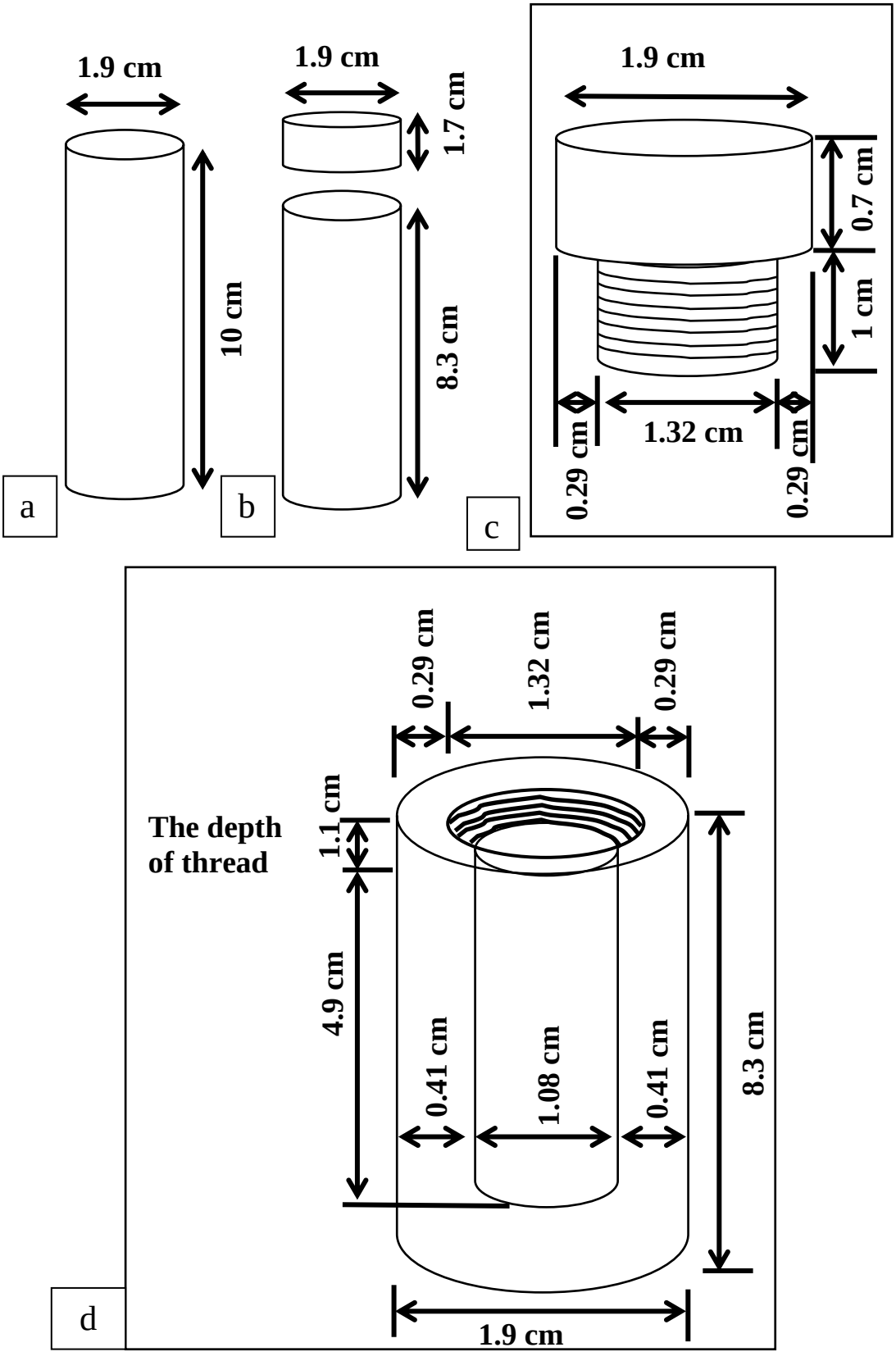

Figure 4-3: Steps in initial design of the niobium container, (a) niobium rod, (b) niobium container and its lid, (c) design of the lid and (d) design of the container.

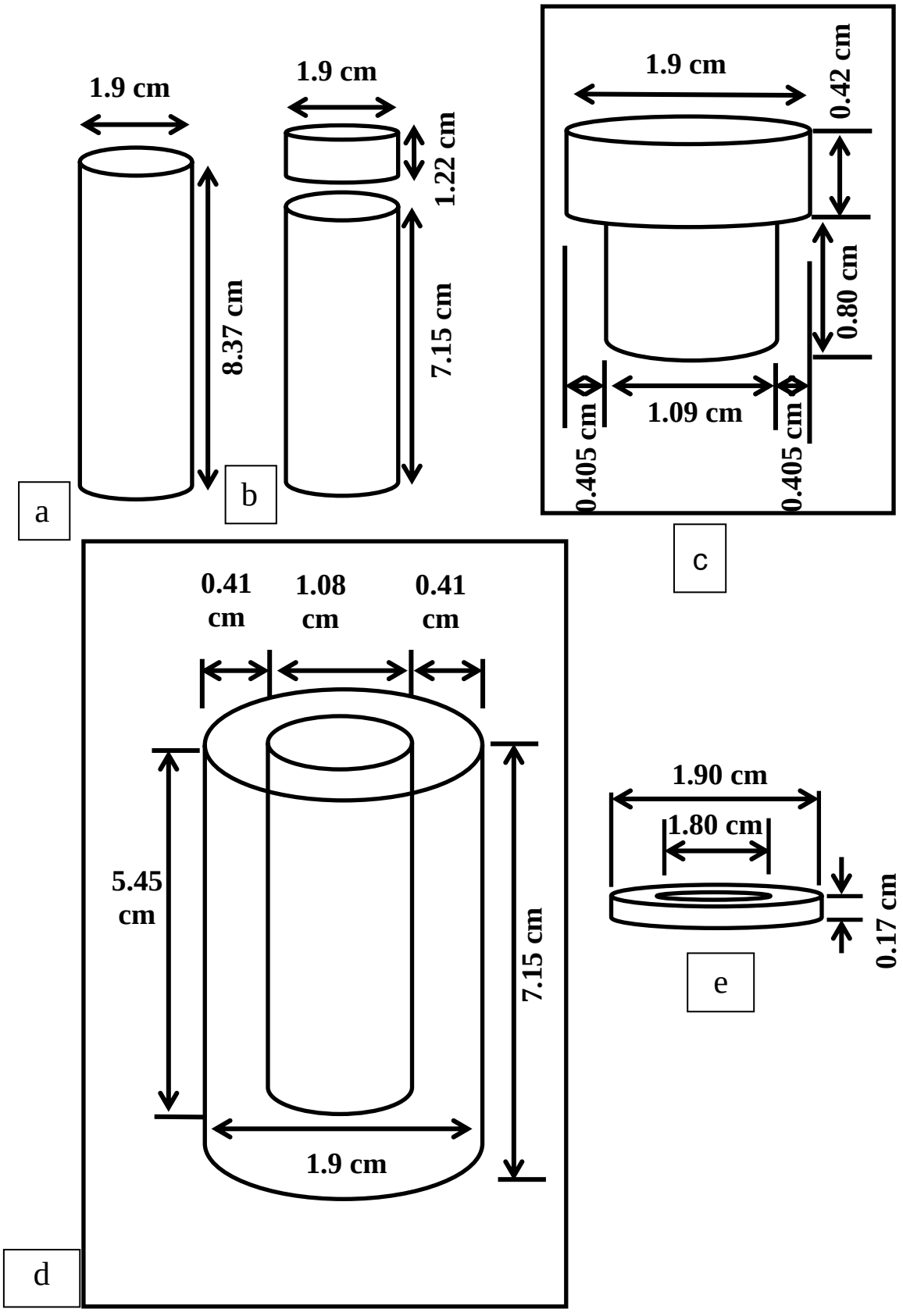

Figure 4-4: Steps in final designing of the Niobium container after modification, (a) closed initial niobium container, (b) niobium container and its lid, (c) final design of lid, (d) final design of container and (e) stainless steel washer.

Figure 4-5: The photographs of Niobium container designing, (a) initial design after damage and (b) final design after modification.

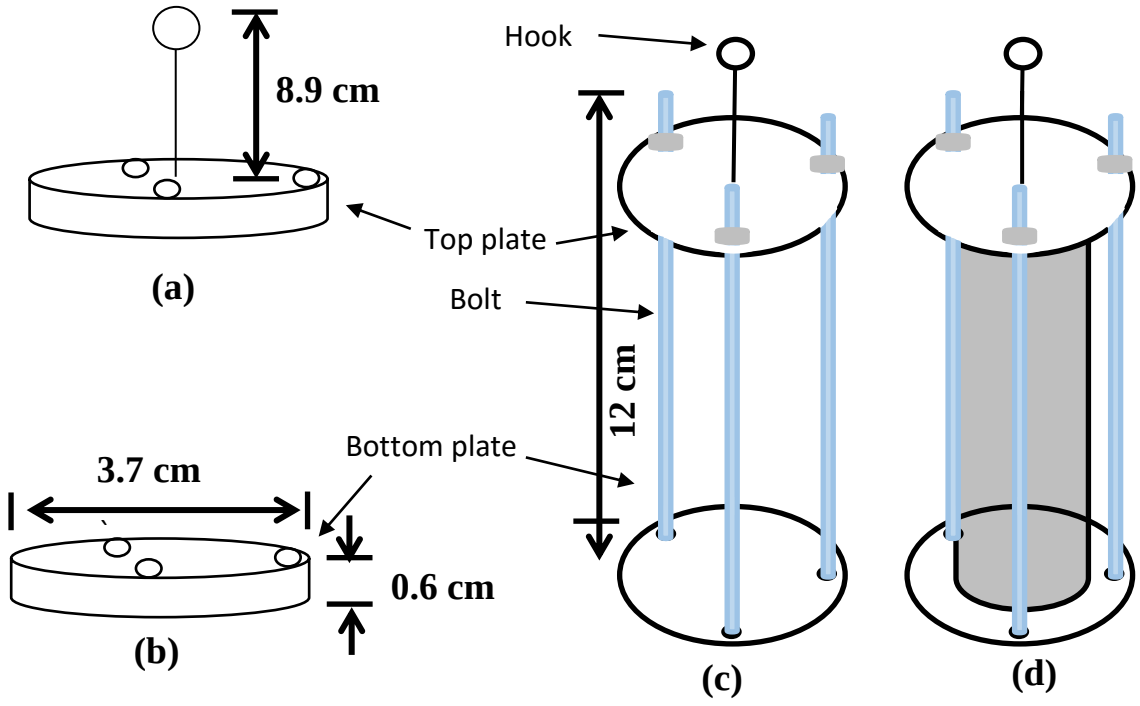

Figure 4-6: Step in design of the chamber, (a) top plate, (b) bottom plate, (c) chamber and (d) container inside the chamber.

Figure 4-7: Photograph of the Niobium container inside its chamber.

Figure 4-8: Attachment means of a thermocouple to the Niobium container.

Figure 4-9 explains the schematic diagram of growth system.

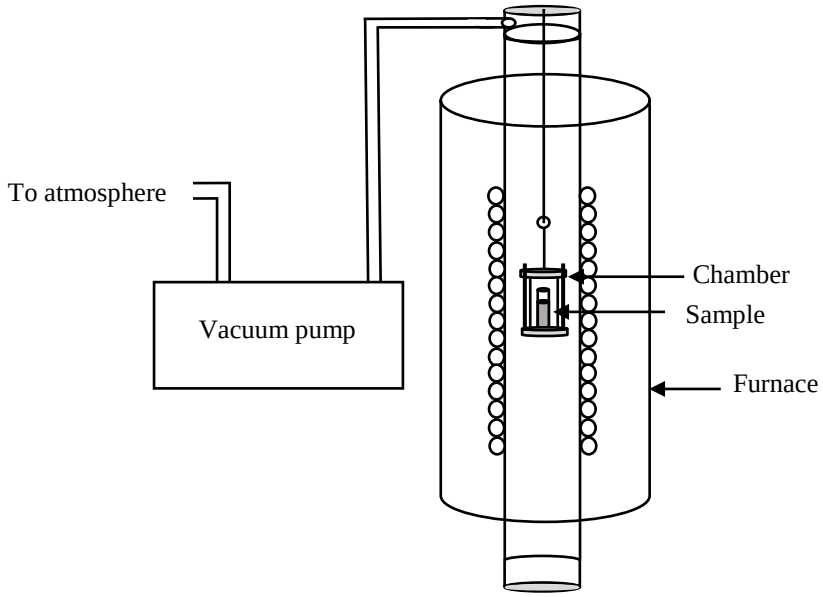

Figure 4-9: Schematic diagram illustrates growth system.

4.5: X-ray powder diffraction device

In this research, X-ray powder diffraction (XRD) measurements were carried out on a Philips PW1710 device which used Cu Kα radiation at room temperature (λ = 1.54056 Å). The inter-planar spacing and the crystal orientations can be estimated from the XRD pattern. When X-ray radiation passes through the sample, the radiation will reflect when incident on the electrons inside the atoms.

4.6: Sample preparation

4.6.1: Raw materials

The raw materials used to prepare InSb are indium In (50 g as 2-5 mm diameter beads), and antimony Sb (25 g as 1-5 mm diameter beads). These initial elements had purity of 5N (99.999%). The supplier was Sigma-Aldrich Company Ltd.

4.6.2: Materials synthesis

Synthesis off stoichiometric InSb involves the preparation of InSb samples from elemental indium and antimony. The ratio of In atoms to Sb atoms in the homogenised sample should be 1:1. Since the atomic weights of In and Sb are 114.82 and 121.75 amu respectively, the ratio by weight should be 1:1.06.

A quartz tube was cleaned before loading the initial material to make sure that there were no contaminations present. The raw materials were kept in a glove box and inserted into the quartz tube in the same glove box after weighing each substance. The tube was then inserted into the Niobium container, which was sealed using the chamber. The whole process was carried out inside the glove box which filled by argon, so that the materials were sealed under argon atmosphere for the rest of preparation processes.

Extreme care was taken in the transfer of material from glove box to its place inside the furnace, to maintain the accuracy of material composition (conserve the raw materials inside the quartz tube).

4.6.3: Samples investigated in this research study

4.6.3.1: Purchased sample (InSb wafer)

Undoped InSb (111) single crystal wafer 50.5mm diameter, 962-977 µm thickness, n-type, and carrier concentration $7.2\times10^{+13}$ – $1.90\times10^{+14}$ Cm^{-3} was supplied by Wafer Technology LKTD. This wafer was cut to form two different shapes: Bridge and rectangular shapes.

4.6.3.2: Samples fabrication

Four samples have been prepared, two undoped polycrystalline InSb and two doped polycrystalline InSb at different dopping levels:

- Undoped InSb: one is with high cooling rate, and the other with low cooling rate.
- Doped InSb: both samples doped with Te but for different doping levels: one with 0.1%, and the other with 0.25%.

All four samples above are rectangular in shape.

4.6.4: Samples doping

Many elements were studied as a dopant for InSb such as C, Ge and Te [4.14, 4.15] , D. L. Partin et al. [4.16] they reported that the doped InSb with Te samples have good sensitivity to a magnetic field than undoped.

In this work undoped and doped n-type InSb semiconductor with Te are examined as thermomagnetic materials. The higher doping will increase the scattering of electrons by donor atoms, which leads to lower device sensitivity to a magnetic field [4.13, 4.15].

The best element for doping InSb is one that increases both charge carriers (electron and hole) to the optimal value to obtain higher thermomagnetic power and Nernst voltage than the element that increases one type of charge carriers.

There are two reasons why the Te has become the best candidate for doping InSb. These are:

1- It has six electrons in the external shell, when substituted with Sb will enrich the material with extra one electron.
2- Lower melting and higher boiling points than the temperature of the furnace during the production of InSb, which ensures that the melt will be homogenous. In addition, low Te evaporation is associated with this sample preparation method.

There are many published works where Te was used as a doping element for InSb [4.1, 4.15-4.28].

The Te raw material was lump, the supplier was Sigma-Aldrich Company Ltd. Thus, it was grinded to make the weighing process easier, as much as sufficient for doping. The InSb is doped by adding Te to the raw materials inside quartz tube before placing in furnace. The doping level of Te is 0.1%, and 0.25% of the overall weight of the raw materials (In & Sb).

4.6.5: Samples geometry

The samples shape must have these characteristics:

1- The length of sample should be long enough relative to width to get higher amount of the Nernst coefficient [4.17, 4.29, 4.30].
2- The geometrical magneto-resistance is minimised when the sample length is much longer than its width [4.31, 4.32].

The length of the main sample should be three or four times its width [4.33]. Most of the authors have suggested the use of the Bridge shape for their samples [4.15, 4.17-4.21, 4.29, 4.30, 4.33, 4.34], some of them have used also Fat-Bridge shape [4.17, 4.30]. There are two reasons why the Bridge shape has been preferred. These are :

1- Wide head at the edges provides good attachment to heating or cooling bath [4.17].
2- The existence of arm helps to prevent warping of the current flux lines [4.29].

For the above reasons, the samples were cut with two shapes: one as Bridge shape and the other is rectangular shape with dimensions $12 \times 3 \times 1$ mm^3, as shown in Figure 4-10, 4-11.

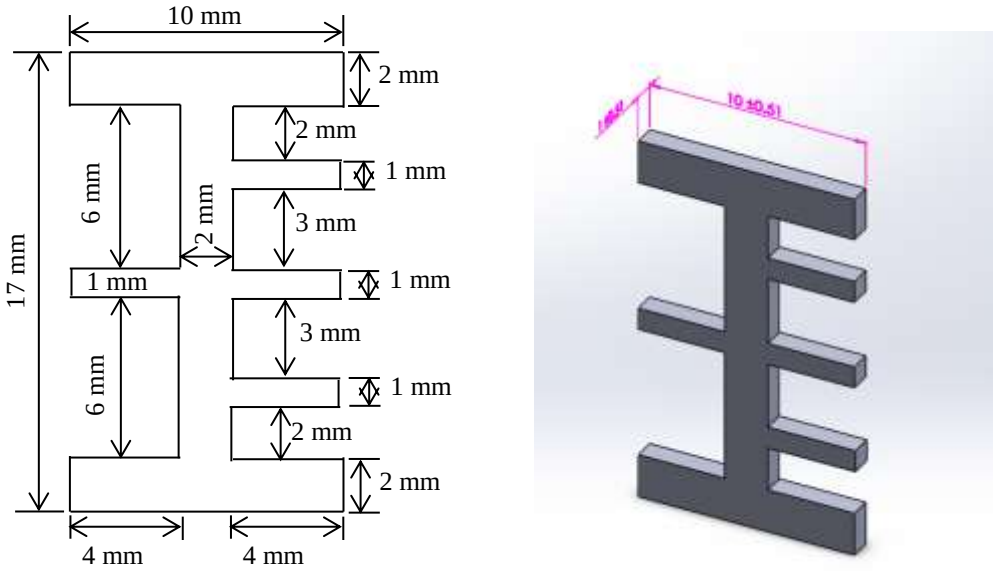

Figure 4-10: The design of bridge shape.

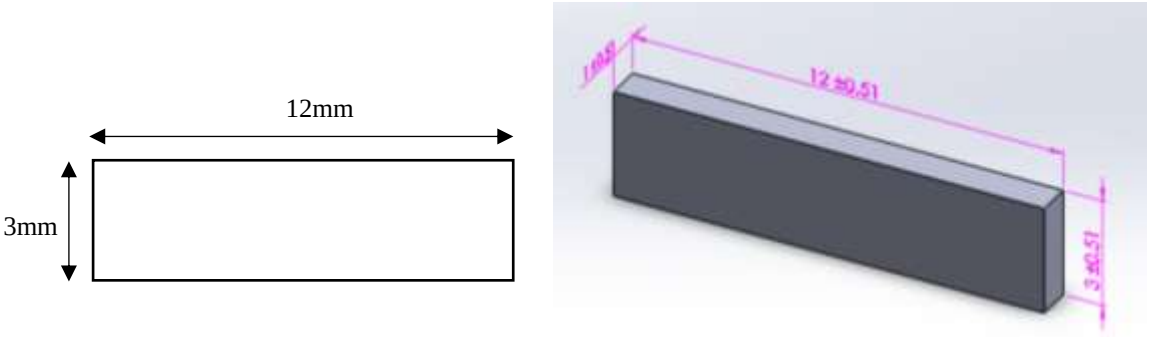

Figure 4-11: The design of rectangular shape.

4.6.6: Samples cutting

The samples were cut to form two different shapes by using two different techniques; the Bridge shape sample was cut using a laser cutter, which is accurate and has a resolution of ±10 µm. The rectangular shape samples were cut by diamond disk cutter with accuracy within 0.01 mm.

4.6.7: Samples polishing

The surface of InSb wafer, the undoped and doped InSb samples after cutting were rough. Therefore, the polishing is very necessary before measuring the seebeck coefficient and the resistivity by using 4 multifunctional probes. The polishing process remove any oxidation layers that may have occurred due to the reaction between sample surface and environmental. The error which might have happened when calculated by using 4-multiprobe function because of the oxidation layers will be minimised. A Struers (Rotopol-35) machine was used to polish the samples (undoped and doped with Te). The polisher has a disc speed control facility to adjust its rotation, emery paper was attached on the top of this disc. The most important thing to do before polishing starts is to determine what type of abrasive will be applied. The first stage, starts with a rough abrasive and each subsequent stage uses a finer abrasive gradually, which means lower grit abrasives, until the polishing was achieved. In addition, the polishing process is used to remove imperfections on the sample surface like pits, nicks, lines and scratches. The gradation in finer abrasives will leave progressively finer lines that are not visible to the naked eye, to get bright and smooth surface as much as possible.

The polishing was carry out using different grades of emery papers which have grit numbers range from 2000 to 4000 with water lubrication. Final polishing was done using the diamond paste (1 μm particle size) with oil lubrication. Microstructural examination was carried out using a light optical microscope (Nikon, ECLIPSE LV100). Figure 4-12 shows optical microscope photos of single crystal InSb before and after polishing.

4.6.8: Samples etching

The sample was etched by using cp4 etchant, which has composition $5NH_3$: 3HF : $3CH_3COOH$ for 1 Sec under room temperature [4.35] in order to analysis the microstructure of the InSb sample (doped and undoped with Te). Figure 4-13

shows the microstructure of InSb doped with 0.25% with Te, this Figure confirms that the sample is polycrystalline due to the crystal boundaries.

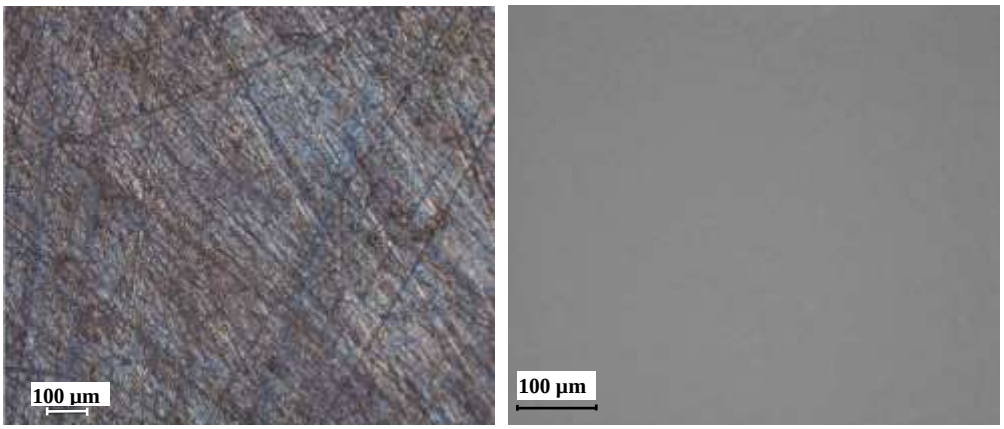

Figure 4-12: Optical microscope photos for single crystal InSb before and after polishing.

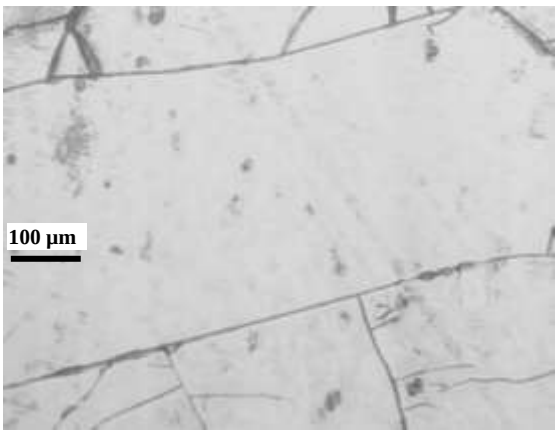

Figure 4-13: Optical microscope photo for polycrystalline InSb after etching.

4.7: Material production

4.7.1: Undoped samples

The chamber was suspended inside the furnace by a hook that was welded to the upper stainless steel plate and the system was closed tightly. The system was evacuated to a vacuum level of 5×10^{-2} mbar, it takes 10 min to achieve this level of vacuum. Then the furnace is raised to the temperature of 800 °C, which was reached

within 15 min. The furnace temperature was kept constant at 800 °C for 2 hours to obtain a homogenous melt of the raw materials.

A controlled turn-off of the furnace was performed to reduce its temperature from 800 °C to 400 °C over 1 hour. It is followed by a further decrease in temperature from 400 °C to 200 °C over 1 hour and eventually a final temperature drop from 200 °C to 150 °C was made over 30 min. The vacuum pump was turned off after closing the valve to keep the vacuum inside the furnace at a reasonably low level.

The sample was removed from the furnace when its temperature had reached a room temperature. The sample removed from the quartz tube by gently breaking the tube, to prevent any damage to the sample.

XRD analysis of pure InSb (first sample) was performed and the result is shown in Figure 4-14. From the XRD spectra it can be observed that there is an imbalance in the amount of indium and antimony which is necessary to make perfect InSb. The amount of antimony should be increased to balance with the indium amount as much as possible. Consequently, the ratio between In and Sb was changed to 1:1.0759.

To achieve a better quality crystal, the time that the furnace stable temperature should be increased and the rate of temperature cooling should be increased [4.36]. It was decided to increase the time at which the furnace temperature was kept constant at 800 °C.

Changes were made on the above process to obtain better InSb as much as possible. The furnace was operated at a constant temperature of 800 °C for 2 hours and 45 min to get homogenous melt and better quality in one orientation than others. The temperature was reduced manually at a rate of 2 °C per min as the furnace does not have a temperature controller. The manually controlled cooling process to reduce the furnace temperature to 400 °C took 3 hours and 20 min to

complete. The furnace was then turned off to reduce the temperature from 400 °C to 175 °C. Figure 4-15 shows the XRD spectra for the pure InSb (second sample).

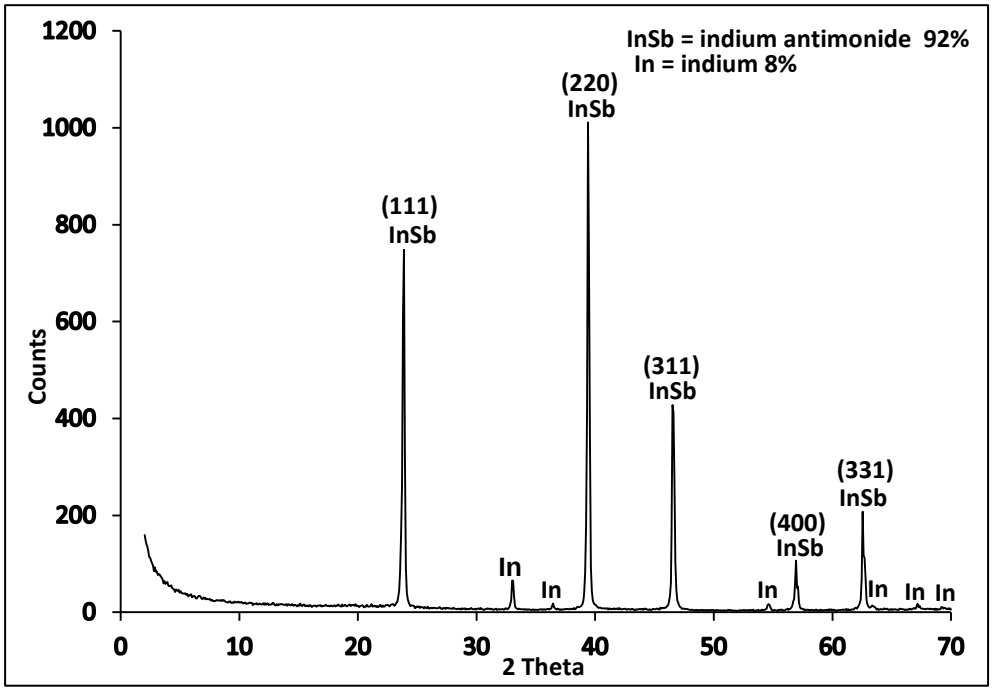

Figure 4-14: The XRD spectra for the first sample (pure InSb).

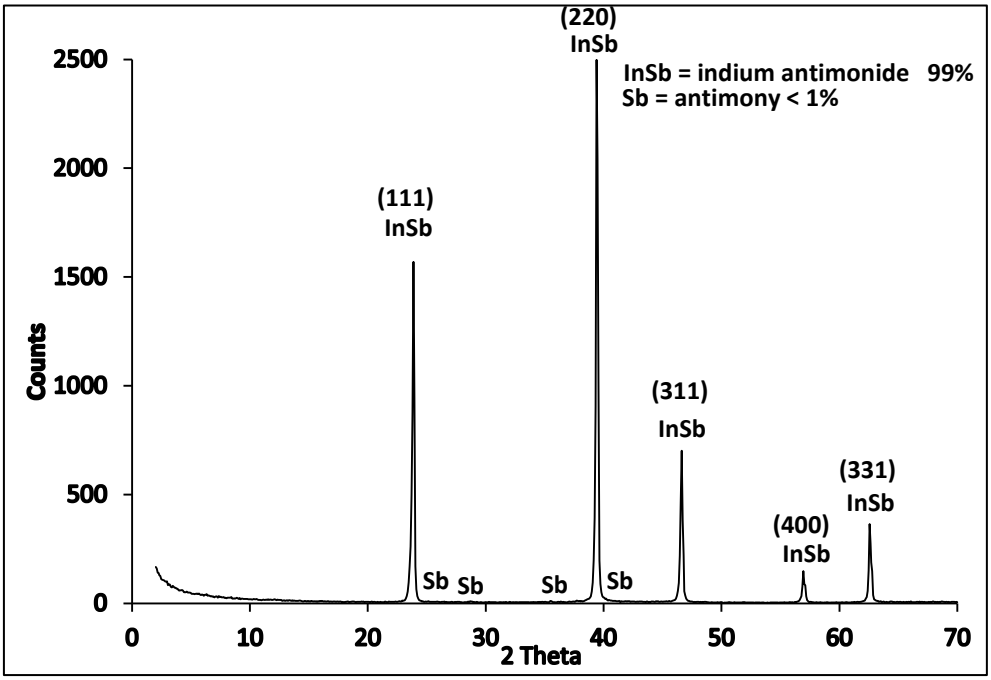

Figure 4-15: The XRD spectra for the second sample (pure InSb).

It can be seen from the XRD spectra that excess antimony appeared in this sample indicating that the amount of antimony should be reduced seven parts from eight. A change was made to use the ratio (1:(1.06+0.0481)). Figure 4-16 shows the XRD spectra for pure InSb (third sample).

All samples were made with small amount of raw materials, because x-ray analysis had been performed to check the perfectness of these samples before experiment test been carried out. In this case, the quartz tube wasn't broken. However, when using a larger amount to produce samples longer than 1.8 cm, it was cracked without any glass losses. The glass of quartz tube was broken by hitting it very gently to extract the sample safely. This crack happened because the thermal volume expansion coefficient of quartz tube relative to the InSb was higher than that for sample. The quartz tube is contracted more than the sample, as a result, there was an increasing pressure from quartz tube wall on the sample. The quartz tube was cracked, even when the temperature was reduced gradually. This is due to one of the intrinsic property of these materials and there is no way to change it.

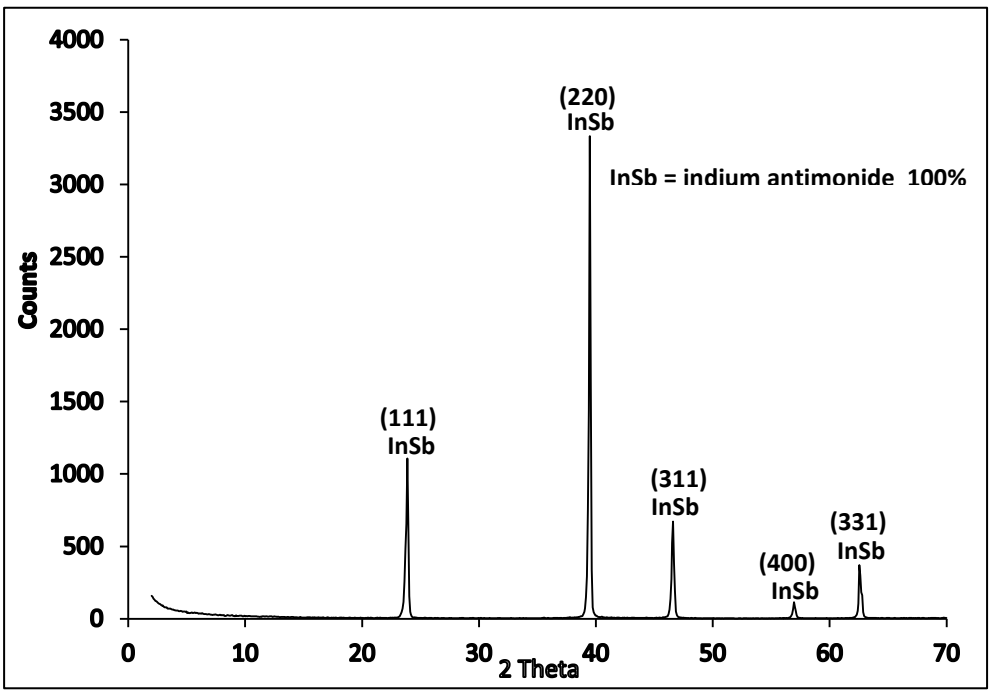

Figure 4-16: The XRD spectra for the third sample (pure InSb).

4.7.2: Doped samples

When doped InSb samples were made, the quartz test tube was broken. The breaking of the tube was happened during the cooling process, as the InSb sample was not spilled outside the quartz.

The attention was drawn to the big difference in temperature between the temperatures of furnace when turn off and when reached the room temperature. In another words, the furnace was cool rapidly. To solve this problem, the temperature rate was reduced manually from 800 °C till 200 °C at cooling rate of 2 °C/minute. The quartz tube after this adjustment was not broken for undoped sample, but it is just crack without any glass losses. The glass of quartz tube is broken by very gently hitting to extract the sample safely.

The conditions to produce material were different from that for the previous undoped InSb sample. A new undoped InSb sample was made under the same above condition, to provide an ability to compare between samples.

Figures 4-17 and 4-18 show the XRD spectra for doped samples with Te at doping levels of 0.1% and 0.25%, respectively. It can be seen that the maximum peak occurrs when the orientation is (220).

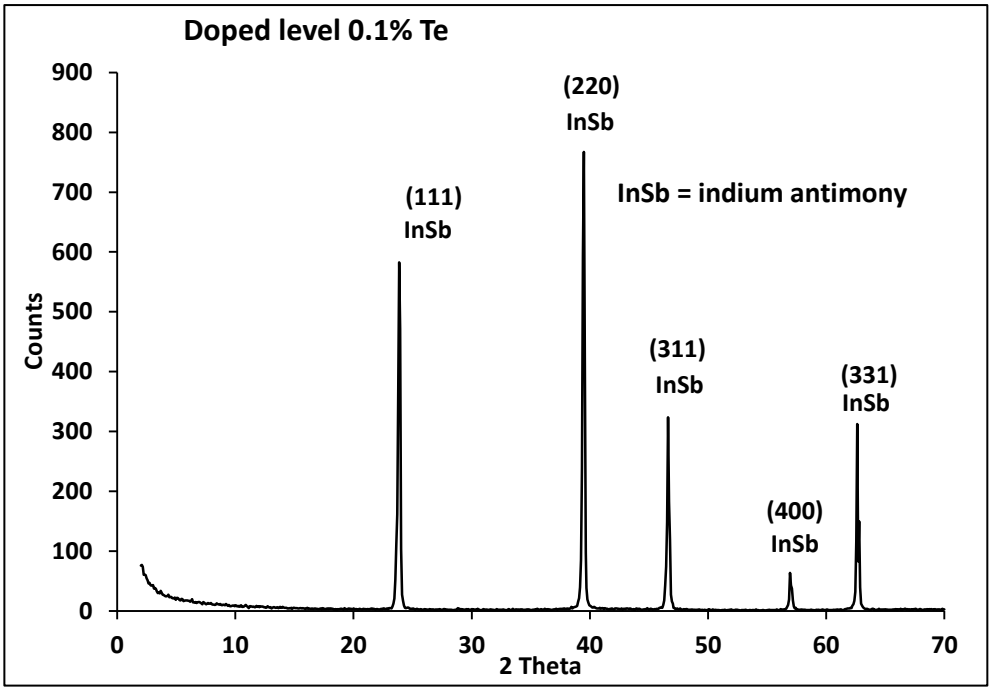

Figure 4-17: The XRD spectra for doped sample with 0.1% Te.

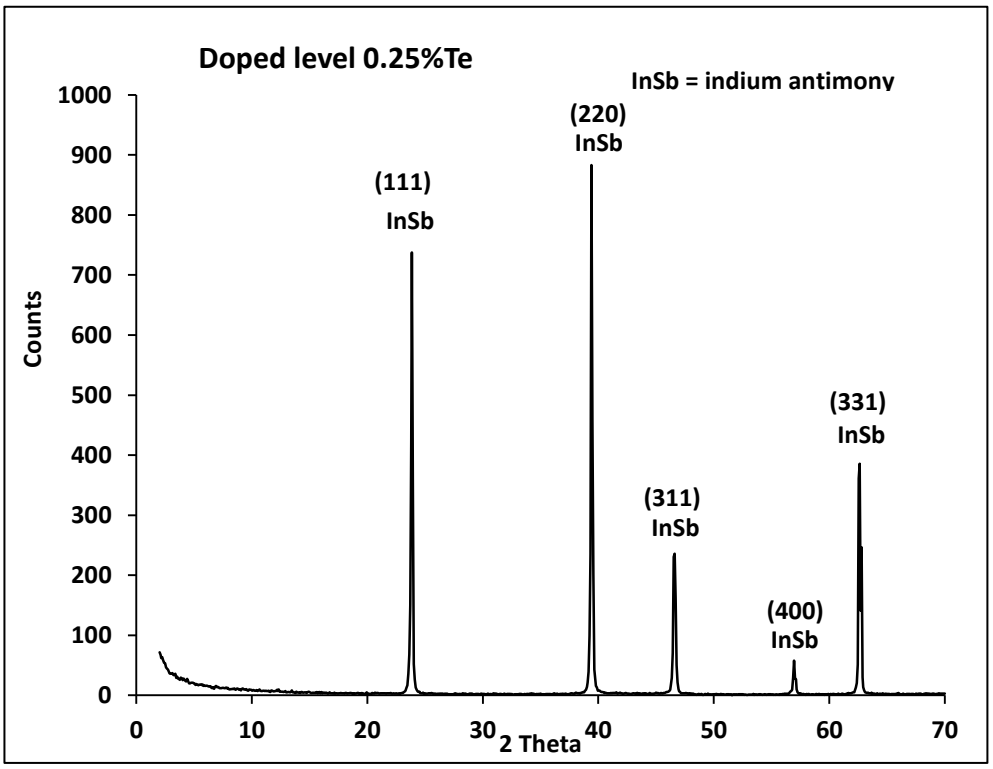

Figure 4-18: The XRD spectra for doped sample with 0.25% Te.

References

[4.1] K. Terashima, "Low-defect InSb crystal growth by InN doping," *J. Cryst. Growth*, vol. 47, no. 5–6, pp. 746–748, Nov. 1979.

[4.2] M. H. Lin and S. Kou, "Czochralski pulling of InSb single crystals from a molten zone on a solid feed," *J. Cryst. Growth*, vol. 193, no. 3, pp. 443–445, Oct. 1998.

[4.3] http://www.microchemicals.com/products/wafers/silicon_ingot_production.html

[4.4] D. B. Gadkari, "Advances of the Vertical Directional Solidification Technique for the Growth of High Quality GaSb Bulk Crystals," vol. 6, pp. 65–73, 2012.

[4.5] K. W. Benz and G. Müller, "GaSb and InSb crystals grown by vertical and horizontal travelling heater method," *Journal of Crystal Growth*, vol. 46, no. 1. pp. 35–42, 1979.

[4.6] D. B. Gadkari, K. B. Lal, a. P. Shah, and B. M. Arora, "Growth of high mobility InSb crystals," *J. Cryst. Growth*, vol. 173, no. 3–4, pp. 585–588, 1997.

[4.7] A. A. Ebnalwaled, "Evolution of growth and enhancement in power factor of InSb bulk crystal," *J. Cryst. Growth*, vol. 311, no. 19, pp. 4385–4390, 2009.

[4.8] K. W. Benz and G. Müller, "GaSb and InSb crystals grown by vertical and horizontal travelling heater method," *Journal of Crystal Growth*, vol. 46, no. 1. pp. 35–42, 1979.

[4.9] R. G. van Welzenis and B. K. Ridley, "On the properties of InSb quantum wells," *Solid. State. Electron.*, vol. 27, no. 2, pp. 113–120, Feb. 1984.

[4.10] J. Zhou, M. Larrousse, W. R. Wilcox, and L. L. Regel, "Directional solidification with ACRT," *J. Cryst. Growth*, vol. 128, no. 1–4, pp. 173–177, Mar. 1993.

[4.11] K. F. Hulme and J. B. Mullin, "Indium antimonide—A review of its preparation, properties and device applications," *Solid. State. Electron.*, vol. 5, no. 4, pp. 211–IN10, Jul. 1962.

[4.12] D. G. Avery, D. W. Goodwin, W. D. Lawson, and T. S. Moss, "Optical and Photo-Electrical Properties of Indium Antimonide," *Proc. Phys. Soc. Sect. B*, vol. 67, no. 10, pp. 761–767, 2002.

[4.13] A. Ebnalwaled, "Hopping conduction and dielectric properties of InSb bulk crystal," *Ijens.Org*, vol. 11, no. 6, pp. 194–207, 2011.

[4.14] D. L. Partin, J. Heremans, and C. M. Thrush, "Doping profiles for indium antimonide magnetoresistors," *Sensors Actuators A Phys.*, vol. 69, no. 1, pp. 39–45, 1998.

[4.15] H. Nakamura, K. Ikeda, and S. Yamaguchi, "Transport property and energy

conversion of nernst elements in strong magnetic field," *Nippon Kinzoku Gakkaishi/Journal Japan Inst. Met.*, vol. 61, no. 12, pp. 1318–1325, 1997.

[4.16] J. Heremans, C. Thrush, and D. Morelli, "Geometrical magnetothermopower in n- and p-type InSb," *Phys. Rev. B*, vol. 65, no. 3, pp. 1–8, 2001.

[4.17] K. Ikeda, H. Nakamurpa, and S. Yamaguchi, "Geometric contribution to the measurement of thermoelectric power and Nernst coefficient in a strong magnetic field," *XVI ICT "97. Proc. ICT"97. 16th Int. Conf. Thermoelectr. (Cat. No.97TH8291)*, no. 6, pp. 155–158, 1997.

[4.18] H. Nakamura, K. Ikeda, and S. Yamaguchi, "Transport Coefficients of Indium Antimonide in a Magnetic Field," *Jpn. J. Appl. Phys.*, vol. 38, no. Part 1, No. 10, pp. 5745–5749, 1999.

[4.19] H. Nakamura, K. Ikeda, and S. Yamaguchi, "Physical model of Nernst element," in Seventeenth International Conference on Thermoelectrics. *Proceedings ICT98 (Cat. No.98TH8365)*, no. 7, pp. 97–100, 1998.

[4.20] H. Nakamura, K. Ikeda, and S. Yamaguchi, "Transport coefficients of InSb in a strong magnetic field," *in XVI ICT "97. Proceedings ICT"97. 16th International Conference on Thermoelectrics (Cat. No.97TH8291)*, pp. 142–146, 1997.

[4.21] S. Yamaguchi, K. Ikeda, H. Nakamura, K. Kuroda, and O. Motojima, "A fusion study of thermoelectric conversion in magnetic fields," *Fusion Eng. Des.*, vol. 41, no. 1–4, pp. 555–559, 1998.

[4.22] S. Yamaguchi, T. Matsumoto, J. Yamazaki, N. Kaiwa, and A. Yamamoto, "Thermoelectric properties and figure of merit of a Te-doped InSb bulk single crystal," *Appl. Phys. Lett.*, vol. 87, no. 20, pp. 1–3, 2005.

[4.23] K. IKEDA, H. NAKAMURA, S. YAMAGUCHI, and K. KURODA, "Measurement of transport properties of thermoelectric materials in the magnetic field.," *Journal of Advanced Science*, vol. 8, no. 3/4. pp. 147–152, 1996.

[4.24] G. N. Kozhemyakin, "Influence of ultrasonic vibrations on the growth of semiconductor single crystals," *Ultrasonics*, vol. 35, no. 8, pp. 599–604, 1998.

[4.25] S. H. Park, T. Y. Song, J. H. Lee, H. S. Kim, J. H. Ha, and Y. K. Kim, "Development of InSb cryogenic detector for ultra high-resolution energy spectroscopy," *in IEEE Nuclear Science Symposium Conference Record*, vol. 2, pp. 1587–1589, 2007.

[4.26] D. B. Gadkari, K. B. Lal, and B. M. Arora, "Growth of undoped and Te doped InSb crystals by vertical directional solidification technique," *Bull. Mater. Sci.*, vol. 21, no. 2, pp. 127–131, Apr. 1998.

[4.27] A. A. Boguslavskii, V. V Sazonov, S. M. Sokolov, V. S. Zemskov, M. R. Raukhman, and V. P. Shalimov, "Influence of Microaccelerations on the Impurity Distribution in the InSb:Te Crystals Grown in Orbital Flights by the Method of Floating Zone Melting," *Cosm. Res.*, vol. 42, no. 2, pp. 148–154, 2004.

[4.28] D. B. Gadkari and B. M. Arora, "Characterization of p and n-type bulk InSb crystals grown by vertical directional solidification technique," *Indian J. Pure Appl. Phys.*, vol. 38, no. 4, pp. 237–242, 2000.

[4.29] M. R. El-Saden and F. W. Thomas, "Nernst effect in indium antimonide," *J. Appl. Phys.*, vol. 36, no. 1, pp. 181–183, 1965.

[4.30] M. A. Kinch, "Fundamental physics of infrared detector materials," *J. Electron. Mater.*, vol. 29, no. 6, pp. 809–817, Jun. 2000.

[4.31] H. Okumura, Y. Hasegawa, H. Nakamura, and S. Yamaguchi, "A computational model of thermoelectric and thermomagnetic semiconductors," *in Eighteenth International Conference on Thermoelectrics. Proceedings, ICT'99 (Cat. No.99TH8407)*, vol. 2, no. 1 999, pp. 209–212, 1999.

[4.32] J. P. Heremans, C. M. Thrush, and D. T. Morelli, "Geometrical magnetothermopower in semiconductors," *Phys. Rev. Lett.*, vol. 86, no. 10, pp. 2098–2101, 2001.

[4.33] E. H. Putley, *The Hall Effect and Related Phenomena Semi-Conductor Monographs*. Butterworth, 1960.

[4.34] K. Ikeda, H. Nakamura, I. Yanenaga, and S. Yamaguchi, "Transport coefficients of Ge in magnetic fields," *Seventeenth Int. Conf. Thermoelectr. Proc. ICT98 (Cat. No.98TH8365)*, no. 1 998, pp. 277–279, 1998.

[4.35] P. Walker and W. H. Tarn, *Handbook of Metal Etching*, Walker, Pe. CRC Press LLC, 1991.

[4.36] K. Terashima, "Low-defect InSb crystal growth by InN doping," *J. Cryst. Growth*, vol. 47, no. 5–6, pp. 746–748, Nov. 1979.

CHAPTER 5

Measuring Systems

5.1: Introduction

A magnetic field has two types: DC magnetic field and AC magnetic field. In this work, the effect of DC magnetic field on undoped and doped polycrystalline InSb was studied. In addition, minimising the Righi-Leduc effect for undoped and doped InSb n-type semiconductors under AC magnetic field was investigated.

This chapter describes the experimental techniques that were employed to investigate the thermomagnetic parameters and resistivity. A measuring setup was designed to be suitable for obtaining the maximum DC magnetic field density at a temperature difference from 0 °C to 80 °C. Some modifications were adopted to adapt the previous design to be suitable for measurements under AC magnetic field. The experimental techniques were developed to be appropriate to examine thermomagnetic parameters, including the Seebeck, Nernst coefficients, Righi-Leduc and hybrid voltages and thermomagnetic power.

5.2: 4-Multifunctional probe

An apparatus for measuring the Seebeck coefficient and electrical resistivity at room temperature is used in this study to determine these two quantities. The apparatus is referred to as the multifunction probe [5.1, 5.2-5.4].

The device was held by four micro-positioners with plastic arms to minimise heat loss. These micro-positioners were set on a metal platform and adjusted to attach the specimen from four different directions. All four micro-positioners have the ability to move the arms in three directions (XYZ axes). This feature enables the device to adapt with different specimen geometries. The specimen holds on a square plastic (specimen holder). The specimen holder was set on a motorised stage to be able to move up and down to fix positions that facilitate the attachment of probes. The movement of the motorised stage was controlled by computer for specimen loading/unloading.

The measurements need appropriate currents (probes and heater) which dependent on the specimen properties. An automatic control was employed for a single DC power source by connection to a computer. A relay module was used for the rapid swapping of the probes that pass current and voltage readings. A Labview 2011 in the computer connected to the device was developed by [5.2] to remotely control all equipment and measurement.

The four multifunctional probes follow the Van der Pauw method to measure resistivity where four probes contact a sample at its edges. The probe is made of copper tube (30 mm length and 1.6 mm diameter) and contains an inner constantan wire. These two conductors (copper tube and constantan wire) are welded at the tip and the junction forms thermocouples and electrical contacts. The junction is electroplated with copper to ensure that the heads of probes are in good electrical contacts with the sample. One of these probes comprises a built-in heater to raise the probe temperature, as shown in Figure 5-1.

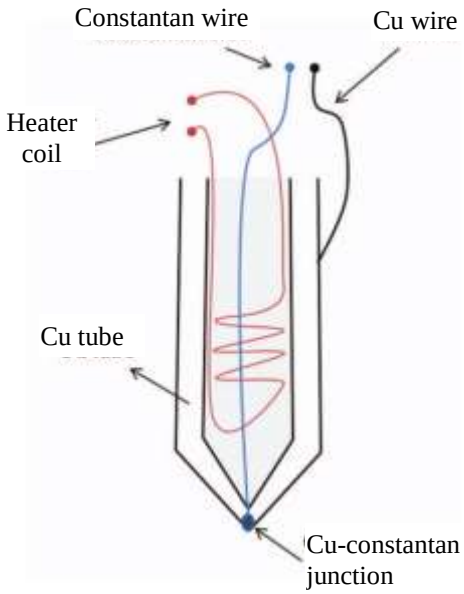

Figure 5- 1: Schematic diagram illustrates the probe with an internal heater coil [5-2].

The Seebeck coefficient can be determined by establishing a temperature difference in the sample. A temperature difference was made by passing a current into the heater coil inserted in the copper tube of one of the four probes (probe A). The temperature difference between the hot probe (probe A) and contrast probe (probe D) is ~3 K.

To measure the electrical resistivity of the sample accurately, the resistance between each probe and the sample was checked to achieve a good contact, by keeping the resistance of the sample to its minimum value. A constant DC current was supplied between two contrast probes and the voltage was measured across the two other probes.

The specimen geometries and contacts did not require a special preparation in this technique. Also, it is appropriate for both bulk and thin film materials, as shown in Figure 5-2. This device can measure within 20 sec both the Seebeck coefficient and electrical resistivity with good accuracy (relative error is less than 5% and 4% respectively).

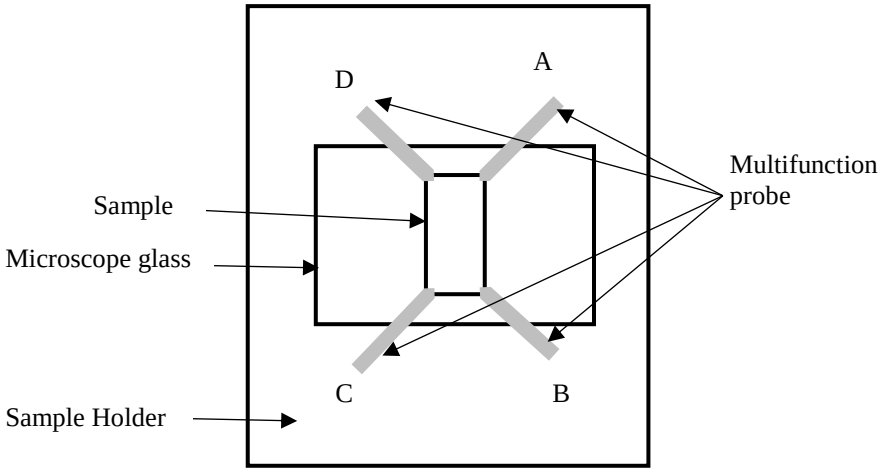

Figure 5- 2: Schematic diagram illustrates the 4-multifunctional probe device.

5.3: Setup under DC magnetic field

The field of thermo-magnetism was first studied in the 1960s [5.1, 5.5]. In those days, induction of a strong magnetic field involved large losses of energy. This is the main reason why the thermo-magnetic effect could not be heavily studied during that time. Nowadays, improvements in superconducting magnets give us higher induction efficiencies for strong magnetic fields. A few years ago, researchers began to work on a measuring system for transport coefficients under a strong magnetic field to estimate the efficiency of thermo-magnetic materials [5.1, 5.5].

When an external magnetic field is applied to a semiconductor sample in addition to temperature gradient, the transport coefficient of TM is more complicated than would otherwise be in the absence of a magnetic field. The transport coefficient changes under a magnetic field due to the thermomagnetic effects.

The thermoelectric properties are enhanced by the application of a magnetic field, due to the increased electrical resistivity and reduced thermal conductivity [5.6].

5.3.1: DC magnetic field

An electromagnet (4-inch diameter pole) was used to produce a magnetic field when a DC current passed through its coils. The material of the magnet core is usually iron. Each pole piece is clamped in place by an Allen screw. When these screws are turned, the pole pieces may easily be moved to give the required gap, which is adjustable from zero to 6.5 cm.

The magnetic flux density produced depends on the spacing between poles and the value of current. The poles are composed of small regions, called magnetic domains, which act like tiny magnets. Before the supply current of the electromagnet is turned on, the magnetic moments in the iron core point in random directions, so their tiny magnetic fields cancel each other, and the iron has no large-scale magnetic field. When a current is passed through the wire wrapped around the iron, its magnetic field penetrates the iron, and causes the moments to be aligned to the magnetic field, so their tiny magnetic fields add to the wire's field, creating a large magnetic field that extends into the space around the magnet. When larger current passes through the wire coil, more moments are in alignment, and the stronger magnetic field is produced. Finally, if all the moments are generally lined up, the further increases in the current causes slight increases in the magnetic field; this phenomenon is called saturation.

An electrical DC power supply was used to apply voltages up to 60 V which passed high electrical current up to 60 A. This power supply was used to induce DC magnetic flux density. The maximum field obtained was less than 1.2 T for 1 Cm gap between poles.

5.3.2: Gaussmeter

A gaussmeter by LakeShore (455DSP) was used to measure the direction and the magnetic flux density of the magnetic field.

The gaussmeter probe must be inserted inside the gap between the poles (vertical to the magnetic field). The direction and magnitude of the magnetic flux density were identified respectively by the sign and reading on the gaussmeter.

5.3.3: Experimental setup

The thermomagnetic phenomena depend on magnetic field. The experimental setup should be designed to accumulate all components on a board with small thicknesses to obtain high magnetic flux density. The experimental setup involves hot and cool sides, heat sink component to make good heat transfer and silver paint to make electrical contact. Then the sample holder fixes the sample between two poles of electromagnetic vertically.

5.3.3.1: Heat sink compound

The surface roughness of any adjacent materials will create an air gap between them. This is true even for small roughness values. A heat sink compound was used to occupy all of these microscopic imperfections on the surface, which could otherwise trap air and reduce the heat transfer performance. The air is a very poor conductor of heat, possessesing a thermal conductivity of 2.624×10^{-2} W/m.K at 300 K. Therefore, heat sink compound is used to fill these air gaps to achieve good heat transfer from the hot side to the sample. It is important to select high performance heat sink compound to ensure that the temperature on the hot side is the same as the temperature on the area of the sample which is attached to the hot side as well as the cool side.

Titan thermal compound (thermal conductivity > 4.5 W/m.K) was used in this study to obtain good thermal contact between the InSb surface and the hot and cool sides.

5.3.3.2: The hot side of the thermoelectric device

The hot side is the side on which the temperature can be raised to produce temperature gradient in the sample. There are two reasons for the thermoelectric module being used as the hot side. These are:

1- Normal heaters contain a wire which carries electric current to heat them up. This process will produce or induce a magnetic field which affects the measurements and causes error.
2- The thickness of the thermoelectric module is small, so that it will enable application of the largest magnetic flux density by making the overall thickness of the printed circuit board (PCB), including all components, less than 1 cm.

A thermoelectric module (Peltier cooler with N=127) with dimensions of $40 \times 40 \times 3.8\ mm^3$ was used.

To measure the temperature of the hot side, a groove is made on the internal surface of the copper plate so that a K-type thermocouple can be installed between the copper plate and the thermoelectric module. The copper plate dimension was $42 \times 42 \times 1\ mm^3$. Heat sink compound is placed as a sink compound inside the groove. Subsequently, a K-type thermocouple was put inside the groove surrounding the heat sink compound to achieve good thermal contact between them. Finally, the copper plate and thermoelectric device are fixed together by four brass bolts close to each corner. The overall thickness of the hot side is approximately 5mm.

5.3.3.3: The cool side of the thermoelectric device

The cool side is the side that absorbs heat from the sample because the temperature of the cool side starts at room temperature and the sample temperature increases gradually.

Two copper plates with larger volumes than the hot side were used as a heat sink; the dimensions of the two plates together were $30 \times 30 \times 5$ mm^3.

To measure the temperature of the cool side, the same procedure was used as mentioned on the hot side but on the internal surface for the upper copper plate.

The overall thickness of the PCB with all components mounted on it is within 0.9-1 mm, so it is possible to fit it in between the electromagnet poles, which will provide the highest magnetic field. Figure 5-3 shows the PCB, including the cool and hot sides and the sample placed over them.

5.3.3.4: Paint conductive adhesive

The electrical contact between the sample surface and the thin copper wires is necessary for measurements of longitudinal and transverse voltages, in order to calculate the thermoelectric and thermomagnetic coefficients.

In this work, a silver paint (electrically conductive) was used to make an electrical contact between the wafer surface and the lead (volume resistivity 0.001 Ω.cm). A small amount of silver paint is dropped on the sample surface and then enameled copper wire (with its insulation stripped from the ends) is attached to the paint. The silver paint is cured by placing the sample inside an oven for 5-10 min at a temperature of 121-148 °C.

Ebnalwaled [5.7] and Senthilkumar et al. [5.8] reported that the use of silver conducting paste was successful as a contact.

The voltage was measured to calculate the transport coefficient as shown in Figure 5-4.

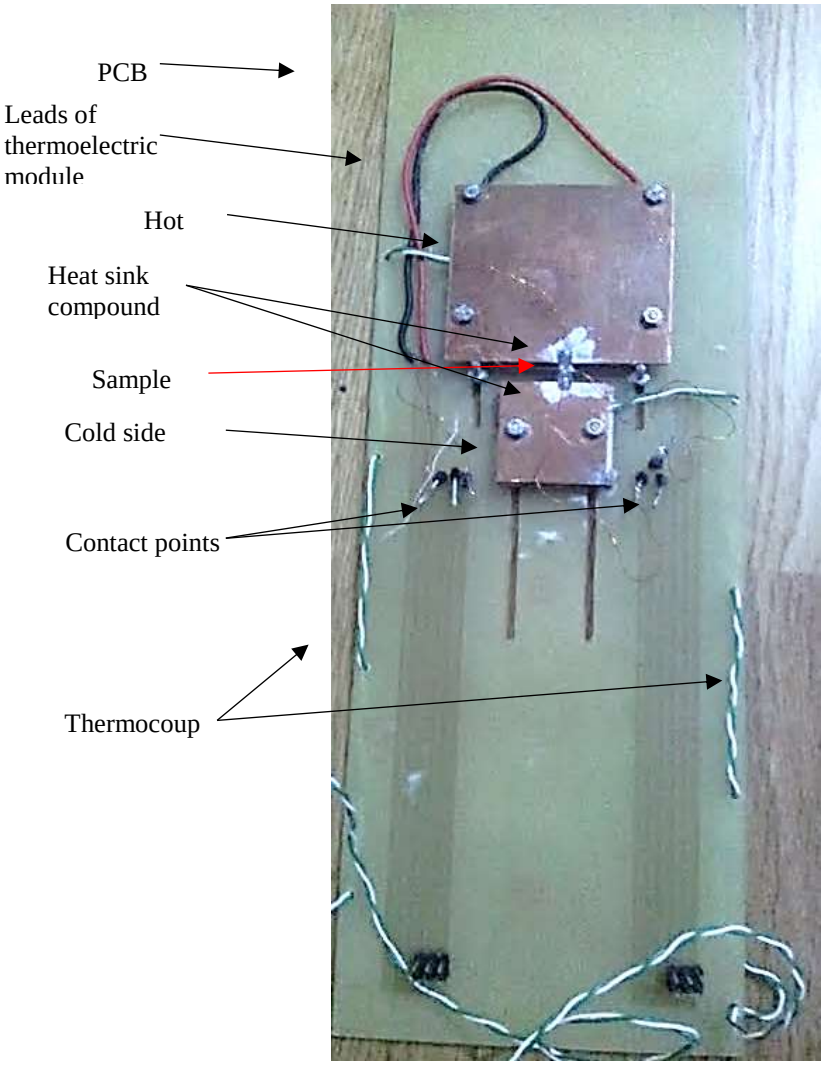

Figure 5- 3: The PCB contains hot, cool sides and the thermocouples that were used to measure the temperature of both sides.

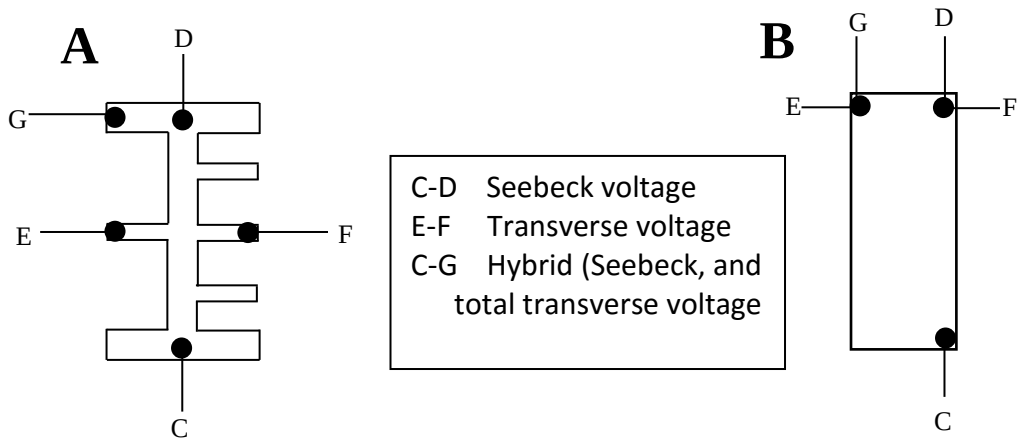

Figure 5- 4: The connection points that were used to calculate the transverse coefficient of InSb samples, a: bridge shape and b: rectangular shape.

5.3.3.5: The sample holder

Two holders, on both sides of the electromagnetic device, were aligned in the middle of the two poles and could balance the PCB in an orientation perpendicular to the magnetic flux density, as shown in Figure 5-5a.

To enable the magnetic field direction to be reversed by changing the polarity of the power supply, a two-way changeover switch was used to reverse the current direction, which in turn reversed the magnetic field direction. Figure 5-5b shows the switch that was used to reverse the magnetic field direction.

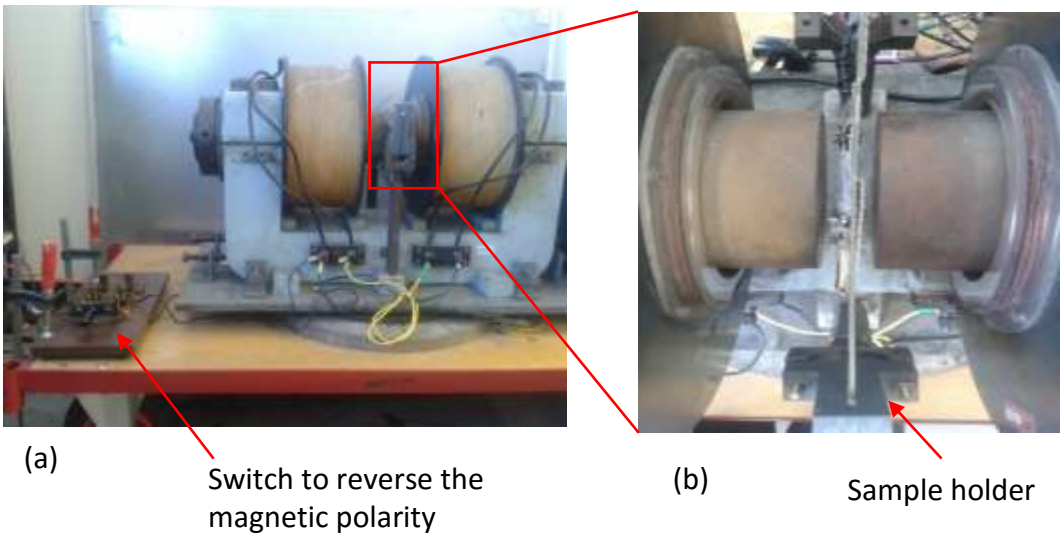

Figure 5- 5: The setup of separating the three components of transverse voltage under the magnetic field, a: the switch was used to reverse the direction of the magnetic field b: the PCB holder in electromagnetic device.

Figure 5-6 shows the magnetic field direction (Forward) on the sample.

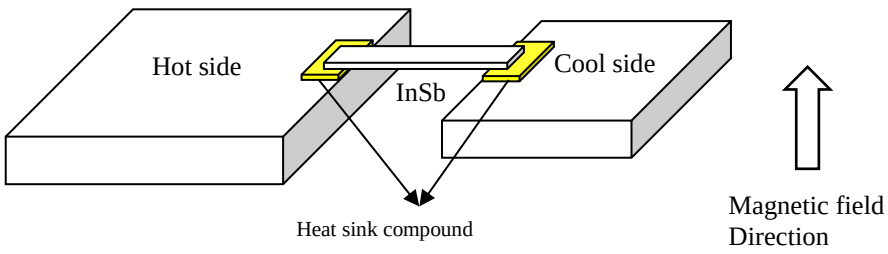

Figure 5- 6: Schematic diagram showing a sample under forward magnetic field and temperature gradient directions.

5.3.4: Measuring resistivity

The resistivity is calculated by measuring the electrical current which passes longitudinally through the sample and the voltage between any two points on the current path [5.9].

Resistivity is generally temperature dependent; hence, it changes at different points in the sample due to the variations in temperature. When a current passes through a sample, some heat is always released into the sample volume due to Joule heating and thermoelectric effects [5.10]. To minimise the effect of Joule heating on the resistivity measurements, the measurements are made at low density and reversed current.

When the electrical current flows through the sample, a temperature gradient is produced due to the thermoelectric effect and a voltage is generated due to this temperature gradient. This generate significant error when measuring the electrical resistivity. In order to minimise the effects of the Seebeck voltage, the resistivity was measured by taking a reading with the current in one direction and then quickly taking a reading with the current reversed [5.4, 5.9]. Thus the voltage that is generated between two points:

$$V_{x1} = V_{IR} + V_s \quad \text{.....(5.1)}$$

$$V_{x2} = V_{IR} + V_s \quad \text{.....(5.2)}$$

where V_{IR} is the voltage due to the resistivity of materials and V_s is the voltage due to the Seebeck voltage.

Subtracting Eq. (5.2) from Eq. (5.1) :

$$V_{IR} = \frac{(V_{x1} - V_{x2})}{2} \quad \text{.....(5.3)}$$

The resistance is calculated using Ohm's law:

$$R = \frac{V}{I} \quad \text{.....(5.4)}$$

where: R is resistance, V is the voltage between (C, D), I is the electrical current, as shown in Figure 5-7.

The resistivity increased with increasing the magnetic field [5.2,5.10-5.15].

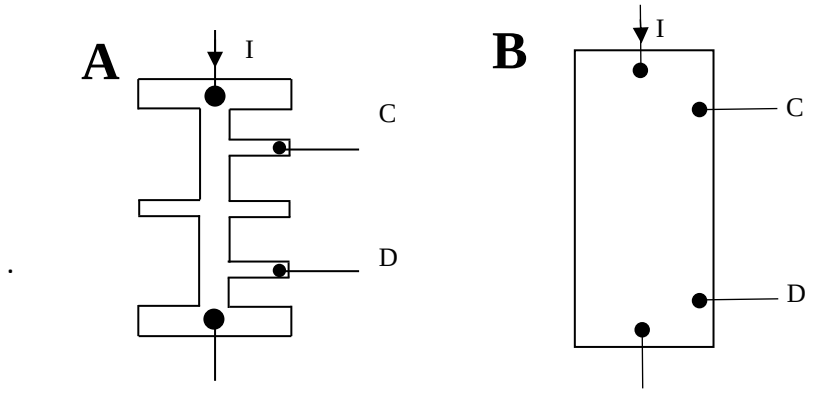

Figure 5- 7: The connected points which were used to calculate the resistance of each InSb sample, a: bridge shape and b: rectangular shape.

A DC power supply from Time Electronics Ltd was used to change the electrical polarity (current direction) by manually operating a switch as quickly as possible. The maximum current it can supply is 99.99 mA at 25 V, as shown in Figure 5-10. Copper wire was used to connect the sample with the circuit.

The resistivity is calculated using the following equation:

$$\rho = R\frac{\mathbb{A}}{L} \quad \text{.....(5.5)}$$

where ρ is the resistivity; $\mathbb{A}$ is the cross-sectional area and L is the length of sample. Figure 5-8 shows the setup to measure the resistivity.

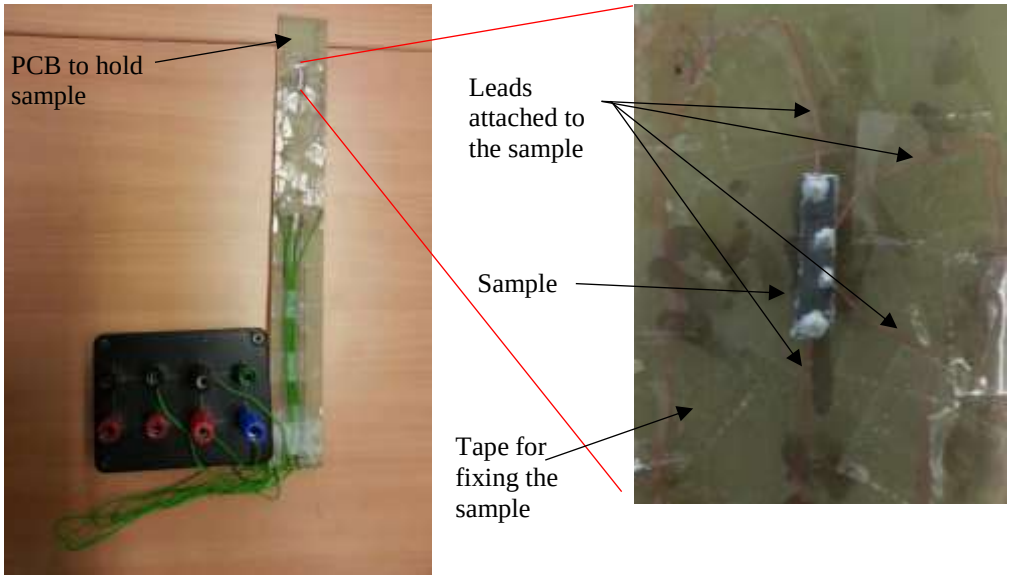

Figure 5-8: The PCB contains samples that were used to measure the resistivity with and in the absence of the magnetic field.

5.4: Setup under AC magnetic field

The setup contains a core that induced magnetic field and some modification on the previous components that accumulated on PCB.

5.4.1: The core under AC magnetic field excitation

A C-shape core was used to induce an AC magnetic field by winding it with copper wire. The core was made using many layers of lamination to reduce eddy currents that can be induced by exposure to the AC magnetic field. The magnetic field strength produced by this core was from 0 T to 0.5 T at 50 Hz frequency. The air gap between two ends of the core was 2.5 – 3 cm, as shown in Figure 5-9.

Figure 5-9: The C-core used to induce the AC magnetic Field between 0-0.5 T.

5.4.2.: Design setup modification

Three modifications were made to improve the accuracy of measuring thermo-magnetic effects.

5.4.2.1: Thermocouple type

The AC and DC magnetic fields can, in principle, affect the thermometer readings. This topic is best described under two headings [5.16]:

(i) Electromagnetic Effect (EM) can change the electromagnetic properties of a thermocouple. The fundamental reason could be the magnetisation of the sensor materials, sensor permeability, Hall effect of the sensor materials or TE (or TM) phenomena (e.g., the Nernst effect due to subjecting the thermocouple to thermal gradient and magnetic fields being perpendicular to each other [5.17]).

(ii) Magnetoresistive effect induces voltage across the wires; the form of the wire twist and the non-perfect electrical contacts are very necessary to consider.

(iii) Induction heating (IH) is where an eddy current is induced due to the changes in magnetic field on conducting materials, causing an increase in the local

temperature of the conductor. Thermocouples could be heated by eddy currents, thus affecting their temperature readings.

A K-type thermocouple (chromel – alumel) was used as it is highly sensitive to temperature difference. In addition, it has a positive sensitivity to magnetic fields (if the magnetic field is perpendicular to the heat flow), which means the output temperature measurement will be more than the real temperature reading. The K-type thermocouple has very small error in temperature readings. This is perhaps due to the very small effect of magnetoresistance and electromagnetic effects under DC magnetic field. This is on account of the way that the thermocouple wires spin. The way wires spin leads to a change in the incidence angle between magnetic field and the electrical charge inside wires. Then they approximately cancel each other. In addition, the eddy current is already not exist under DC magnetic field.

The reported error in temperature readings from K-type thermocouples was below 10 mK under DC magnetic field of 2.7 mT at the nitrogen-boiling point -195.8°C. The error was less than 1 mK under DC magnetic field of 2.5 mT at the Gallium fixed point 29.7646 °C for magnetic fields parallel and perpendicular to the charge carrier motion. It was apparent that the error in the temperature measurement decreased as temperature increased. Also, it increased as magnetic flux density increased. It was less than 15 mK under DC magnetic field of 5.3 mT at the nitrogen-boiling point -195.8 °C [5.16].

In AC magnetic field the eddy current will be induced in the magnetic thermocouple material and this effect cannot be ignored. Thus, it causes an error in the temperature measurement. The reported error in temperature readings from K-type thermocouples deduced that the error under AC magnetic field was higher than that under DC magnetic field [5.16]. The error was 40 mK under AC magnetic field of 15.5 mT at Ice point 0 °C. It was 22 mK under DC magnetic field of 15.5 mT at the Gallium fixed point 29.7646 °C [5.16].

The T-type thermocouple is made from non-effective magnetic material. It is made from copper – constantan. In addition, this type of thermocouple is non-sensitive for a magnetic field. Thus, it is used to minimize both EM, magnetoresistance and IH effects [5.18]. In this work, the T-type thermocouples was exchanged in the setup measurement system under the AC magnetic field to minimise EM, magnetoresistance and IH effects.

The reported error in temperature readings from T-type thermocouples was below 1 mK under DC and AC magnetic fields of various levels and various temperatures [5.16]. Table 5-1 explains the sensitivity of each type of thermocouple to a magnetic field.

Table 5- 1: Thermocouple characteristics table.

ANSI/ ASTM	Symbol Single	Generic Name	Individual Conductor	Magnetic
T	TP TN	Copper Constantan, Nominal Composition: 55%Cu, 45%Ni	Blue Red	No No
J	JP JN	Iron Constantan, Nominal Composition: 55%Cu, 45%Ni	White Red	Yes No
E	P EN	Chromel, Nominal Composition: 90%Ni, 10%Cr Constantan, Nominal Composition: 55%Cu, 45%Ni	Purple Red	No No
K	KP KN	Chromel, Nominal Composition: 90%Ni, 10%Cr Alumel, Nominal Composition: 95%Ni, 2%Mn, 2%Al	Yellow Red	No Slightly
N	NP NN	Nicrosil, Nominal Composition: 84.6%Ni, 14.2%Cr, 1.4%Si Nisil, Nominal Composition: 95.5%Ni, 4.4%Si, 1%Mg	Orange Red	No Slightly
S	SP SN	Platinum 10% Rhenium Pure Platinum	Black Red	No No
R	RP RN	Platinum 13% Rhenium Pure Platinum	Black Red	No No
B	BP BN	Platinum 30% Rhenium Platinum 6% Rhenium	Gray Red	No No
C	P N	Tungsten 5% Rhenium Tungsten 26% Rhenium	Green Red	No No

5.4.2.2: Hot and cool sides

An eddy current is a circular electrical current which induces heat and magnetic fields in the opposite direction to the initial magnetic field. These effects will cause an error in the temperature readings. The copper plates which were put over the hot side and cool side were removed because they induced edge currents under the AC magnetic field. According to the reasons above, the surface of thermoelectric modules were used as the hot and cool sides.

The thermoelectric device (Peltier cooler, N=127, N is the No. of legs inside thermoelectric module) is a good candidate because its surface has good thermal conductivity, and there is no eddy current that will be induced under the AC magnetic field because its surface is an isolating material. The temperature on the surface of thermoelectric devices is checked over whole surface, the difference between the centre and edge is approximately 1 °C. Therefore, the thermoelectric module has good uniform gradient distribution. Thus, it is a good candidate for use as the hot and cool sides. The thermocouples were attached to the surface of thermoelectric devices using copper foil tape with a small amount of heat sink compound to achieve good heat transfer, as shown in Figure 5-10.

Figure 5-10: The new set up after revising the hot and cool sides.

5.4.2.3: The magnetic shielding

A potential difference is induced when a conducting wire is moved through a DC magnetic field, or when an AC magnetic flux cuts through a wire. This potential induces an error in the voltage readings.

The use of magnetic shielding to surround the sample reduces the effect of AC magnetic field on any components connected to the sample. Telshield Company provides a simple, quick and economical ferromagnetic foil that can be used to protect these components from unwanted magnetic interfaces. When the components are encased in a complete enclosure, the ferromagnetic foil carries the stray fields around it as a result of a high conductance to magnetic flux. This is achieved by using shielding material made from alloys which have high permeability and the action is illustrated in Figure 5-11.

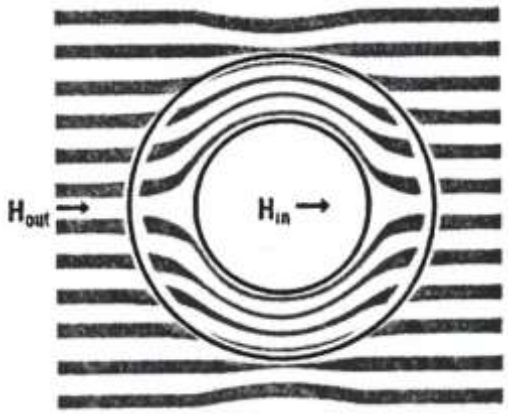

Figure 5-11: The foil behaviour under a magnetic field [5.19].

When the magnetic shielding is placed in a magnetic field, the permeability of this alloy is increased by increasing the magnetic field. It operates at high flux density (reducing the effect of the magnetic field on material shielded by this alloy), as shown in Figure 5-12.

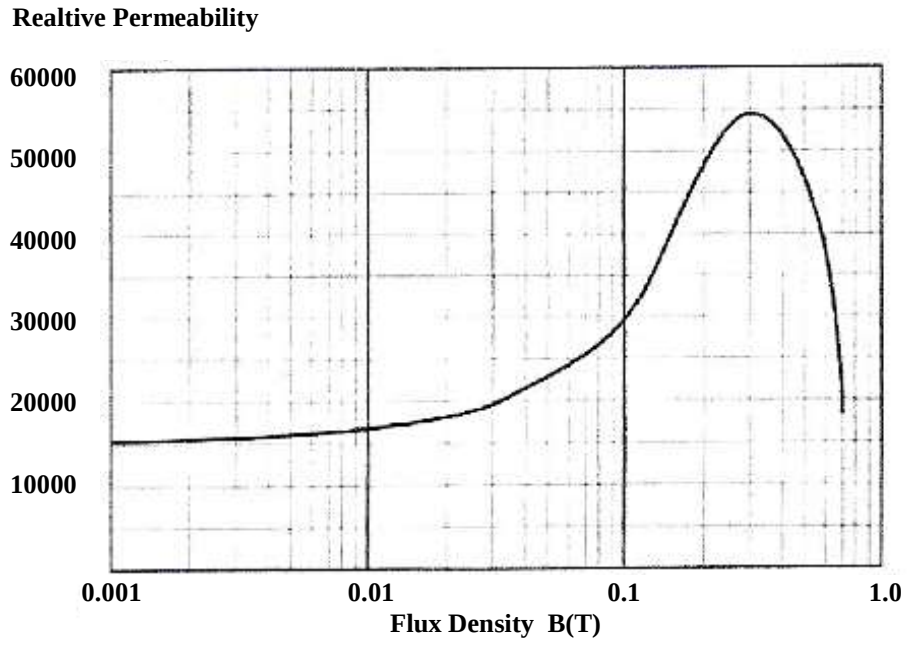

Figure 5-12: The relationship between relative permeability and flux density subjected to the magnetic shield [5.19].

The shield has a peak permeability of 0.3 T. It acts as a good magnetic shield, which minimises the error in measurements.

The ferromagnetic foil is used to shield the wires connected to the multi-meter for measurement of Seebeck and transverse voltages. This ferromagnetic foil minimises any effect of the AC magnetic field induction on these wires and eliminates the possibility of detecting any noise signal from the surroundings. By having this arrangement, the measured voltage represents Seebeck and transverse voltages as accurately as possible. Figure 5-13 shows a photograph of the magnetic shielding around the sample.

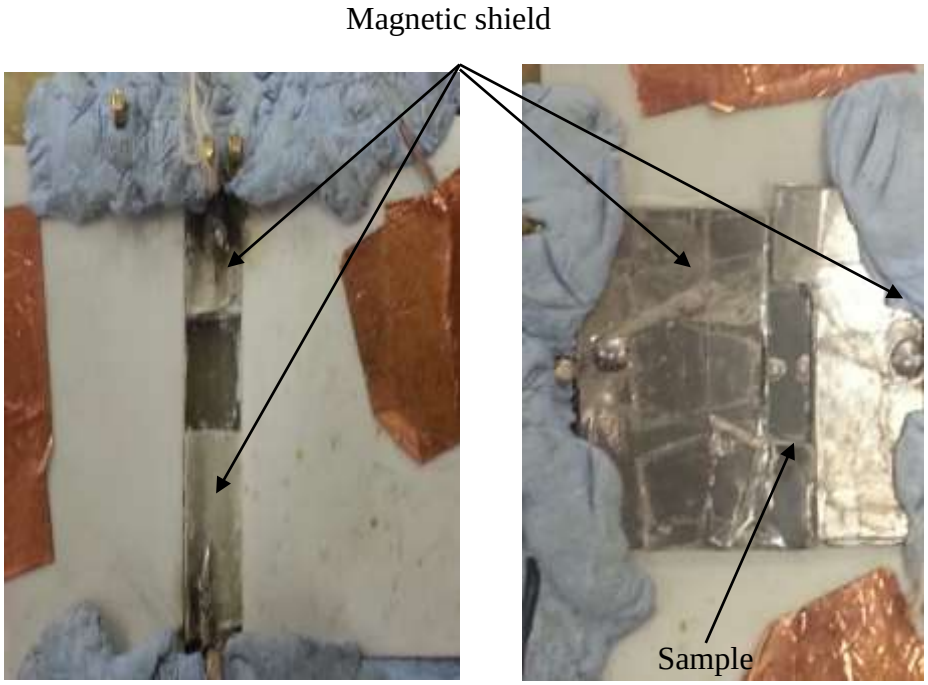

Figure 5-13: The magnetic shielding protecting the wires.

5.4.2.4: Shielded wire

A shielded wire was used instead of the printed circuit board line on PCB to minimise the effect of AC magnetic field (induced voltage) on the measuring results.

5.4.3: Measurement of transverse voltage under AC magnetic field

The transverse voltage induced under the AC magnetic field is a sine wave, as the primary current supplying to the C-core is sinusoidal signal and consequently, the magnetic field produced is also sinusoidal. When the electrons moved from the hot side to the cool side and were exposed to the magnetic field that is perpendicular to the charge carrier's path, they deviated to one side, depending on the magnetic field direction (this is related to the first half period of the sinusoidal magnetic wave signal). On the second half, the magnetic field direction changes to the opposite values and the electrons deviate to the opposite side accordingly. Thus, a sine wave voltage is produced as a transverse voltage.

References

[5.1] H. Nakamura, K. Ikeda, and S. Yamaguchi, "Transport coefficients of InSb in a strong magnetic field," in *XVI ICT "97. Proceedings ICT"97. 16th International Conference on Thermoelectrics (Cat. No.97TH8291)*, pp. 142–146, 1997.

[5.2] J. García-Cañadas and G. Min, "Multifunctional probes for high-throughput measurement of Seebeck coefficient and electrical conductivity at room temperature," *Rev. Sci. Instrum.*, vol. 85, no. 4, p. 043906, 2014.

[5.3] J. Heremans, C. Thrush, and D. Morelli, "Geometrical magnetothermopower in n- and p-type InSb," *Phys. Rev. B*, vol. 65, no. 3, pp. 1–8, 2001.

[5.4] S. Yamaguchi, K. Ikeda, H. Nakamura, K. Kuroda, and O. Motojima, "A fusion study of thermoelectric conversion in magnetic fields," *Fusion Eng. Des.*, vol. 41, no. 1–4, pp. 555–559, 1998.

[5.5] H. Nakamura, K. Ikeda, and S. Yamaguchi, "Physical model of Nernst element," in *Seventeenth International Conference on Thermoelectrics. Proceedings ICT98 (Cat. No.98TH8365)*, no. 7, pp. 97–100, 1998.

[5.6] R. W. Ure, Jr., Theory of Materials for Thermo-electric and Thermo-magnetic Devices, *proceedings of the TEEE*, 51, 699, 1963.

[5.7] A. A. Ebnalwaled, "Evolution of growth and enhancement in power factor of InSb bulk crystal," *J. Cryst. Growth*, vol. 311, no. 19, pp. 4385–4390, 2009.

[5.8] V. Senthilkumar, M. Thamilselvan, K. Premnazeer, S. K. Narayandass, D. Mangalaraj, B. Karunagaran, K. Kim, and J. Yi, "Characterization of p-type In-Sb thin films prepared by vacuum evaporation," *Vacuum*, vol. 79, no. 3–4, pp. 163–170, 2005.

[5.9] R. Bowers, R. W. Ure, J. E. Bauerle, and A. J. Cornish, "InAs and InSb as thermoelectric materials," *J. Appl. Phys.*, vol. 30, no. 6, pp. 930–934, 1959.

[5.10] M. R. El-Saden and F. W. Thomas, "Nernst effect in indium antimonide," *J. Appl. Phys.*, vol. 36, no. 1, pp. 181–183, 1965.

[5.11] H. Okumura, Y. Hasegawa, H. Nakamura, and S. Yamaguchi, "A computational model of thermoelectric and thermomagnetic semiconductors," *in Eighteenth International Conference on Thermoelectrics. Proceedings, ICT'99 (Cat. No.99TH8407)*, vol. 2, no. 1 999, pp. 209–212, 1999.

[5.12] H. Nakamura, K. Ikeda, and S. Yamaguchi, "Transport Coefficients of Indium Antimonide in a Magnetic Field," *Jpn. J. Appl. Phys.*, vol. 38, no. Part 1, No. 10, pp. 5745–5749, 1999.

[5.13] C. Uher and H. J. Goldsmid, "A comparison of thermomagnetic materials for use at room temperature," *J. Phys. D. Appl. Phys.*, vol. 5, no. 8, pp. 1478–1488, 2002.

[5.14] M. Hamabe, S. Yamamoto, S. Yamaguchi, H. Takahashi, H. Okumura, I. Yonenaga, T. Sasaki, and K. Watanabe, "Magnetic field effect for improvement of thermoelectric conversion: A proposal for Nernst-Seebeck element," *Proc. ICT'03. 22nd Int. Conf. Thermoelectr. (IEEE Cat. No.03TH8726)*, pp. 567–570,

2003.

[5.15] W. M. Yim and A. Amith, “Bi-Sb alloys for magneto-thermoelectric and thermomagnetic cooling,” *Solid. State. Electron.*, vol. 15, no. 10, pp. 1141–1165, Oct. 1972.

[5.16] S. Beguš, J. Bojkovski, J. Drnovšek, and G. Geršak, “Magnetic effects on thermocouples,” *Meas. Sci. Technol.*, vol. 25, no. 3, p. 035006, 2014.

[5.17] T. G. Kollie, R. L. Anderson, J. L. Horton, and M. J. Roberts, “Large thermocouple thermometry errors caused by magnetic fields,” *Rev. Sci. Instrum.*, vol. 48, no. 5, p. 501, 1977.

[5.18] http://www.thermo-kinetics.com/thermocouples.

[5.19] Data sheet available on website:

https://www.cartech.com/products.aspx. [access on 1/8/2012]

CHAPTER 6

Results & Discussions

6.1: Introduction

This chapter explores the performance of the different bulk samples (undoped single InSb crystal, undoped and doped polycrystalline InSb), by testing them under both DC and AC magnetic fields and for various temperature gradients. The results were discussed and analysed with regard to the effects of applying various magnetic flux density and temperature differences between the hot and cool sides by using the setup measurement, as described in Chapter Five.

The Nernst effect and Righi-Leduc effect are in the opposite direction which resulted in minimising the total transverse voltage. The AC magnetic field was used to investigate the ability to minimise the Righi-Leduc voltage and then increase the output voltage.

The results were analysed based on the methodology presented in Chapter Five. The values of magnetic flux density were determined using a gaussmeter. The results for changing the DC magnetic field direction and density were investigated to examine the thermomagnetic effects. The resistivity was calculated in all samples. The results for changing the AC magnetic field density were also investigated to examine the thermomagnetic effects.

6.2: Material production

6.2.1: X-ray diffraction

The x-ray powder diffraction analyses for undoped samples are comparable to the x-ray diffraction results obtained by [6.1, 6.2], which are themselves in agreement with JCPDS-ICDD card No. 6-208, as shown in Figure 6-1. They show prominent peaks from (111), (220), (311), (400) and (331), with the highest peak at (220), which is in full agreement with others [6.3,6.4].

XRD analysis of pure InSb (first sample), as shown in Figure 4-14, indicates that there is an imbalance in the amount of indium and antimony, because the antimony boiling point becomes lower under a vacuum [6.5]. However, XRD analysis of pure InSb (third sample) is relatively balanced in the amount of the raw materials after changing the In/Sb ratio.

The XRD spectra for samples produced by this method (growth from melt) are comparable to the samples that were prepared by vertical Bridgman method. The samples produced in this work are polycrystalline.

The difference is that the samples obtained by the growth from melt method were n-type, while samples obtained by the vertical Bridgman were p-type [6.1, 6.6]. The n-type behavior of InSb made in this study was caused by crystal defect and oxygen contaminant; the latter existed in the argon environment inside the Niobium container even though it was under vacuum conditions. The argon gas contains O_2 2% and CO_2 20% inside the argon cylinder [6.7]; the oxygen reacts with In atoms to produce In_2O_3 [6.8]. Cation vacancies are thereby produced due to the reduction of indium atoms owing to reaction with oxygen molecular. The samples were produced with two types of charge carriers: electrons and holes.

The XRD spectra for doped samples with Te at doping levels of 0.1% and 0.25%, respectively is in good agreement with [6.2,6.3] regarding the maximum peak and its orientation.

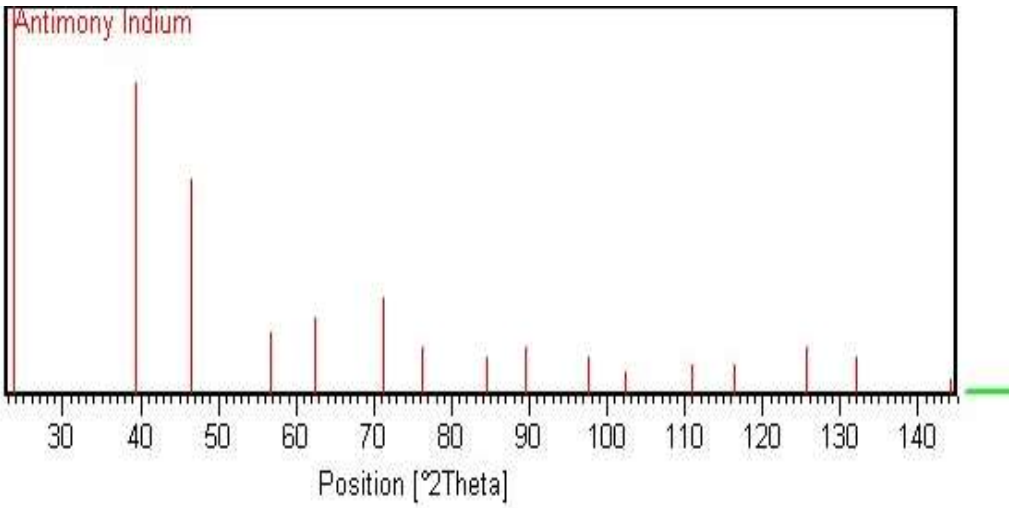

Wave length (Å) : 1.54860							
	d-Value (Å)	Relative Intensity (%)	Angle (2θ		d-Value (Å)	Relative Intensity (%)	Angle (2θ
1-	3.7400	100	23.772	9-	1.0950	12	89.412
2-	2.2900	80	39.312	10-	1.0243	10	97.532
3-	1.9530	55	46.459	11-	0.9880	6	102.458
4-	1.6200	16	56.783	12-	0.9349	8	110.962
5-	1.4860	20	62.446	13-	0.9071	8	116.247
6-	1.3230	25	71.216	14-	0.8657	12	125.696
7-	1.2470	12	76.300	15-	0.8434	10	131.938
8-	1.1453	10	84.532	16-	0.8098	4	144.062

Figure 6- 1: The standard pattern x-ray diffraction analyses for InSb.

In addition, the inter-planar spacing d_{hkl} was calculated for pure InSb samples using Bragg's equation.

$$d_{hkl} = \frac{N\lambda}{2sin\theta} \quad \text{.....(6.1)}$$

Table 6-1 explains a comparison between the d factors, which are calculated from measurements taken of pure InSb and for the standard cubic InSb crystals. It shows a good agreement with the standard crystals values and with results obtained by [6.1].

Table 6- 1: The comparison between standard d values and the calculated values for the obtained samples.

(hkl) plane corresponding to InSb	d_{hkl} for standard cubic InSb Crystals (A°)	d_{hkl} for obtained InSb Polycrystalline (A°)
(111)	3.74	3.725
(220)	2.29	2.280
(311)	1.953	1.946
(400)	1.62	1.615
(331)	1.486	1.482

6.2.2: EDX analysis

The EDX analysis has been performed for undoped polycrystalline InSb sample, the results confirm that the raw materials were off-stoichiometric composition, as explained in Table 6-2:

Table 6- 2: The weight and No. of atoms% of raw materials in undoped polycrystalline sample.

Undoped InSb sample	Raw materials	
	"In"	"Sb"
Weight %	49.85	50.15
No. of atoms %	51.31	48.69

The table above illustrates that the number of In atoms in the produced sample was lower than those for Sb atoms. The difference between the numbers of In and Sb atoms was 2.62%.

6.2.3: Samples crystal structure

The crystal structure of undoped samples was investigated. Optical microscopic photos were taken of the samples before and after reducing cooling rate. Figure 6-2 shows the crystal boundaries under optical microscope.

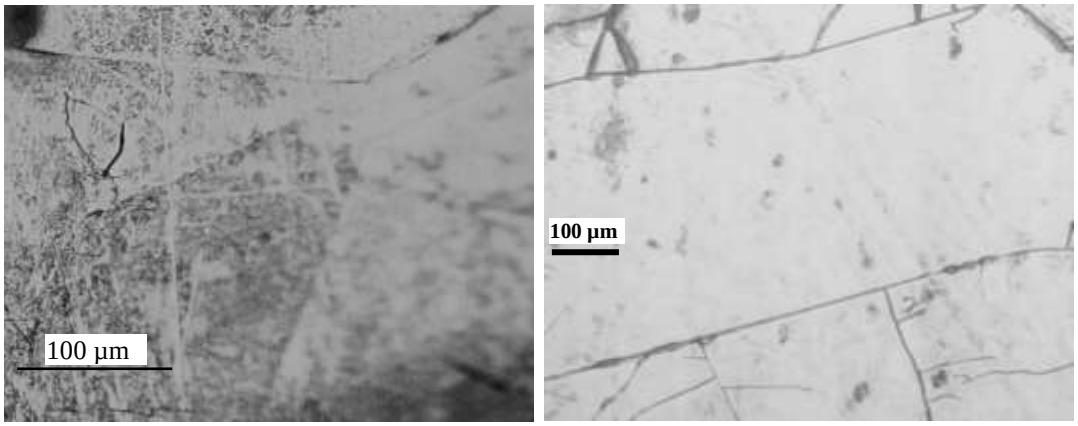

(a) (b)

Figure 6- 2: Optical microscope photos show the crystal boundaries for undoped polycrystalline InSb, (a) before and (b) after reducing cooling rate.

According to the optical microscope photos above, the samples are polycrystalline. The grain size range for the sample before reducing cooling rate is from 120 µm to 160 µm and for after reducing cooling rate is from 260 µm to 330 µm .

6.3: Results under the DC magnetic field

In the figures showing data presented in this chapter, lines between points are joint according to scatter with smooth lines, apart from figures showing the Variation of the Seebeck voltage, Seebeck coefficient and hybrid transverse voltage with temperature difference.

6.3.1: Measurement of the magnetic flux density

The two windings of the electromagnetic device were connected in series. This could achieve a maximum magnetic flux density of 1 T for a 1 cm gap between the two poles. In this work, the magnetic flux density between 0 to 1.0 T was used to investigate the magneto-thermoelectric and thermomagnetic properties of InSb. In addition, the thermoelectric properties of InSb were measured in the absence of the magnetic field.

The magnetic flux density is measured by using a Gaussmeter. Figure 6-3 below shows the relationship between the magnetic flux density and the DC current at different gaps between the two poles.

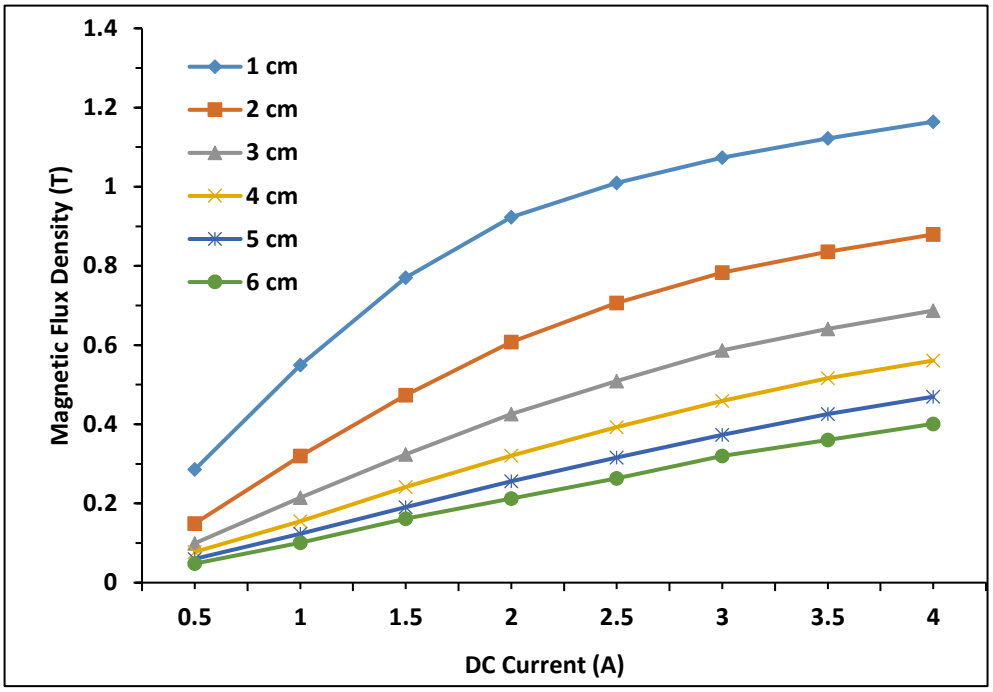

Figure 6- 3: Variation of the magnetic flux density with DC electrical current for various gaps between poles.

6.3.2: Transport coefficients

All samples that have been measured in this section were examined under the DC magnetic field and are listed in Table 6-3.

Table 6- 3: The samples were examined in this study.

	Abbreviation	Sample's full name
1.	USB	Undoped single crystal InSb for Bridge shape.
2.	USR	Undoped single crystal InSb for rectangular shape.
3.	UPB	Undoped polycrystalline InSb before reducing cooling rate for rectangular shape.
4.	UPA	Undoped polycrystalline InSb after reducing cooling rate for rectangular shape.
5.	DP0.1%	Doping polycrystalline InSb with 0.1% doping at a rate 0.1% for the rectangular shape.
6.	DP0.25%	Doped polycrystalline InSb with "Te" doping at a rate 0.25% for the rectangular shape.

6.3.2.1: Seebeck coefficient in the absence of the magnetic field

The Seebeck voltage is measured between the hot and cool sides of all samples, as was illustrated in Chapter Five. For further information about the samples, see Appendix 1. Figure 6-4 shows the relationship between the Seebeck voltage and the temperature difference for USB sample. The Seebeck coefficient for mean temperature difference is obtained by calculating the slope of the line ($\delta = \Delta V_\delta / \Delta T$).

The Seebeck voltage in Figure 6-4 is increased significantly (in the negative direction) with increased temperature difference, due to the fact that semiconductor single crystal InSb is operated in the intrinsic region at room temperature. In this regime both carriers' concentration is increased with increasing temperature. This effect is called (ampibolar effect), the numbers of both holes and electrons increase until close to the other. Both charge carriers move from hot side to cool side, which in turn creates two opposite electrical fields. For more information see section 2.7. The Seebeck voltage increases due to the summation of the opposite electrical fields. The Seebeck coefficient for USB sample is 257.6 µV/°C comparable with other publications which utilized InSb doped with Te that range between -270 µV/K and -290 µV/K [6.9-6.12].

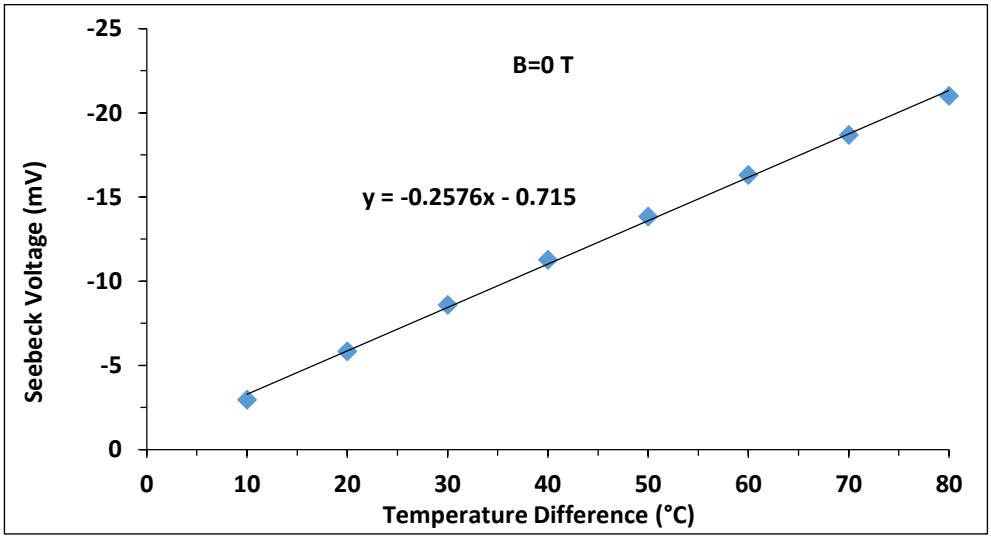

Figure 6- 4: Variation of the Seebeck voltage with temperature difference for USB sample.

The Seebeck voltage of all other samples has the same behavior as that for UBS sample. For further information about the samples, see Appendix 2.

To investigate the repeatability of the Seebeck coefficient in the absence of the magnetic field, undoped single crystal InSb in the bridge shape was used. The calculation was repeated four times. Figure 6-5 shows the standard deviation of the Seebeck coefficient for different temperature differences for USB sample. For further information about the samples, see Appendix 3.

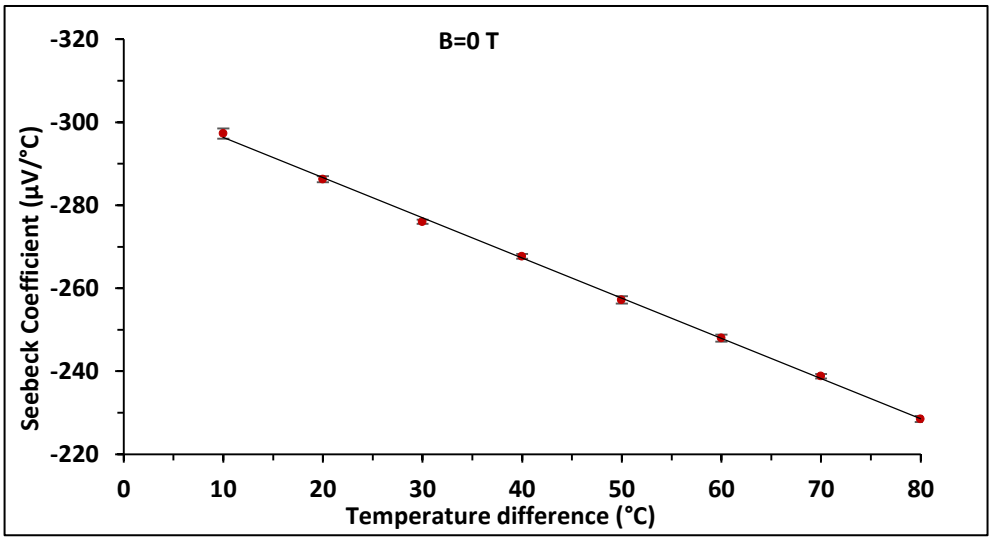

Figure 6- 5: The repeatability of the Seebeck coefficient in the absence of the magnetic field for USB sample.

Table 6-4 gives the maximum and minimum estimated values for Seebeck coefficient according to standard deviation in the absence of the magnetic field for USB sample.

Table 6- 4: The values of Seebeck coefficient under standard deviation for USB sample in the absence of the magnetic field.

ΔT °C	$\hat{\delta}$ µV/°C	$\check{\delta}$ µV/°C	Standard deviation	Percentage
10	-298.545	-296.055	1.244655	0.8%
20	-287.033	-285.567	0.732575	0.5%
30	-276.519	-275.481	0.518813	0.3%
40	-268.292	-267.108	0.591608	0.4%
50	-258.1	-256.3	0.899537	0.7%
60	-248.852	-247.148	0.852447	0.6%
70	-239.332	-238.268	0.531507	0.4%
80	-229.232	-227.768	0.732006	0.6%

The Figure 6.5 and Table 6-4 show that all standard deviations of all temperatures are from 0.51 to 1.24 depending on temperature difference. These results indicate that the experiments have good repeatability.

The Seebeck coefficient for USB sample was calculated by dividing potential difference over temperature difference for each point. Figure 6-6 shows the relationship between the Seebeck coefficient and the temperature difference.

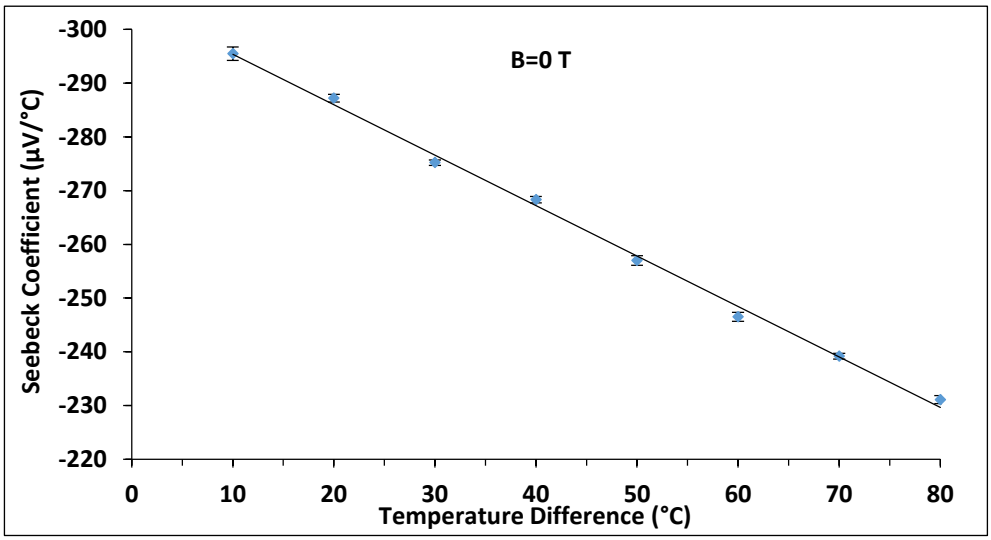

Figure 6- 6: Variation of the Seebeck coefficient with temperature difference for USB sample.

The Seebeck coefficient is decreased considerably (in the negative direction) with increased temperature difference, due to increasing both charge carrier types (electrons and holes), as mentioned above. The thermal conductivity is increased by adding an ambipolar thermal conductivity term. In addition, the recombination of each charge with its opposite charge could lead to an increase in the temperature of the sample. The increase in thermal conductivity and temperature of the sample leads to a decrease in the temperature difference between the two ends (hot and cool sides). This process leads to a decrease in the Seebeck coefficient. This behavior is in full agreement with what other authors have found [6.9, 6.13-6.18].

The Seebeck coefficient for bridge shapes is higher than that for rectangular shapes, because the area attached to the hot side is larger for the former than for the latter, as shown in Figure 6-7. This means it is larger, according to Fourier Law:

$$Q = \kappa A \frac{dT}{dx} \quad \text{.....(6.2)}$$

From eq. (6.2) the large area resulted in high heat which in turn raised the temperature of the hot side and lowered the temperature of the cool side. This process leads to an increase in the Seebeck coefficient.

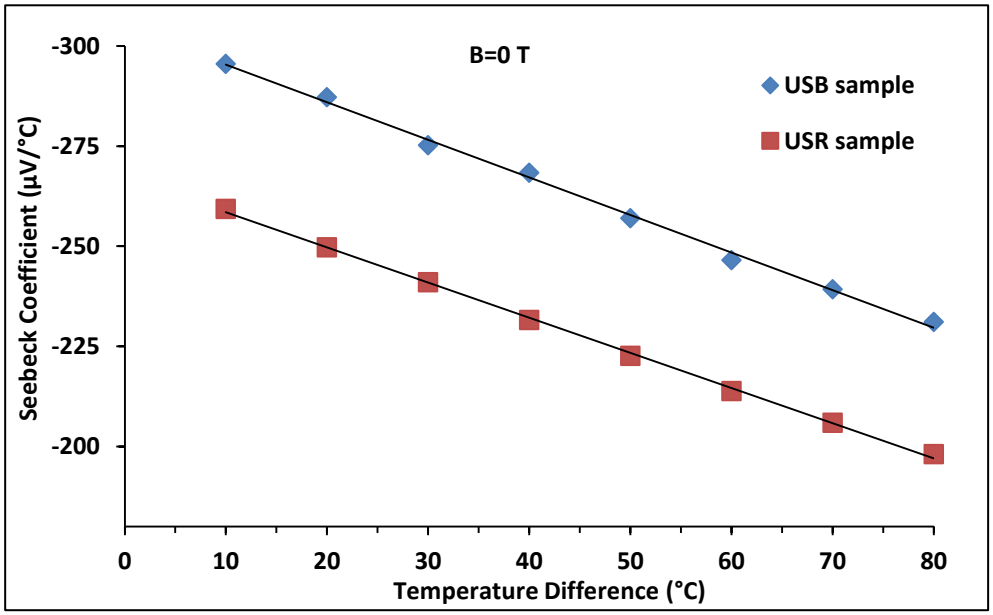

Figure 6- 7: Variation of the Seebeck coefficient with temperature difference for USB, USR samples.

Figure 6-8 shows the relationship between the Seebeck coefficient and the temperature difference for UPB sample.

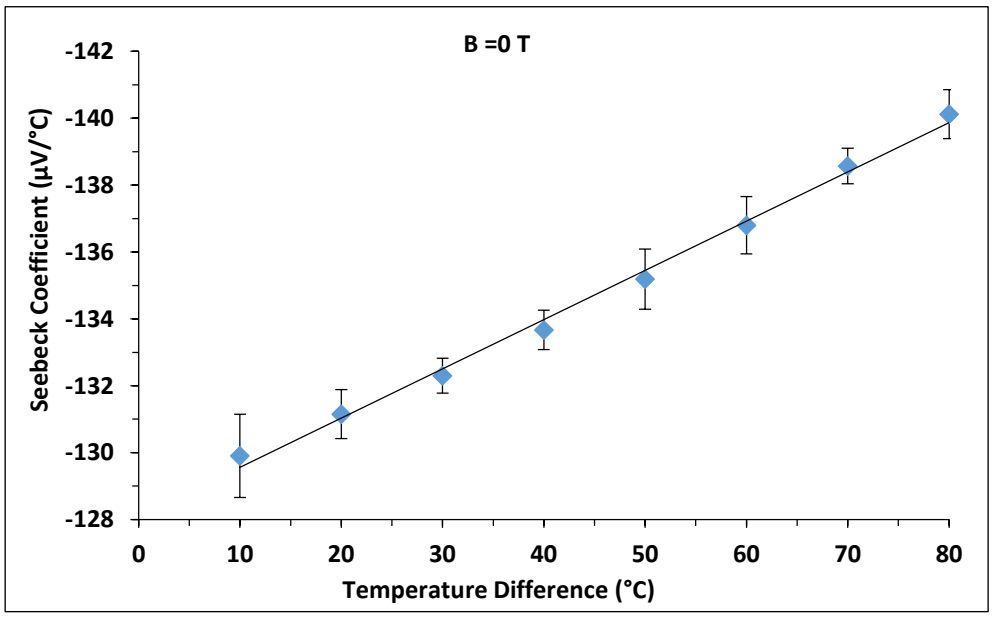

Figure 6- 8: Variation of the Seebeck coefficient with temperature difference for UPB sample.

The Seebeck coefficient is increased slightly (in the negative direction) with increased temperature difference. It is lower than and has opposite behavior to USR sample. The UPB behavior is due to the existence of both charge carriers (electrons and holes) inside the sample. Both electrons and holes are created due to the crystal point defects. In addition, the reaction between oxygen atoms and In melt produce In_2O_3, which led to enrichment of Sb and then created cation vacancies. These charge carriers make the Seebeck coefficient lower than that of the sample with just one type of carrier or fewer carrier numbers [6.19-6.21]. The UPA behavior is due to the number of charge carriers that are excited being lower than those for the same temperature of the hot side, which means the sample is operated in the extrinsic region near room temperature.

Figure 6-2 shows the difference between the crystal boundaries size before and after reducing cooling rate under optical microscope. The annealing process changes the physical properties of a material. These changes consist of grain size refinement, improved machinability and cold formability, minimized or eliminated structural non-homogeneity, restored ductility and relieved internal stresses [6.22,6.23].

The Seebeck coefficient for UPA sample is lower than that for UPB sample. This is due to the improved arrangement of the atoms in sites that could lead to increased electrical and thermal conductivity. Hence, the scattering of charge carriers with other charge carriers, as well as ionized impurity and with crystal boundaries, has been reduced. This in turn leads to the reduction in the Seebeck coefficient [6.24].

The Seebeck coefficient for DP0.1% sample is lower than that for UPA sample. This is due to an increase in the number of charge carriers (both electrons and holes) as a result of the doping. The added Te atoms occupy the position of Sb atoms in the lattice site mutually, which releases one extra free electron from each Te atom. In other words, the Sb atoms, which leave the lattice site, accumulate and lead to the appearance of cation vacancies (positive charge carrier) [6.9, 6.23]. The Seebeck coefficient for DP0.25% sample is higher than that for DP0.1% sample in spite of the

increase in charge carriers (electrons and holes). This might be due to the increased number of the collisions between charge carriers, crystal boundaries and with Te atoms that take the site position of Sb atoms.

The Seebeck coefficient for UPA, DP0.1% and DP0.25% samples has the same behavior as that for UPB sample in the absence of the magnetic field. However, each sample has a lower value than the previous sample, apart from the DP0.25%, which has a higher value than that for DP0.1%. The slope of the line in the graphs reduces from 0.9383, to 0.8786, 0.1472, 0.2237 and 0.0858 before increasing to 0.0545 for USB, USR, UPB, UPA, DP0.1% and DP0.25% samples respectively. This is due to the same reasons mentioned above. For further information about the samples, see Appendix 4.

The relationship between the Seebeck coefficients of all samples with different temperature difference is shown in figure 6-9.

To check the accuracy and reliability of the Seebeck coefficient values calculated by measuring the voltages from the setup as described in Chapter Five, the 4-multifunction probes have been used to check the Seebeck coefficient values of all samples under the investigation. Table 6-5 explains a comparison between the Seebeck coefficient values by using two different techniques.

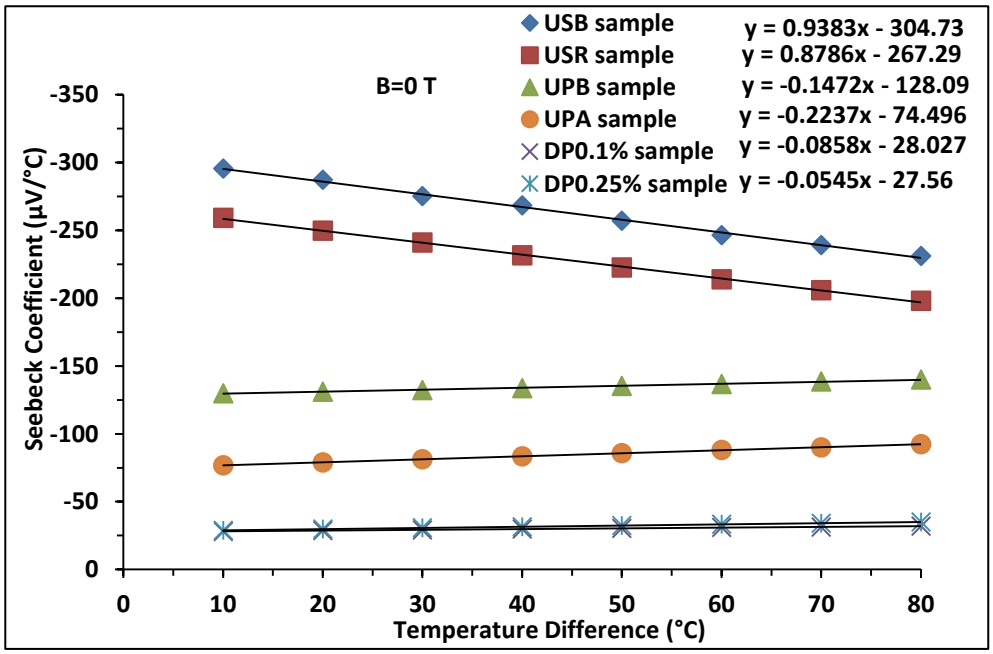

Figure 6- 9: Variation of the Seebeck coefficient with temperature difference of all samples.

Table 6- 5: The comparison of Seebeck coefficient values µV/°C between two different techniques.

Sample details / Method of measurement	Undoped InSb			Doped InSb with "Te"	
	Single crystal	Polycrystalline			
		Before	After	0.1%	0.25%
4-probe	-230	-139.5	-92.6	-30.9	-32.7
Set up described in thesis	-223.1	-135.3	-85.7	-30.3	-32.3

The measurements have confirmed that all samples were n-type, due to the negative value of the Seebeck coefficient. This result is in full agreement with the data sheet from the supplier for USB and USR samples. It is also in general agreement with other researchers [6.24]. In addition, InSb doped with Te [6.5, 6.9-6.12, 6.18, 6.25, 6.26]. For the samples made in this work, the type of the sample is determined by the summation of electron and hole charge carrier numbers. This result corresponds with other researchers [6.9].

6.3.2.2: Resistivity

The resistance for USB sample was calculated by using Eq. (5.4) as was illustrated in Chapter Five. Figure 6-10 shows the relationship between the resistance and the magnetic flux density.

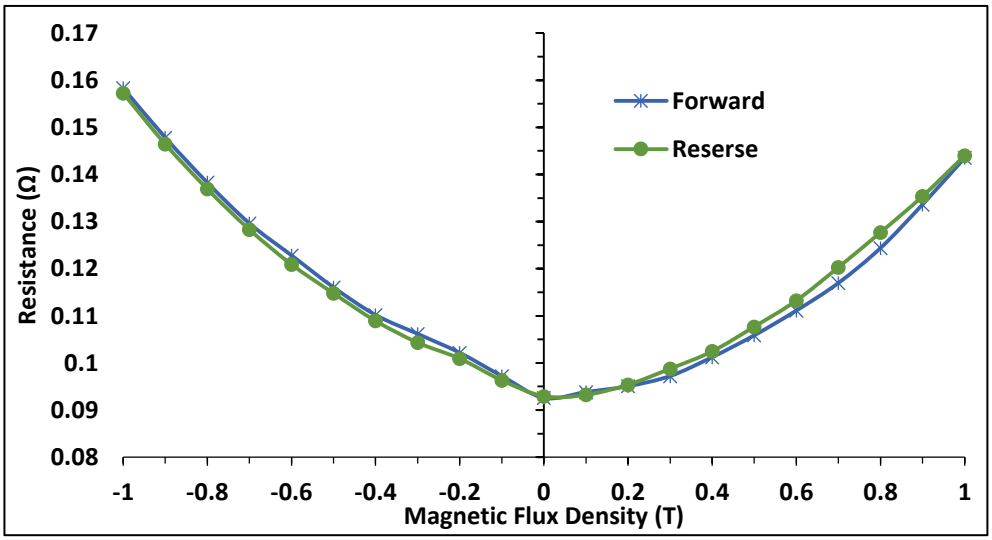

Figure 6- 10: Variation of the resistance with the DC magnetic flux density for USB sample.

The resistance increases with increasing the magnetic flux density in both directions. In addition, the resistance values calculated using the forward and reverse currents are asymmetrical with the direction of the magnetic flux density.

The resistivity for USB sample was calculated by using Eq. (5.5). Figure 6-11 shows the relationship between the resistivity and the magnetic flux density.

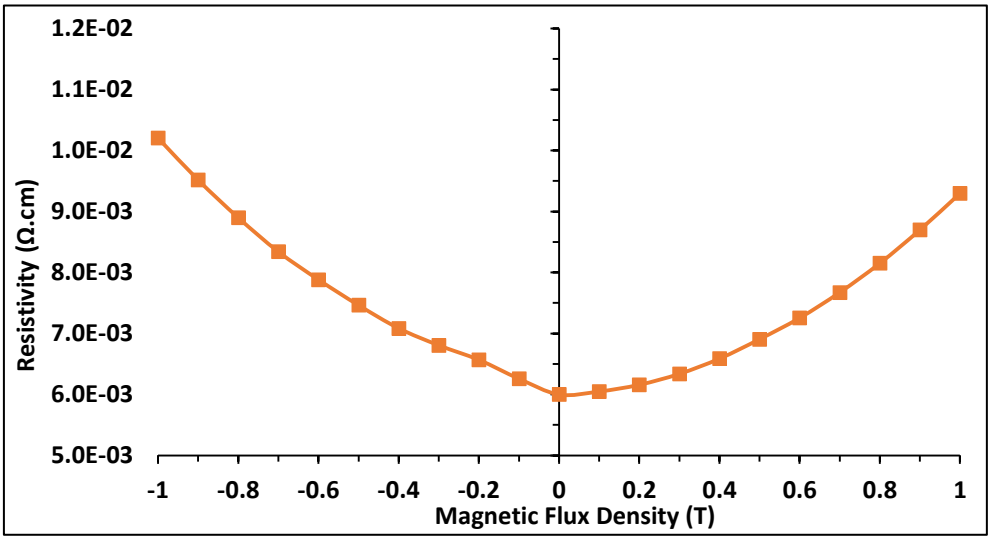

Figure 6- 11: Variation of the resistivity with the DC magnetic flux density for USB sample.

The value of the resistivity for undoped single crystal InSb 5.137E-03 Ω.cm can be compared with [6.13] in which they utilized doped single crystal InSb with Te and obtained a resistivity of 3.0E-03 Ω.cm. In addition, the behavior of the resistivity as asymmetric with the magnetic field directions is not in full agreement.

The resistivity increased with increasing the magnetic flux density as the effect of Lorentz force on the electrical charges increased:

$$F = q\vartheta B \quad \text{.....(6.3)}$$

where: q is the electrical charge and ϑ is the charge carrier velocity.

The two graphs above show that the resistance and resistivity are asymmetric with the magnetic field directions. This is due to the fact that the electrical current that passes through the sample produces the Ettinshausen effect (transverse

temperature difference). The Ettingshausen effect in turn produces the Nernst and Righi-Leduc effects (longitudinal electrical field and temperature difference respectively). The latter produces the Nernst and Righi-Leduc effects (transverse electrical field and temperature difference respectively). These voltages are continuously produced. These effects will produce sequential longitudinal voltages (the Nernst voltage + Seebeck voltage from the temperature difference), which act in the opposite direction. The total longitudinal voltage is equal to the initial longitudinal voltages (power supply) plus the sequential voltages. In other words, it increases or decreases the total electrical field supplied to the two ends of the sample. The total longitudinal voltage is dependent on the value of sequential voltages, which depends on the magnetic field direction. As a result, the total electrical field increases or decreases the current pass through the material. It increases in forward magnetic field direction and reduces in reverse magnetic field direction. Thus, this process has an effect on the calculated value of the resistance as it was increased in reverse magnetic field case and reduced in forward magnetic field case.

To confirm this, the resistance and resistivity were calculated for two connected points in the middle of the sample. Figure 6-12 shows the relationship between the resistivity and magnetic flux density for USR sample.

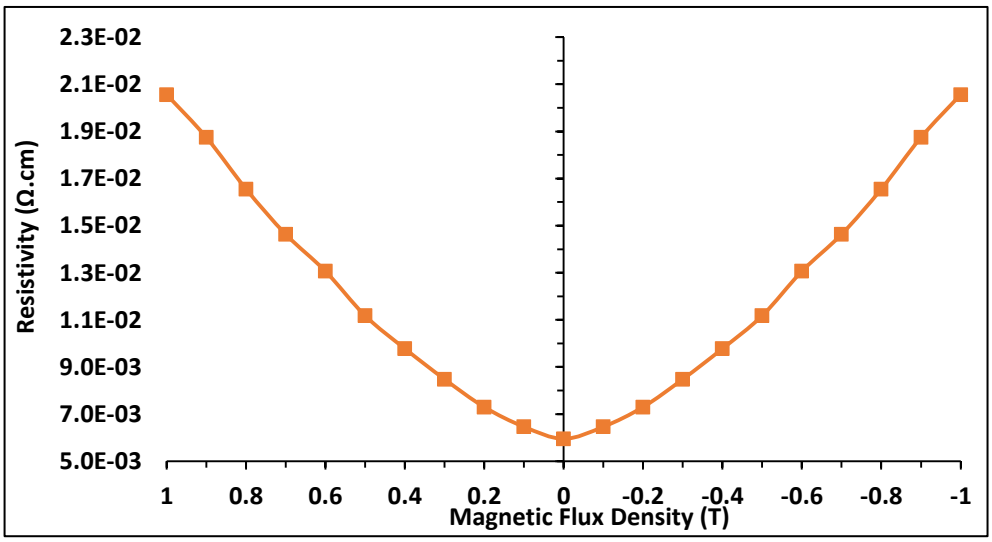

Figure 6- 12: Variation of the resistance with the DC magnetic flux density for USR sample (middle connection).

It is apparent that the resistivity is symmetrical with respect to the magnetic field directions. In addition, the resistance increases with an increase in the magnetic flux density in both directions. Figure 6-13 shows the relationship between the resistivity and magnetic flux density for USR sample (side connection).

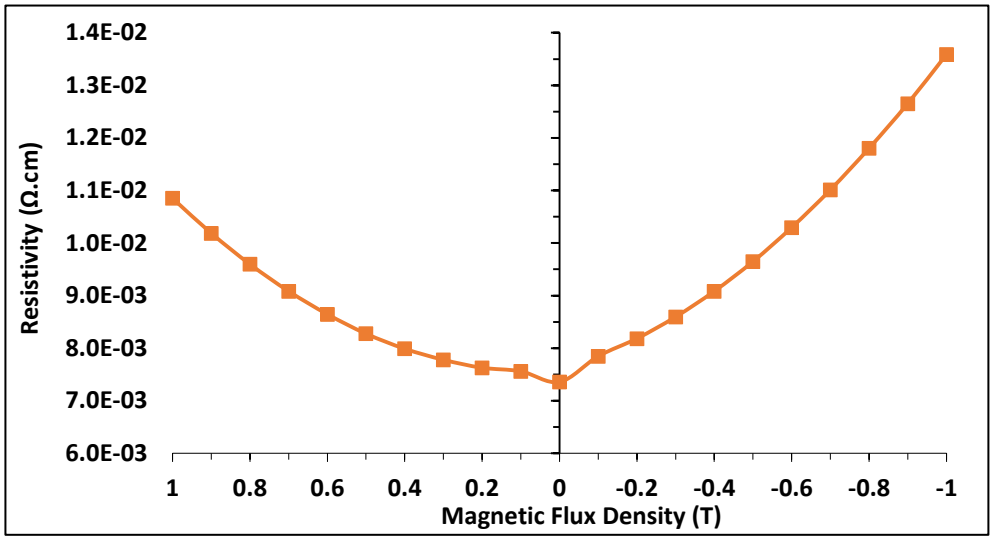

Figure 6- 13: Variation of the resistivity with the DC magnetic flux density for USR sample (side connection).

The relationship between the resistivity of all rectangular shaped samples with the magnetic flux density is shown in Figure 6-14.

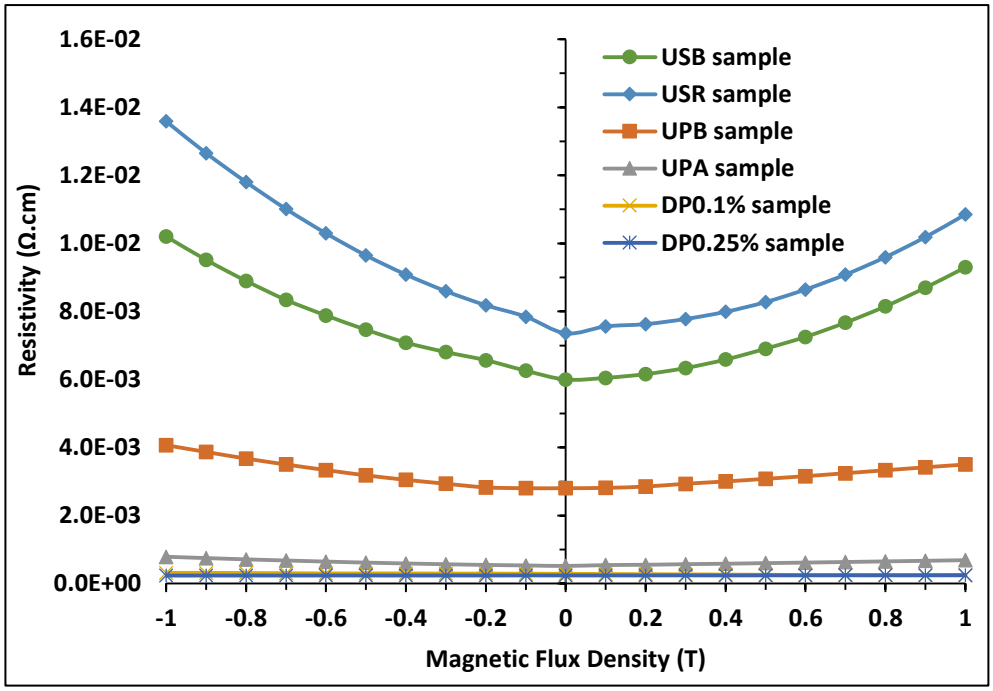

Figure 6- 14: Variation of the resistivity with the DC magnetic flux density of all samples of rectangular shape.

The resistivity of USR sample shows a similar behavior to that for USB sample under the magnetic field (at all magnetic flux densities and same connection method). The values are higher than those for USB sample with and without applying the magnetic field (at all magnetic flux densities). This is due to the increased distortion of the current flux lines. These connected points add value to the resistance and thus increase the resistivity.

Figure 6-14 shows that the increase in the resistivity for polycrystalline materials is less than that for single crystal due to increasing the collision between charge carriers with other charge carriers, as well as ionized impurity and with crystal boundaries [6.24]. It can also be seen that the difference between the resistivity values in the opposite magnetic field direction for USR, UPB, UPA, DP0.1% and DP0.25% samples reduces gradually. The values are 0.00273, 0.00056, 0.0001, 0.000072 and 0.000011 Ω.cm respectively. This is due to the increase in the thermal conductivity of the sample, which leads to reducing the sequential longitudinal voltages (as was mentioned above), then reducing the difference between the resistivity at different magnetic field directions. For further information about the samples, see Appendix 5.

The resistivity for UPB, UPA, DP0.1% and DP0.25% samples has similar behavior to that for USR sample with and without applying the magnetic field (at all magnetic flux densities). Each sample has a lower value than the previous sample, except for DP0.25% sample, which has a higher value than DP0.1% sample. This is due to the same reasons that were mentioned regarding the Seebeck coefficient of these samples in the absence of the magnetic field. For further information about the samples, see Appendix 5.

To check the accuracy and reliability of the resistivity values, calculated by measuring the voltages and currents from setup measurement as described in Chapter Five, the 4-multifunction probes were used to measure the resistivity values of all samples. Table 6-6 explains a comparison of the resistivity values measured using two different techniques.

Table 6- 6: Comparison of the resistivity values Ω.cm between two different techniques.

Sample details / Method of measurement	Undoped InSb			Doped InSb with "Te"	
	Single crystal	Polycrystalline		0.1%	0.25%
		Before	After		
4-probe	5.1297E-03	7.01E-04	3.91E-04	2.3181E-04	1.7018E-04
Set up described in thesis	7.358E-03	2.80E-03	5.18E-04	2.870E-04	2.390E-04

6.3.2.3: Seebeck coefficient under the magnetic field

To investigate the repeatability of the Seebeck coefficient under the DC magnetic field, undoped single crystal InSb with the rectangular shape was used because USB sample was broken. Figure 6-15 shows the standard deviation of the Seebeck coefficient and different temperature differences under the magnetic flux density of 0.1 and 1 T for USR sample. The calculation was repeated four times.

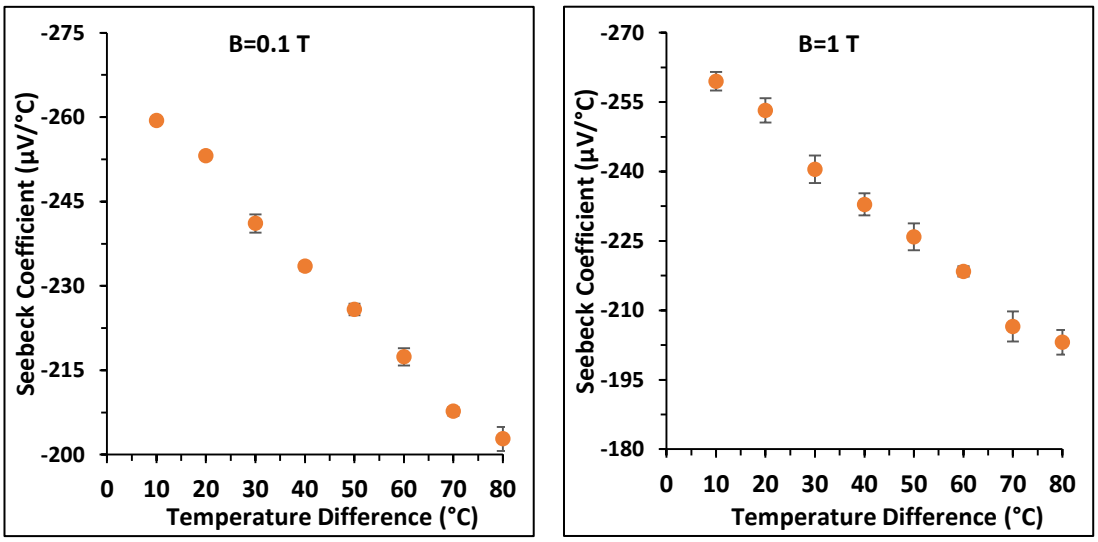

Figure 6- 15: The repeatability of the Seebeck coefficient with the DC magnetic flux density 0.1 T and 1 T for USR sample.

Table 6-7 gives the maximum and minimum estimated values for Seebeck coefficient according to standard deviation under the DC magnetic field for USR sample.

Table 6- 7: The values of Seebeck coefficient under standard deviation for USR sample under the DC magnetic field.

0.1 T				
ΔT °C	$\hat{\delta}$ μV/°C	$\check{\delta}$ μV/°C	Standard deviation	Percentage
10	-259.694	-259.106	0.294392	0.2%
20	-253.692	-252.508	0.591608	0.4%
30	-242.735	-239.465	1.635033	1.3%
40	-234.232	-232.768	0.732006	0.6%
50	-226.821	-224.779	1.021029	0.9%
60	-218.933	-215.867	1.532699	1.4%
70	-208.462	-206.938	0.761577	0.7%
80	-204.94	-200.66	2.140093	2.1%
1 T				
ΔT °C	$\hat{\delta}$ μV/°C	$\check{\delta}$ μV/°C	Standard deviation	Percentage
10	-261.522	-257.478	2.022375	1.5%
20	-255.821	-250.579	2.621068	2.0%
30	-243.465	-237.535	2.965356	2.4%
40	-235.263	-230.537	2.362908	2.0%
50	-228.784	-223.016	2.883719	2.5%
60	-219.512	-217.288	1.112055	1.0%
70	-209.763	-203.237	3.262923	3.2%
80	-205.755	-200.445	2.654556	2.6%

The graphs above show that all standard deviations of all temperatures under 0.1 T are from 0.29 to 2.14 and from 1.11 to 3.26 under 1 T depending on temperature difference. These results indicate that the experiments have a good repeatability. The standard deviation of the Seebeck coefficient under the magnetic field 1 T is higher than that under 0.1 T. The latter is higher than that in the absence of the magnetic field being applied. This is due to the effect of the magnetic field on the motion of charge carriers, which leads to change in the mobility of charge carriers depending on the scattering of charge carriers with other electrical charges carriers, ionized impurity and crystal boundaries. For further information about the samples, see Appendix 3.

The Seebeck coefficient for USB sample was calculated under the magnetic flux density from 0 T to 1 T. Figure 6-16 shows the relationship between the Seebeck coefficient and the temperature difference for different magnetic field directions and densities.

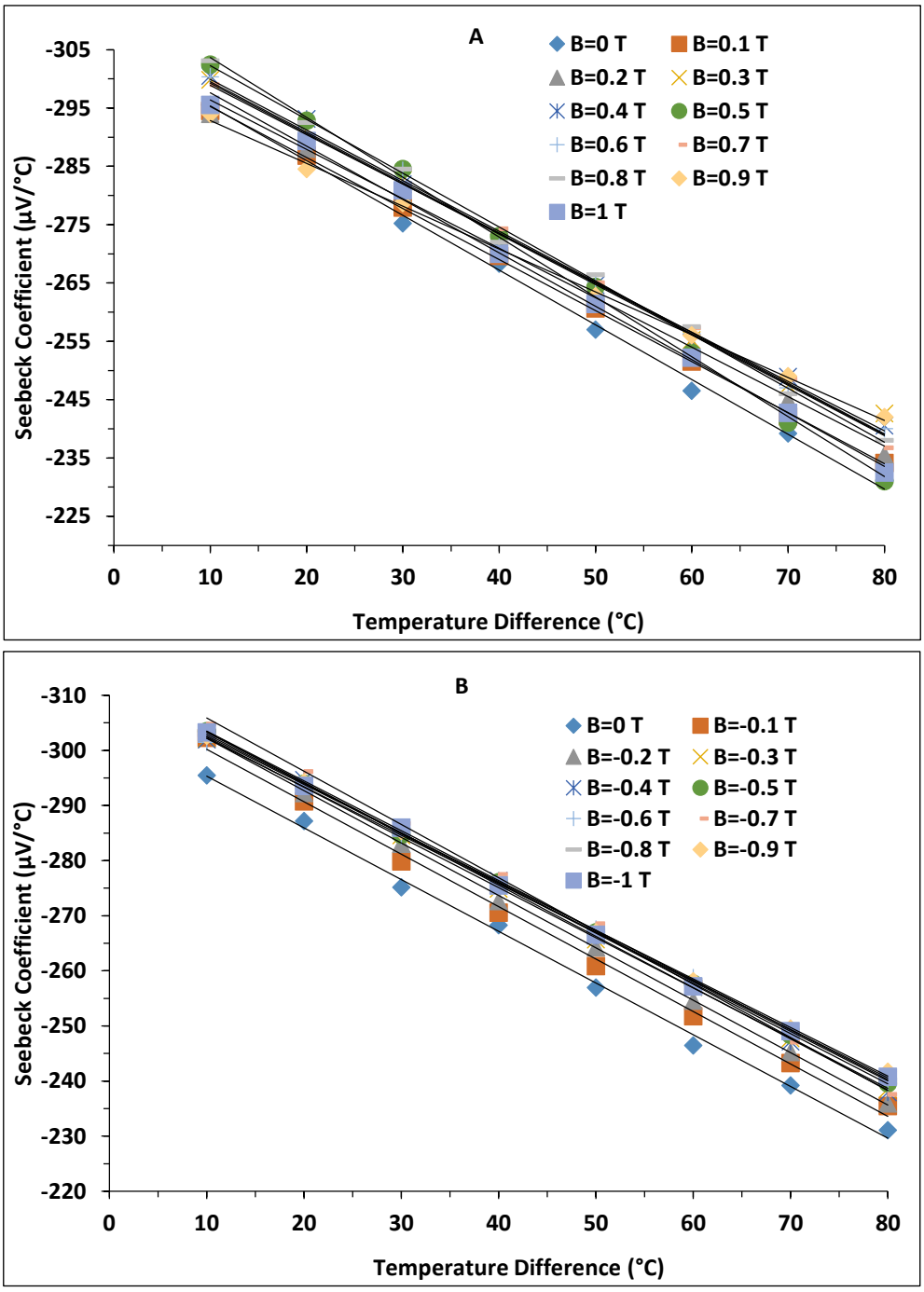

Figure 6- 16: Variation of the Seebeck coefficient with temperature difference for *various DC magnetic flux densities for USB sample*, a*: forward magnetic field and b: reverse magnetic field.*

The Seebeck coefficient for USB sample is reduced significantly (in a negative direction) with increased temperature difference at all magnetic flux densities. It gradually increases (in a negative direction) with increasing magnetic flux density for the magnetic field in both directions up to 0.3 T. This is because the magnetic field reduces the thermal conductivity, which in turn increases the Seebeck coefficient. Levelling off then occurs with slight fluctuation up to 1 T (the change in values are

within the standard deviation), as the thermal conductivity reaches its minimum value at the lowest possible level. The values of the Seebeck coefficient are in full agreement with [6.10, 6.14, 6.25, 6.26].

Figure 6-17 shows the relationship between the Seebeck coefficient for mean temperature difference 35 °C and the magnetic field variations in magnitude and direction for USB sample.

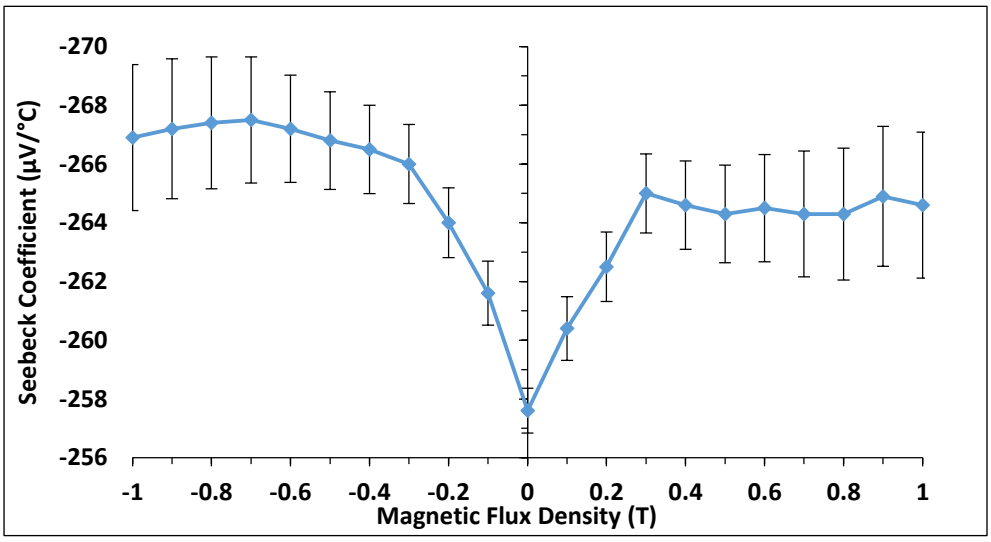

Figure 6- 17: Variation of the Seebeck coefficient with the DC magnetic flux density for USB sample.

The longitudinal motion of electrons from the hot to cool side under the magnetic field will produce the Nernst and Righi-Leduc effects (transverse electrical field and temperature difference respectively). The latter produces the Nernst and Righi-Leduc effects (longitudinal electrical field and temperature difference respectively). These voltages are continuously produced. These effects produce sequential longitudinal voltages (Seebeck voltage due to temperature difference from the Righi-Leduc effects and Nernst voltage), which act in the opposite direction. The total longitudinal voltage is equal to the initial longitudinal voltage (Seebeck voltage) plus the sequential voltages and the misalignment voltage. The misalignment voltage is independent of magnetic field direction but the sequential voltages are dependent on the magnetic field direction. The total longitudinal voltage is increased or decreased depending on the value of the misalignment voltages and the direction of the magnetic field.

As shown in Figure 6-17, the Seebeck coefficient is asymmetrical with the direction of the magnetic flux density. This is due to the position of the longitudinal contact points that had deviation in a perpendicular to heat flux. In addition, the sequential voltage is not symmetrical with the magnetic field directions, as mentioned above. This result is in full agreement with other research [6.11, 6.25, 6.26].

Figure 6-18 shows the relationship between the Seebeck coefficient and the temperature difference at different magnetic flux densities for UPB sample.

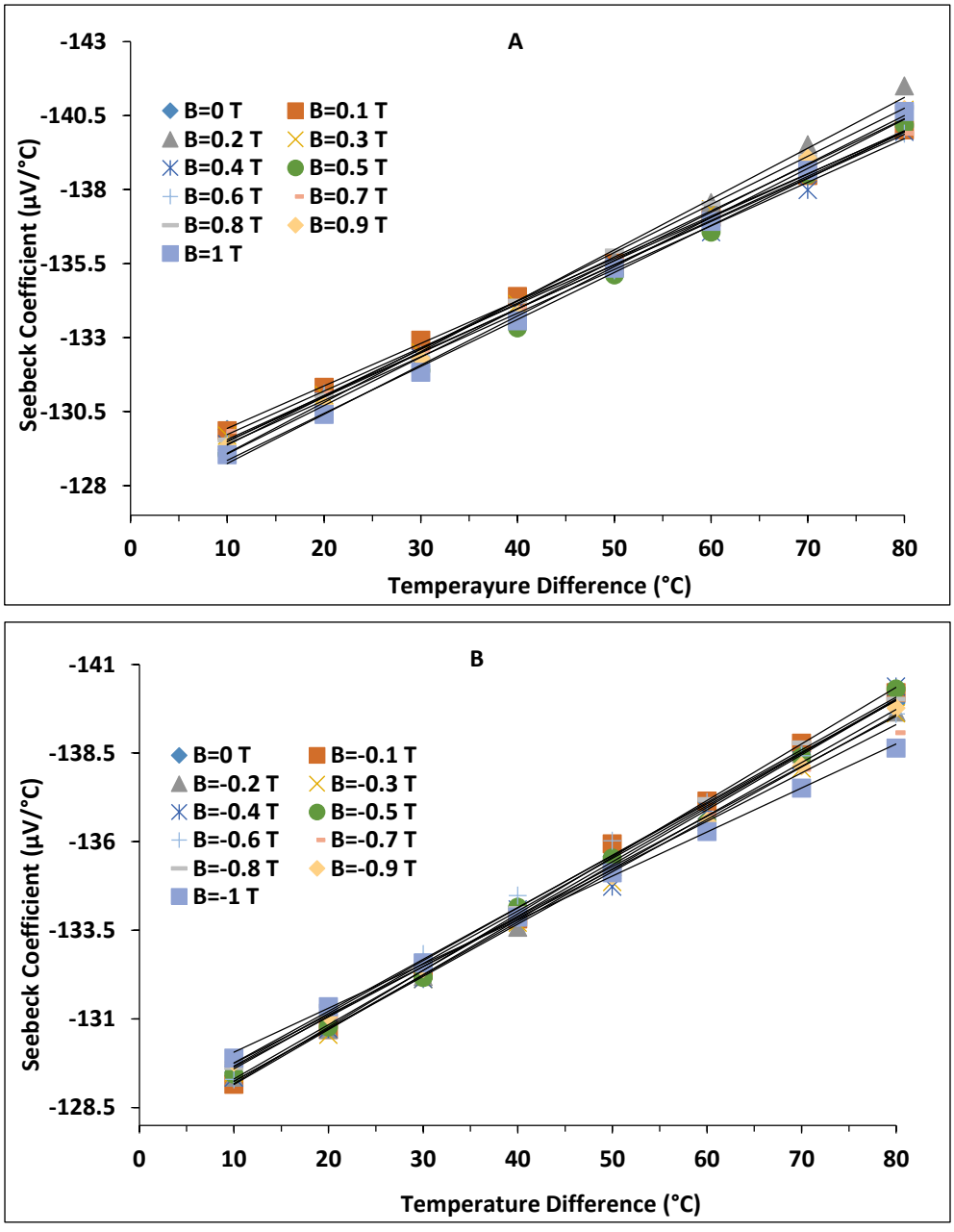

Figure 6- 18: Variation of the Seebeck coefficient with temperature difference for various DC magnetic flux densities for UPB sample, a: forward magnetic field and b: reverse magnetic field.

The Seebeck coefficient is increased slightly (in a negative direction) with increased temperature difference at all magnetic flux densities, while it fluctuates with the increase in magnetic flux density. This is due to the low variation in the resistivity under the magnetic field, low change in thermal conductivity, as mentioned in the resistivity section for the same sample.

Figure 6-19 shows the relationship between the Seebeck coefficient for mean temperature difference 35 °C and the direction of the magnetic field for UPB sample.

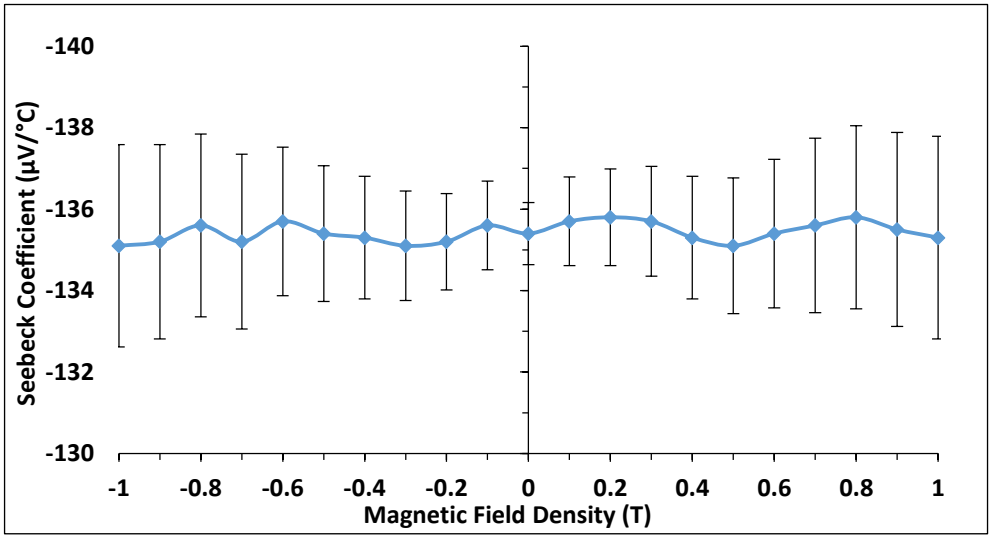

Figure 6- 19: Variation of the Seebeck coefficient with the DC magnetic flux density for UPB sample.

The Seebeck coefficient fluctuates gradually with an increase in the magnetic flux density for both magnetic field directions. The reason for this is the same as mentioned above.

The Seebeck coefficient for UPA, DP0.1% and DP0.25% samples has similar behavior as that for UPB sample. However, each sample has lower value than the previous sample, except that DP0.25% has a higher value than that for DP0.1%. This is due to the same reason that was mentioned regarding the Seebeck coefficient of these samples in the absence of the magnetic field. For further information about the samples, see Appendices 6 and 7.

The relationship between the Seebeck coefficients for mean temperature difference of all samples with magnetic flux density is shown in Figure 6-20.

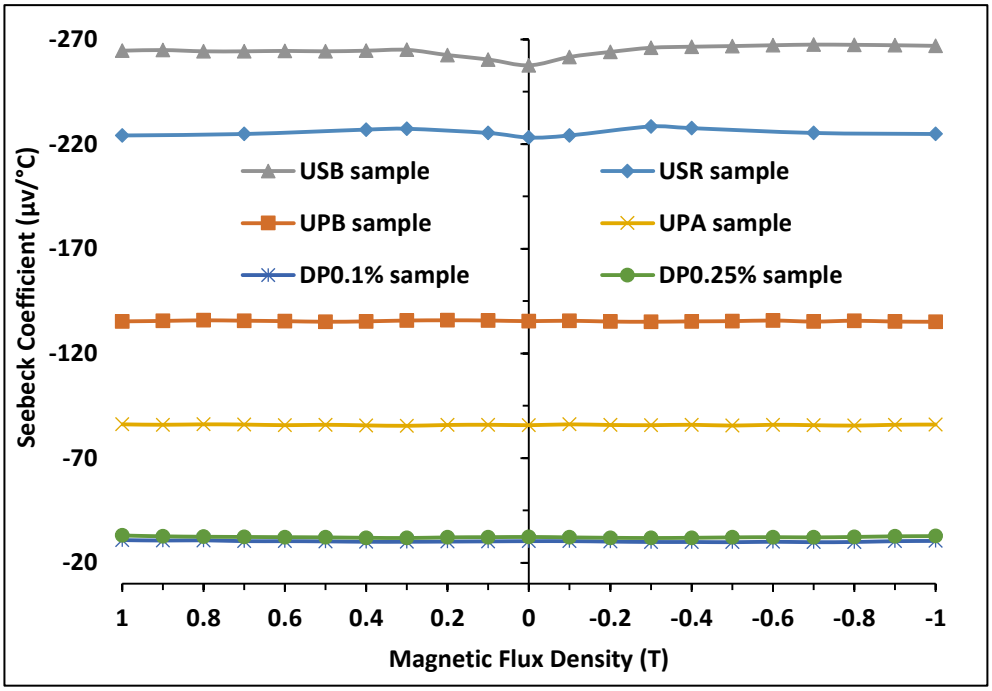

Figure 6- 20: Variation of the Seebeck coefficient with the DC magnetic flux density of all samples.

It can be seen that the Seebeck coefficient does not increase with increasing magnetic flux density for both directions of all samples.

6.3.2.4: Total transverse voltage under the magnetic field

The total transverse voltage of all samples was measured under the magnetic flux density ranging 0 to 1 T as was illustrated in Chapter Five. For further information about the samples, see Appendix 1. Figure 6-21 shows the relationship between total transverse voltage and temperature difference at different magnetic flux densities for USB sample.

The total transverse voltage increases significantly (in a negative direction) with increased temperature difference at all magnetic flux densities, as shown in Figure 6-21. It decreases gradually (in a negative direction) with an increase in the magnetic flux density for the reversed magnetic field and increases slightly for the forward magnetic field. It can also be seen that in all reversed magnetic flux density,

the results are of positive values that then reduce slightly to negative values. Meanwhile, of all forward magnetic flux density, as well as cases in the absence of the magnetic field, total transverse voltages are of negative values and then increase significantly in the negative direction to more negative values. This is due to the total transverse voltage being a summation of the three parameters (misalignment, Nernst and Righi-Leduc voltages). To understand this combined effect adequately, discussion on the individual effect of each parameter will be presented below. The total transverse voltage for USR and UPB samples has the same behavior as that for USB sample but with lower values. This is due to the same reason that was mentioned regarding the Seebeck coefficient for USR sample in the absence of the magnetic field.

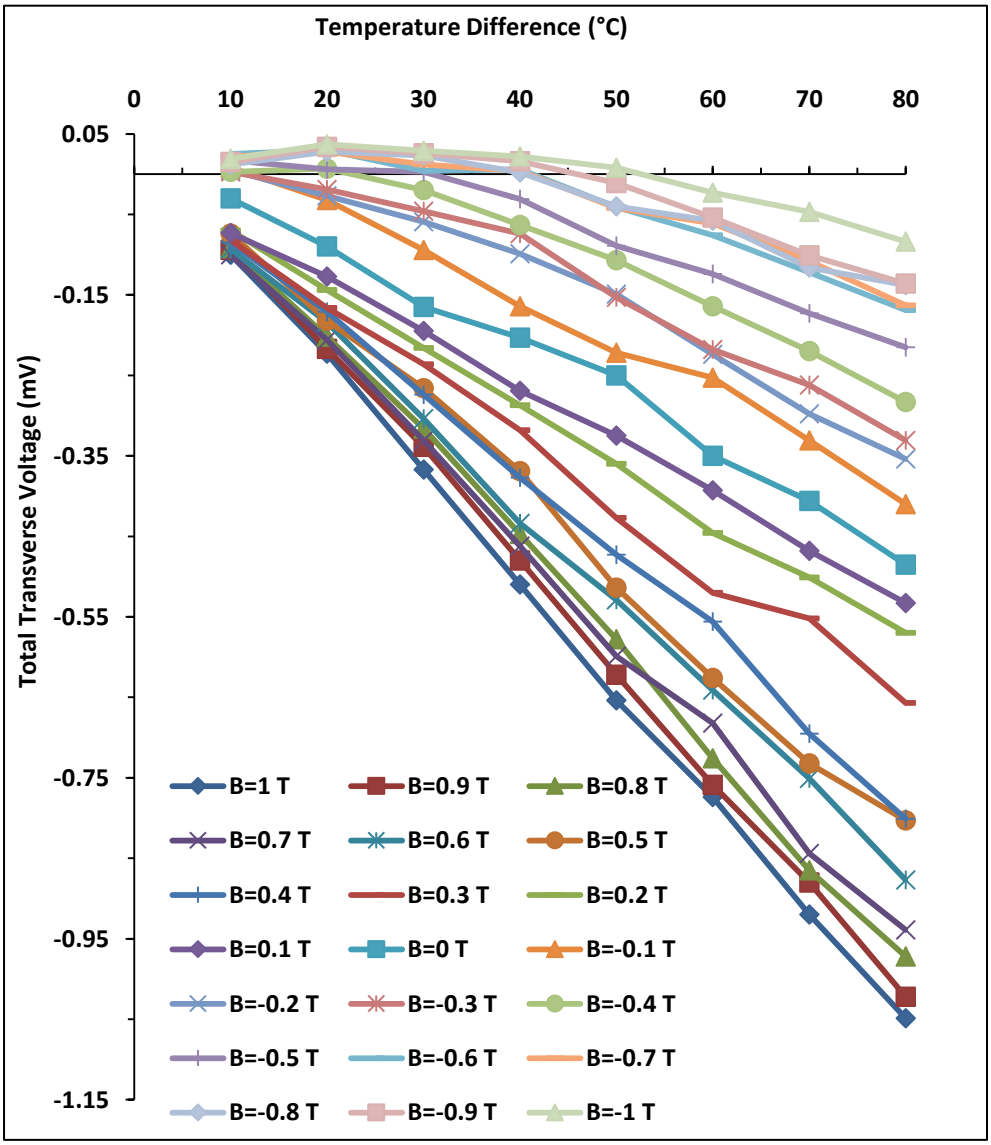

Figure 6- 21: Variation of the total transverse voltage with temperature difference for various DC magnetic flux densities for USB sample.

Figure 6-22 shows the relationship between total transverse voltage and temperature difference for different magnetic flux densities for UPA sample.

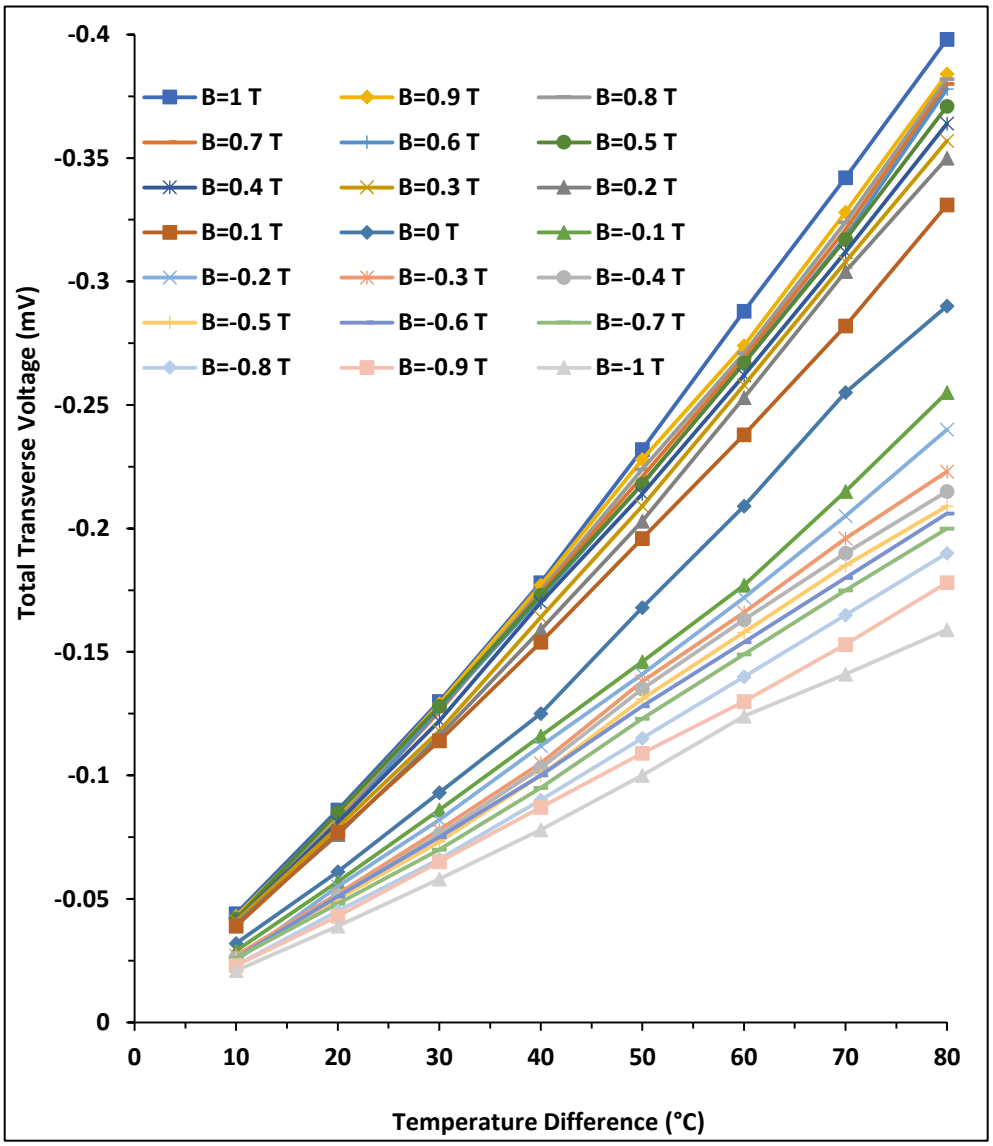

Figure 6- 22: Variation of the total transverse voltage with temperature difference for various DC magnetic flux densities for UPA sample.

The total transverse voltage for UPA has the same behavior as that for USB sample but it begins with negative values and then increases considerably for both magnetic field directions.

The total transverse voltage for UPA, Dp0.1% and Dp0.25% samples has the same behavior as that for USB sample. However, each sample displays a lower value than the previous sample. This is for the same reason that has been mentioned

regarding the total transverse voltage for USB sample under the magnetic field. For further information about the samples, see Appendix 8.

The relationship between the total transverse voltage of all samples with temperature difference for magnetic flux density 0.4 and 1 T in both directions is shown in Figure 6-23.

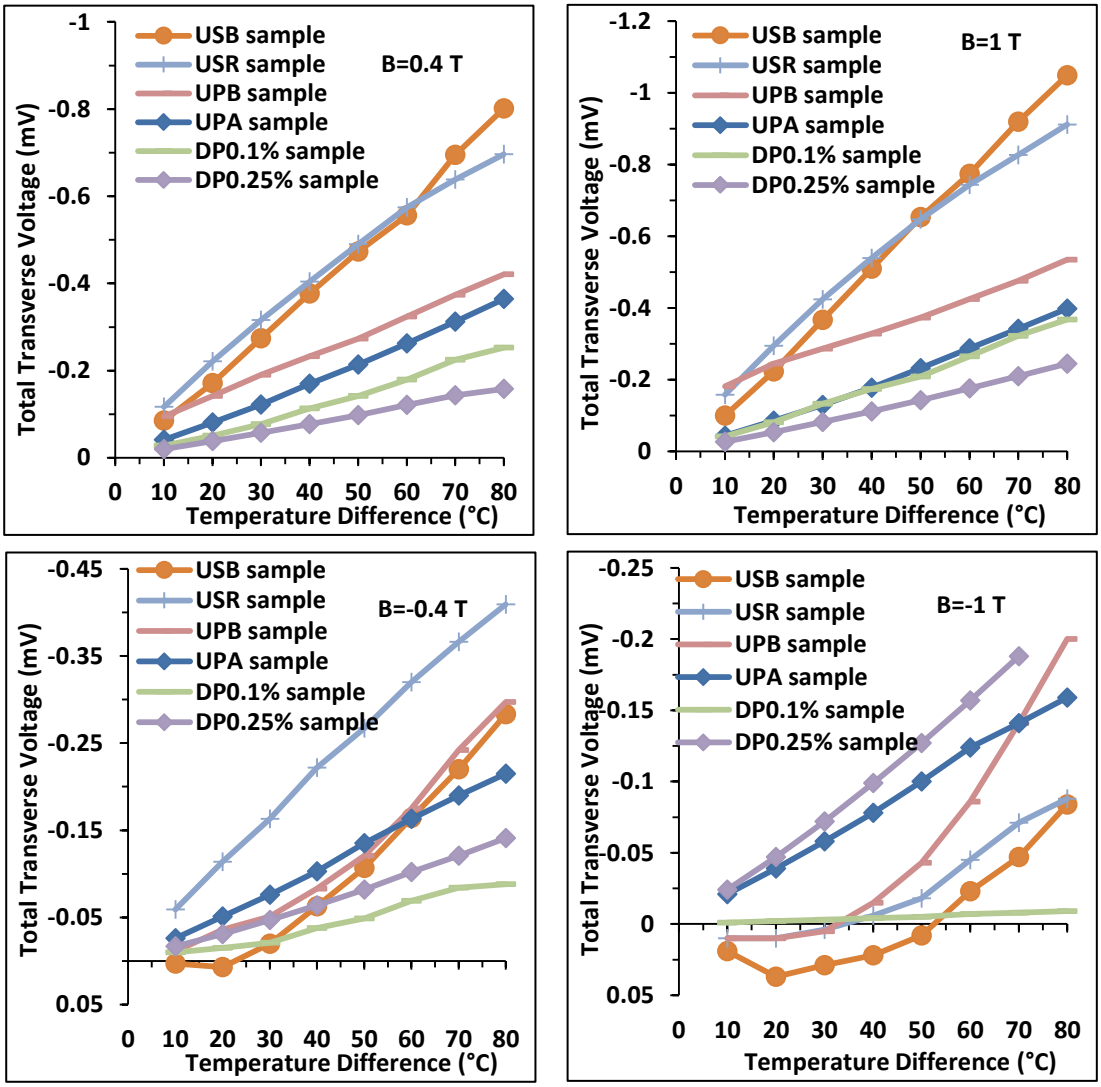

Figure 6- 23: Variation of the total transverse voltage with temperature difference for DC magnetic flux density 0.4, 1 T in both directions of all samples.

The total transverse voltage measured across the two central arms V_y, is due to three effects. The first is the Nernst effect and its voltage is denoted by V_N. The second is the Righi-Leduc effect, which causes a rise in temperature difference in the y direction, thereby producing a voltage difference V_{RL} in the y direction via the

Seebeck effect. The third can result from the misalignment of the two lead wires. The temperatures at the two lead contacts may differ since temperature gradient is applied in the x direction. This temperature difference induces a potential difference V_T also via the Seebeck effect. Thus,

$$V_y = V_N + V_{RL} + V_T \quad \text{.....(6.4)}$$

The first term of the Eq. (6.4) is the Nernst voltage. It is a desired term and it depends on the magnetic field direction; the other two components need to be cancelled to calculate the Nernst effect. The second term is reversed with the reversal magnetic field direction. However, because of the lag of the Righi-Leduc transverse temperature difference when responding to a change in direction of the magnetic field, this change does not reverse the temperature direction as fast as the time taken to reverse the magnetic field. The third term is independent of the magnetic field direction. Hence, the total transverse voltage with the magnetic field direction (before change its direction) is,

$$V_{y1} = V_N + V_{RL} + V_T \quad \text{.....(6.5)}$$

By changing the magnetic field direction and measuring it immediately after change:

$$V_{y2} = -V_N + V_{RL} + V_T \quad \text{.....(6.6)}$$

Subtracting Eq. (6.6) from Eq. (6.5),

$$V_N = \frac{(V_{y1} - V_{y2})}{2} \quad \text{.....(6.7)}$$

In this manner the voltage difference is due to the Nernst effect only, as determined by [6.15]. The Nernst voltage was calculated under the magnetic field from 0 T to 1 T for undoped InSb using Eq. (6.7).

The change in the power supply polarity will cause a rapid change in the magnetic field direction. The lag time for swapping the temperature direction (Righi-Leduc effect) has been studied. This is due to the time that the sample requires to

reach equilibrium then increase the temperature difference again in the opposite direction. The change in the transverse temperature gradient direction due to the change in the magnetic field direction reduced the values of the thermal time constants. Practically, this change was between 8 sec to 10 sec.

6.3.2.5: Nernst voltage

The Nernst voltage of all samples was calculated by using Eq. (6.5) to (6.7) under the magnetic flux density from 0 T to 1 T. For further information about the samples, see Appendix 9. Figure 6-24 shows the relationship between the Nernst voltage and the temperature difference for different magnetic flux densities for USB sample.

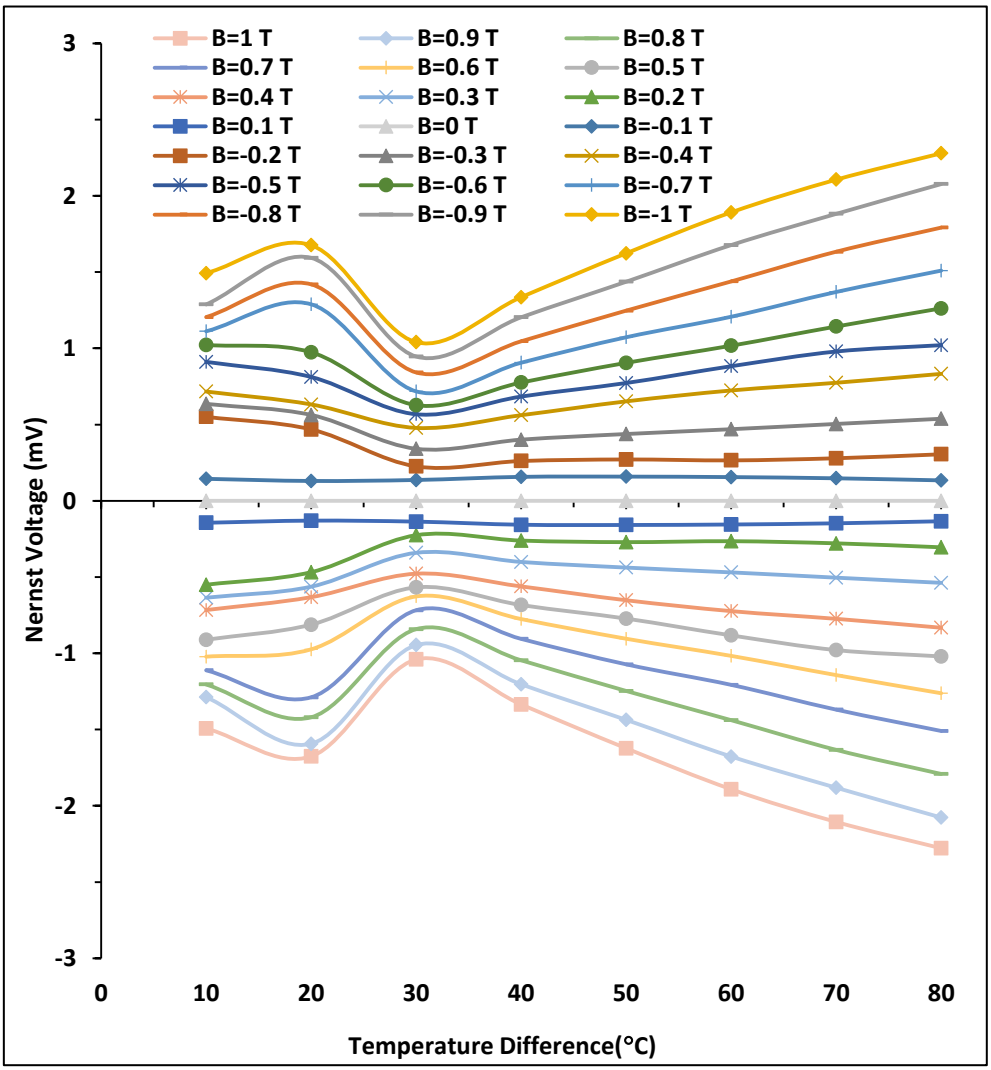

Figure 6- 24: Variation of the Nernst voltage with temperature difference for various DC magnetic flux densities for USB sample.

The Nernst voltage has positive values for the reverse magnetic field and it increases gradually with increasing temperature difference from 30 °C to 80 °C. This is due to the increasing number of both charge carriers (electrons and holes) deviating under the Lorentz force with increasing temperature (ambipolar effect). It also increases gradually with increasing magnetic flux density (in a negative direction) due to the increasing Lorentz force for the reverse magnetic field, and then increasing the number of deviated charge carriers. This is due to the increased magnetic force, which deviates charge carriers' path (electrons and holes) via the Lorentz effect. The opposite occurs for the forward magnetic field. Thus, the behavior of the Nernst voltage with temperature difference from 10 °C to 30 °C randomly responds to the magnetic field. I can attribute this to the low kinetic energy that the charge carriers possess, which in turn leads to a weak response to the magnetic field.

The Nernst voltage for USR sample has similar behavior to that for USB sample under the magnetic field (at all magnetic flux densities), while the values are lower than those for USB sample. This is due to the same reason mentioned regarding the increased Seebeck coefficient of USR sample in the absence of the magnetic field. The Nernst voltage for temperatures from 30 °C to 80 °C for the rectangular shape has a lower slope than for the bridge shape; the slope was 0.0251 for the Bridge shape and 0.0041 for the rectangular shape under the magnetic flux density of 1 T. This is due to the increased distortion of the current flux line by putting two transverse connected points on the sample surface. In addition, this is due to the collection of most of the charge carriers by the transverse contact points as they travel from the hot to cool sides. The rest of charge carriers pass through the distance between the connected points. The number of charge carriers deviates due to being subjected to the magnetic field, increasing gradually. This is dependent on the speed of charge carriers.

The Nernst voltage for UPB, UPA, DP0.1% and DP0.25% samples has the same behavior as that for USR sample under the magnetic field (at all magnetic flux densities). This behavior is opposite to the behavior of the same samples related to the total transverse voltage. This is due to the same reasons mentioned regarding the Seebeck coefficient of these samples in the absence of the magnetic field. The

slope of the Nernst voltage at the same temperature difference is approximately similar for USR, UPB, UPA, DP0.1% and DP0.25% samples under the magnetic flux density for various temperature differences. This is due to the same reason mentioned above, as shown in Figure 6-24. For further information about the samples, see Appendix 10.

The relationship between the Nernst voltages of all samples with temperature difference for different forward magnetic flux densities is shown in Figure 6-25.

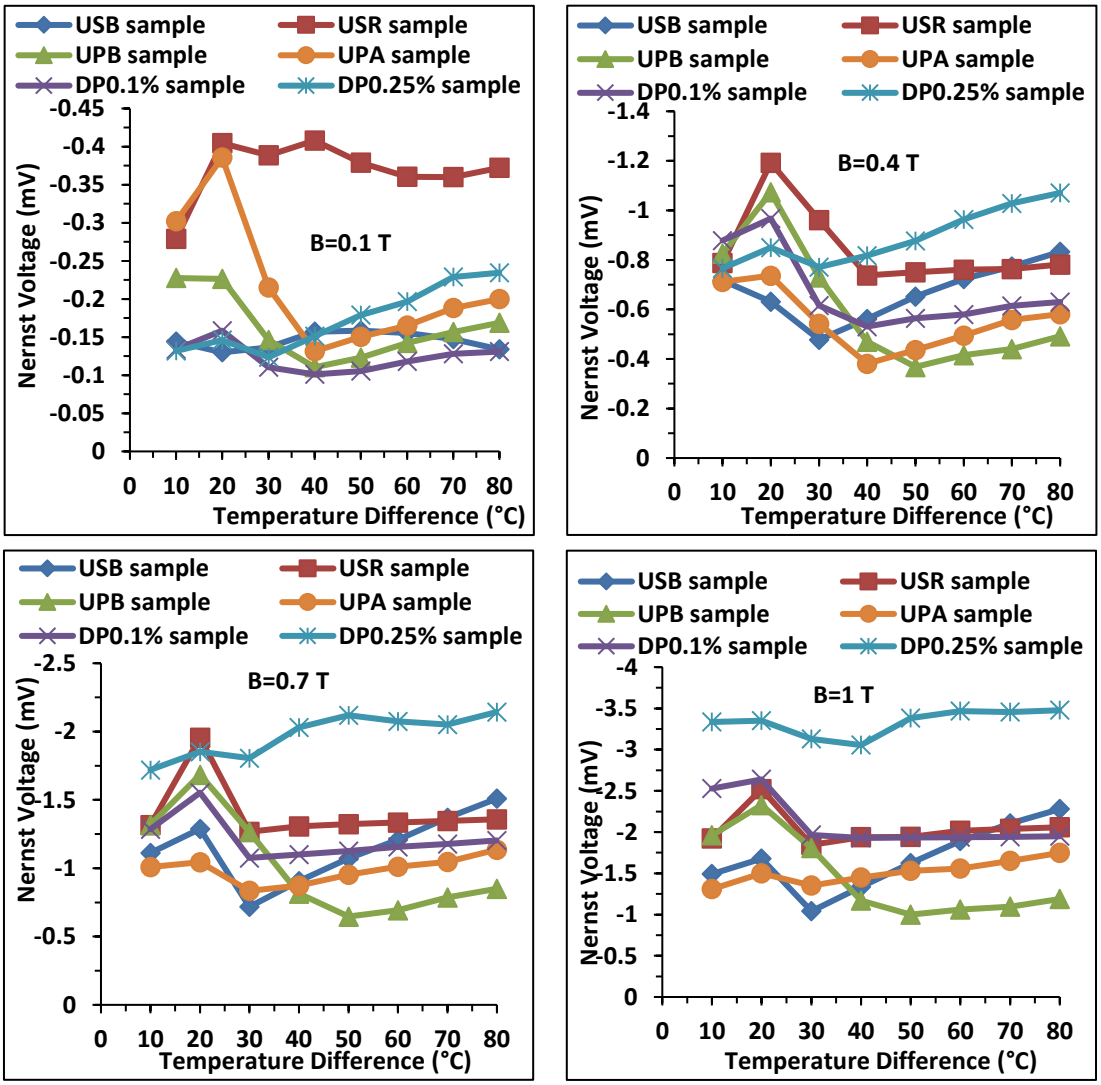

Figure 6- 25: Variation of the Nernst voltage with temperature difference for various forward magnetic flux densities of all samples.

It can be seen that the Nernst voltage increases significantly for DP0.25% sample under magnetic field except 0.1 T. The behavior for both DP0.1% and 0.25% under magnetic flux density 0.1 T might be due to the low mobility of charge carriers,

owing to increasing the scattering of charge carriers with other electrical charge carriers, ionized impurity and crystal boundaries. This makes the value μB less than 10^4 T.cm^2.V^{-1}.Sec^{-1} for which mean it operates as a good thermomagnetic material.

6.3.2.6: Righi-Leduc voltage

The Righi-Leduc voltage of all samples was calculated by using Eq. (6.5) to (6.6) under the magnetic flux density from 0 T to 1 T. For further information about the samples, see Appendix 9. Figure 6-26 shows the relationship between the Righi-Leduc voltage and the temperature difference for various magnetic flux densities.

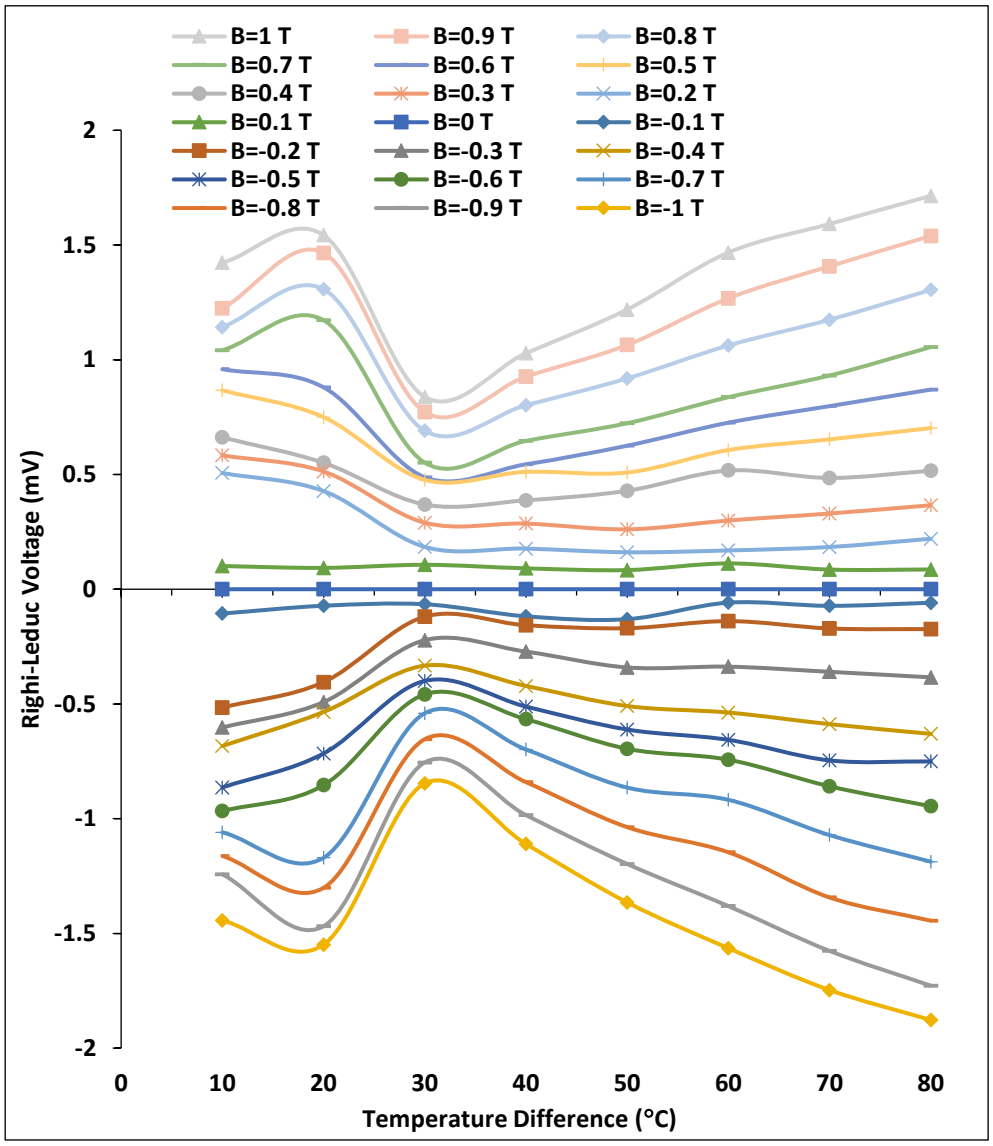

Figure 6- 26: Variation of the Righi-Leduc voltage with temperature difference for various DC magnetic flux densities for USB sample.

The Righi-Leduc voltage has positive values for the forward magnetic field. Its behaviors are as those of the Nernst voltage for USB sample but in the opposite direction. In addition, the values of Righi-Leduc voltage are not equal in magnitude at different magnetic field directions. This is due to its dependence on the thermal energy that the charge carriers have, which is not quantitated value but increased with increasing temperature. In addition, the Righi-Leduc voltage looks similar to Nernst voltage behavior. This might be due to the high difference between the mobility of electrons and holes, which establish as high temperature at the side that accumulated electrons before increasing the temperature of the opposite side that accumulated holes.

The Righi-Leduc voltage for USR sample has the same behavior as that for USB sample under the magnetic field (at all magnetic flux densities). This behavior is similar to the behavior of the same samples related to the Nernst voltage for the same reason. In addition, the Righi-Leduc voltage should be decreased with increasing both charge carriers. This is dependent on the large difference between the mobility of electrons and holes. The Righi-Leduc voltage for temperatures from 30 °C to 80 °C with the rectangular shaped sample has a lower slope than the bridge shape. The slope was 0.0321 for the Bridge shape and 0.0074 for the rectangular shape under the magnetic flux density of 1 T. This is due to the same reasons mentioned regarding the Nernst coefficient for USB sample (thermal charge carriers instead of electrical charge carriers).

The Righi-Leduc voltage for UPB, UPA, DP0.1% and DP0.25% samples displays similar behavior as that for USR sample under the magnetic field (at all magnetic flux densities). This behavior is similar to the behavior of the same samples related to the Nernst voltage for the same reason. The slope of the Righi-Leduc voltage at various temperature differences of all samples has the same behavior as mentioned on Nernst voltages, as shown in Figure 6-26. For further information about the samples, see Appendix 11.

The relationship between the Righi-Leduc voltages of all samples with temperature difference for different forward magnetic flux densities is shown in

Figure 6-27. It can be seen from Figure 6-27 that the Righi-Leduc voltage increases significantly for Dp0.25% sample under magnetic field except 0.1 T. This is for the same reason mentioned in Nernst voltage.

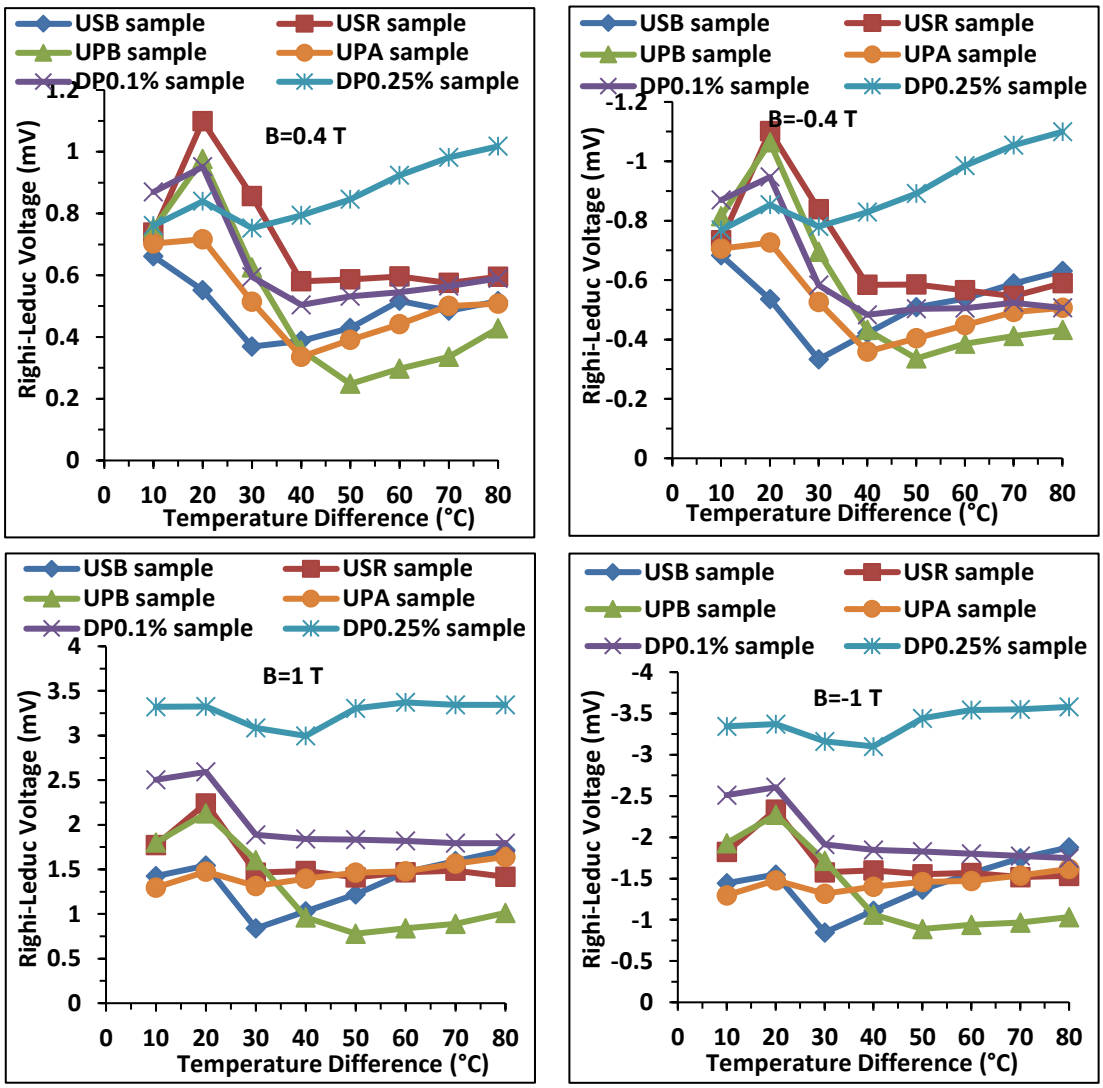

Figure 6- 27: Variation of the Righi-Leduc voltage with temperature difference for various forward magnetic flux densities of all samples.

6.3.2.7: Misalignment voltage

The misalignment voltage of all samples was measured as that for total transverse voltage, but in the absence of the magnetic field at different temperature differences. For further information about all samples see Appendix 1. Figure 6-28 shows the relationship between the misalignment voltage of the two lead wires and the temperature difference for USB sample.

The misalignment voltage in Figure 6-28 is increased significantly (in a negative direction) with increasing temperature difference. This is due to the increase in energy loss owing to the collision of the charge carriers with crystal defects [6.24].

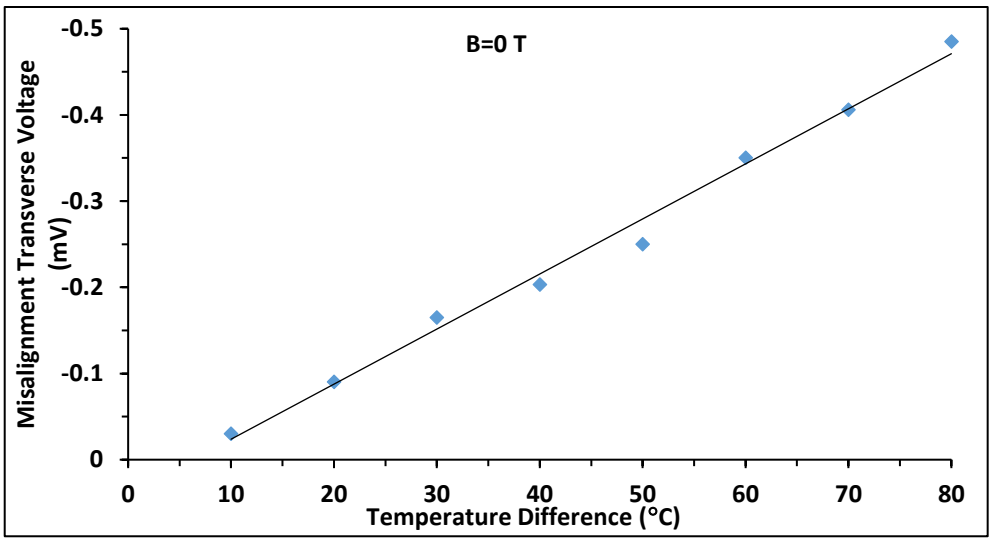

Figure 6- 28: Variation of the misalignment voltage with temperature difference for USB sample in the absence of the magnetic field.

The misalignment voltage for USR, UPB, UPA, DP0.1% and DP0.25% samples has the same behavior as that for USB sample. The behavior is due to the same reasons mentioned regarding the misalignment voltage for USB sample. The increases in the thermal conductivity reduce the misalignment voltage due to the reduction in the temperature difference between two different points. For further information about the samples, see Appendix 12.

6.3.2.8: Nernst coefficient

The Nernst coefficient for USB sample was calculated from Nernst voltage. Its value is dependent on the temperature gradient, the Nernst voltage and the width of the sample. It is obtained by the following equation:

$$N = \frac{V_N}{\Delta T} * \frac{L}{B \times W} = \frac{V_N}{\Delta T \times B} * \frac{17_{mm}}{2_{mm}} \quad \text{.....(6.8)}$$

Where L is the length of the sample and W is the width of the sample.

The Nernst coefficient is calculated under magnetic flux density from 0 T to 1 T for undoped InSb. Figure 6-29 shows the relationship between the Nernst coefficient and the temperature difference at different magnetic flux densities for USB sample.

The Nernst coefficient in Figure 6-29 has positive values for the reverse magnetic field. It decreases very slightly with increasing temperature difference from 30 °C to 80 °C. This is due to the increase in the number of charge carriers being less than the increase of temperature differences, because the sample operates at the beginning of the intrinsic regime. The Nernst coefficient increases significantly to its highest value for the magnetic flux density from 0 T to 0.1 T; it then decreases gradually with an increase in the magnetic flux density up to 1 T. This is because the Nernst coefficient is inversely proportional with the magnetic field. The opposite occurs for the forward magnetic field. Thus, the behavior during temperature difference from 10 °C to 30 °C and under the magnetic flux density from 0.1 up to 1 T is due to the same reason mentioned in Nernst voltage section. The Nernst coefficient values are in full agreement with [6.12, 6.14] that confirmed that the Nernst coefficient was decreased by increasing the magnetic field.

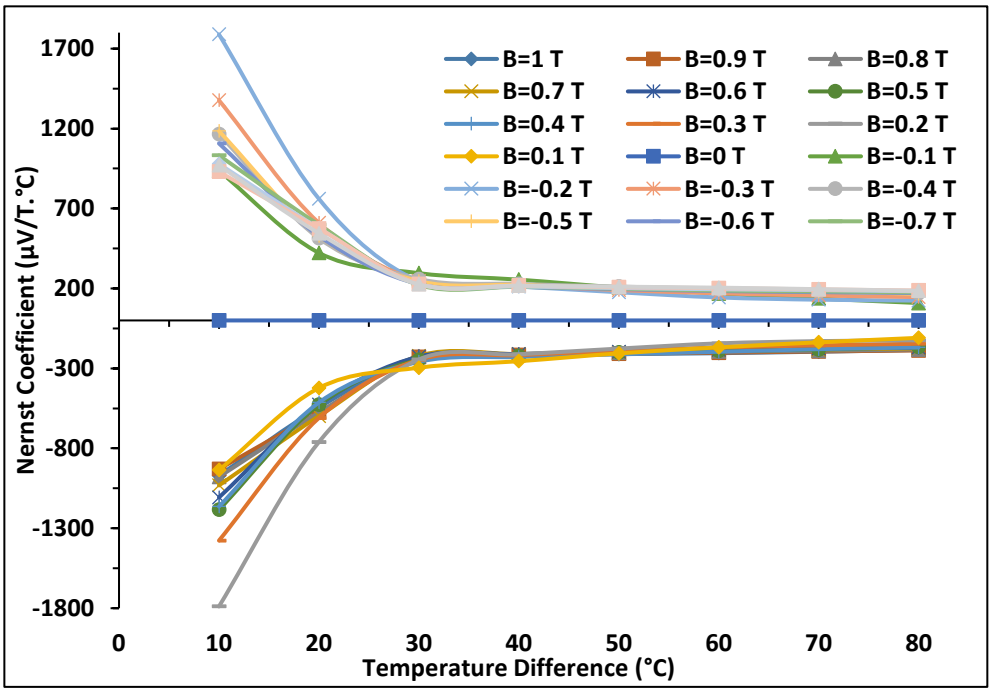

Figure 6- 29: Variation of the Nernst coefficient with temperature difference for various DC magnetic flux densities for USB sample.

The Nernst coefficient for USR, UPB, UPA, DP0.1% and DP0.25% samples has the same behavior as that for USR sample under the magnetic field (at all magnetic flux densities). This behavior is similar to the behavior of the same samples related to the Nernst voltage for the same reason. For further information about the samples, see Appendix 13.

The relationship between the Nernst coefficient of all samples with temperature difference for different forward magnetic flux densities is shown in Figure 6-30.

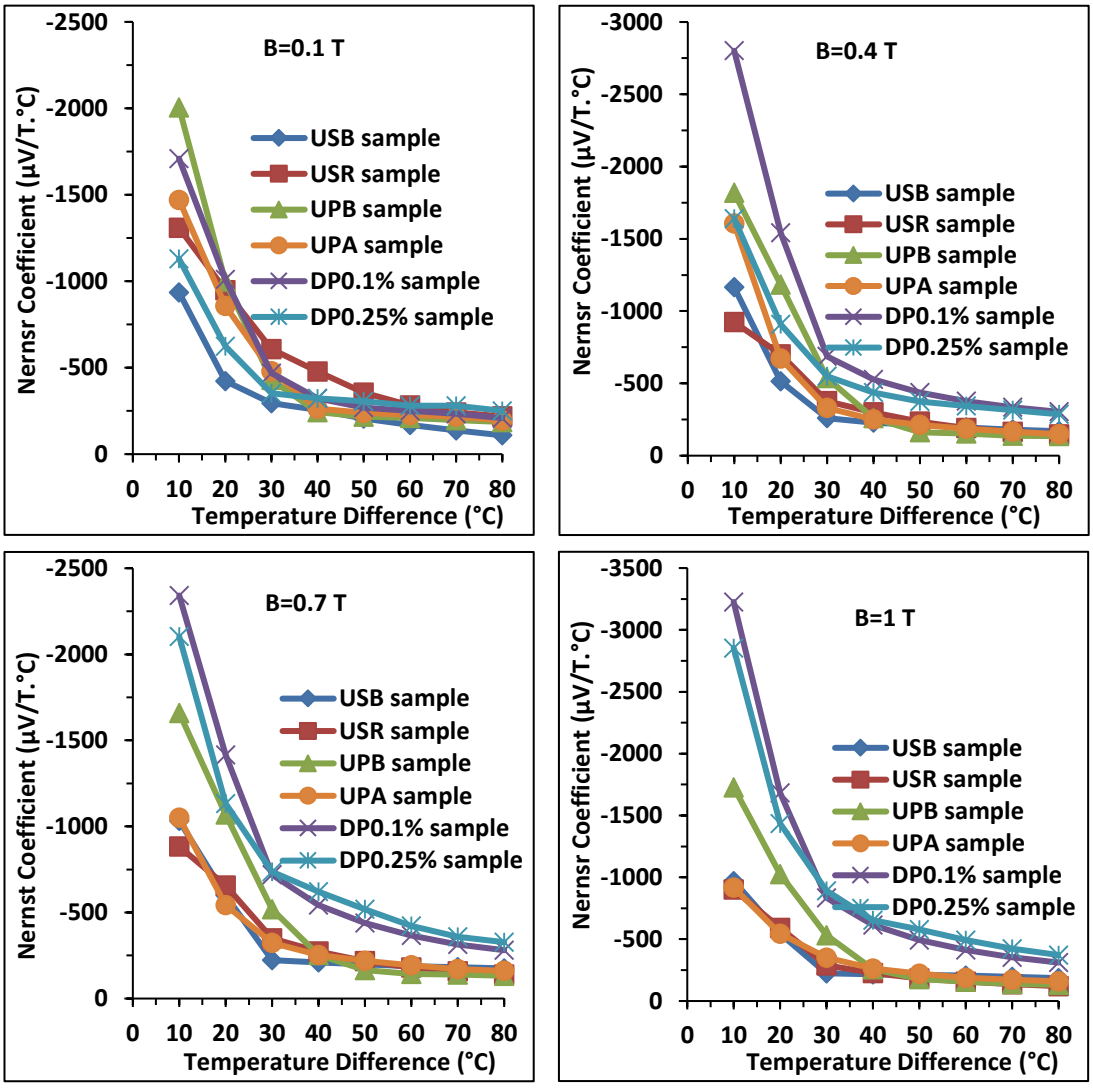

Figure 6- 30: Variation of the Nernst coefficient with temperature difference for various forward magnetic flux densities of all samples.

It can be seen from Figure 6-27 that the behavior of the Nernst coefficient is similar to the behavior of Nernst voltage of all samples.

6.3.2.9: Thermomagnetic power

The thermomagnetic power of all samples was calculated under the magnetic flux density from 0 T to 1 T by multiplying the Nernst coefficient by magnetic flux density NB. For further information about the samples, see Appendix 9. Figure 6-31 shows the relationship between the thermomagnetic power and temperature difference at different magnetic flux densities for USB sample.

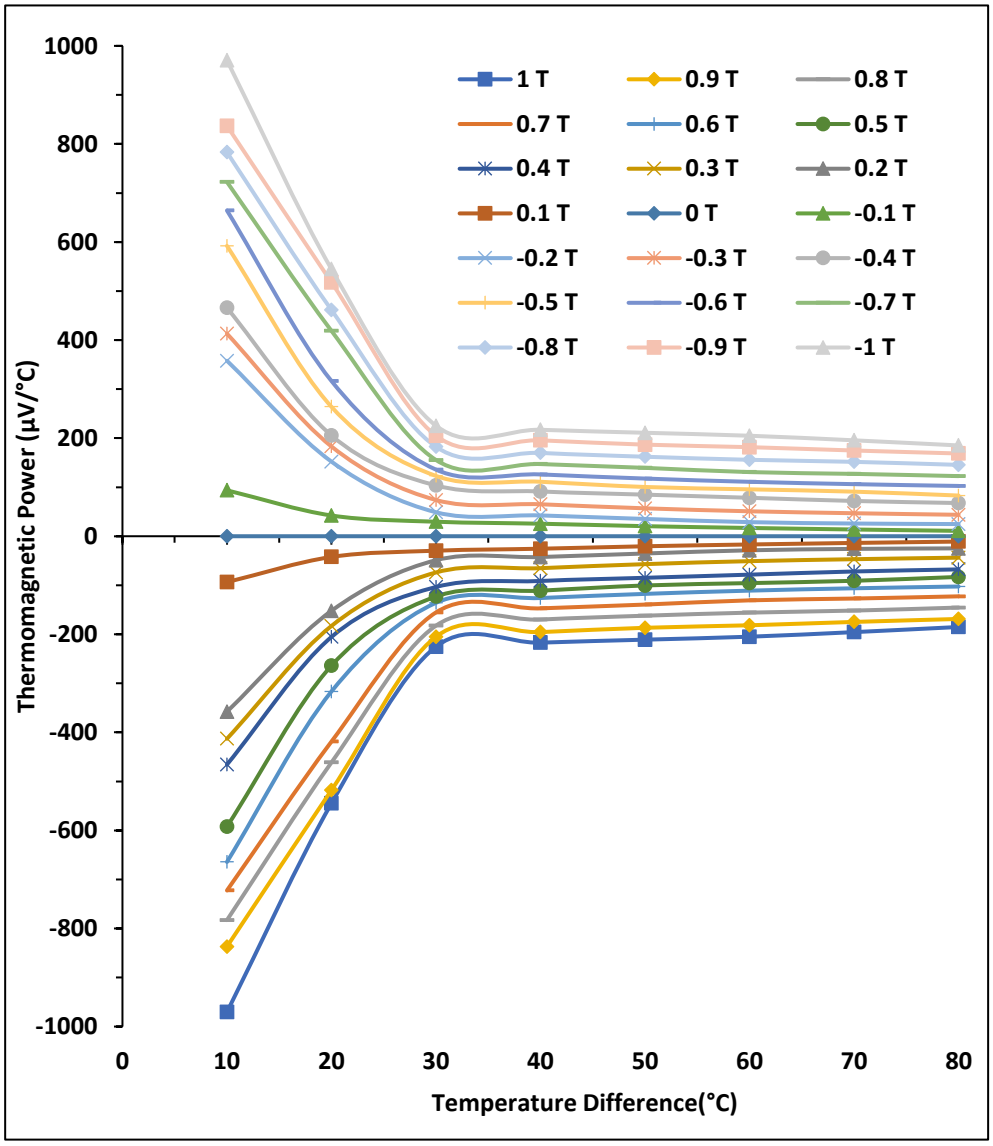

Figure 6- 31: Variation of the thermomagnetic power with temperature difference for various DC magnetic flux densities for USB sample.

The thermomagnetic power has positive values for the reverse magnetic field. It decreases very slightly for temperature differences from 30 °C to 80 °C. This is due to the same reason that was mentioned regarding the Nernst coefficient for USB sample. It also increases slightly with an increase in the magnetic flux density at all magnetic flux densities due to the increasing Lorentz force. The opposite occurs for the forward magnetic field, as the thermomagnetic power is equal to the Nernst coefficient multiplied by the magnetic flux density. Thus, the behavior of the thermomagnetic with temperature difference from 10 °C to 30 °C and under magnetic flux density from 0.1 up to 1 T is due to the same reason mentioned in the Nernst voltage section.

Figure 6-31 shows that the USB sample can generate more electrical power by increasing magnetic field in both directions but less by increasing temperature differences. The thermomagnetic power values are in full agreement with [6.13] that confirmed that the thermomagnetic power reduced by increasing the temperature differences. In addition, the thermomagnetic power increased by increasing the magnetic field for reversed magnetic field direction.

The thermomagnetic power for USR, UPB, UPA, DP0.1% and DP0.25% samples has the same behavior as that for USR sample under the magnetic field (at all magnetic flux densities). This behavior is similar to the behavior of the same samples related to the Nernst voltage for the same reason. For further information about the samples, see Appendix 14.

The relationship between the thermomagnetic powers of all samples with temperature difference for different forward magnetic flux densities is shown in Figure 6-32.

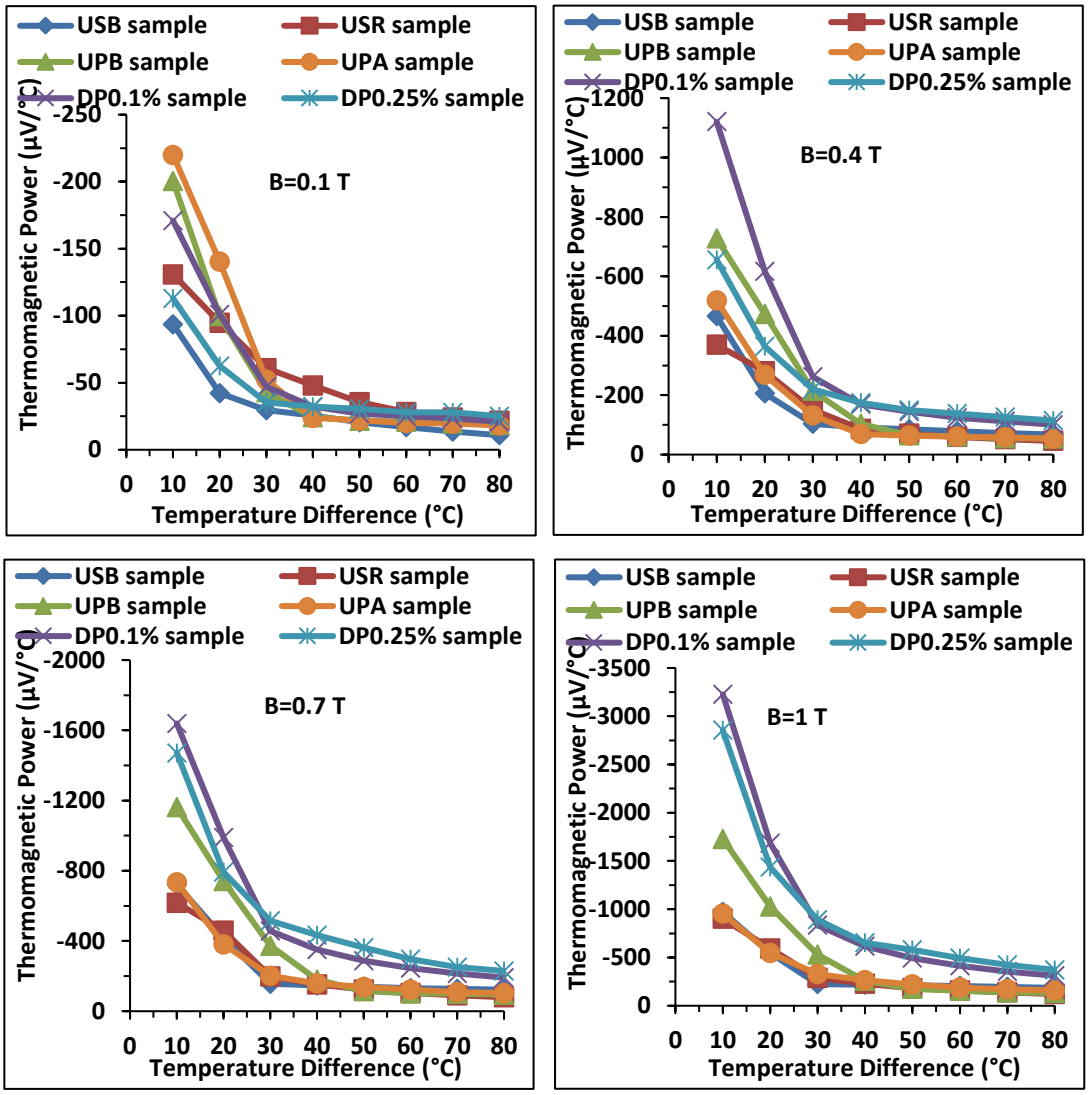

Figure 6- 32: Variation of the thermomagnetic power with temperature difference for various forward magnetic flux densities of all samples.

It can be seen from Figure 6-29 that the behavior of the thermomagnetic power is similar to the behavior of Nernst voltage of all samples.

Figure 6-33 shows the relationship between the thermomagnetic power and magnetic flux density at different temperature differences for USB sample.

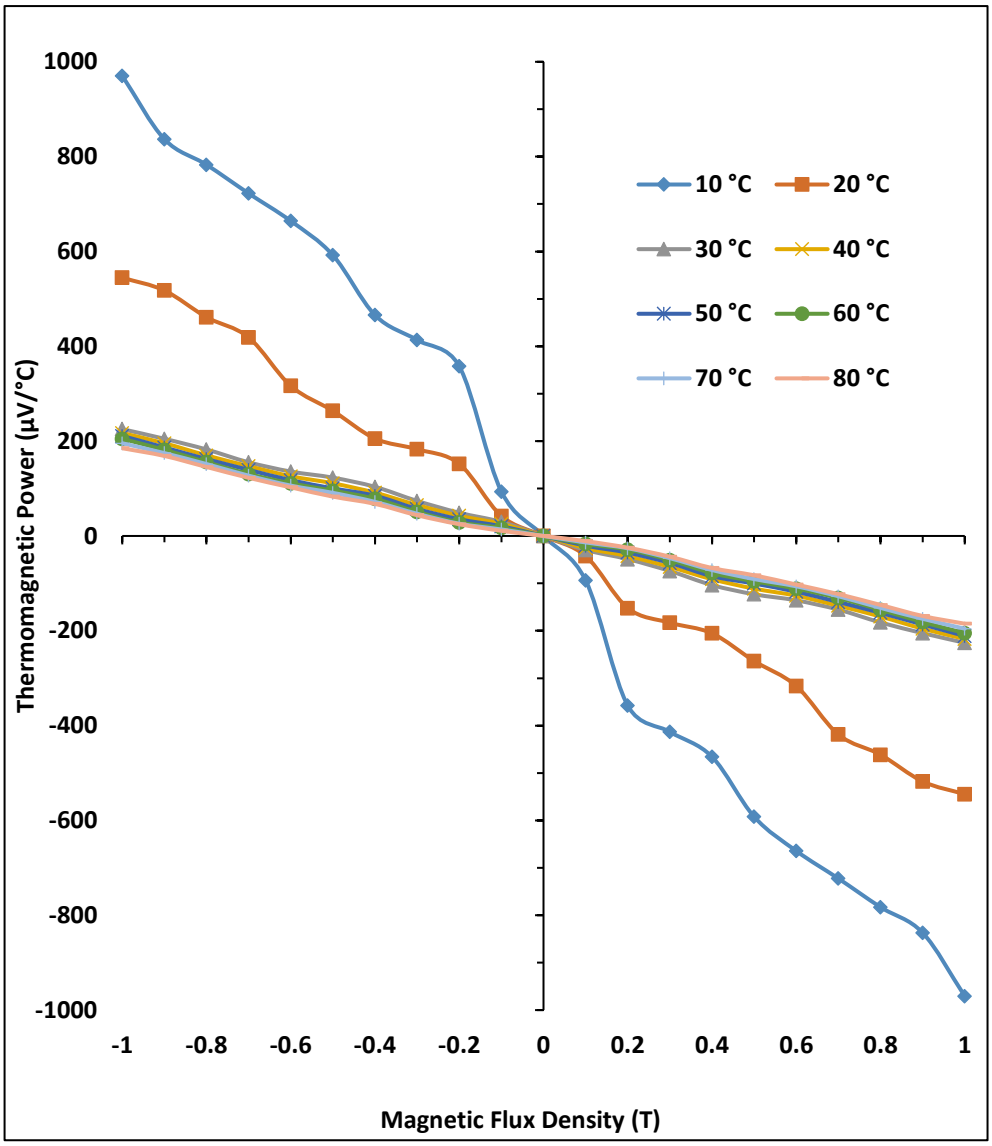

Figure 6- 33: Variation of the thermomagnetic power with the DC magnetic flux density for various temperature differences for USB sample.

The behavior of the relationship between the thermomagnetic power and magnetic flux density at different temperature differences for USB sample has the same behavior as that for the relationship between the thermomagnetic power and temperature difference at different magnetic flux densities for the same sample. The behavior of the thermomagnetic power values is in full agreement with [6.9-6.11, 6.14, 6.18, 6.25].

The thermomagnetic power for USR, UPB, UPA, DP0.1% and DP0.25% samples has the same behavior as that for USB sample with and without the applied

magnetic field (at all magnetic flux densities). For further information about the samples, see Appendix 15.

6.3.2.10: Hybrid transverse (Seebeck+total transverse) voltage

The hybrid transverse voltage is the summation of Seebeck plus total transverse voltages. It was measured in all samples under the magnetic flux density from 0 T to 1 T, as illustrated in Chapter Five, to check the effect of magnetic field on the total output voltage. For further information about the samples, see Appendix 1. Figure 6-34 shows the relationship between the hybrid voltage and temperature difference at different magnetic flux densities for USB sample.

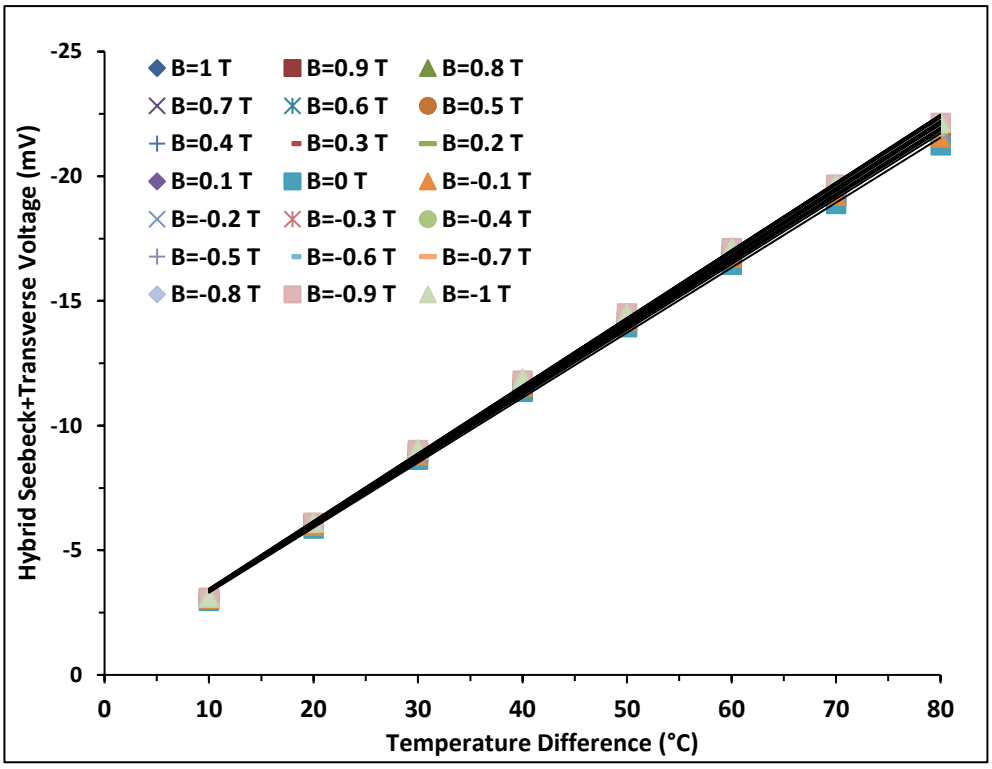

Figure 6- 34: Variation of the hybrid transverse voltage with temperature difference for various DC magnetic flux densities for USB sample.

The hybrid transverse voltage has negative values, and it increases significantly (in a negative direction) with increasing temperature difference for both magnetic field directions. It increases slightly with increasing the forward magnetic field until 0.8 T, then it decreases gradually. For the reverse magnetic field, the hybrid transverse voltage increases until 0.7 T and then decreases up to 1 T. The hybrid

transverse voltage is equal to the summation of the two parameters: Seebeck voltage and total transverse voltage. It cannot be fully understood without first understanding each parameter separately.

The values of the hybrid voltages are in full agreement with [6.12, 6.27] that confirmed that the obtained voltage was the summation of the Seebeck plus Nernst voltages.

The relationship between the hybrid voltages of all samples with temperature difference for different forward magnetic flux densities is shown in Figure 6-35.

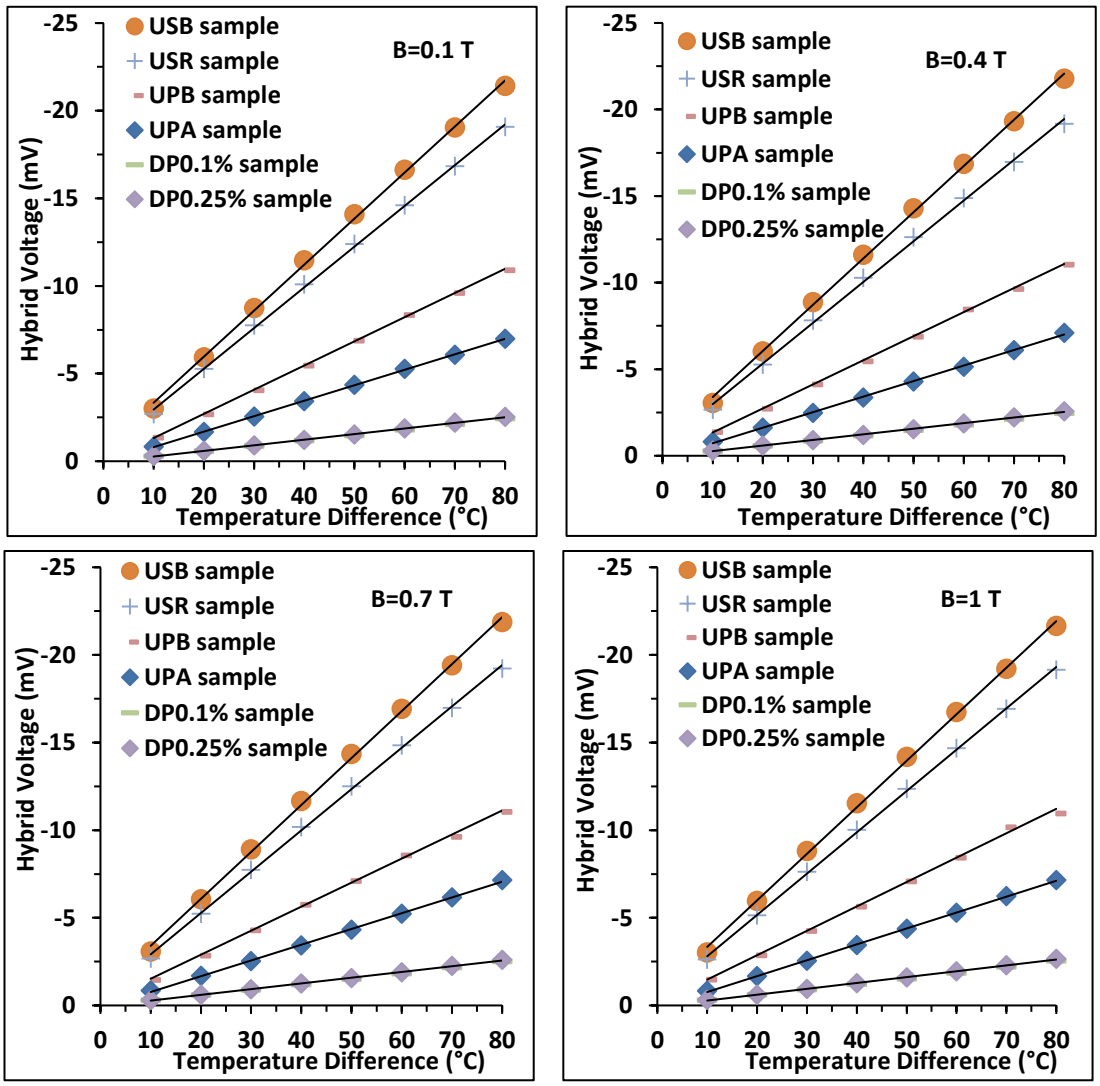

Figure 6- 35: Variation of the Hybrid voltage with temperature difference for various forward magnetic flux densities of all samples.

The behavior of all samples with rectangular shapes is as that for the Bridge shape, except the hybrid transverse voltage is approximately equal to the summation of the Seebeck voltage and half of the transverse voltage

The hybrid voltage for USR, UPB, UPA, DP0.1% and DP0.25% samples has the same behavior as that for USB sample with and without the applied magnetic field (at all magnetic flux densities). This behavior is similar to the behavior of the same samples regarding the Seebeck coefficient for the same reason related to each sample. For further information about the samples, see Appendix 16.

Figure 6-36 shows the relationship of the three parameters (Seebeck (V_s), total transverse (V_t) and hybrid transverse voltages (V_{s+t})) with the temperature difference.

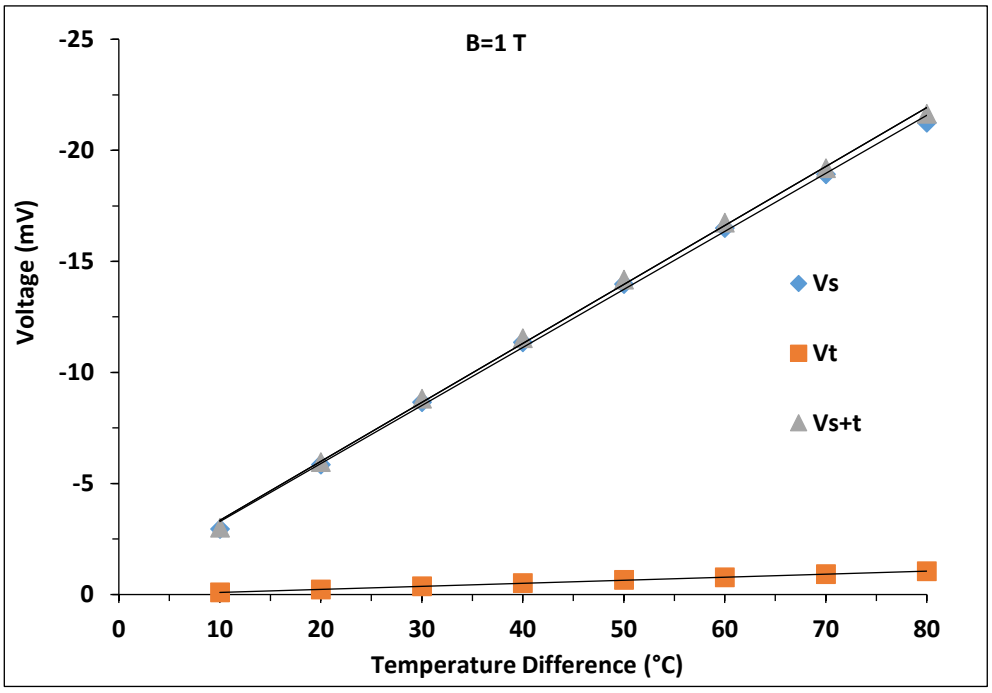

Figure 6- 36: Variation of the three parameters (Seebeck, total transverse, hybrid transverse voltages) with temperature difference for DC magnetic flux density 1T for USB sample.

It can be seen from Figure 6-33 that the behavior of hybrid voltage is similar to the behavior of Seebeck coefficient of all samples. It increases significantly (in a negative direction) with increasing temperature differences. For further information about the samples, see Appendices 1 and 17.

6.4: Results under the AC magnetic field

6.4.1: Measurement the magnetic flux density

A secondary winding of copper wire was used to measure the magnetic flux density of the core through the induction of magnetic flux. The copper wire was wound around one edge end as soon as possible. The electro motive force (e.m.f) is induced in the secondary coil or circuit. This effect occurs according to Faraday's first law (wherever the number of magnetic lines of force (flux) linking with a coil or circuit changes). It is known as electromagnetic induction and exists as long as the coil is linking the flux.

$$V = -\frac{d\varphi}{dt} = -\frac{d}{dt}\mathcal{N}\mathbb{A}B\cos(\omega t) = -\omega\mathcal{N}\mathbb{A}B_{max} \quad \text{.....(6.9)}$$

where: φ is the flux linkage= $\mathcal{N}\mathbb{A}B$; ω is the angular frequency ω=2πf; f is the frequency and $\mathcal{N}$ is the number of turns. The core flux B=B_{max}cos(ωt).

The r.m.s value of V (V_{peak}) is given by :

$$V = -\frac{2\pi f\mathcal{N}\mathbb{A}B}{\sqrt{2}} = -4.44f\mathcal{N}\mathbb{A}B \quad \text{.....(6.10)}$$

The magnetic flux density in air gap is dependent on the length of the air gap :

$$B = \frac{\mu_0\,\mathcal{N}I}{g} \quad \text{(for small gap ~ mm) .....(6.11)}$$

where: μ_0 is the permeability of free space; g is the air gap length. The above equation is for small gap only and will become more complicated for big gap. Figure 6-37 shows the relationship between the magnetic flux density and the AC current.

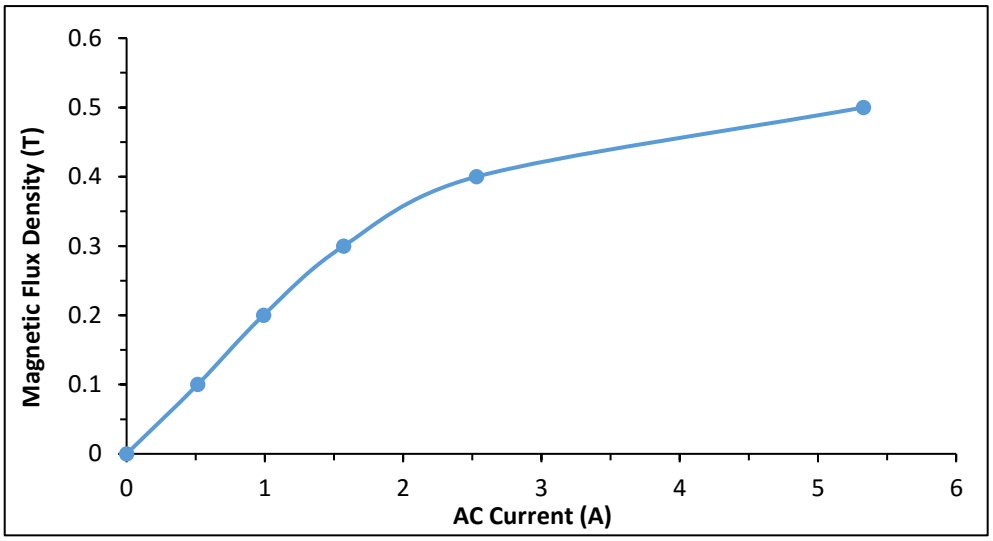

Figure 6- 37: Variation of the AC magnetic flux density with AC electrical current.

6.4.2: Transport coefficients

All samples measured in this section were under the AC magnetic field, and had rectangular shape.

The Seebeck coefficient for mean temperature difference 35 °C was calculated by measuring Seebeck voltage, as mentioned under DC magnetic field. This measurement utilized a DC voltmeter. To prevent the effect of the AC magnetic field on wires connected to the InSb to measure voltages, the magnetic shielding was used as illustrated in Chapter Five.

6.4.2.1: Seebeck coefficient under the magnetic field

USR sample was used to check the repeatability of the Seebeck coefficient under the AC magnetic field. The measurement was repeated four times. Figure 6-38 shows the standard deviation of the relationship between the Seebeck coefficient and the temperature difference under magnetic flux density of 0.1 and 0.5 T for USR sample.

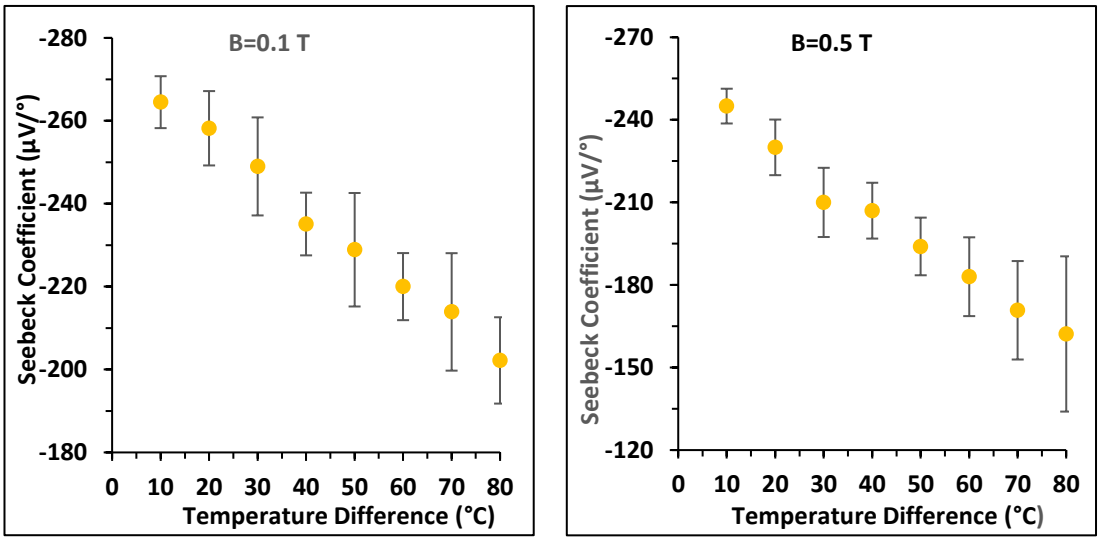

Figure 6- 38: The repeatability of the Seebeck coefficient for AC magnetic flux density 0.1 T and 0.5 T for USR sample.

Table 6-8 gives the maximum and minimum estimated values for Seebeck coefficient according to standard deviation under the DC magnetic field for USR sample.

Table 6- 8: The values of Seebeck coefficient under standard deviation for USR sample under the AC magnetic field.

0.1 T				
ΔT °C	$\hat{\delta}$ μV/°C	$\check{\delta}$ μV/°C	Standard deviation	Percentage
10	-270.76	-258.24	6.260125	4.8%
20	-268.914	-253.786	7.564211	5.9%
30	-266.108	-248.358	8.874991	7.1%
40	-260.189	-243.211	8.488657	6.9%
50	-256.57	-237.71	9.429804	7.9%
60	-251.806	-233.427	9.189188	7.8%
70	-248.24	-228.789	9.725773	8.5%
80	-243.757	-224.193	9.781985	8.7%
0.5 T				
ΔT °C	$\hat{\delta}$ μV/°C	$\check{\delta}$ μV/°C	Standard deviation	Percentage
10	-251.318	-238.682	6.317898	5.2%
20	-245.634	-229.366	8.13429	7.0%
30	-237.76	-218.907	9.42673	8.6%
40	-232.207	-213.793	9.206825	8.6%
50	-228.396	-206.004	11.19568	10.8%
60	-223.102	-199.898	11.6018	11.6%
70	-218.063	-196.165	10.94893	11.1%
80	-215.011	-192.989	11.01106	11.4%

The graphs above show that all standard deviations of all temperatures under 0.1 T are from 6.26 to 14.16 and for 0.5 T from 6.31 to 28.21 depending on temperature difference. They also show that the deviation among four tests is small, which indicates that the results are repeatable. The standard deviation of the Seebeck coefficient under the AC magnetic field is higher than that under the DC magnetic field for the same value. This might be due to the e.m.f induced in the wires (wires used to measure the Seebeck voltage) and the sample under the AC magnetic field. For further information about the samples, see Appendix 3.

The change in the direction of the magnetic field alters the polarity of the produced transverse voltage (Nernest and Righi-Leduc voltages). The frequency of the power supply was 50 Hz. This means that the effect of each Nernst or Righi-Leduc voltage will change the polarity with time (50 pulse per sec). Additionally, the e.m.f is induced in the wires (wires used to measure the Seebeck voltage) and the sample under the AC magnetic field. The high values for the standard deviation under magnetic field are due to the two reasons above.

The Seebeck coefficient for mean temperature difference 35 °C was calculated by measuring Seebeck voltage, as mentioned under DC magnetic field. Figure 6-39 shows the relationship between the Seebeck coefficient and the magnetic flux density for USR sample.

The Seebeck coefficient in Figure 6-39 has no noticeable change in value with increased magnetic flux density because the change is within the standard deviation.

The Seebeck coefficient shows the same behavior for USR sample as that of all other samples (UPB, UPA, DP0.1% and DP0.25%). The sample displays a lower value than that for the previous samples, apart from DP0.25% sample, which has a higher value than DP0.1% sample. This is due to the same reasons that were mentioned regarding the Seebeck coefficient of these samples in the absence of the magnetic field. For further information about the samples, see Appendix 18.

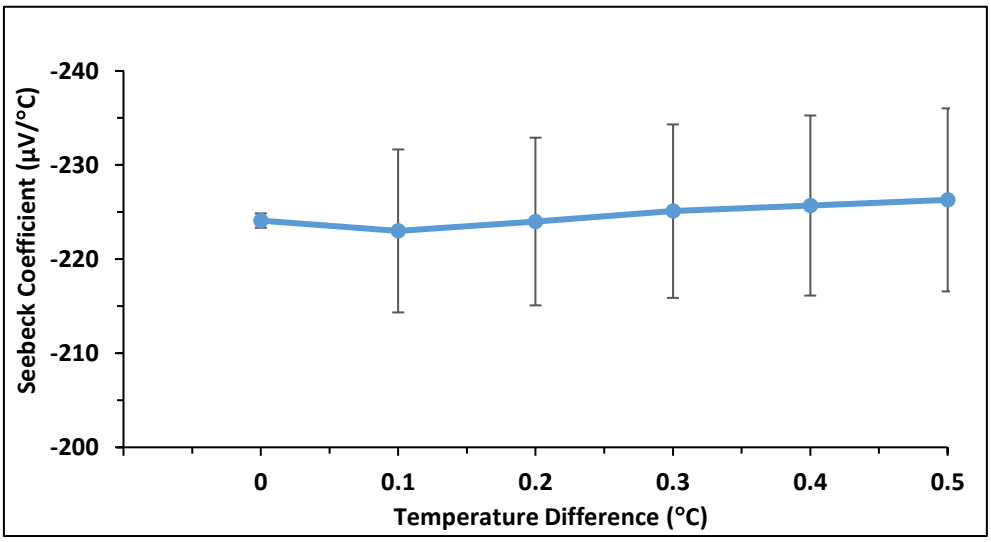

Figure 6- 39: Variation of the Seebeck coefficient with the AC magnetic flux density for USR sample.

6.4.2.2: voltage measured transversely under the magnetic field

The change in the direction of the magnetic field applied to the sample alters the direction of the transverse temperature difference produced by the Nernst and Righi-Leduc effects. The time over which the AC power supply changes its polarity is 0.01 sec. In contrast, the thermal lag times that were measured practically of the samples, as discussed previously, are between 8 sec and 10 sec. The sample cannot change the temperature difference direction within the 0.01 sec. This means that the Righi-Leduc effect can be dismissed. The misalignment voltage is not dependent on the magnetic field direction. The transverse voltage in this case is the sum of the Nernst voltage and the misalignment voltage.

There is an additional factor that contributes to the transverse voltage under the AC magnetic field. This is the voltage that is induced by the flux linkage in the leads and the sample according to Faraday's law:

$$e.m.f = -\mathcal{N}\frac{d\emptyset}{dt} \quad \text{.....(6.12)}$$

The magnetic shielding was also used in this measurement but unfortunately the induced voltage is still higher than Nernst voltage, so all the transverse voltage measured was related to induced voltage rather than Nernst voltage.

The voltage measured transversely (true r.m.s value by using AC voltmeter) was measured under the magnetic flux density of all samples. The comparison between the measurement of AC voltmeter and oscilloscope was made and the results were close to each other.

The voltage measured transversely is measured for USR sample under the magnetic flux density from 0 T to 0.5 T. Figure 6-40 shows the relationship between voltage measured transversely and the time required by the sample to reach a temperature difference of 80 °C under 0.1 T.

Figure 6-41 shows the voltage measured transversely for USR sample as a function of the time required by the sample to reach a temperature difference of 80 °C for different magnetic flux densities. The voltage measured transversely in Figure 6-41 fluctuates slightly with increased time, while the temperature increases at all magnetic flux densities. This is due to fluctuations in both the Nernst voltage and the electromagnetic induction. For further information about the samples, see Appendix 19.

To identify that a large part of the voltage measured transversely is due to the electromagnetic induction, a comparison between copper wire and USR sample was made under the same conditions. Both samples produce similar voltage measured transversely as illustrated in Table 6-6, due to the independence of the electromagnetic induction of the materials.

Table 6-9 explains that the voltage measured transversely for both samples is very close. This means the electromagnetic induction is the maximum part of the voltage measured transversely in terms of both voltage and fluctuation. This part is independent of temperature gradient. The other part is the Nernst voltage, which is dependent on the material having minimum value and fluctuation. For this reason the above results do not vary significantly with increasing the temperature difference.

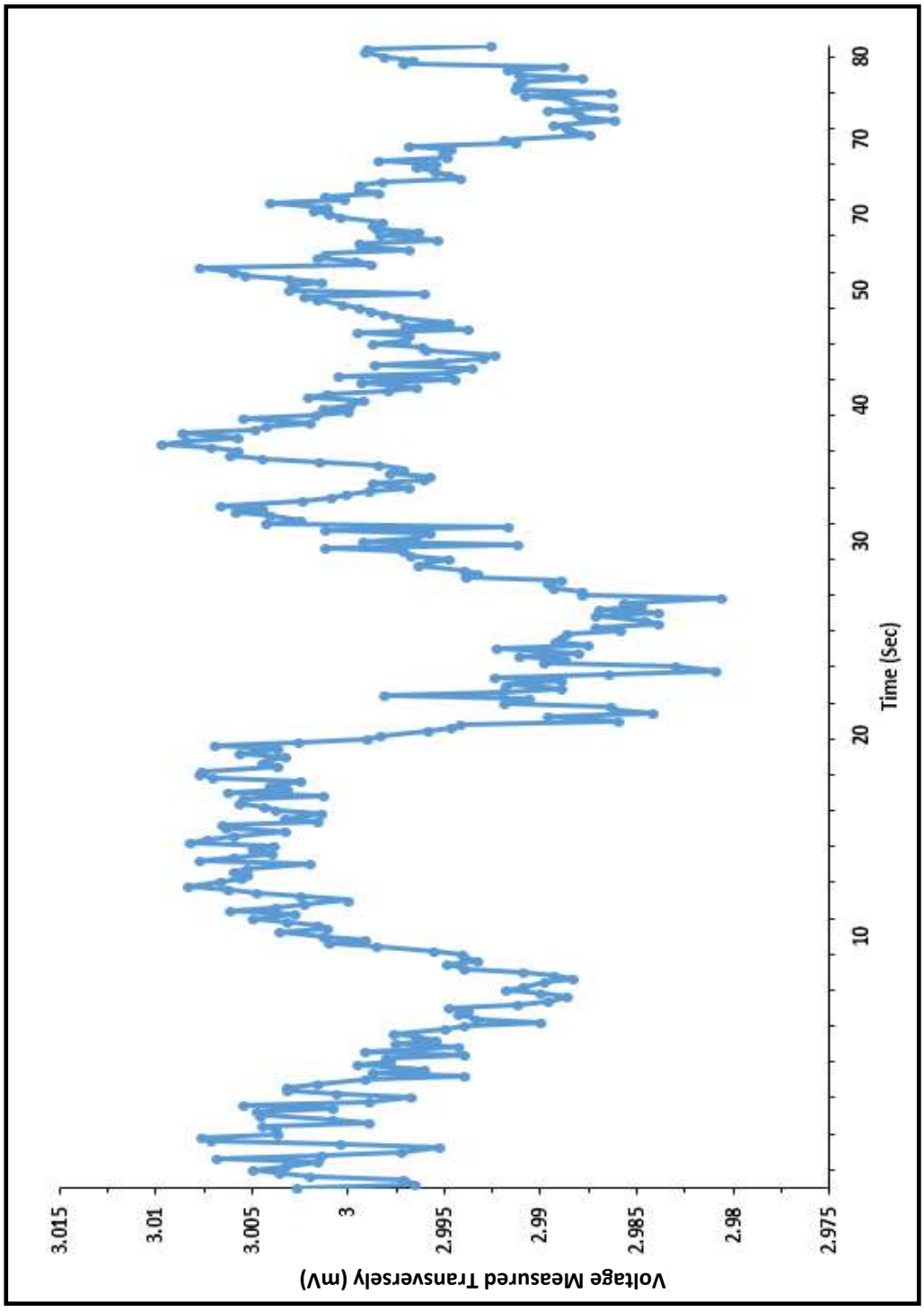

Figure 6- 40: Variation of the voltage measured transversely with time for AC magnetic flux density 0.1T for USR sample.

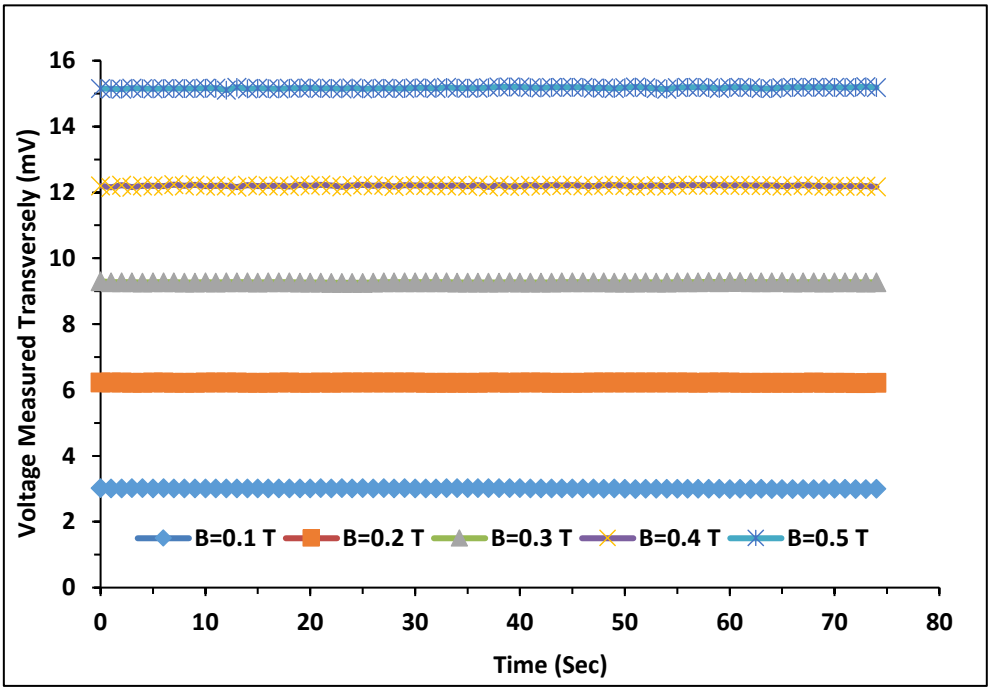

Figure 6- 41: Variation of the voltage measured transversely with time for various AC magnetic flux densities for USR sample.

Table 6-9 : Comparison of transverse voltage between USR sample and copper wire.

Magnetic Flux Density (T)	Sample	voltage measured transversely (mV)
0.1	USR	3.029
	Copper wire	3.220
0.2	USR	6.23
	Copper wire	6.490
0.3	USR	9.273
	Copper wire	9.628
0.4	USR	12.196
	Copper wire	12.834
0.5	USR	15.154
	Copper wire	16.278

References

[6.1] a. a. Ebnalwaled, "Evolution of growth and enhancement in power factor of InSb bulk crystal," *J. Cryst. Growth*, vol. 311, no. 19, pp. 4385–4390, 2009.

[6.2]] D. B. Gadkari, "Detached growth in the vertical directional solidification technique : Progress in quality of the bulk InSb crystals on earth," *Int. J. Sci. Res. Publ*., vol. 4, no. 5, 2014.

[6.3 D. B. Gadkari, K. B. Lal, and B. M. Arora, "Growth of undoped and Te doped InSb crystals by vertical directional solidification technique," *Bull. Mater. Sci*., vol. 21, no. 2, pp. 127–131, Apr. 1998.

[6.4] S. R. Vishwakarma, a. K. Verma, R. S. N. Tripathi, S. Das, and Rahul, "Study of structural property of n-type indium antimonide thin films," *Indian J. Pure Appl. Phys*., vol. 50, no. 5, pp. 339–346, 2012.

[6.5] http://www.powerstream.com/vapor-pressure.htm.

[6.6] A. Ebnalwaled, "Hopping conduction and dielectric properties of InSb bulk crystal," *Ijens.Org*, vol. 11, no. 6, pp. 194–207, 2011.

[6.7] https://webcache.googleusercontent.com/search?q=cache:6ebn8mTZZzQJ:https://www.boconline.co.uk/internet.lg.lg.gbr/en/images/tg-8303-argon-v1.3410_39591.pdf%3Fv%3D3.0+&cd=1&hl=en&ct=clnk&gl=uk

[6.8] Z. Saglam, S. B. Bayram, and M. Saglam, "A Dependence of Crystallinity of In_2O_3 Thin Films by a Two-Step Heat Treatment of Indium Films on the Heating Atmosphere," *J. Mod. Phys.*, vol. 01, no. 06, pp. 360–363, 2010.

[6.8] H. Nakamura, K. Ikeda, and S. Yamaguchi, "Transport coefficients of InSb in a strong magnetic field," *XVI ICT "97. Proc. ICT"97. 16th Int. Conf. Thermoelectr. (Cat. No.97TH8291)*, no. 1, pp. 1–6, 1997.

[6.9] H. Nakamura, K. Ikeda, and S. Yamaguchi, "Physical model of Nernst element," *in Seventeenth International Conference on Thermoelectrics. Proceedings ICT98 (Cat. No.98TH8365)*, 1998, no. 7, pp. 97–100.

[6.10] K. Ikeda, H. Nakamura, and S. Yamaguchi, "Geometric contribution to the measurement of thermoelectric power and Nernst coefficient in a strong magnetic field," *in XVI ICT "97. Proceedings ICT"97. 16th International Conference on Thermoelectrics (Cat. No.97TH8291)*, 1997, no. 6, pp. 155–158.

[6.11] H. Okumura, S. Yamaguchi, H. Nakamura, K. Ikeda, and K. Sawada, "Numerical computation of thermoelectric and thermomagnetic effects," *in Seventeenth International Conference on Thermoelectrics. Proceedings ICT98 (Cat. No.98TH8365)*, 1998, pp. 10–13.

[6.12] S. Yamaguchi, K. Ikeda, H. Nakamura, K. Kuroda, and O. Motojima, "A fusion study of thermoelectric conversion in magnetic fields," *Fusion Eng. Des*., vol. 41, no. 1–4, pp. 555–559, 1998.

[6.13] H. Nakamura, K. Ikeda, and S. Yamaguchi, "Transport Coefficients of Indium Antimonide in a Magnetic Field," *Jpn. J. Appl. Phys*., vol. 38, no. Part 1, No. 10,

pp. 5745–5749, Oct. 1999.

[6.14] M. R. El-Saden and F. W. Thomas, "Nernst effect in indium antimonide," *J. Appl. Phys*., vol. 36, no. 1, pp. 181–183, 1965.

[6.15] K. Ikeda, H. Nakamura, and S. Yamaguchi, "Geometric contribution to the measurement of thermoelectric power and Nernst coefficient in a strong magnetic field," *in XVI ICT "97. Proceedings ICT"97. 16th International Conference on Thermoelectrics (Cat. No.97TH8291)*, 1997, no. 6, pp. 155–158.

[6.16] H. NAKAMURA, K. IKEDA, S. YAMAGUCHI, and K. KURODA, "Transport coefficients of thermoelectric semiconductor InSb-a candidate for the Nernst element.," *Journal of Advanced Science*, vol. 8, no. 3/4. pp. 153–157, 1996.

[6.17] K. IKEDA, H. NAKAMURA, S. YAMAGUCHI, and K. KURODA, "Measurement of transport properties of thermoelectric materials in the magnetic field.," *Journal of Advanced Science*, vol. 8, no. 3/4. pp. 147–152, 1996.

[618] T. M. Tritt and M. A. Subramanian, "Thermoelectric Materials, Phenomena, and Applications: A Bird's Eye View," *MRS Bull*., vol. 31, no. 03, pp. 188–198, Mar. 2006.

[6.19] R. W. J. Ure, "Theory of materials for thermoelectric and thermomagnetic devices," *Proc. IEEE*, vol. 51, no. 5, 1963.

[6.20] G. J. Snyder and E. S. Toberer, "Complex thermoelectric materials.," *Nat. Mater*., vol. 7, no. 2, pp. 105–114, 2008.

[6.21] R. C. Sharma, *Principles of heat treatment of steels*. New Age International, 2003.

[6.22] K. H. Prabhudev, *Handbook of Heat Treatment of Steels*. Tata McGraw-Hill Education, 1988.

[6.23] D. M. Rowe, *CRC Handbook of thermoelectrics*. 1995.

[6.24] H. Nakamura, K. Ikeda, and S. Yamaguchi, "Transport property and energy conversion of nernst elements in strong magnetic field," *Nippon Kinzoku Gakkaishi/Journal Japan Inst. Met.*, vol. 61, no. 12, pp. 1318–1325, 1997.

[6.25] G. Sareminia, F. Zahedi, S. Eminov, and A. Karamian, "Cleaning method of InSb [1̄1̄1] B of n-InSb [111] A/B for the growth of epitaxial layers by liquid phase epitaxy," *J. Semicond*., vol. 32, no. 5, p. 056001, May 2011.Intermetallic Semiconducting Films, H. H. Wieder, Corona, California, first edition, 1970.

[6.26] M. Hamabe, S. Yamamoto, S. Yamaguchi, H. Takahashi, H. Okumura, I. Yonenaga, T. Sasaki, and K. Watanabe, "Magnetic field effect for improvement of thermoelectric conversion: A proposal for Nernst-Seebeck element," *Proc. ICT'03. 22nd Int. Conf. Thermoelectr. (IEEE Cat. No.03TH8726)*, pp. 567–570, 2003.

CHAPTER 7

Conclusions & Future Work

7.1: Conclusions

The main aim of the research in this thesis was to enhance the harvesting of waste heat under magnetic field environment. This study has shed light on the processes involved in enhancing the output power of thermomagnetic materials. The main conclusions are:

1- Establish simple and effective material synthesis facilities and procedures, which are based on open quartz tube inside a niobium container, because the traditional way requires a glass blower to seal the quartz tube. A novel feature in this procedure is using open quartz tube inside a niobium container and the latter inside chamber. This technique owing to conserve the tube under inert gas environment and to keep the quartz tube vertically inside the furnace. The time and temperature of the furnace were controlled at optimum values. This procedures proved to be successful for synthesis of pure undoped and doped InSb materials with Te at different doping level of 0.1% and 0.25%.

2- The In/Sb ratio was identified the production material, whether it is stoichiometric or has excess of In or Sb. In this thesis the preparation of pure

InSb off-stoichiometric was achieved successfully by utilizing the optimum In/Sb ratio (1:(1.06+0.0481)). The XRD and EDX analysis confirmed these results.

3- The annealing process changes the physical properties of a material such as grain size refinement. Reducing of the cooling rate during the fabrication process of undoped polycrystalline InSb, improves the arrangement of atoms in lattice site and increasing crystal size, Figure 6-11 confirmed this result. This increment in crystal size will increase the conductivity and then enhance the thermomagnetic parameters.

4- Reducing the Seebeck coefficient and electrical resistivity and increasing the Nernst, Righi-Leduc voltages and thermomagnetic power of the materials have been achieved by controlling the In/Sb ratio off stoichiometric and by doping the samples with Te. The samples examined were of dimensions $12 \times 3 \times 1$ mm^3 and produced the results below for temperature difference of 80 °C and under a DC magnetic field of 1 T: resistivity reduced by around 45%, Seebeck coefficient reduced by around 7%, Nernst voltage increased by around 0.69%, Righi-Leduc voltage increased by around 1.36% and thermomagnetic power increased around 2.08%. These results indicate that the carrier concentration is increased. The cation vacancies have been increased with increasing doping level (increasing the doping level of Te from 0.1% to 0.25%). If the two charge carrier concentrations (electron and hole) approach to be close to each other, the Nernst voltage and thermomagnetic power will be increased.

5- The enhancement of Nernst, Righi-Leduc voltages and thermomagnetic power have been achieved by increasing the applied magnetic field due to the enlargement in the Lorentz force and temperature difference for all samples. In addition, the number of charge carriers and their thermal energy which are excited thermally, increase with increasing temperature difference.

The different behaviour of Nernst, Righi-Leduc voltages and thermomagnetic power between temperature differences from 10 °C to 30 °C for all magnetic flux density need further investigation for more clarifications.

6- The Righi-Leduc voltage reduces the output voltage due to its opposite polarity with Nernst voltage. To maximise the output voltage, the Righi-Leduc voltage should be minimised. This process has been utilized in this thesis by using AC magnetic field due to the changing in its polarity with time.

7- Attempts have been made to decrease the Righi-Leduc voltage and then maximise the output voltage by using AC magnetic field. Unfortunately, the induced voltage in the wires connected to sample caused an error in measurements of the output voltage. The induced voltage remained high despite attempts were made to minimise it through shielding.

7.2: Future work

This study has also highlighted several potential areas which warrant further investigation to be carried out in the future.

1- The experimental results indicate that thermomagnetic parameters (Nernst, Righi-Leduc voltages and thermomagnetic power) for Bridge shape was higher than that for rectangular shape of undoped single crystalline sample. Further works are required to make bigger samples (undoped and doped with Te of different doping levels) to be more consistent with the Bridge shape.

2- The minimising of Righi-Leduc voltage is the main factor to increase the output voltage from thermomagnetic material. Further Investigation is required to minimise the induced voltage which induced by AC magnetic field and then measuring the transverse voltage.

3- If there is a success in minimising the induced voltage, further research will be required to measure the hybrid transverse (Seebeck + total transverse) voltages under AC magnetic field. The hybrid voltage will be increased due to the minimised Righi-Leduc voltage.

4- The experimental results also indicate that doping with Te enhances the thermomagnetic power and Nernst voltage. Further Investigation is required to check the effect of increasing the doping level. The doping levels should be used from 0.1 % to 0.5 % in increments of 0.05 %. The optimum value of the doping ratio, which gives maximum thermomagnetic power and highest Nernst voltage, could then be obtained. In this way the study cover wider scope.

5- Further investigations are required to explain the behaviour of Nernst and Righi-Leduc voltages, Nernst coefficient and thermomagnetic power with temperature differences between 10 °C and 30°C under all magnetic flux densities. In addition to, the behaviour of same parameters under magnetic field of 0.1 T with various temperature difference.

6- The experimental results indicate that doping with Te enhances the Righi-Leduc voltage. The Righi-Leduc effect should decrease with increasing both charge carriers. Further researches are required to explain the increasing Righi-Leduc voltages when the materials has both charge carriers.

7- Further studies are required to check the effect of doping with another material such as Sn with different doping levels. Then check the optimum value to get maximum enhancement of the output voltage.

Appendix 1:

The Seebeck, transverse and hybrid transvers voltages for USB sample for various temperature differences and magnetic flux densities.

B (T) \ ΔT (°C)		10	20	30	40	50	60	70	80
1	V_s	-2.955	-5.848	-8.657	-11.35	-13.97	-16.49	-18.92	-21.24
	V_t	-0.100	-0.223	-0.367	-0.510	-0.654	-0.774	-0.920	-1.049
	V_{s+t}	-3.014	-5.956	-8.810	-11.536	-14.173	-16.738	-19.200	-21.641
0.9	V_s	-2.94	-5.785	-8.572	-11.27	-13.9	-16.46	-18.95	-21.37
	V_t	-0.094	-0.217	-0.339	-0.480	-0.622	-0.759	-0.880	-1.022
	V_{s+t}	-2.987	-5.873	-8.741	-11.400	-14.186	-16.849	-19.191	-21.723
0.8	V_s	-3.031	-5.956	-8.801	-11.52	-14.18	-16.76	-19.22	-21.6
	V_t	-0.092	-0.202	-0.316	-0.447	-0.578	-0.726	-0.865	-0.972
	V_{s+t}	-3.081	-6.070	-8.939	-11.712	-14.391	-16.980	-19.472	-21.895
0.7	V_s	-2.99	-5.887	-8.706	-11.44	-14.09	-16.67	-19.15	-21.52
	V_t	-0.100	-0.206	-0.331	-0.462	-0.599	-0.682	-0.844	-0.939
	V_{s+t}	-3.074	-6.047	-8.905	-11.655	-14.346	-16.910	-19.408	-21.860
0.6	V_s	-3.003	-5.901	-8.744	-11.45	-14.10	-16.67	-19.14	-21.54
	V_t	-0.093	-0.184	-0.304	-0.434	-0.529	-0.641	-0.751	-0.877
	V_{s+t}	-3.066	-6.022	-8.896	-11.666	-14.352	-16.941	-19.474	-21.818
0.5	V_s	-3.024	-5.952	-8.797	-11.52	-14.17	-16.7	-19.11	-21.42
	V_t	-0.074	-0.182	-0.266	-0.369	-0.514	-0.626	-0.732	-0.803
	V_{s+t}	-3.057	-6.068	-8.911	-11.682	-14.302	-16.881	-19.38	-21.796
0.4	V_s	-3.005	-5.936	-8.755	-11.47	-14.12	-16.66	-19.15	-21.56
	V_t	-0.085	-0.171	-0.274	-0.377	-0.473	-0.556	-0.695	-0.801
	V_{s+t}	-3.059	-6.028	-8.880	-11.621	-14.290	-16.868	-19.329	-21.783
0.3	V_s	-2.998	-5.911	-8.737	-11.45	-14.08	-16.64	-19.11	-21.54
	V_t	-0.082	-0.166	-0.236	-0.318	-0.427	-0.520	-0.552	-0.657
	V_{s+t}	-3.043	-5.993	-8.851	-11.581	-14.298	-16.803	-19.462	-21.827
0.2	V_s	-2.94	-5.82	-8.622	-11.35	-13.98	-16.53	-18.98	-21.33
	V_t	-0.070	-0.144	-0.216	-0.287	-0.360	-0.446	-0.501	-0.570
	V_{s+t}	-3.047	-5.965	-8.801	-11.536	-14.158	-16.676	-19.137	-21.516
0.1	V_s	-2.945	-5.813	-8.592	-11.28	-13.89	-16.40	-18.83	-21.17
	V_t	-0.073	-0.127	-0.195	-0.269	-0.325	-0.393	-0.468	-0.533
	V_{s+t}	-3.007	-5.915	-8.729	-11.452	-14.078	-16.620	-19.030	-21.409

0	V_s	-2.955	-5.827	-8.579	-11.26	-13.83	-16.29	-18.68	-21
	V_t	-0.030	-0.090	-0.165	-0.203	-0.250	-0.350	-0.406	-0.485
	V_{s+t}	-2.970	-5.872	-8.6415	-11.363	-13.957	-16.452	-18.892	-21.242
-0.1	V_s	-3.023	-5.931	-8.73	-11.43	-14.04	-16.56	-18.99	-21.35
	V_t	0.008	-0.032	-0.094	-0.164	-0.222	-0.253	-0.331	-0.410
	V_{s+t}	-3.054	-5.986	-8.816	-11.569	-14.202	-16.739	-19.225	-21.559
-0.2	V_s	-3.031	-5.954	-8.785	-11.51	-14.15	-16.70	-19.15	-21.51
	V_t	0.005	-0.027	-0.059	-0.099	-0.149	-0.224	-0.298	-0.354
	V_{s+t}	-3.050	-6.040	-8.887	-11.658	-14.305	-16.894	-19.378	-21.786
-0.3	V_s	-3.021	-5.956	-8.802	-11.55	-14.20	-16.77	-19.25	-21.64
	V_t	0.003	-0.019	-0.046	-0.074	-0.153	-0.218	-0.262	-0.331
	V_{s+t}	-3.088	-6.05	-8.939	-11.708	-14.362	-16.959	-19.46	-21.944
-0.4	V_s	-3.02	-5.967	-8.822	-11.58	-14.25	-16.82	-19.29	-21.67
	V_t	0.003	0.007	-0.02	-0.063	-0.107	-0.164	-0.22	-0.283
	V_{s+t}	-3.092	-6.1	-8.988	-11.791	-14.496	-17.064	-19.572	-22.017
-0.5	V_s	-3.035	-5.975	-8.822	-11.58	-14.25	-16.83	-19.31	-21.71
	V_t	0.017	0.006	0.003	-0.031	-0.089	-0.124	-0.173	-0.215
	V_{s+t}	-3.111	-6.113	-9.003	-11.804	-14.496	-17.13	-19.648	-22.109
-0.6	V_s	-3.015	-5.951	-8.796	-11.55	-14.23	-16.81	-19.31	-21.71
	V_t	0.025	0.03	0.004	0.006	-0.041	-0.076	-0.122	-0.169
	V_{s+t}	-3.1	-6.126	-9.004	-11.828	-14.538	-17.139	-19.666	-22.154
-0.7	V_s	-3.048	-6.01	-8.878	-11.65	-14.33	-16.91	-19.39	-21.76
	V_t	0.022	0.028	0.012	0.004	-0.042	-0.061	-0.108	-0.163
	V_{s+t}	-3.116	-6.123	-9.018	-11.829	-14.548	-17.152	-19.688	-22.168
-0.8	V_s	-3.028	-5.977	-8.834	-11.60	-14.27	-16.85	-19.34	-21.75
	V_t	0.012	0.028	0.023	0.002	-0.04	-0.058	-0.116	-0.138
	V_{s+t}	-3.101	-6.113	-9.011	-11.788	-14.528	-17.146	-19.686	-22.159
-0.9	V_s	-3.027	-5.969	-8.823	-11.57	-14.24	-16.82	-19.32	-21.74
	V_t	0.015	0.034	0.026	0.016	-0.011	-0.054	-0.101	-0.136
	V_{s+t}	-3.109	-6.109	-9.017	-11.809	-14.511	-17.126	-19.671	-22.141
-1	V_s	-3.033	-5.969	-8.829	-11.58	-14.25	-16.82	-19.31	-21.72
	V_t	0.019	0.037	0.029	0.022	0.008	-0.023	-0.047	-0.084
	V_{s+t}	-3.119	-6.118	-9.058	-11.898	-14.505	-17.137	-19.708	-22.142

The Seebeck, transverse and hybrid transvers voltages for USR sample for various temperature differences and magnetic flux densities.

B (T) \ ΔT (°C)		10	20	30	40	50	60	70	80
1	V_s	-2.454	-4.853	-7.197	-9.488	-11.72	-13.91	-16.05	-18.14
	V_t	-0.158	-0.295	-0.424	-0.539	-0.647	-0.744	-0.827	-0.912
	V_{s+t}	-2.617	-5.137	-7.617	-10.01	-12.349	-14.663	-16.913	-19.15
0.7	V_s	-2.527	-4.984	-7.365	-9.68	-11.92	-14.1	-16.21	-18.27
	V_t	-0.15	-0.281	-0.398	-0.511	-0.61	-0.694	-0.779	-0.861
	V_{s+t}	-2.676	-5.233	-7.73	-10.174	-12.502	-14.826	-16.973	-19.211
0.4	V_s	-2.55	-5.032	-7.442	-9.781	-12.04	-14.24	-16.37	-18.44
	V_t	-0.117	-0.221	-0.316	-0.404	-0.49	-0.574	-0.638	-0.696
	V_{s+t}	-2.668	-5.273	-7.828	-10.275	-12.627	-14.883	-16.984	-19.177
0.1	V_s	-2.596	-5.11	-7.55	-9.886	-12.16	-14.31	-16.37	-18.36
	V_t	-0.089	-0.181	-0.265	-0.341	-0.41	-0.473	-0.517	-0.565
	V_{s+t}	-2.685	-5.269	-7.755	-10.08	-12.386	-14.595	-16.82	-19.065
0	V_s	-2.699	-5.284	-7.753	-10.09	-12.32	-14.44	-16.44	-18.32
	V_t	-0.079	-0.151	-0.215	-0.27	-0.32	-0.364	-0.4	-0.441
	V_{s+t}	-2.7769	-5.436	-7.985	-10.318	-12.539	-14.858	-16.826	-18.777
-0.1	V_s	-2.684	-5.264	-7.738	-10.08	-12.32	-14.46	-16.47	-18.36
	V_t	-0.077	-0.145	-0.206	-0.27	-0.321	-0.366	-0.407	-0.451
	V_{s+t}	-2.718	-5.33	-7.832	-10.229	-12.562	-14.865	-16.796	-18.697
-0.4	V_s	-2.628	-5.163	-7.618	-9.982	-12.26	-14.45	-16.54	-18.55
	V_t	-0.059	-0.114	-0.163	-0.222	-0.267	-0.32	-0.366	-0.409
	V_{s+t}	-2.72	-5.298	-7.786	-10.195	-12.468	-14.688	-16.887	-19.129
-0.7	V_s	-2.596	-5.1	-7.506	-9.825	-12.08	-14.24	-16.35	-18.38
	V_t	-0.021	-0.049	-0.08	-0.112	-0.157	-0.197	-0.255	-0.309
	V_{s+t}	-2.618	-5.15	-7.586	-9.937	-12.199	-14.381	-16.616	-18.88
-1	V_s	-2.55	-5.031	-7.414	-9.734	-11.98	-14.16	-16.27	-18.28
	V_t	0.01	0.01	0.004	-0.006	-0.018	-0.045	-0.071	-0.088
	V_{s+t}	-2.523	-4.934	-7.276	-9.56	-11.797	-14.056	-16.285	-18.384

The Seebeck, transverse and hybrid transvers voltages for UPB sample for various temperature differences and magnetic flux densities.

ΔT (°C) / B (T)		10	20	30	40	50	60	70	80
1	V_s	-1.290	-2.594	-3.912	-5.248	-6.602	-7.971	-9.358	-10.764
	V_t	-0.181	-0.245	-0.287	-0.329	-0.373	-0.425	-0.476	-0.535
	V_{s+t}	-1.4635	-2.8471	-4.2354	-5.6246	-7.0731	-8.4254	-9.9854	-11.145
0.9	V_s	-1.293	-2.600	-3.923	-5.261	-6.615	-7.985	-9.3758	-10.782
	V_t	-0.164	-0.222	-0.264	-0.308	-0.356	-0.404	-0.455	-0.51
	V_{s+t}	-1.4529	-2.8244	-3.8574	-5.551	-6.9961	-8.3757	-9.7318	-11.144
0.8	V_s	-1.295	-2.605	-3.928	-5.271	-6.630	-8.005	-9.3969	-10.804
	V_t	-0.148	-0.204	-0.249	-0.292	-0.338	-0.389	-0.441	-0.493
	V_{s+t}	-1.4245	-2.8048	-4.1598	-5.5637	-6.9565	-8.3648	-9.7254	-11.351
0.7	V_s	-1.298	-2.609	-3.935	-5.275	-6.632	-8.003	-9.3893	-10.788
	V_t	-0.137	-0.193	-0.237	-0.277	-0.321	-0.371	-0.425	-0.478
	V_{s+t}	-1.4424	-2.8428	-4.2809	-5.7304	-7.0815	-8.5531	-9.6082	-11.043
0.6	V_s	-1.295	-2.606	-3.931	-5.268	-6.621	-7.991	-9.3780	-10.777
	V_t	-0.118	-0.179	-0.224	-0.265	-0.311	-0.359	-0.414	-0.464
	V_{s+t}	-1.3872	-2.7674	-4.1481	-5.5555	-7.0268	-8.3437	-9.7	-11.123
0.5	V_s	-1.290	-2.596	-3.915	-5.248	-6.6	-7.965	-9.3508	-10.752
	V_t	-0.106	-0.159	-0.203	-0.249	-0.292	-0.347	-0.399	-0.446
	V_{s+t}	-1.3826	-2.7305	-4.1305	-5.5813	-6.919	-8.2837	-9.7168	-11.081
0.4	V_s	-1.294	-2.602	-3.925	-5.265	-6.619	-7.985	-9.3655	-10.765
	V_t	-0.095	-0.142	-0.19	-0.233	-0.273	-0.324	-0.374	-0.421
	V_{s+t}	-1.3635	-2.723	-4.1185	-5.4636	-6.8824	-8.4516	-9.644	-11.049
0.3	V_s	-1.296	-2.607	-3.932	-5.273	-6.628	-8.001	-9.388	-10.795
	V_t	-0.082	-0.128	-0.173	-0.214	-0.254	-0.303	-0.351	-0.4
	V_{s+t}	-1.3358	-2.6715	-4.0685	-5.4880	-6.9195	-8.3444	-9.601	-11.129
0.2	V_s	-1.295	-2.604	-3.928	-5.265	-6.622	-7.997	-9.3929	-10.808
	V_t	-0.069	-0.113	-0.158	-0.197	-0.24	-0.283	-0.341	-0.392
	V_{s+t}	-1.3115	-2.6738	-4.0454	-5.4053	-6.7996	-8.2062	-9.6464	-11.035
0.1	V_s	-1.298	-2.611	-3.941	-5.285	-6.640	-8.011	-9.3958	-10.796
	V_t	-0.053	-0.091	-0.129	-0.169	-0.212	-0.261	-0.317	-0.379
	V_{s+t}	-1.3331	-2.6704	-4.0476	-5.4485	-6.8698	-8.3381	-9.5997	-10.897

0	V_s	-1.299	-2.610	-3.933	-5.270	-6.622	-7.9901	-9.375	-10.777
	V_t	-0.021	-0.045	-0.085	-0.127	-0.153	-0.205	-0.27	-0.357
	V_{s+t}	-1.3115	-2.6485	-4.0075	-5.4355	-6.9055	-8.3495	-9.654	-11.040
-0.1	V_s	-1.291	-2.598	-3.922	-5.260	-6.620	-7.9916	-9.379	-10.781
	V_t	-0.019	-0.044	-0.075	-0.111	-0.145	-0.193	-0.264	-0.345
	V_{s+t}	-1.2373	-2.5043	-3.8305	-5.17	-6.5811	-8.0551	-9.5569	-11.054
-0.2	V_s	-1.293	-2.600	-3.922	-5.258	-6.611	-7.9773	-9.362	-10.758
	V_t	-0.017	-0.042	-0.066	-0.101	-0.139	-0.189	-0.258	-0.335
	V_{s+t}	-1.2291	-2.4955	-3.8187	-5.1798	-6.6013	-8.064	-9.5354	-11.009
-0.3	V_s	-1.294	-2.600	-3.921	-5.258	-6.607	-7.9764	-9.357	-10.753
	V_t	-0.014	-0.039	-0.058	-0.091	-0.13	-0.182	-0.252	-0.315
	V_{s+t}	-1.2476	-2.5045	-3.804	-5.2059	-6.5555	-7.9856	-9.4561	-10.963
-0.4	V_s	-1.295	-2.605	-3.931	-5.273	-6.629	-7.9991	-9.383	-10.783
	V_t	-0.011	-0.036	-0.051	-0.083	-0.121	-0.175	-0.242	-0.297
	V_{s+t}	-1.24	-2.5476	-3.903	-5.2741	-6.6868	-8.127	-9.5712	-11.031
-0.5	V_s	-1.294	-2.602	-3.924	-5.265	-6.620	-7.9862	-9.370	-10.773
	V_t	-0.008	-0.029	-0.042	-0.075	-0.112	-0.165	-0.221	-0.282
	V_{s+t}	-1.157	-2.4393	-3.7748	-5.1866	-6.6217	-8.1149	-9.5983	-11.096
-0.6	V_s	-1.293	-2.605	-3.933	-5.278	-6.638	-8.0097	-9.394	-10.790
	V_t	-0.006	-0.018	-0.029	-0.063	-0.099	-0.149	-0.205	-0.269
	V_{s+t}	-1.1765	-2.4241	-3.7224	-5.1362	-6.589	-8.0707	-9.555	-11.068
-0.7	V_s	-1.297	-2.608	-3.933	-5.270	-6.623	-7.991	-9.371	-10.762
	V_t	-0.004	-0.011	-0.02	-0.049	-0.085	-0.13	-0.191	-0.251
	V_{s+t}	-1.1413	-2.345	-3.624	-5.0195	-6.4722	-7.9504	-9.5644	-11.066
-0.8	V_s	-1.296	-2.61	-3.936	-5.277	-6.629	-8.0018	-9.389	-10.789
	V_t	-0.002	-0.004	-0.008	-0.037	-0.069	-0.115	-0.173	-0.238
	V_{s+t}	-1.154	-2.374	-3.6595	-5.0402	-6.4819	-7.9738	-9.6057	-11.016
-0.9	V_s	-1.297	-2.608	-3.933	-5.271	-6.622	-7.9880	-9.369	-10.767
	V_t	0.002	0.004	-0.002	-0.028	-0.059	-0.102	-0.158	-0.22
	V_{s+t}	-1.1344	-2.3718	-3.6561	-5.0579	-6.5219	-7.9764	-9.49	-10.971
-1	V_s	-1.299	-2.612	-3.938	-5.277	-6.628	-7.9913	-9.366	-10.752
	V_t	0.01	0.01	0.005	-0.015	-0.043	-0.086	-0.141	-0.2
	V_{s+t}	-1.1385	-2.365	-3.6868	-5.1421	-6.5044	-7.9837	-9.4939	-11.048

The Seebeck, transverse and hybrid transvers voltages for UPA sample for various temperature differences and magnetic flux densities.

B (T) \ ΔT (°C)		10	20	30	40	50	60	70	80
1	V_s	-0.775	-1.574	-2.391	-3.234	-4.095	-4.975	-5.88	-6.797
	V_t	-0.044	-0.086	-0.13	-0.178	-0.232	-0.288	-0.342	-0.398
	V_{s+t}	-0.834	-1.6665	-2.536	-3.4397	-4.3735	-5.286	-6.239	-7.137
0.9	V_s	-0.778	-1.574	-2.39	-3.228	-4.088	-4.968	-5.87	-6.793
	V_t	-0.043	-0.084	-0.129	-0.177	-0.228	-0.274	-0.328	-0.384
	V_{s+t}	-0.829	-1.661	-2.528	-3.424	-4.313	-5.2375	-6.172	-7.0882
0.8	V_s	-0.773	-1.566	-2.379	-3.221	-4.085	-4.969	-5.875	-6.797
	V_t	-0.042	-0.082	-0.127	-0.175	-0.224	-0.271	-0.324	-0.382
	V_{s+t}	-0.829	-1.659	-2.481	-3.3685	-4.2707	-5.197	-6.1695	-7.113
0.7	V_s	-0.77	-1.567	-2.384	-3.226	-4.088	-4.968	-5.866	-6.785
	V_t	-0.041	-0.081	-0.126	-0.174	-0.221	-0.269	-0.321	-0.38
	V_{s+t}	-0.846	-1.68	-2.5285	-3.415	-4.3065	-5.222	-6.1669	-7.1465
0.6	V_s	-0.766	-1.555	-2.366	-3.195	-4.046	-4.928	-5.835	-6.77
	V_t	-0.041	-0.08	-0.127	-0.172	-0.218	-0.267	-0.318	-0.378
	V_{s+t}	-0.8285	-1.649	-2.493	-3.346	-4.2920	-5.1575	-6.1115	-7.1005
0.5	V_s	-0.764	-1.552	-2.36	-3.195	-4.056	-4.944	-5.848	-6.775
	V_t	-0.042	-0.085	-0.128	-0.173	-0.218	-0.267	-0.317	-0.371
	V_{s+t}	-0.836	-1.66	-2.509	-3.3950	-4.273	-5.1678	-6.111	-7.0855
0.4	V_s	-0.761	-1.541	-2.346	-3.17	-4.027	-4.905	-5.816	-6.755
	V_t	-0.041	-0.081	-0.122	-0.17	-0.214	-0.262	-0.312	-0.364
	V_{s+t}	-0.8135	-1.6285	-2.4728	-3.3585	-4.2883	-5.1483	-6.0995	-7.1080
0.3	V_s	-0.758	-1.54	-2.344	-3.17	-4.02	-4.899	-5.808	-6.744
	V_t	-0.041	-0.079	-0.118	-0.164	-0.209	-0.258	-0.308	-0.357
	V_{s+t}	-0.8079	-1.62	-2.452	-3.406	-4.2825	-5.221	-6.074	-7.0625
0.2	V_s	-0.76	-1.539	-2.345	-3.18	-4.038	-4.92	-5.83	-6.763
	V_t	-0.04	-0.076	-0.116	-0.159	-0.203	-0.253	-0.304	-0.35
	V_{s+t}	-0.7912	-1.624	-2.486	-3.3095	-4.21	-5.128	-6.1035	-7.055
0.1	V_s	-0.77	-1.562	-2.38	-3.22	-4.083	-4.966	-5.864	-6.776
	V_t	-0.039	-0.077	-0.114	-0.154	-0.196	-0.238	-0.282	-0.331
	V_{s+t}	-0.8315	-1.6745	-2.54	-3.4266	-4.3485	-5.2728	-6.0683	-6.9845

0	V_s	-0.768	-1.557	-2.369	-3.203	-4.06	-4.94	-5.841	-6.765
	V_t	-0.032	-0.061	-0.093	-0.125	-0.168	-0.209	-0.255	-0.29
	V_{s+t}	-0.804	-1.615	-2.474	-3.346	-4.255	-5.205	-6.114	-7.032
-0.1	V_s	-0.755	-1.534	-2.34	-3.174	-4.038	-4.927	-5.841	-6.775
	V_t	-0.029	-0.057	-0.086	-0.116	-0.146	-0.177	-0.215	-0.255
	V_{s+t}	-0.8339	-1.6538	-2.4853	-3.351	-4.259	-5.1729	-6.1345	-7.073
-0.2	V_s	-0.757	-1.536	-2.342	-3.17	-4.024	-4.91	-5.826	-6.772
	V_t	-0.025	-0.055	-0.082	-0.112	-0.141	-0.172	-0.205	-0.24
	V_{s+t}	-0.832	-1.6462	-2.4962	-3.3588	-4.2567	-5.2101	-6.17	-7.1155
-0.3	V_s	-0.771	-1.562	-2.375	-3.21	-4.066	-4.944	-5.845	-6.771
	V_t	-0.027	-0.052	-0.078	-0.105	-0.138	-0.166	-0.196	-0.223
	V_{s+t}	-0.8668	-1.6959	-2.5363	-3.439	-4.3395	-5.2831	-6.198	-7.163
-0.4	V_s	-0.77	-1.558	-2.372	-3.209	-4.073	-4.954	-5.856	-6.775
	V_t	-0.026	-0.051	-0.076	-0.103	-0.135	-0.163	-0.19	-0.215
	V_{s+t}	-0.8698	-1.7452	-2.6313	-3.5159	-4.4305	-5.3569	-6.2248	-7.1399
-0.5	V_s	-0.77	-1.555	-2.364	-3.196	-4.05	-4.928	-5.831	-6.758
	V_t	-0.026	-0.05	-0.073	-0.1	-0.131	-0.158	-0.185	-0.209
	V_{s+t}	-0.8809	-1.7462	-2.6292	-3.5145	-4.4298	-5.3691	-6.3022	-7.1983
-0.6	V_s	-0.77	-1.565	-2.385	-3.224	-4.085	-4.965	-5.865	-6.778
	V_t	-0.026	-0.051	-0.075	-0.1	-0.128	-0.154	-0.18	-0.206
	V_{s+t}	-0.8935	-1.783	-2.6556	-3.579	-4.4669	-5.3766	-6.306	-7.2965
-0.7	V_s	-0.78	-1.585	-2.406	-3.244	-4.102	-4.977	-5.865	-6.777
	V_t	-0.026	-0.048	-0.07	-0.095	-0.123	-0.149	-0.175	-0.2
	V_{s+t}	-0.885	-1.7696	-2.6512	-3.5535	-4.4437	-5.3469	-6.3594	-7.2372
-0.8	V_s	-0.785	-1.59	-2.412	-3.254	-4.109	-4.98	-5.865	-6.767
	V_t	-0.023	-0.045	-0.066	-0.09	-0.115	-0.14	-0.165	-0.19
	V_{s+t}	-0.896	-1.787	-2.6767	-3.5913	-4.499	-5.4198	-6.333	-7.237
-0.9	V_s	-0.78	-1.58	-2.402	-3.245	-4.105	-4.985	-5.88	-6.788
	V_t	-0.023	-0.043	-0.065	-0.087	-0.109	-0.13	-0.153	-0.178
	V_{s+t}	-0.8925	-1.78	-2.687	-3.612	-4.5265	-5.439	-6.3425	-7.242
-1	V_s	-0.77	-1.566	-2.387	-3.231	-4.094	-4.975	-5.871	-6.783
	V_t	-0.021	-0.039	-0.058	-0.078	-0.1	-0.124	-0.141	-0.159
	V_{s+t}	-0.8985	-1.7915	-2.7035	-3.598	-4.544	-5.4485	-6.3575	-7.282

The Seebeck, transverse and hybrid transvers voltages for DP0.1% sample for various temperature differences and magnetic flux densities.

B (T) \ ΔT (°C)		10	20	30	40	50	60	70	80
1	V_s	-0.288	-0.580	-0.878	-1.180	-1.488	-1.801	-2.120	-2.445
	V_t	-0.042	-0.081	-0.133	-0.174	-0.209	-0.265	-0.322	-0.368
	V_{s+t}	-0.297	-0.5997	-0.9012	-1.2145	-1.5269	-1.8564	-2.1895	-2.5333
0.9	V_s	-0.284	-0.574	-0.869	-1.169	-1.475	-1.786	-2.103	-2.427
	V_t	-0.04	-0.075	-0.11	-0.158	-0.203	-0.257	-0.301	-0.344
	V_{s+t}	-0.2933	-0.5896	-0.8876	-1.2016	-1.5189	-1.7853	-2.1518	-2.4701
0.8	V_s	-0.280	-0.569	-0.863	-1.163	-1.471	-1.785	-2.105	-2.429
	V_t	-0.038	-0.069	-0.106	-0.152	-0.192	-0.243	-0.295	-0.338
	V_{s+t}	-0.2897	-0.5885	-0.8888	-1.1995	-1.5263	-1.8466	-2.1686	-2.5064
0.7	V_s	-0.276	-0.560	-0.850	-1.145	-1.448	-1.758	-2.075	-2.402
	V_t	-0.035	-0.065	-0.097	-0.139	-0.176	-0.22	-0.267	-0.309
	V_{s+t}	-0.2875	-0.5796	-0.8755	-1.1838	-1.4971	-1.8172	-2.1511	-2.4995
0.6	V_s	-0.276	-0.558	-0.847	-1.142	-1.445	-1.755	-2.073	-2.395
	V_t	-0.032	-0.061	-0.09	-0.13	-0.167	-0.209	-0.258	-0.292
	V_{s+t}	-0.2851	-0.5755	-0.8721	-1.1815	-1.4891	-1.8199	-2.1517	-2.4793
0.5	V_s	-0.278	-0.561	-0.850	-1.145	-1.447	-1.755	-2.070	-2.389
	V_t	-0.031	-0.056	-0.088	-0.123	-0.159	-0.19	-0.239	-0.272
	V_{s+t}	-0.287	-0.5804	-0.8755	-1.182	-1.4958	-1.8113	-2.1425	-2.4645
0.4	V_s	-0.273	-0.554	-0.842	-1.135	-1.436	-1.742	-2.055	-2.374
	V_t	-0.028	-0.051	-0.077	-0.113	-0.142	-0.179	-0.225	-0.253
	V_{s+t}	-0.2829	-0.5738	-0.8671	-1.1735	-1.4795	-1.8036	-2.1329	-2.4536
0.3	V_s	-0.276	-0.560	-0.849	-1.143	-1.443	-1.748	-2.058	-2.374
	V_t	-0.026	-0.05	-0.074	-0.109	-0.137	-0.17	-0.207	-0.239
	V_{s+t}	-0.2887	-0.5798	-0.8722	-1.1846	-1.4921	-1.8056	-2.1284	-2.4621
0.2	V_s	-0.275	-0.556	-0.845	-1.139	-1.440	-1.746	-2.059	-2.380
	V_t	-0.024	-0.041	-0.066	-0.096	-0.123	-0.155	-0.189	-0.221
	V_{s+t}	-0.2842	-0.5722	-0.8711	-1.1718	-1.4906	-1.8042	-2.1288	-2.4682
0.1	V_s	-0.271	-0.550	-0.838	-1.132	-1.434	-1.744	-2.059	-2.383
	V_t	-0.022	-0.039	-0.06	-0.09	-0.1117	-0.149	-0.183	-0.219
	V_{s+t}	-0.2822	-0.57	-0.864	-1.165	-1.473	-1.801	-2.1	-2.425

0	V_s	-0.280	-0.567	-0.858	-1.156	-1.46	-1.769	-2.082	-2.401
	V_t	-0.019	-0.035	-0.055	-0.086	-0.11	-0.144	-0.175	-0.212
	V_{s+t}	-0.2803	-0.5671	-0.8576	-1.1597	-1.469	-1.7795	-2.0912	-2.441
-0.1	V_s	-0.279	-0.564	-0.854	-1.152	-1.454	-1.763	-2.08	-2.402
	V_t	-0.016	-0.028	-0.044	-0.069	-0.087	-0.114	-0.133	-0.161
	V_{s+t}	-0.2803	-0.5709	-0.8639	-1.1709	-1.4827	-1.8011	-2.1483	-2.4666
-0.2	V_s	-0.279	-0.563	-0.853	-1.148	-1.448	-1.754	-2.067	-2.388
	V_t	-0.015	-0.024	-0.036	-0.06	-0.075	-0.099	-0.122	-0.134
	V_{s+t}	-0.2881	-0.5805	-0.8731	-1.1862	-1.5001	-1.825	-2.1481	-2.4609
-0.3	V_s	-0.276	-0.558	-0.846	-1.139	-1.438	-1.743	-2.055	-2.373
	V_t	-0.013	-0.02	-0.028	-0.048	-0.058	-0.076	-0.098	-0.111
	V_{s+t}	-0.2859	-0.5771	-0.8674	-1.1781	-1.486	-1.8031	-2.1267	-2.4532
-0.4	V_s	-0.274	-0.555	-0.842	-1.135	-1.433	-1.738	-2.049	-2.366
	V_t	-0.01	-0.015	-0.021	-0.038	-0.049	-0.069	-0.084	-0.088
	V_{s+t}	-0.2834	-0.5755	-0.8677	-1.1727	-1.4892	-1.8082	-2.1403	-2.4513
-0.5	V_s	-0.276	-0.557	-0.844	-1.137	-1.435	-1.739	-2.049	-2.365
	V_t	-0.009	-0.012	-0.015	-0.031	-0.039	-0.052	-0.067	-0.074
	V_{s+t}	-0.2852	-0.5766	-0.8655	-1.1709	-1.482	-1.7902	-2.1489	-2.4462
-0.6	V_s	-0.27	-0.56	-0.849	-1.144	-1.443	-1.748	-2.059	-2.375
	V_t	-0.008	-0.008	-0.009	-0.022	-0.025	-0.039	-0.05	-0.055
	V_{s+t}	-0.2878	-0.5732	-0.8572	-1.1647	-1.4816	-1.8322	-2.1519	-2.4569
-0.7	V_s	-0.278	-0.560	-0.847	-1.139	-1.437	-1.740	-2.049	-2.363
	V_t	-0.006	-0.004	-0.005	-0.015	-0.018	-0.026	-0.039	-0.042
	V_{s+t}	-0.291	-0.5768	-0.8668	-1.1696	-1.4821	-1.8238	-2.1445	-2.4552
-0.8	V_s	-0.277	-0.559	-0.846	-1.139	-1.437	-1.742	-2.051	-2.367
	V_t	-0.005	-0.001	0	-0.008	-0.009	-0.017	-0.028	-0.034
	V_{s+t}	-0.2875	-0.5785	-0.8707	-1.1734	-1.4801	-1.8393	-2.1613	-2.4951
-0.9	V_s	-0.277	-0.560	-0.850	-1.146	-1.448	-1.759	-2.077	-2.401
	V_t	-0.003	-0.004	-0.005	-0.007	-0.008	-0.010	-0.013	-0.012
	V_{s+t}	-0.2875	-0.5797	-0.8753	-1.1827	-1.4963	-1.841	-2.162	-2.505
-1	V_s	-0.278	-0.563	-0.854	-1.150	-1.453	-1.763	-2.080	-2.403
	V_t	-0.001	-0.002	-0.003	-0.004	-0.005	-0.007	-0.008	-0.009
	V_{s+t}	-0.2873	-0.5845	-0.8798	-1.1876	-1.5084	-1.8441	-2.17	-2.5178

The Seebeck, transverse and hybrid transvers voltages for DP0.25% sample for various temperature differences and magnetic flux densities.

ΔT (°C) / B (T)		10	20	30	40	50	60	70	80
1	V_s	-0.300	-0.6077	-0.923	-1.246	-1.575	-1.913	-2.259	-2.613
	V_t	-0.027	-0.054	-0.082	-0.112	-0.143	-0.176	-0.21	-0.245
	V_{s+t}	-0.309	-0.615	-0.936	-1.259	-1.597	-1.942	-2.289	-2.647
0.9	V_s	-0.300	-0.606	-0.918	-1.238	-1.564	-1.897	-2.237	-2.586
	V_t	-0.024	-0.05	-0.072	-0.105	-0.135	-0.166	-0.198	-0.229
	V_{s+t}	-0.304	-0.613	-0.929	-1.25	-1.583	-1.919	-2.26	-2.617
0.8	V_s	-0.296	-0.5996	-0.910	-1.227	-1.552	-1.883	-2.221	-2.568
	V_t	-0.024	-0.049	-0.074	-0.099	-0.126	-0.156	-0.184	-0.216
	V_{s+t}	-0.304	-0.611	-0.924	-1.244	-1.566	-1.905	-2.241	-2.592
0.7	V_s	-0.296	-0.5998	-0.91	-1.226	-1.547	-1.877	-2.212	-2.556
	V_t	-0.024	-0.045	-0.069	-0.093	-0.119	-0.145	-0.173	-0.206
	V_{s+t}	-0.301	-0.609	-0.923	-1.241	-1.563	-1.893	-2.249	-2.588
0.6	V_s	-0.299	-0.6032	-0.909	-1.224	-1.546	-1.876	-2.209	-2.553
	V_t	-0.021	-0.042	-0.064	-0.086	-0.112	-0.136	-0.163	-0.191
	V_{s+t}	-0.301	-0.608	-0.917	-1.235	-1.56	-1.893	-2.229	-2.577
0.5	V_s	-0.296	-0.5974	-0.905	-1.220	-1.542	-1.870	-2.203	-2.541
	V_t	-0.021	-0.04	-0.061	-0.082	-0.106	-0.131	-0.156	-0.18
	V_{s+t}	-0.3	-0.604	-0.914	-1.231	-1.559	-1.888	-2.223	-2.5713
0.4	V_s	-0.296	-0.5977	-0.904	-1.217	-1.535	-1.86	-2.192	-2.532
	V_t	-0.02	-0.038	-0.057	-0.077	-0.098	-0.121	-0.143	-0.165
	V_{s+t}	-0.296	-0.599	-0.905	-1.213	-1.541	-1.871	-2.215	-2.566
0.3	V_s	-0.294	-0.5941	-0.899	-1.210	-1.528	-1.850	-2.182	-2.517
	V_t	-0.017	-0.033	-0.05	-0.068	-0.087	-0.106	-0.127	-0.15
	V_{s+t}	-0.296	-0.596	-0.9	-1.213	-1.535	-1.868	-2.192	-2.562
0.2	V_s	-0.287	-0.5832	-0.887	-1.200	-1.523	-1.852	-2.189	-2.534
	V_t	-0.017	-0.031	-0.047	-0.064	-0.082	-0.1	-0.118	-0.137
	V_{s+t}	-0.293	-0.596	-0.902	-1.214	-1.536	-1.864	-2.201	-2.549
0.1	V_s	-0.287	-0.5828	-0.887	-1.202	-1.524	-1.856	-2.194	-2.541
	V_t	-0.015	-0.028	-0.043	-0.057	-0.074	-0.092	-0.108	-0.126
	V_{s+t}	-0.294	-0.591	-0.9	-1.209	-1.528	-1.86	-2.196	-2.53

0	V_s	-0.288	-0.5858	-0.892	-1.206	-1.532	-1.862	-2.201	-2.551
	V_t	-0.015	-0.027	-0.038	-0.053	-0.067	-0.081	-0.096	-0.112
	V_{s+t}	-0.293	-0.592	-0.901	-1.216	-1.539	-1.877	-2.215	-2.566
-0.1	V_s	-0.290	-0.5868	-0.892	-1.205	-1.525	-1.856	-2.193	-2.541
	V_t	-0.012	-0.021	-0.033	-0.044	-0.058	-0.073	-0.086	-0.102
	V_{s+t}	-0.294	-0.591	-0.9	-1.209	-1.528	-1.86	-2.196	-2.53
-0.2	V_s	-0.293	-0.5932	-0.896	-1.206	-1.525	-1.851	-2.185	-2.524
	V_t	-0.014	-0.024	-0.037	-0.051	-0.066	-0.081	-0.096	-0.113
	V_{s+t}	-0.293	-0.596	-0.902	-1.214	-1.536	-1.864	-2.201	-2.549
-0.3	V_s	-0.296	-0.5981	-0.905	-1.220	-1.539	-1.861	-2.190	-2.524
	V_t	-0.014	-0.026	-0.04	-0.055	-0.071	-0.087	-0.105	-0.126
	V_{s+t}	-0.296	-0.596	-0.9	-1.213	-1.535	-1.868	-2.192	-2.532
-0.4	V_s	-0.296	-0.5987	-0.906	-1.218	-1.536	-1.86	-2.192	-2.532
	V_t	-0.017	-0.031	-0.047	-0.064	-0.082	-0.102	-0.121	-0.141
	V_{s+t}	-0.296	-0.599	-0.905	-1.213	-1.541	-1.811	-2.205	-2.547
-0.5	V_s	-0.297	-0.5994	-0.906	-1.220	-1.541	-1.868	-2.201	-2.541
	V_t	-0.018	-0.033	-0.051	-0.069	-0.09	-0.112	-0.134	-0.156
	V_{s+t}	-0.3	-0.604	-0.914	-1.231	-1.559	-1.888	-2.223	-2.513
-0.6	V_s	-0.299	-0.6032	-0.911	-1.226	-1.546	-1.874	-2.209	-2.553
	V_t	-0.018	-0.035	-0.054	-0.073	-0.096	-0.117	-0.141	-0.167
	V_{s+t}	-0.301	-0.608	-0.917	-1.235	-1.56	-1.893	-2.229	-2.577
-0.7	V_s	-0.299	-0.6028	-0.913	-1.228	-1.547	-1.873	-2.204	-2.545
	V_t	-0.021	-0.038	-0.059	-0.08	-0.103	-0.126	-0.151	-0.182
	V_{s+t}	-0.301	-0.609	-0.923	-1.241	-1.563	-1.893	-2.249	-2.588
-0.8	V_s	-0.299	-0.6067	-0.919	-1.237	-1.560	-1.888	-2.222	-2.562
	V_t	-0.021	-0.042	-0.064	-0.086	-0.11	-0.137	-0.162	-0.192
	V_{s+t}	-0.304	-0.611	-0.924	-1.244	-1.566	-1.905	-2.241	-2.592
-0.9	V_s	-0.298	-0.6072	-0.918	-1.236	-1.564	-1.897	-2.230	-2.578
	V_t	-0.021	-0.043	-0.067	-0.092	-0.119	-0.147	-0.176	-0.205
	V_{s+t}	-0.304	-0.613	-0.929	-1.25	-1.583	-1.919	-2.26	-2.617
-1	V_s	-0.299	-0.6087	-0.925	-1.247	-1.576	-1.907	-2.245	-2.588
	V_t	-0.024	-0.047	-0.072	-0.099	-0.127	-0.157	-0.188	-0.221
	V_{s+t}	-0.309	-0.615	-0.936	-1.259	-1.597	-1.942	-2.289	-2.647

Appendex 2:

Variation of the Seebeck voltage with temperature difference under various DC magnetic field density for USB sample.

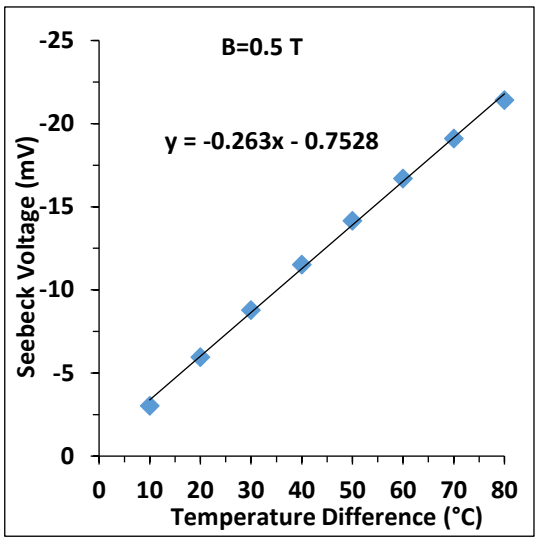

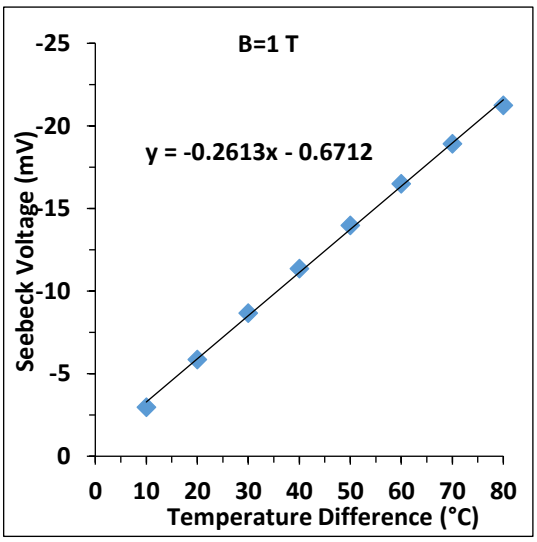

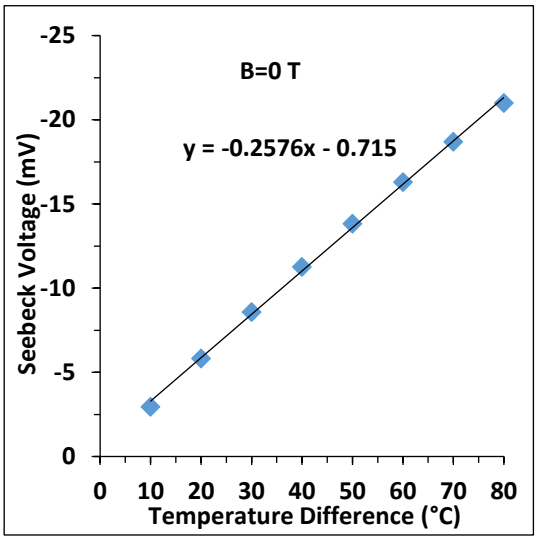

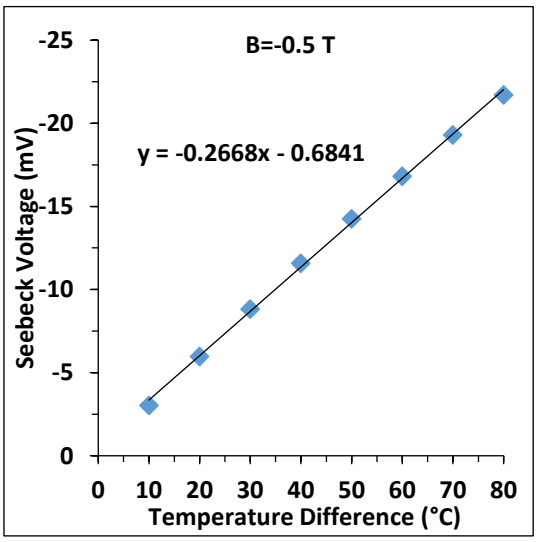

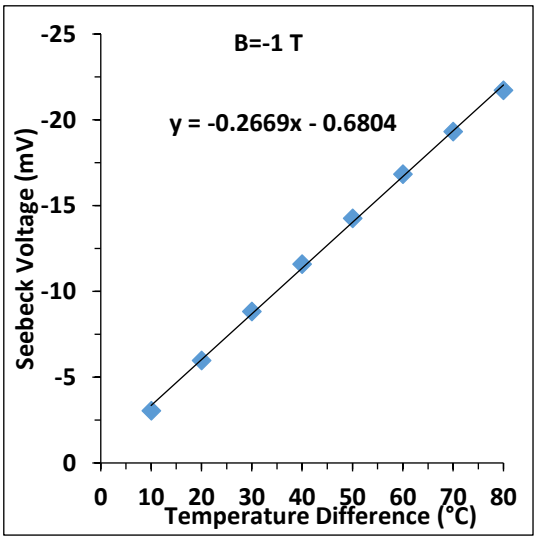

Variation of the Seebeck voltage with temperature difference under various DC magnetic field density for USR sample.

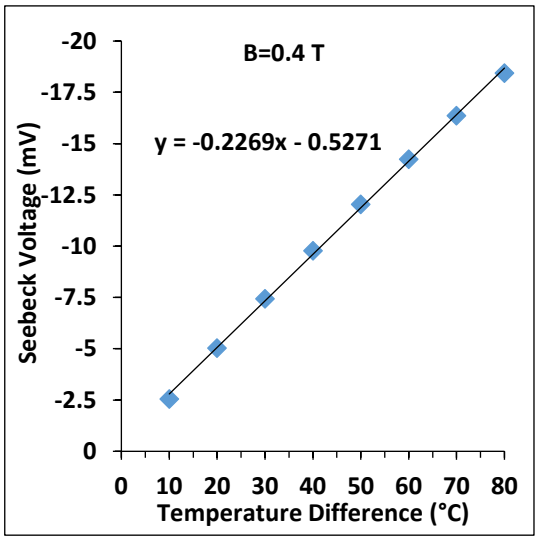

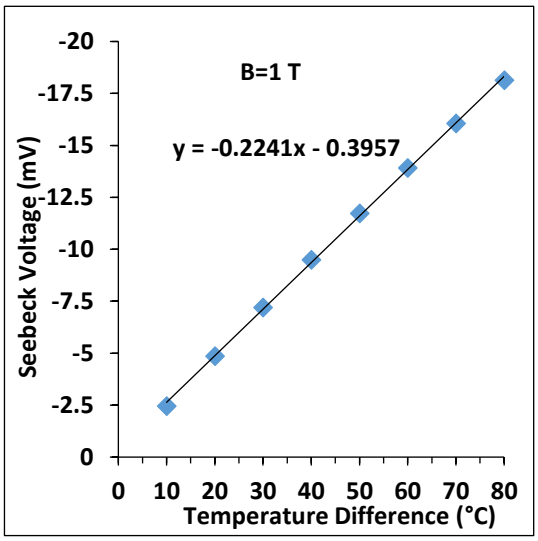

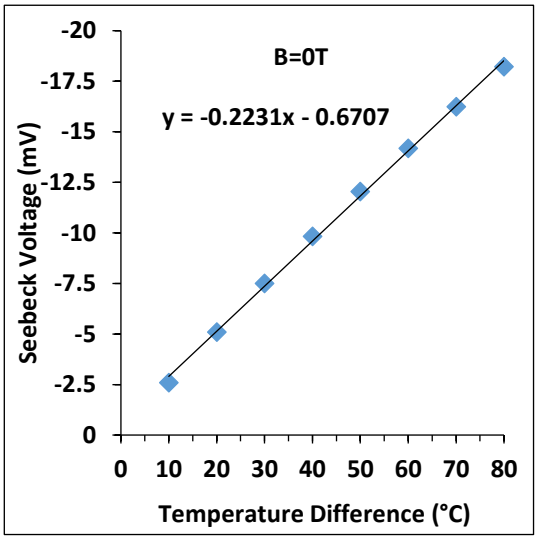

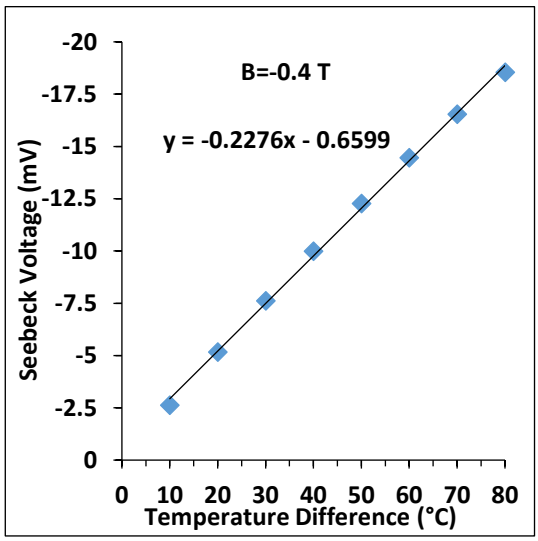

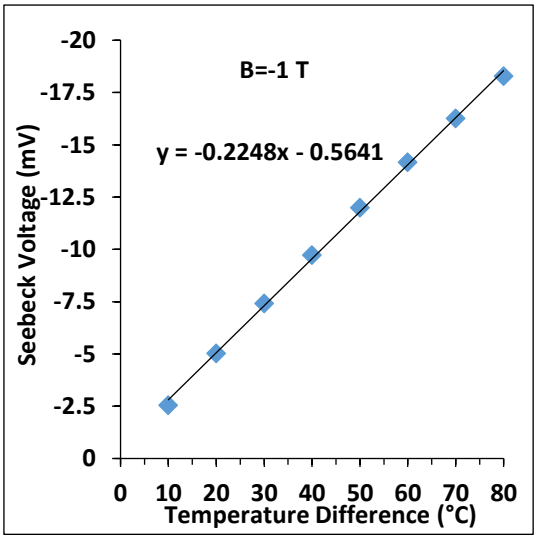

Variation of the Seebeck voltage with temperature difference under various DC magnetic field density for UPB sample.

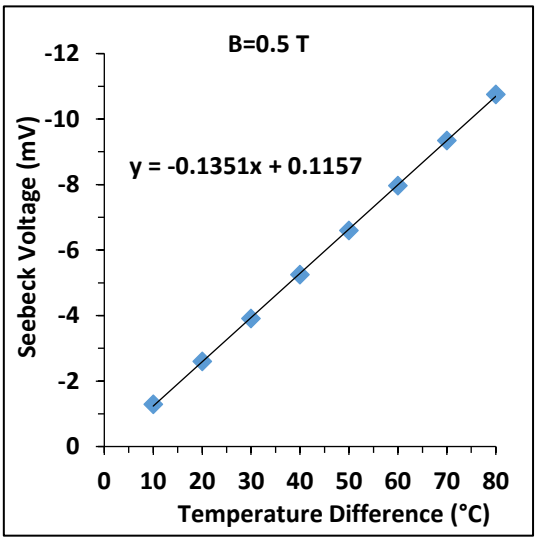

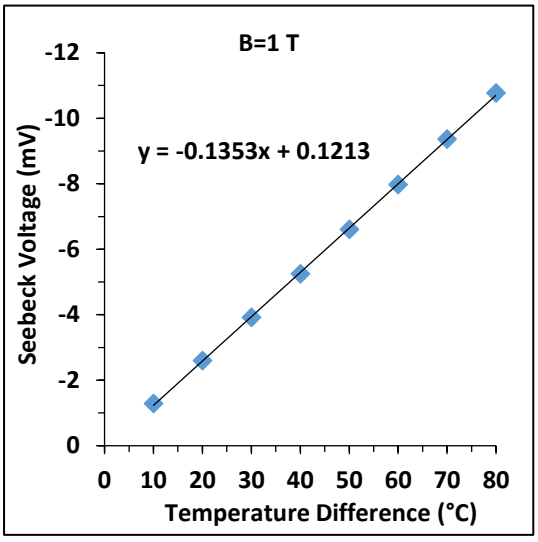

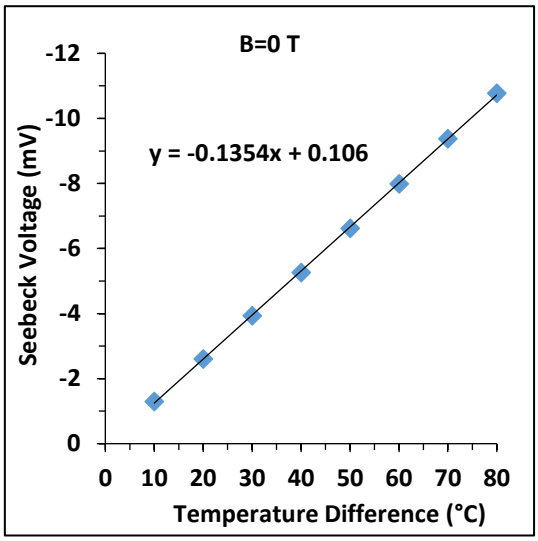

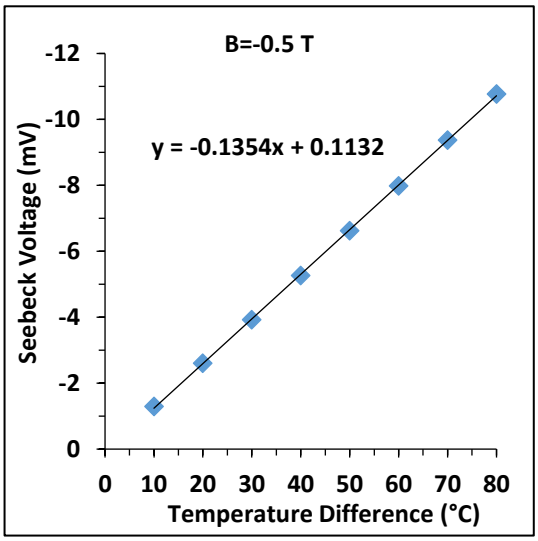

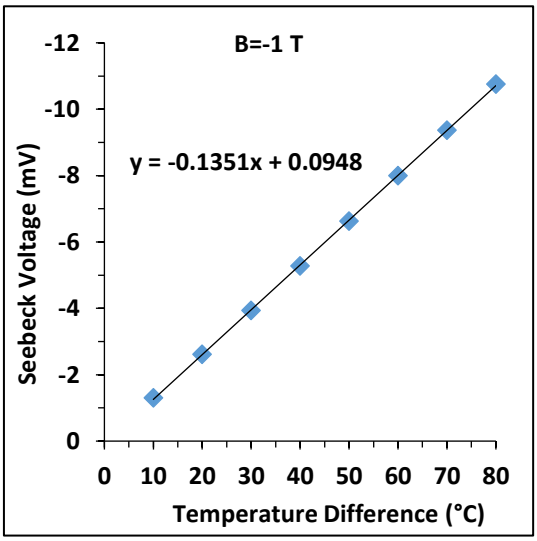

Variation of the Seebeck voltage with temperature difference under various DC magnetic field density for UPA sample.

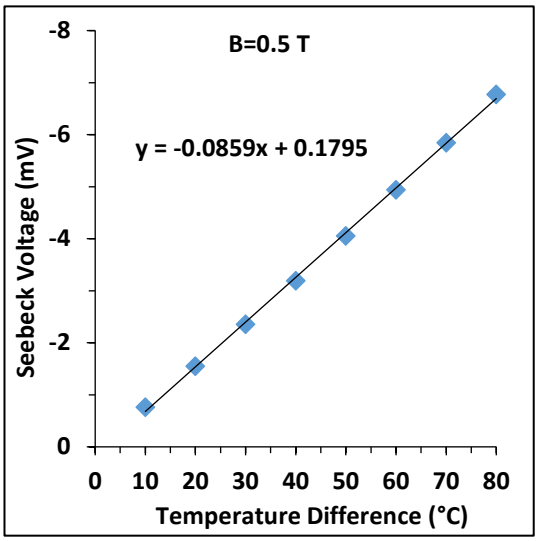

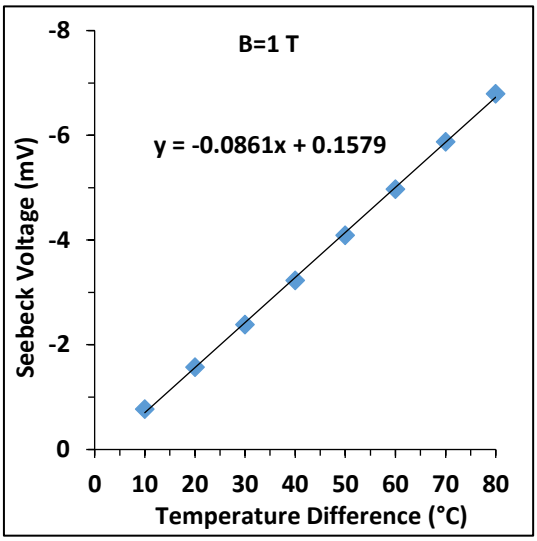

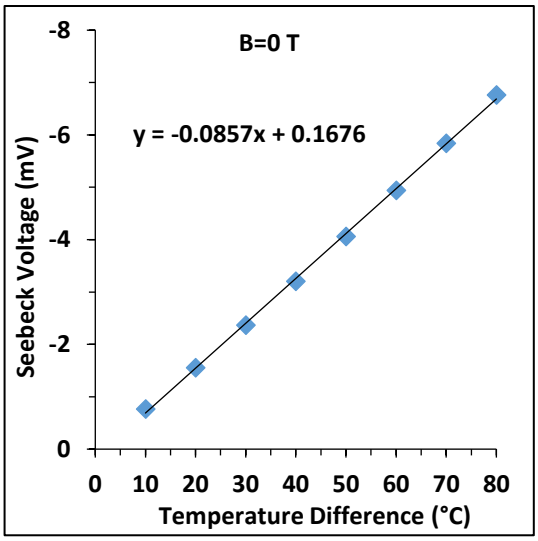

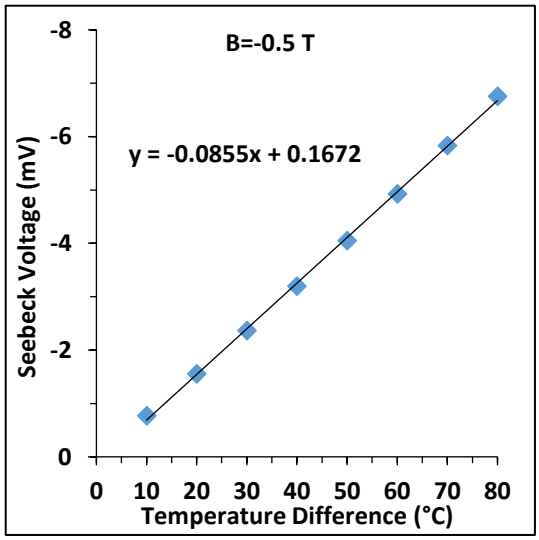

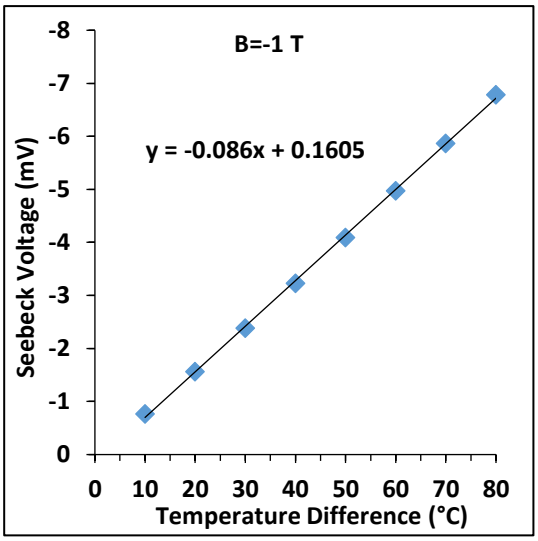

Variation of the Seebeck voltage with temperature difference under various DC magnetic field density for DP0.1% sample.

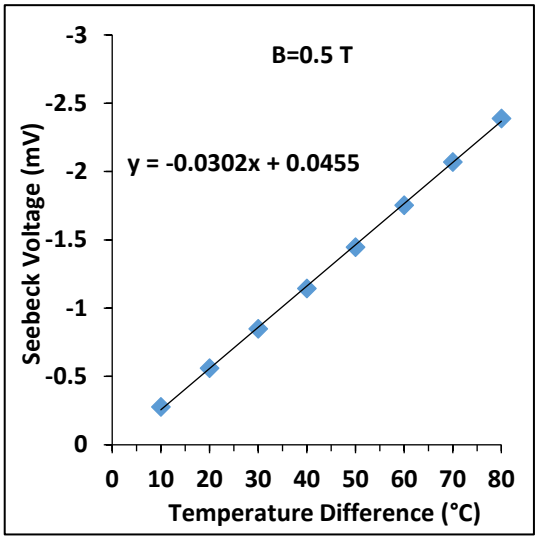

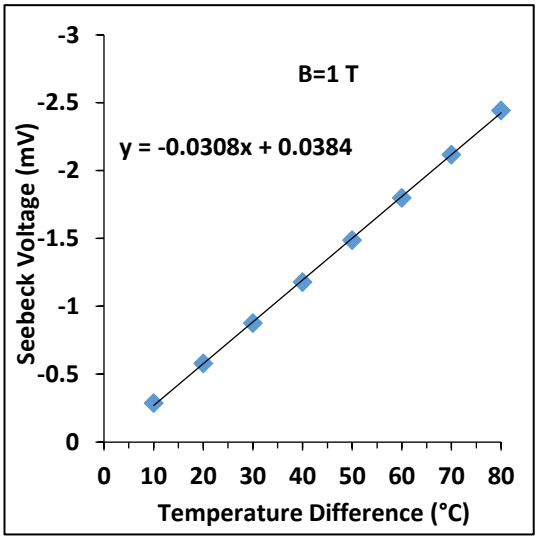

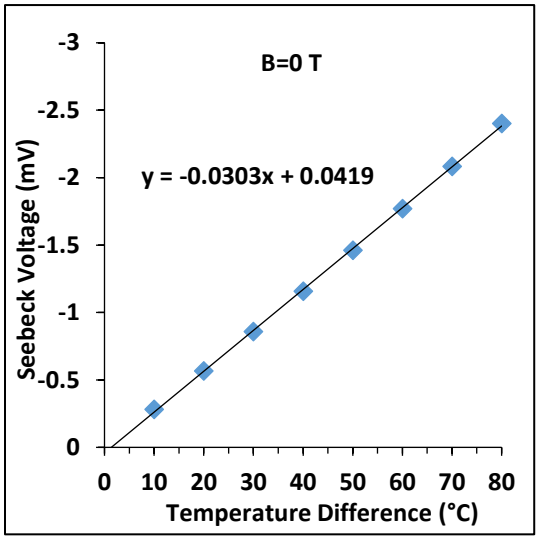

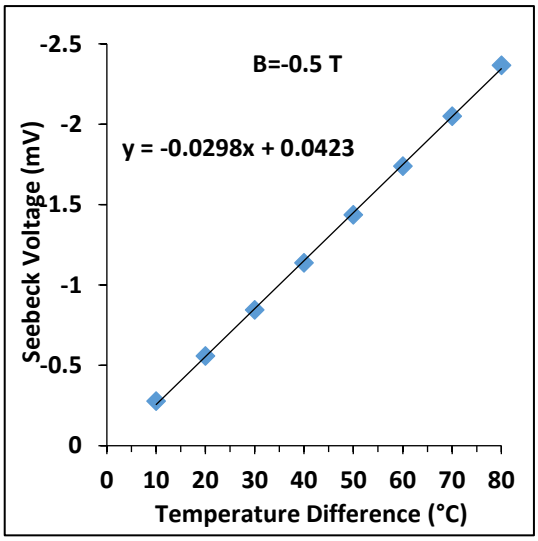

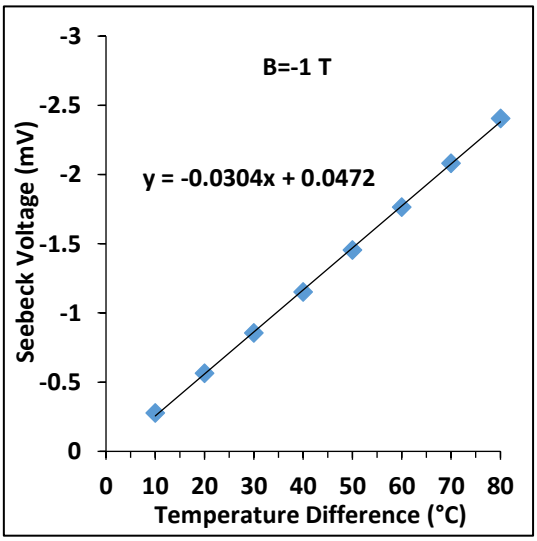

Variation of the Seebeck voltage with temperature difference under various DC magnetic field density for DP0.25% sample.

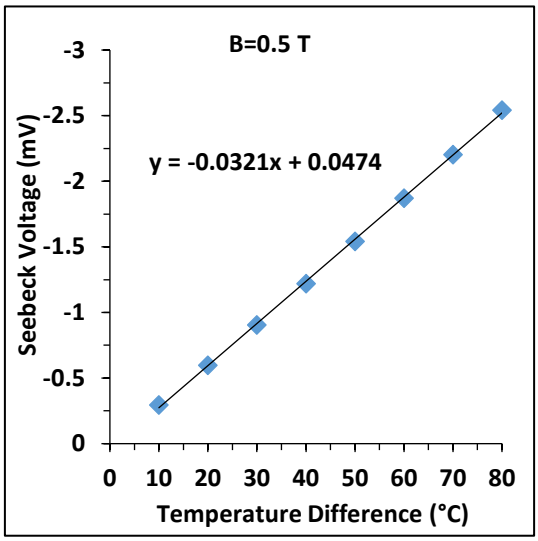

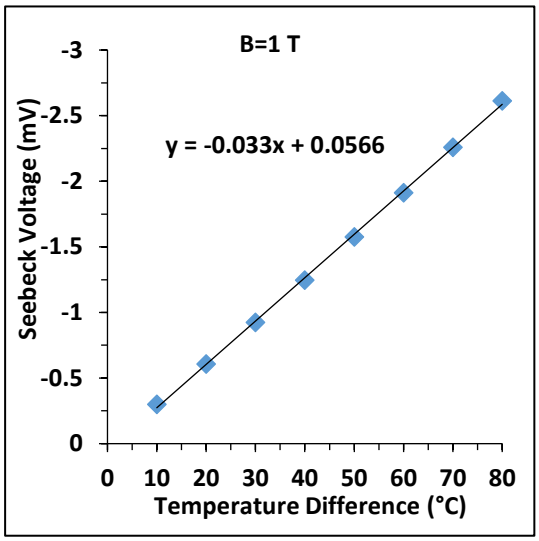

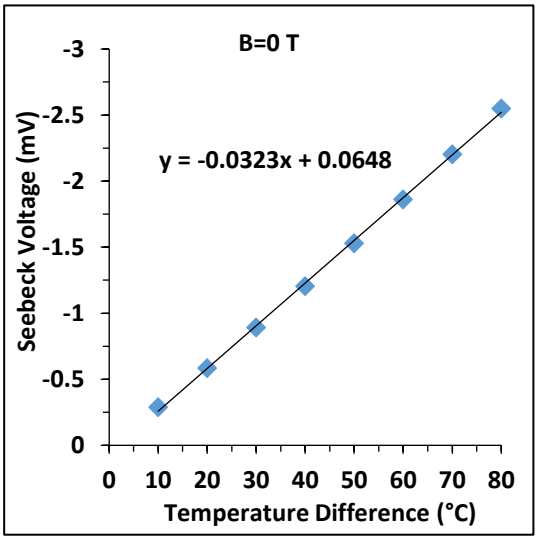

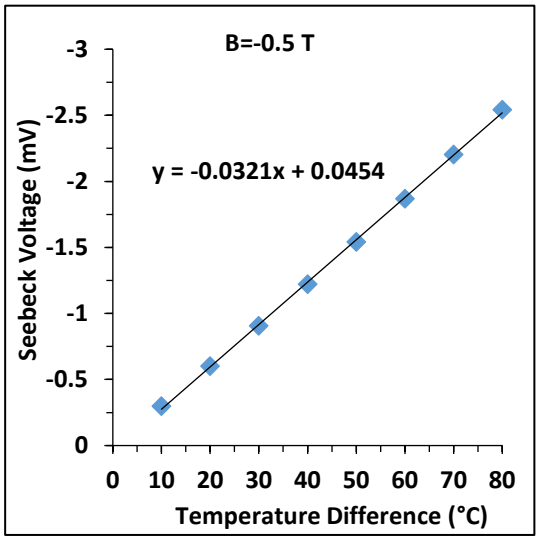

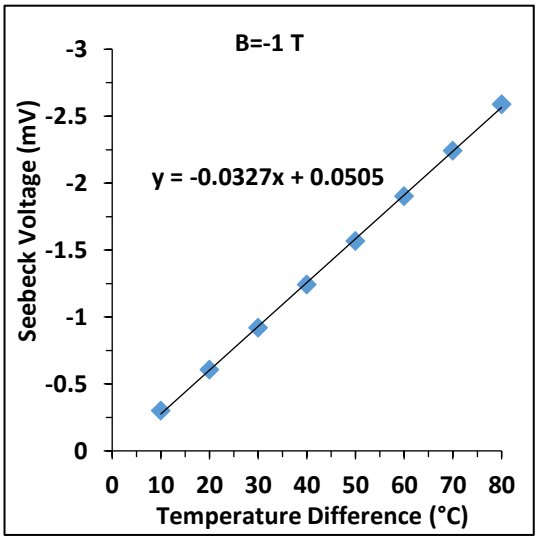

Appendex 3:

Repeatability of the Seebeck coefficient with temperature difference in the absence of the magnetic field for USB sample:

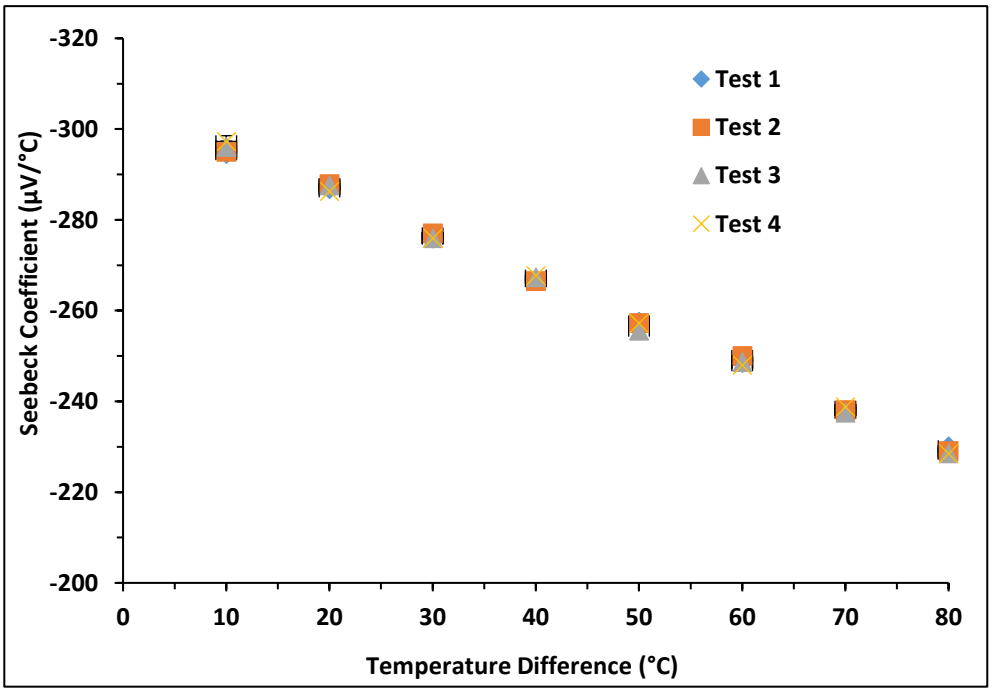

Repeatability of the Seebeck coefficient with temperature difference under the DC magnetic flux density 0.1 T for USR sample:

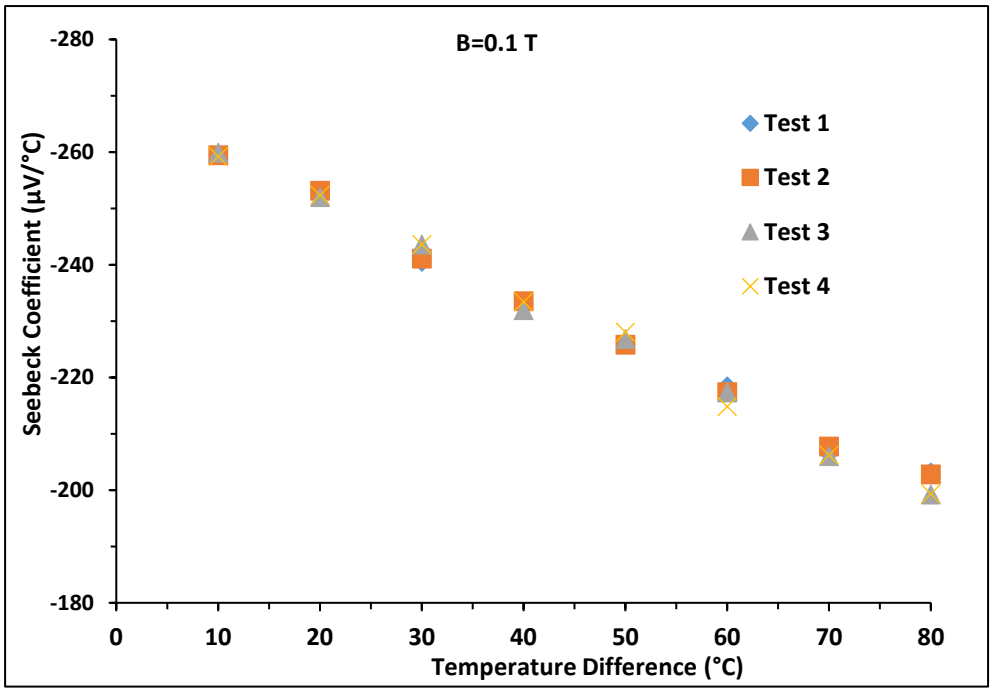

Repeatability of the Seebeck coefficient with temperature difference under the DC magnetic flux density 0.5 T for USR sample:

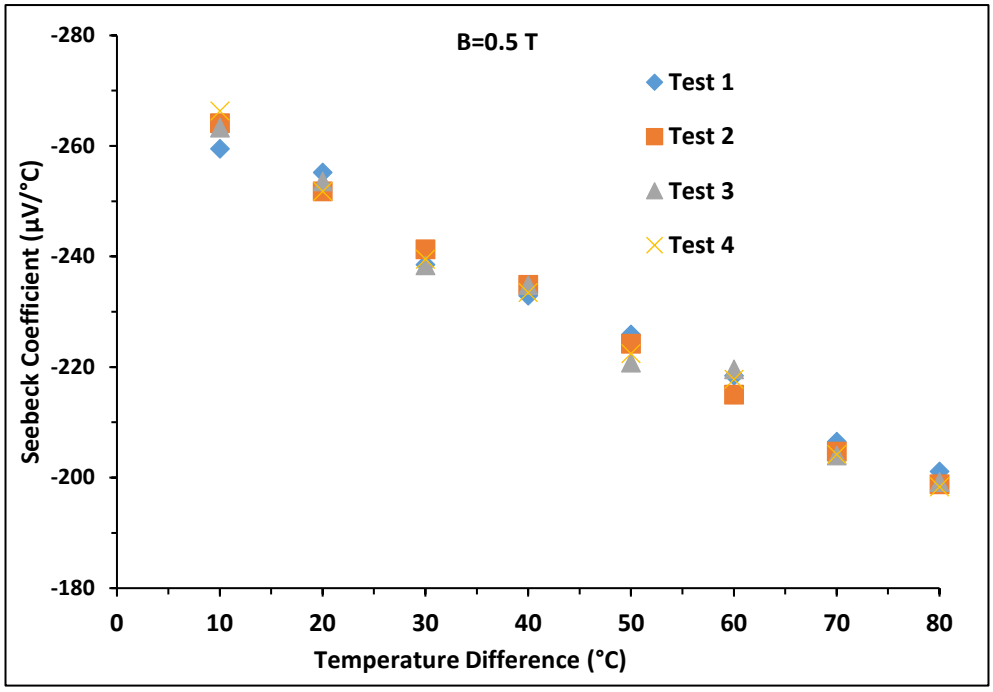

Repeatability of the Seebeck coefficient with temperature difference under the DC magnetic flux density 1 T for USR sample:

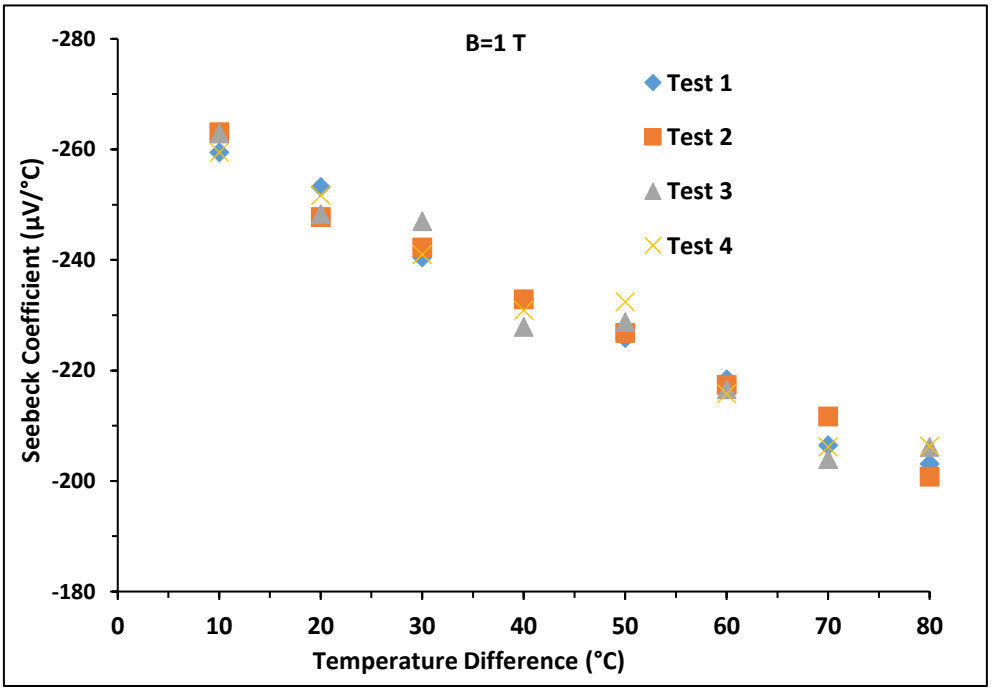

Repeatability of the Seebeck coefficient with temperature difference under the AC magnetic flux density 0.1 T for USR sample:

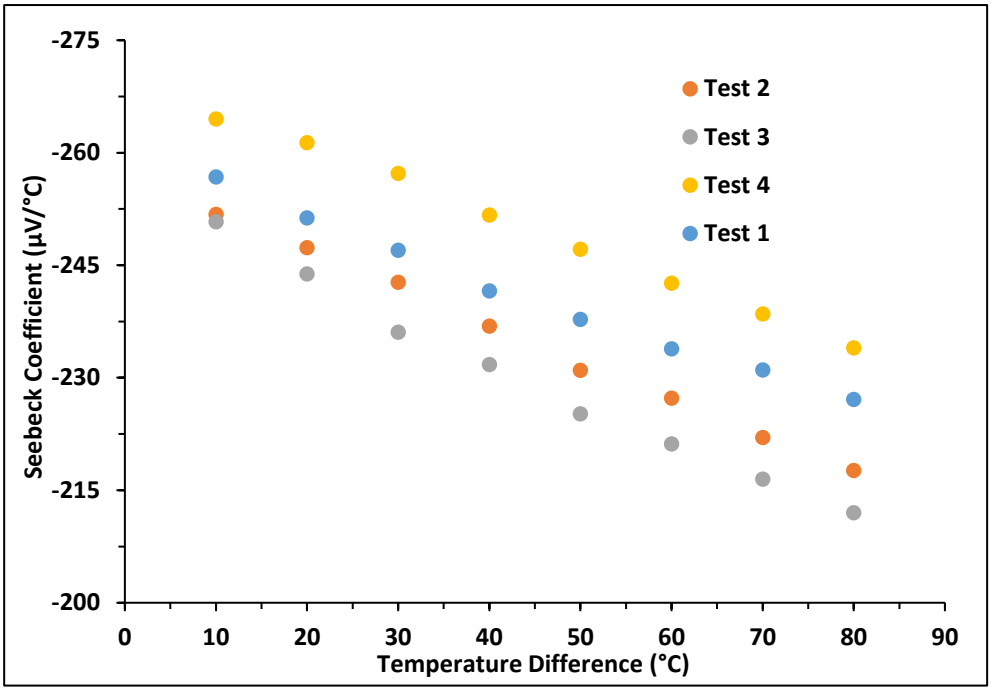

Repeatability of the Seebeck coefficient with temperature difference under the AC magnetic flux density 0.5 T for USR sample:

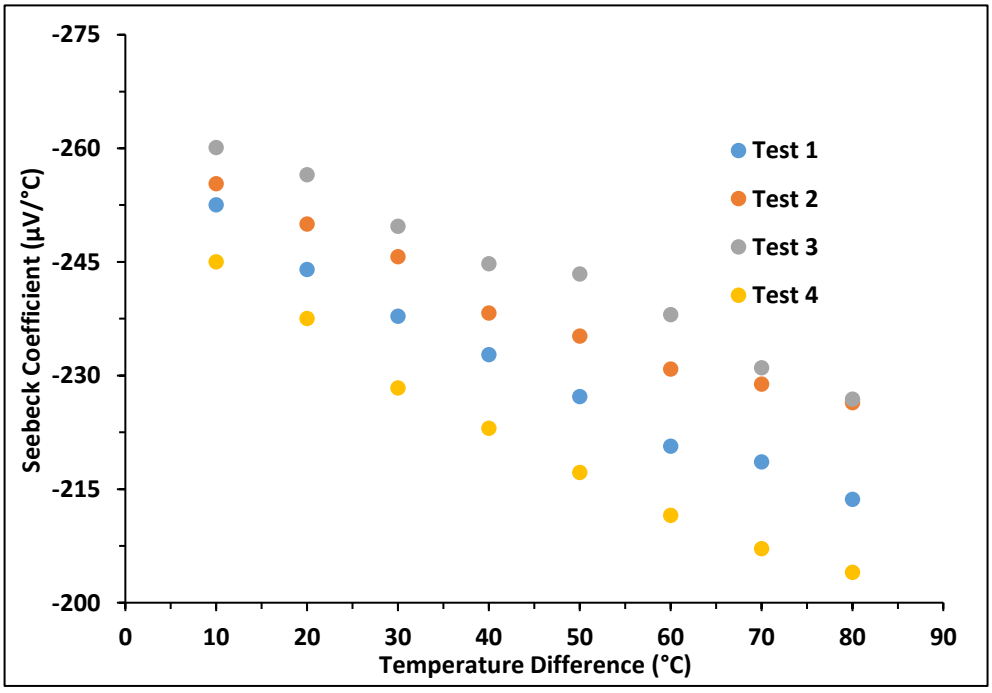

Appendex 4:

Variation of the Seebeck coefficient with temperature difference in the absence of the magnetic field for:

a) USR sample

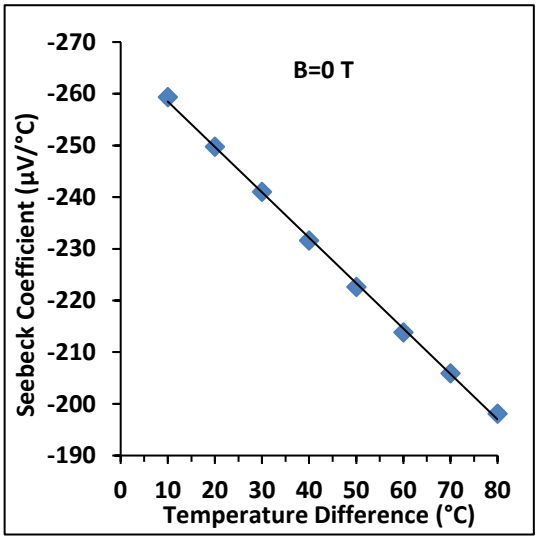

b) UPA sample

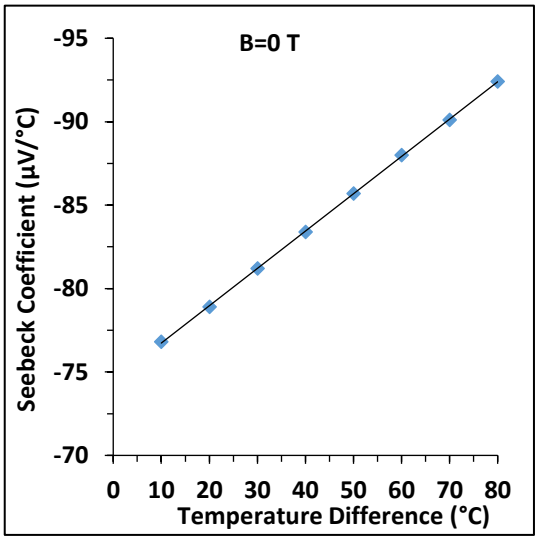

c) DP0.1% sample

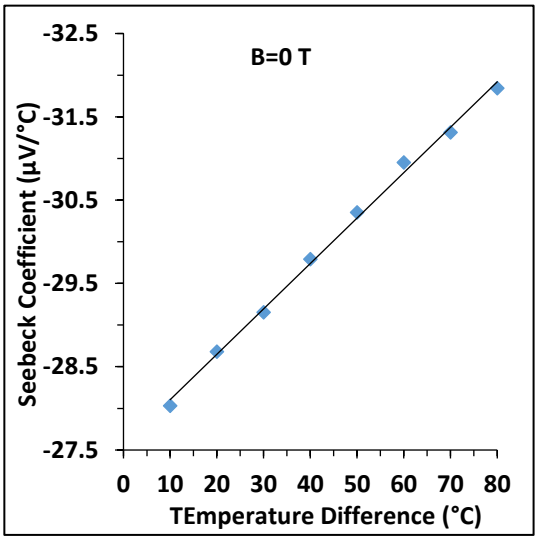

d) DP0.25% sample

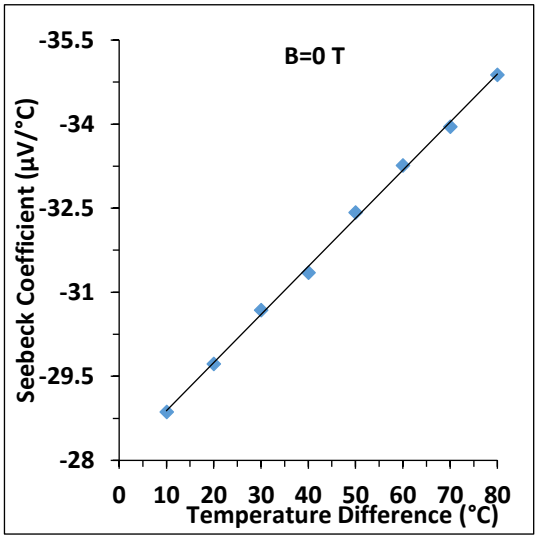

Appendex 5:

Variation of the resistivity with DC magnetic field density for UPB sample.

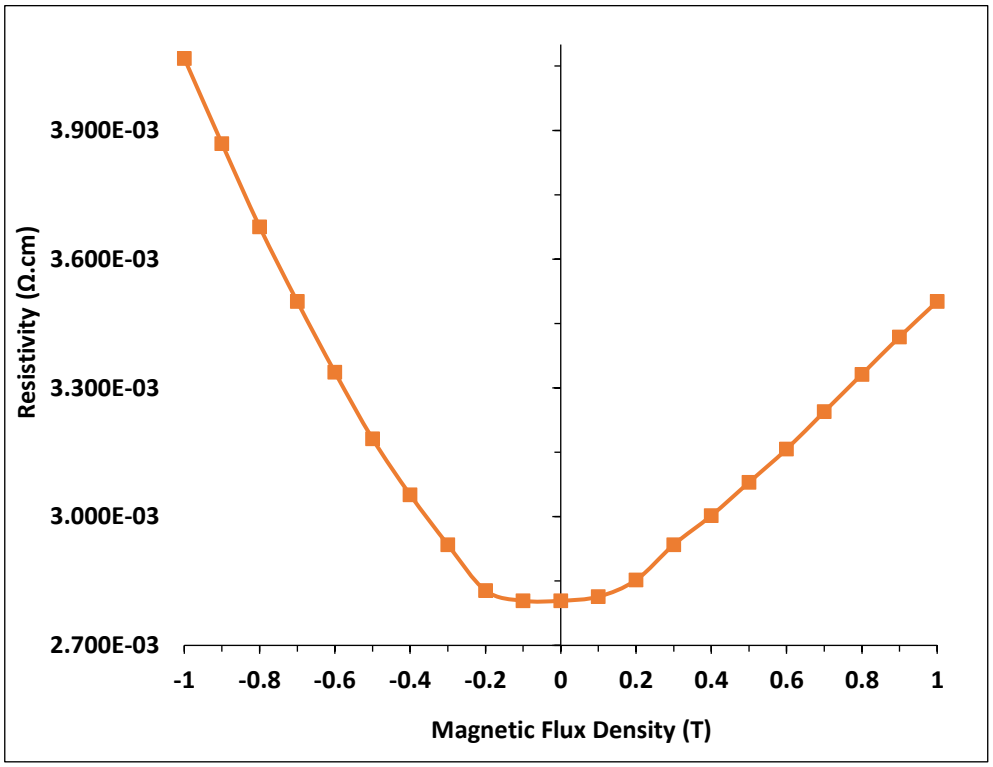

Variation of the resistivity with DC magnetic field density for UPA sample.

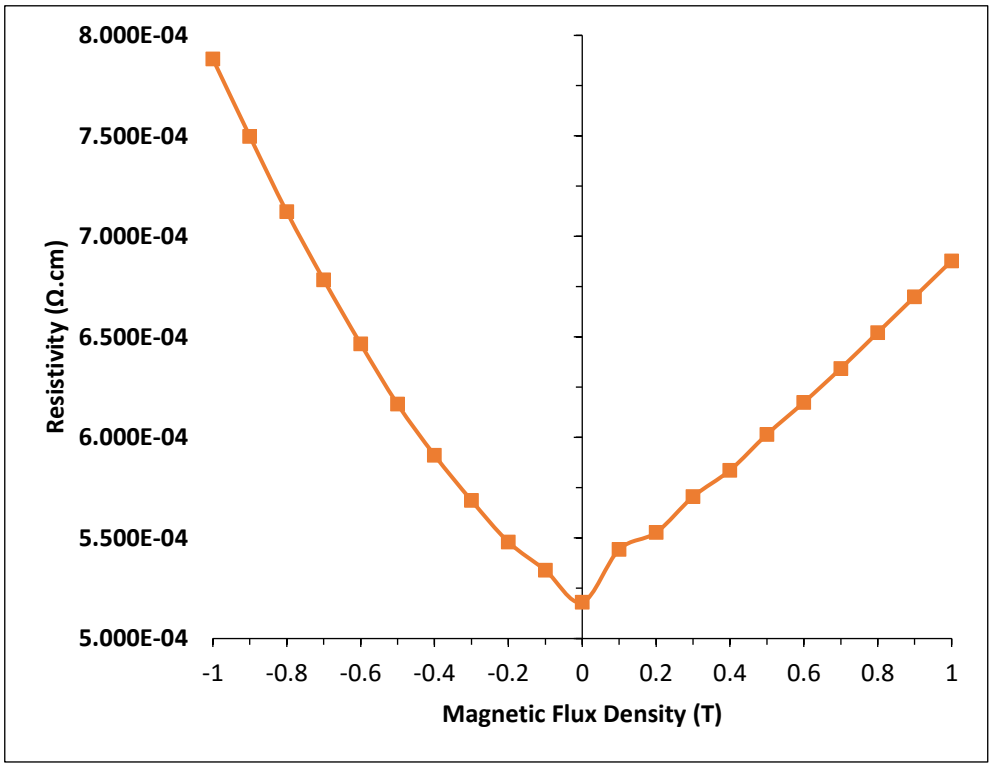

Variation of the resistivity with DC magnetic field density for DP0.1% sample.

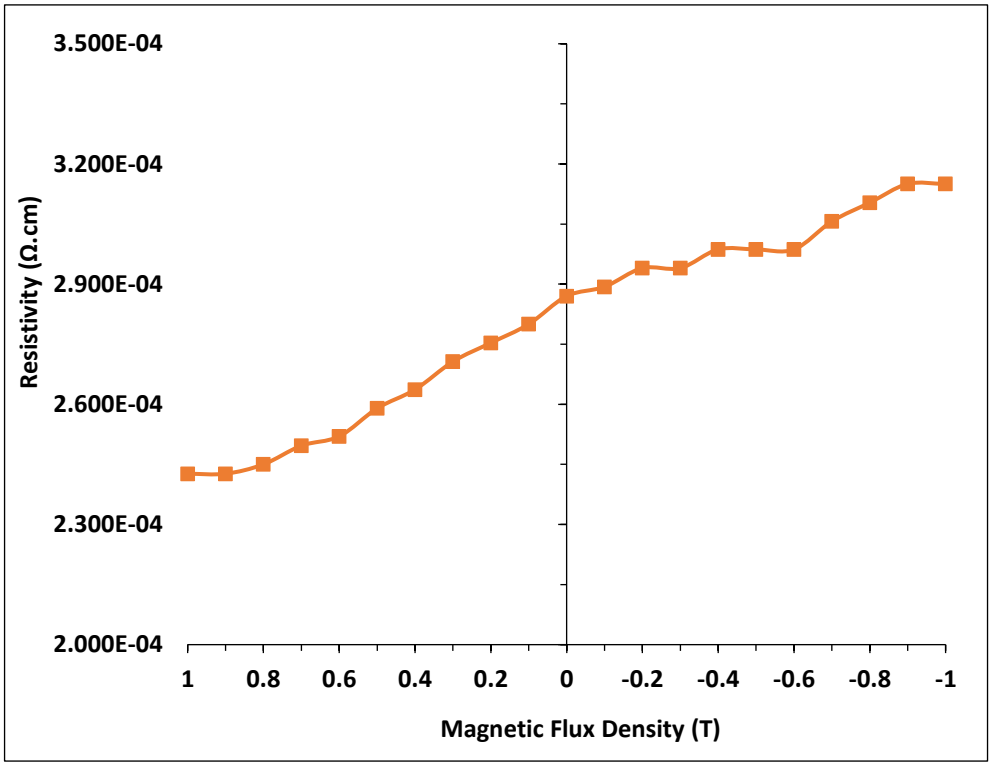

Variation of the resistivity with DC magnetic field density for DP0.25% sample.

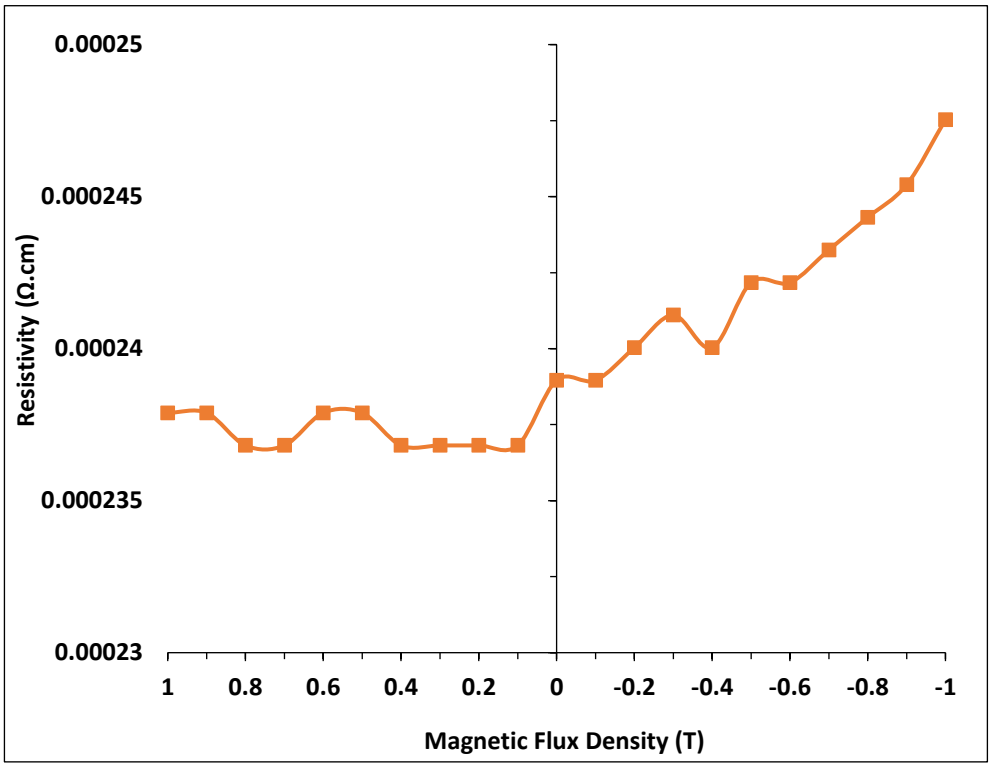

Appendex 6:

Variation of the Seebeck coefficient with temperature difference for USR sample.

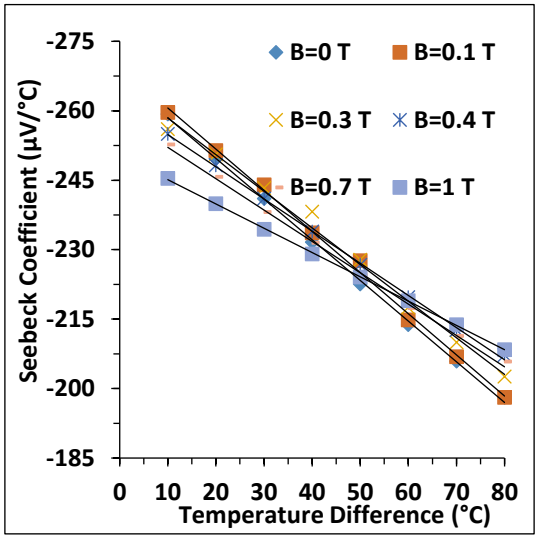

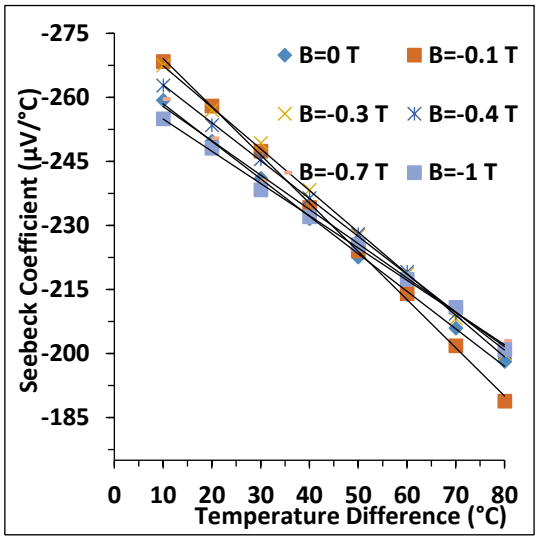

Variation of the Seebeck coefficient with temperature difference for UPA sample.

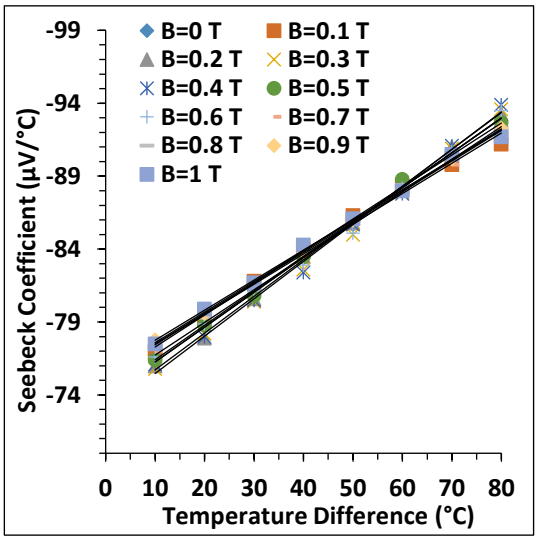

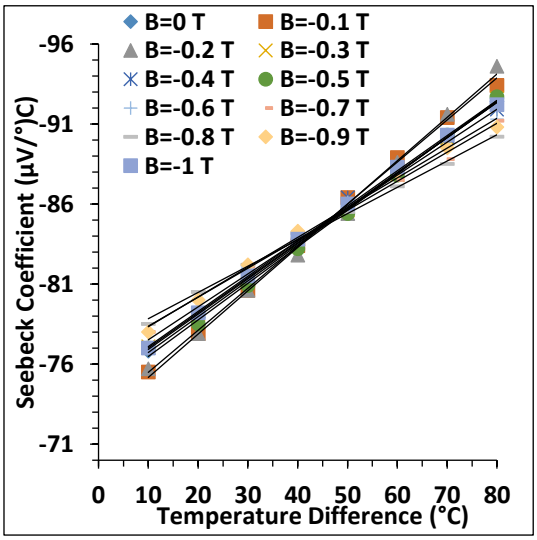

Variation of the Seebeck coefficient with temperature difference for DP0.1% sample.

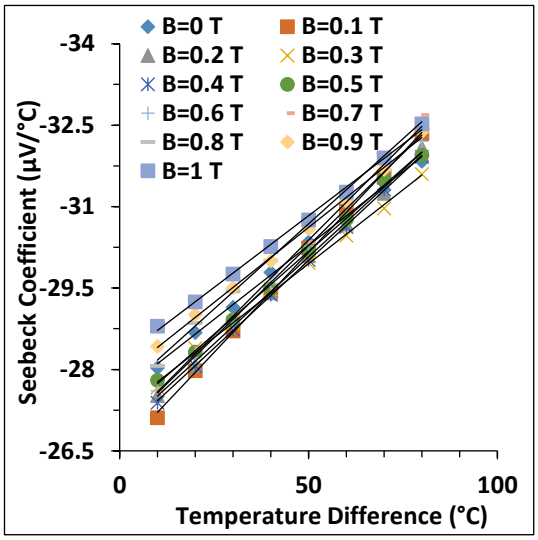

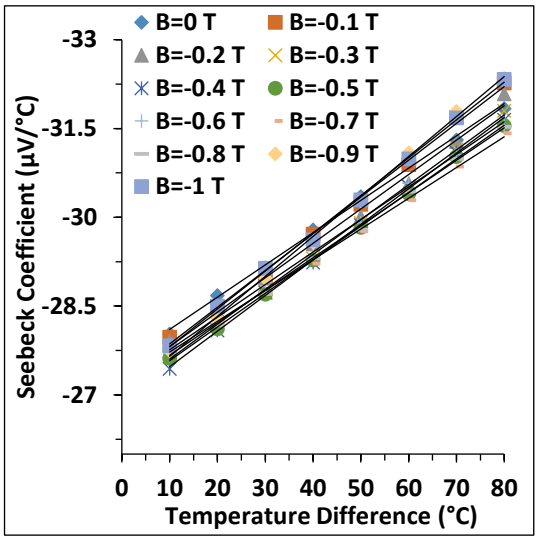

Variation of the Seebeck coefficient with temperature difference for DP0.25% sample.

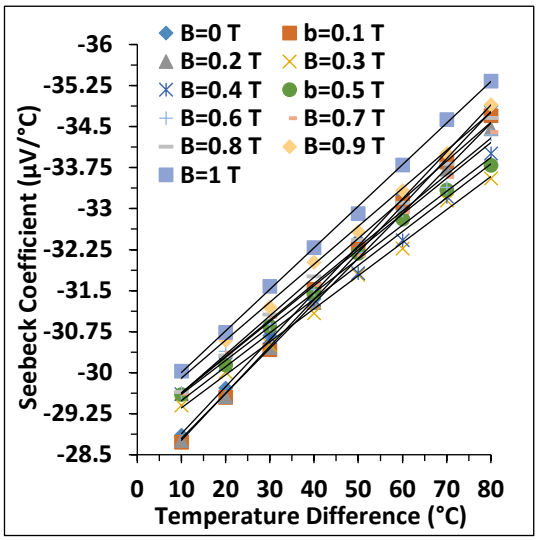

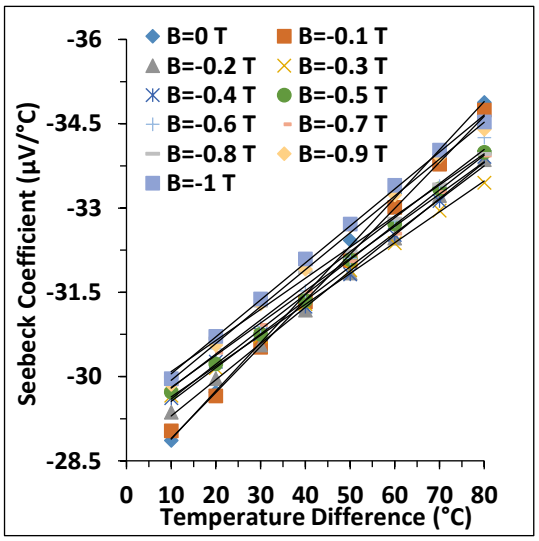

Comparison the Seebeck coefficient with temperature difference under various DC magnetic field density for all samples.

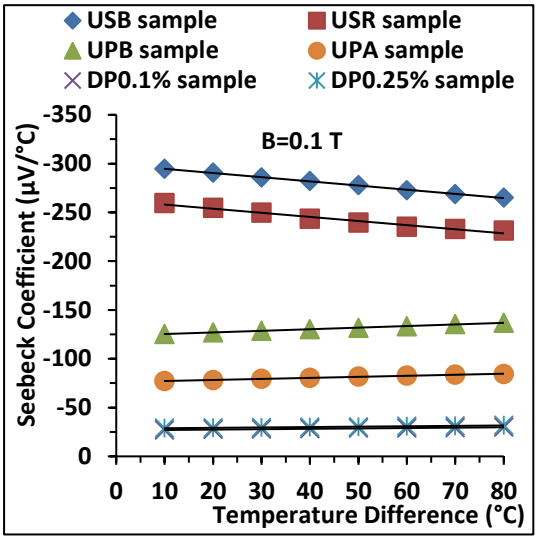

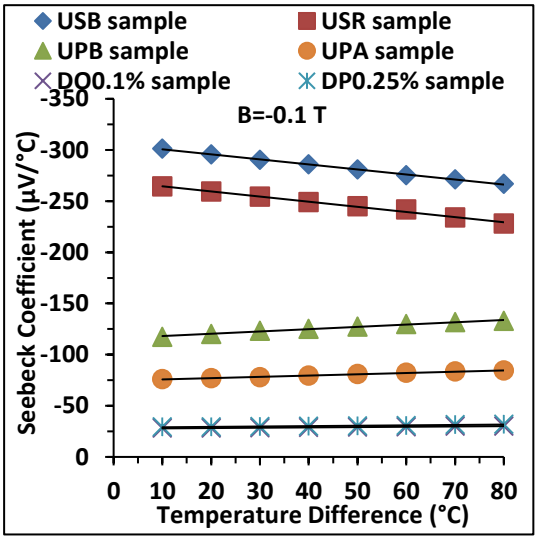

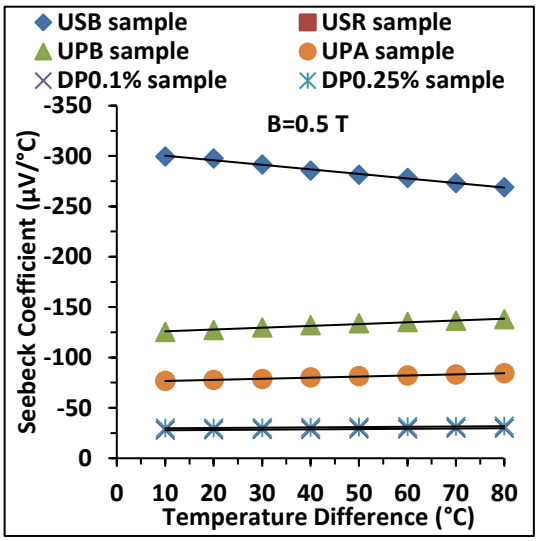

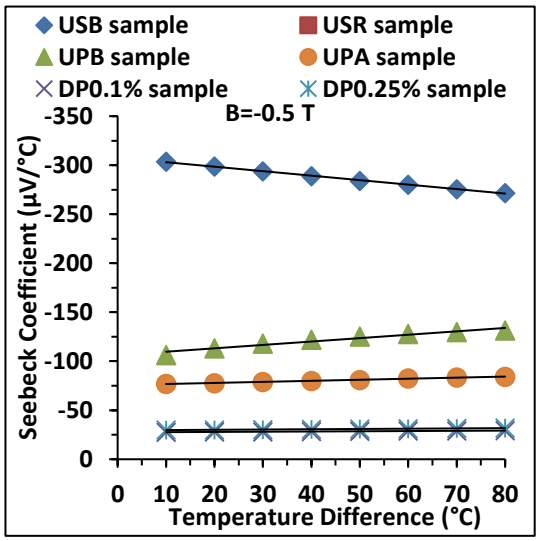

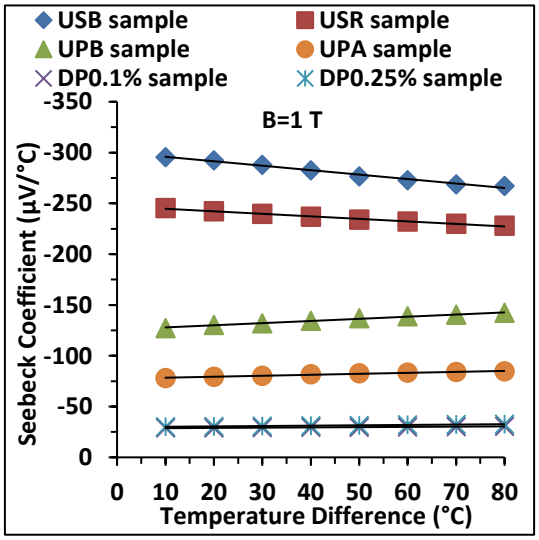

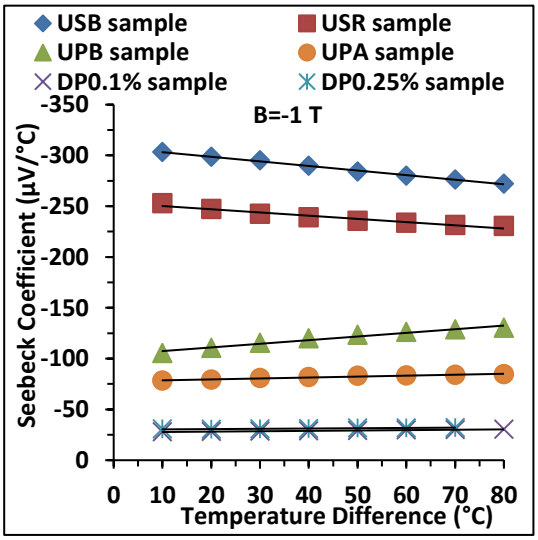

Appendex 7:

Variation of the Seebeck coefficient with DC magnetic field density for:

a) USR sample

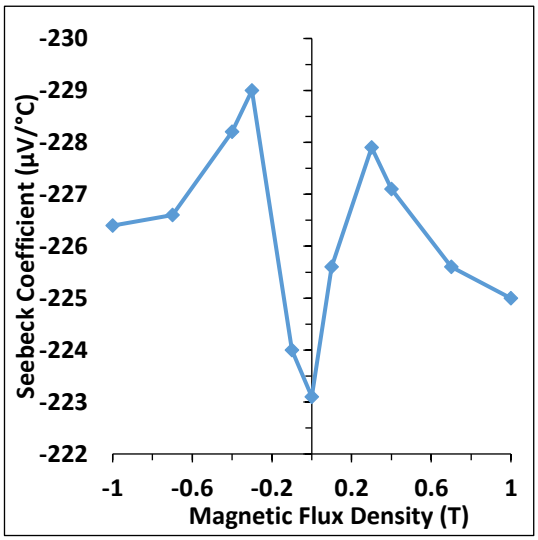

b) UPB sample

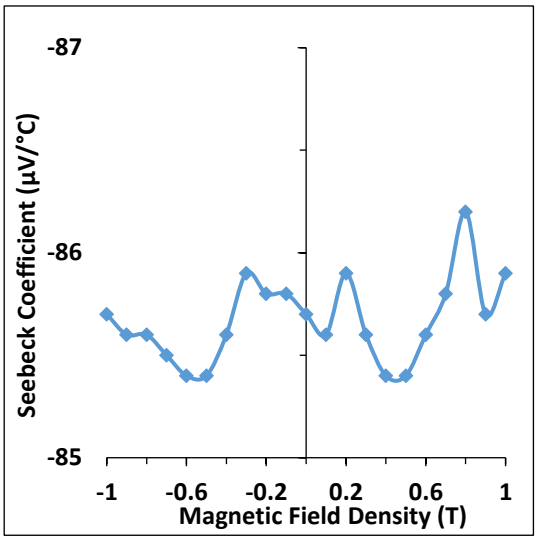

c) DP0.1% sample

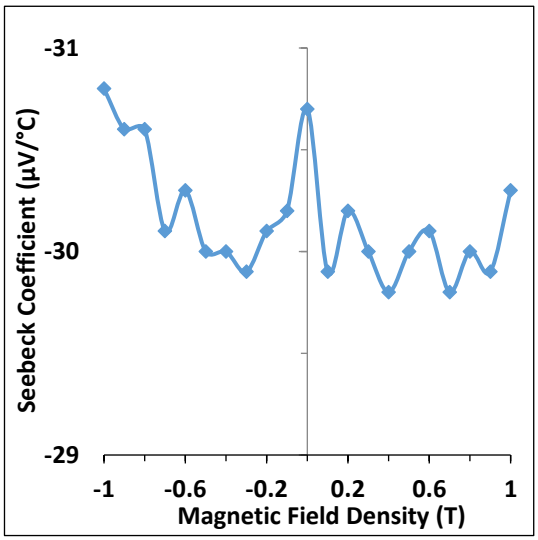

d) DP0.25% sample

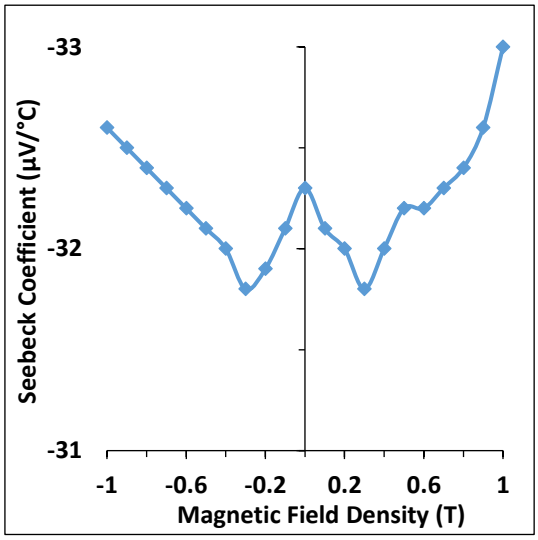

Appendix 8:

Variation of the total transverse voltage with temperature difference at various DC magnetic field density for USR sample.

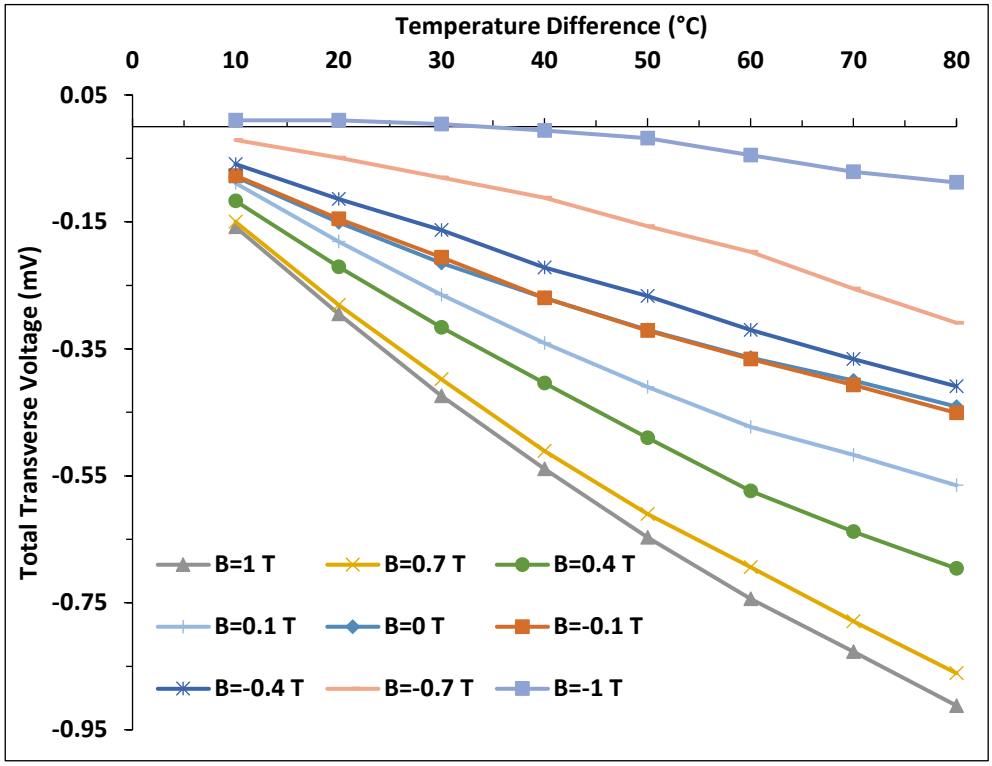

Variation of the total transverse voltage with temperature difference at various DC magnetic field density for UPB samples.

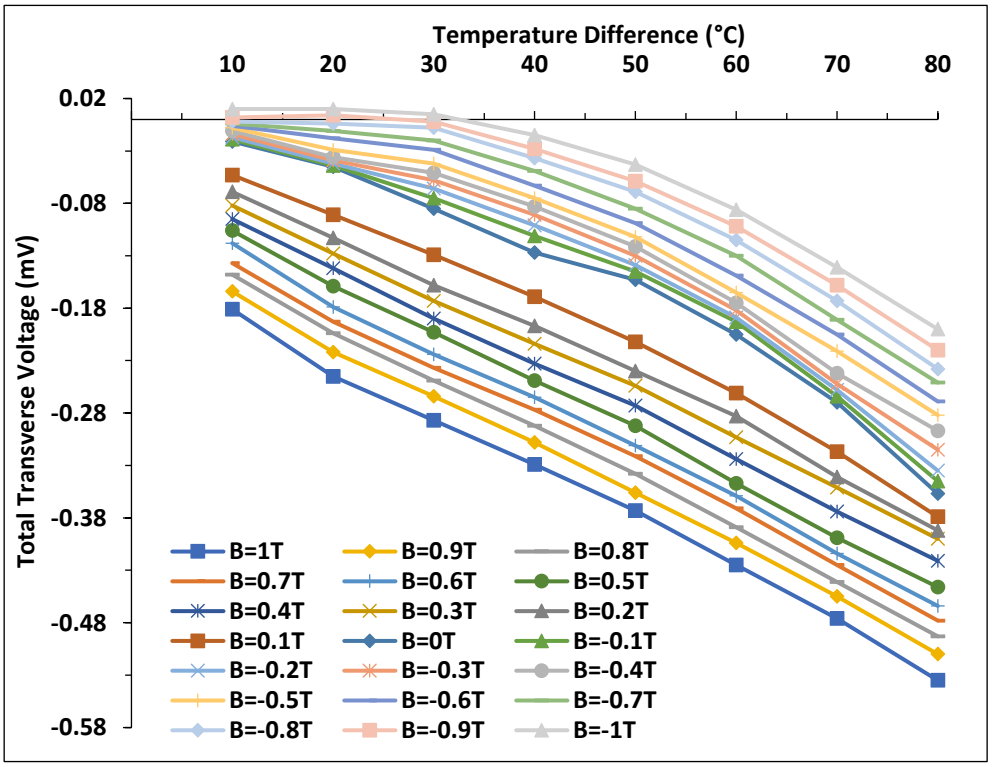

Variation of the total transverse voltage with temperature difference at various DC magnetic field density for DP0.1% samples.

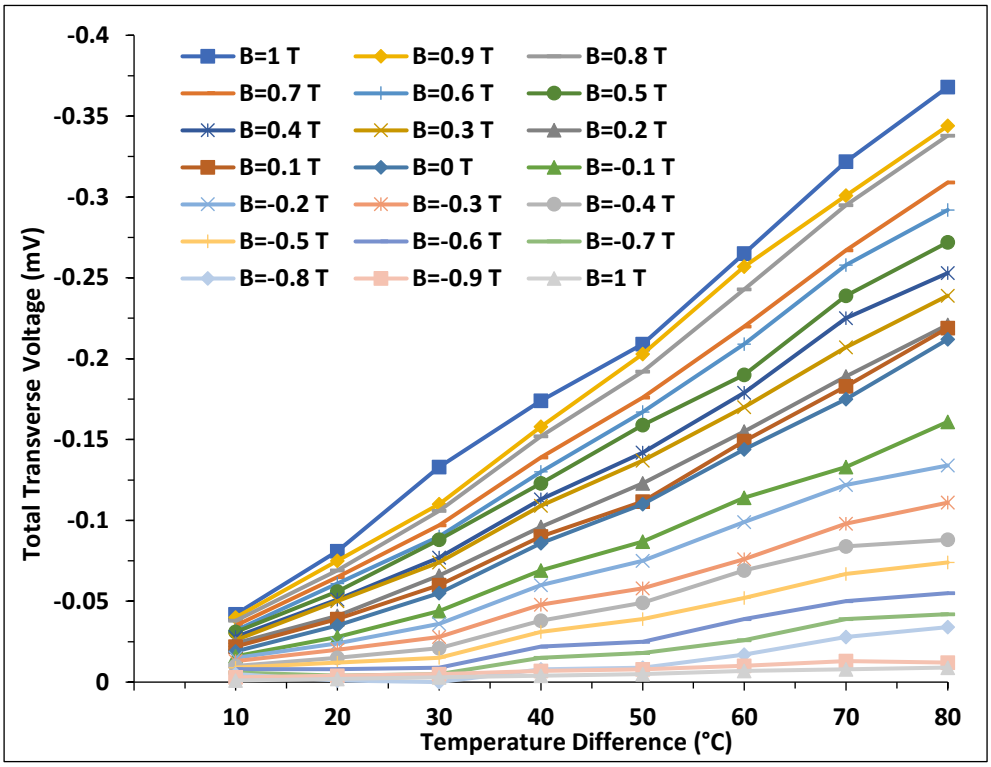

Variation of the total transverse voltage with temperature difference at various Dc magnetic field density for DP0.25% samples.

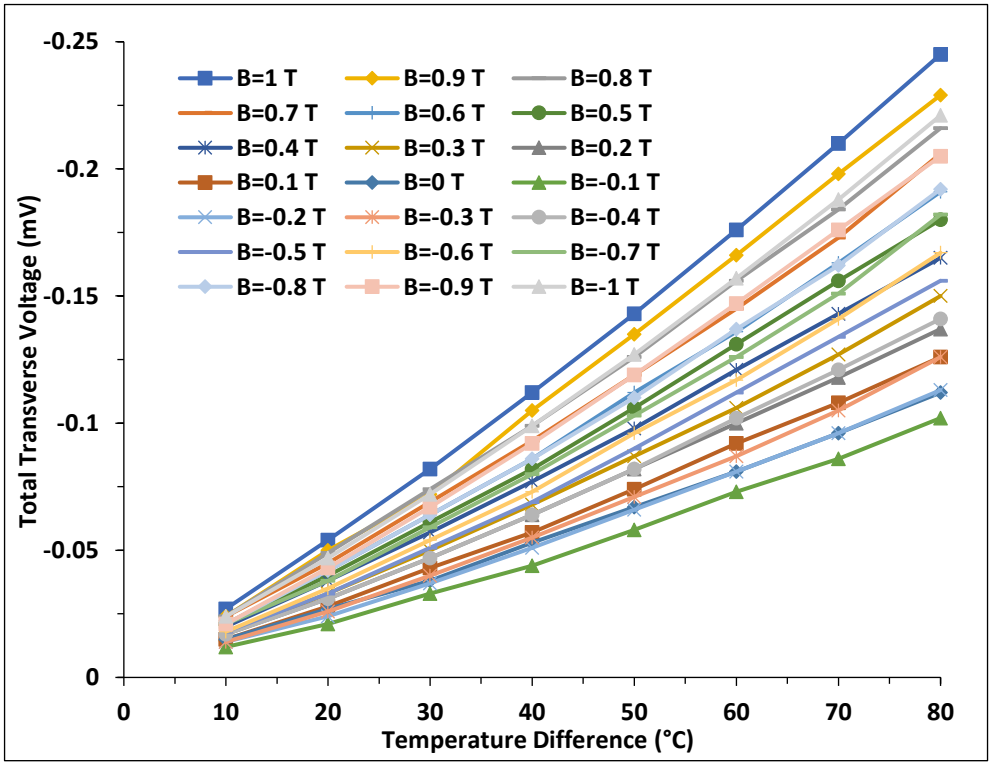

Comparison the total transverse voltage with temperature difference at various Dc magnetic field density for all samples.

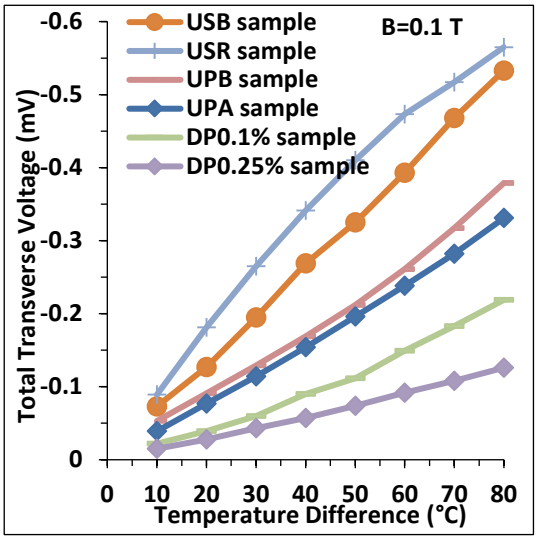

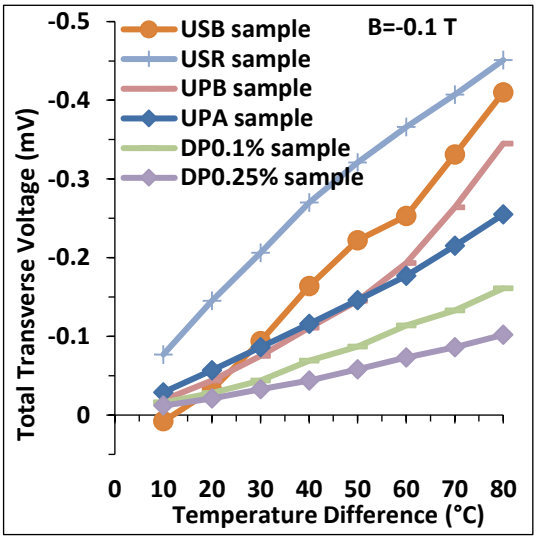

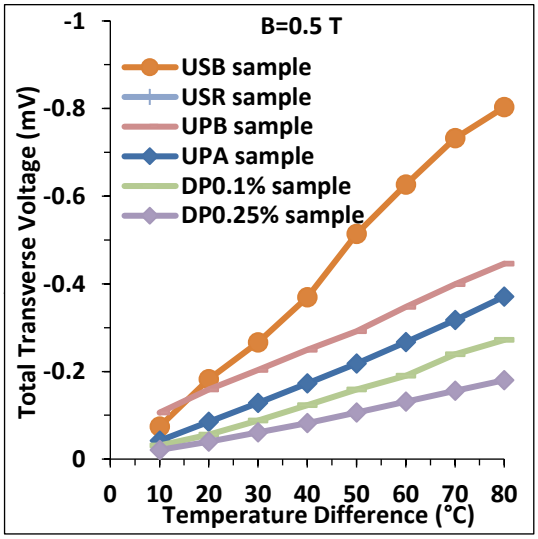

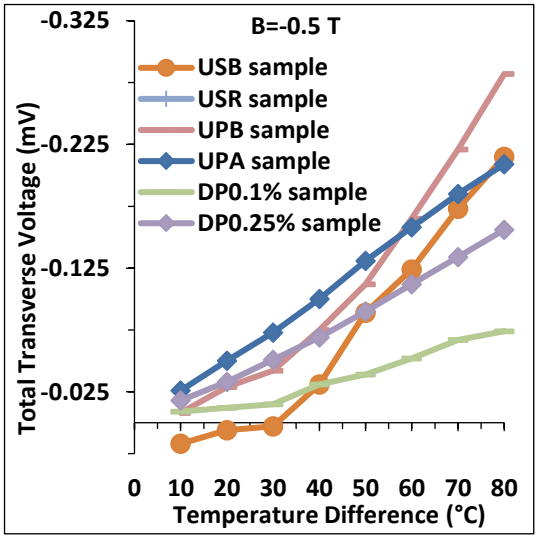

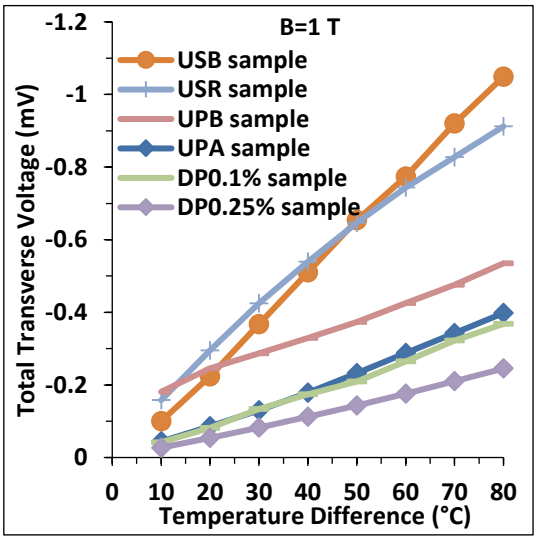

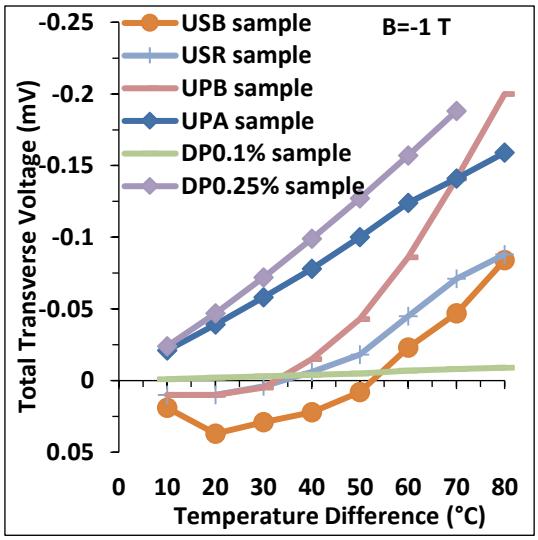

Appendex 9:

The Nernst and Righi-Leduc voltage and thermomagnetic power for USB sample for various temperature differences and magnetic flux densities.

B (T) \ ΔT(°C)		10	20	30	40	50	60	70	80
1	V_N	-1.493	-1.676	-1.040	-1.3355	-1.623	-1.8915	-2.106	-2.2785
	V_R	1.423	1.543	0.838	1.0285	1.219	1.4675	1.592	1.7145
	NB	-970.45	-544.7	-225.33	-217.02	-210.93	-204.91	-195.53	-185.11
0.9	V_N	-1.2875	-1.593	-0.946	-1.2035	-1.4365	-1.677	-1.8815	-2.077
	V_R	1.2235	1.466	0.772	0.9265	1.0645	1.268	1.4075	1.54
	NB	-836.87	-517.72	-204.96	-195.58	-186.73	-181.62	-174.75	-168.75
0.8	V_N	-1.2045	-1.4195	-0.8415	-1.046	-1.247	-1.4385	-1.6335	-1.7915
	V_R	1.1425	1.3075	0.6905	0.802	0.919	1.0625	1.1745	1.3045
	NB	-782.92	-461.33	-182.39	-169.90	-162.1	-155.83	-151.67	-145.51
0.7	V_N	-1.1115	-1.2885	-0.7175	-0.9055	-1.0725	-1.207	-1.3695	-1.5095
	V_R	1.0415	1.1725	0.5515	0.6465	0.7235	0.837	0.9315	1.0555
	NB	-722.47	-418.76	-155.41	-147.15	-139.4	-130.75	-127.13	-122.62
0.6	V_N	-1.022	-0.974	-0.627	-0.7755	-0.9045	-1.017	-1.143	-1.262
	V_R	0.959	0.88	0.488	0.5445	0.6255	0.726	0.798	0.87
	NB	-664.3	-316.55	-135.80	-126.02	-117.58	-110.95	-106.18	-102.53
0.5	V_N	-0.911	-0.812	-0.5675	-0.6835	-0.7725	-0.8825	-0.979	-1.0205
	V_R	0.867	0.75	0.4765	0.5115	0.5085	0.6065	0.653	0.7025
	NB	-592.15	-263.9	-122.99	-111.07	-100.42	-95.604	-90.903	-82.968
0.4	V_N	-0.7165	-0.632	-0.478	-0.5615	-0.652	-0.7235	-0.774	-0.8325
	V_R	0.6615	0.551	0.369	0.3875	0.429	0.5175	0.485	0.5165
	NB	-465.72	-205.4	-103.56	-91.243	-84.79	-78.387	-71.882	-67.634
0.3	V_N	-0.6355	-0.563	-0.341	-0.401	-0.438	-0.4695	-0.504	-0.538
	V_R	0.5835	0.513	0.29	0.286	0.261	0.2995	0.33	0.366
	NB	-413.07	-182.97	-73.883	-65.168	-56.91	-50.862	-46.853	-43.712
0.2	V_N	-0.5505	-0.468	-0.2255	-0.261	-0.271	-0.265	-0.279	-0.305
	V_R	0.5065	0.428	0.1845	0.177	0.161	0.169	0.184	0.22
	NB	-357.82	-152.1	-48.858	-42.418	-35.23	-28.708	-25.885	-24.781
0.1	V_N	-0.144	-0.13	-0.1365	-0.157	-0.1585	-0.1555	-0.1475	-0.134
	V_R	0.101	0.093	0.1065	0.091	0.0835	0.1125	0.0855	0.086
	NB	-93.6	-42.25	-29.575	-25.512	-20.505	-16.858	-13.703	-10.903

0	V_N	0	0	0	0	0	0	0	0
	V_R	0	0	0	0	0	0	0	0
	NB	0	0	0	0	0	0	0	0
-0.1	V_N	-0.144	-0.13	-0.136	-0.157	-0.158	-0.155	-0.147	-0.134
	V_R	-0.106	-0.072	-0.065	-0.118	-0.130	-0.058	-0.072	-0.059
	NB	93.6	42.25	29.575	25.5125	20.505	16.8583	13.7035	10.9031
-0.2	V_N	-0.550	-0.468	-0.225	-0.261	-0.271	-0.265	-0.279	-0.305
	V_R	-0.515	-0.405	-0.119	-0.157	-0.17	-0.139	-0.171	-0.174
	NB	357.825	152.1	48.8583	42.4187	35.23	28.7083	25.8857	24.7812
-0.3	V_N	-0.635	-0.563	-0.341	-0.401	-0.438	-0.469	-0.504	-0.538
	V_R	-0.602	-0.492	-0.222	-0.272	-0.341	-0.337	-0.36	-0.384
	NB	413.075	182.975	73.8833	65.1687	56.91	50.8625	46.8535	43.7125
-0.4	V_N	-0.716	-0.632	-0.478	-0.5615	-0.652	-0.723	-0.774	-0.8325
	V_R	-0.683	-0.535	-0.333	-0.4215	-0.509	-0.537	-0.588	-0.6305
	NB	465.725	205.4	103.566	91.24375	84.79	78.3875	71.8821	67.6343
-0.5	V_N	-0.911	-0.812	-0.567	-0.6835	-0.772	-0.882	-0.979	-1.0205
	V_R	-0.864	-0.716	-0.399	-0.5115	-0.611	-0.656	-0.746	-0.7505
	NB	592.15	263.9	122.991	111.075	100.425	95.6041	90.9035	82.9687
-0.6	V_N	-1.022	-0.974	-0.627	-0.7755	-0.904	-1.017	-1.143	-1.262
	V_R	-0.967	-0.854	-0.458	-0.5665	-0.695	-0.743	-0.859	-0.946
	NB	664.3	316.55	135.808	126.025	117.58	110.954	106.185	102.534
-0.7	V_N	-1.111	-1.288	-0.717	-0.9055	-1.072	-1.207	-1.369	-1.5095
	V_R	-1.059	-1.170	-0.540	-0.6985	-0.864	-0.918	-1.071	-1.1875
	NB	722.475	418.762	155.416	147.156	139.4	130.758	127.135	122.621
-0.8	V_N	-1.204	-1.419	-0.841	-1.046	-1.247	-1.438	-1.633	-1.7915
	V_R	-1.162	-1.301	-0.653	-0.841	-1.037	-1.146	-1.343	-1.4445
	NB	782.925	461.337	182.391	169.906	162.1	155.837	151.675	145.5125
-0.9	V_N	-1.287	-1.593	-0.946	-1.2035	-1.436	-1.67	-1.881	-2.077
	V_R	-1.242	-1.469	-0.755	-0.9845	-1.197	-1.381	-1.576	-1.728
	NB	836.875	517.725	204.966	195.581	186.735	181.625	174.753	168.756
-1	V_N	-1.493	-1.676	-1.04	-1.3355	-1.623	-1.891	-2.106	-2.2785
	V_R	-1.444	-1.549	-0.846	-1.1105	-1.365	-1.564	-1.747	-1.8775
	NB	970.45	544.7	225.333	217.025	210.935	204.912	195.539	185.115

The Nernst and Righi-Leduc voltage and thermomagnetic power for USR sample for various temperature differences and magnetic flux densities.

B (T) \ ΔT(°C)		10	20	30	40	50	60	70	80
1	V_N	-1.921	-2.521	-1.845	-1.936	-1.9415	-2.017	-2.04	-2.0565
	V_R	1.774	2.24	1.465	1.482	1.4105	1.469	1.485	1.4165
	NB	-901.39	-591.46	-288.57	-227.10	-182.20	-157.73	-136.74	-120.62
0.7	V_N	-1.317	-1.9565	-1.267	-1.306	-1.322	-1.3335	-1.3465	-1.359
	V_R	1.23	1.7825	1.045	1.06	1.027	1.0715	1.1045	1.059
	NB	-617.97	-459.02	-198.17	-153.20	-124.06	-104.28	-90.259	-79.710
0.4	V_N	-0.7875	-1.193	-0.961	-0.7375	-0.7505	-0.7605	-0.763	-0.781
	V_R	0.7375	1.099	0.856	0.5805	0.5865	0.5955	0.575	0.595
	NB	-369.51	-279.89	-150.31	-86.514	-70.431	-59.475	-51.146	-45.808
0.1	V_N	-0.279	-0.4045	-0.3885	-0.408	-0.379	-0.3605	-0.36	-0.372
	V_R	0.27	0.3765	0.3405	0.33	0.308	0.3145	0.337	0.244
	NB	-130.91	-94.901	-60.765	-47.861	-35.567	-28.192	-24.131	-21.819
0	V_N	0	0	0	0	0	0	0	0
	V_R	0	0	0	0	0	0	0	0
	NB	0	0	0	0	0	0	0	0
-0.1	V_N	0.279	0.4045	0.3885	0.408	0.379	0.3605	0.36	0.372
	V_R	-0.277	-0.423	-0.417	-0.433	-0.409	-0.411	-0.38	-0.414
	NB	130.9153	94.9019	60.7653	47.8615	35.5676	28.1929	24.1318	21.8192
-0.4	V_N	0.7875	1.193	0.961	0.7375	0.7505	0.7605	0.763	0.781
	V_R	-0.7335	-1.102	-0.838	-0.584	-0.585	-0.565	-0.546	-0.589
	NB	369.51	279.89	150.31	86.514	70.431	59.475	51.146	45.808
-0.7	V_N	1.317	1.9565	1.267	1.306	1.322	1.3335	1.3465	1.359
	V_R	-1.18	-1.696	-0.884	-0.816	-0.755	-0.677	-0.616	-0.6
	NB	617.97	459.02	198.17	153.20	124.06	104.28	-90.259	79.710
-1	V_N	1.921	2.521	1.845	1.936	1.9415	2.017	2.04	2.0565
	V_R	-1.822	-2.335	-1.577	-1.599	-1.551	-1.568	-1.518	-1.534
	NB	901.392	591.465	288.576	227.107	182.202	157.739	136.747	120.621

The Nernst and Righi-Leduc voltage and thermomagnetic power for UPB sample for various temperature differences and magnetic flux densities.

ΔT (°C) / B (T)		10	20	30	40	50	60	70	80
1	V_N	-1.96	-2.327	-1.807	-1.1695	-0.999	-1.06	-1.094	-1.19
	V_R	1.8	2.127	1.605	0.9615	0.779	0.84	0.888	1.012
	NB	-1728.3	-1025.9	-531.14	-257.82	-176.18	-155.78	-137.81	-131.17
0.9	V_N	-1.758	-2.1135	-1.614	-1.0955	-0.903	-0.943	-0.991	-1.075
	V_R	1.615	1.9365	1.435	0.9085	0.7	0.744	0.806	0.922
	NB	-1550.2	-931.86	-474.41	-241.50	-159.25	-138.59	-124.84	-118.49
0.8	V_N	-1.535	-1.865	-1.446	-0.9955	-0.808	-0.8535	-0.924	-0.972
	V_R	1.408	1.706	1.282	0.8245	0.623	0.6695	0.753	0.836
	NB	-1353.5	-822.29	-425.03	-219.46	-142.50	-125.43	-116.4	-107.14
0.7	V_N	-1.3185	-1.684	-1.2675	-0.815	-0.6465	-0.693	-0.787	-0.8505
	V_R	1.2025	1.536	1.1155	0.659	0.4785	0.527	0.632	0.7295
	NB	-1162.6	-742.49	-372.56	-179.67	-114.01	-101.85	-99.141	-93.748
0.6	V_N	-1.129	-1.455	-1.0595	-0.6885	-0.5625	-0.587	-0.661	-0.721
	V_R	1.032	1.321	0.9205	0.5445	0.4045	0.433	0.517	0.614
	NB	-995.57	-641.52	-311.42	-151.78	-99.204	-86.271	-83.268	-79.473
0.5	V_N	-0.979	-1.2505	-0.915	-0.555	-0.471	-0.4963	-0.545	-0.605
	V_R	0.894	1.1365	0.797	0.427	0.332	0.3543	0.416	0.516
	NB	-863.3	-551.35	-268.95	-122.35	-83.067	-72.941	-68.655	-66.687
0.4	V_N	-0.825	-1.073	-0.7295	-0.4695	-0.368	-0.416	-0.4395	-0.4921
	V_R	0.751	0.976	0.6245	0.3575	0.248	0.297	0.3355	0.4281
	NB	-727.5	-473.09	-214.42	-103.50	-64.901	-61.139	-55.365	-54.242
0.3	V_N	-0.678	-0.926	-0.4764	-0.3383	-0.2881	-0.3297	-0.3541	-0.3809
	V_R	0.617	0.843	0.38842	0.2453	0.1871	0.2317	0.2731	0.33797
	NB	-597.87	-408.28	-140.03	-74.579	-50.810	-48.455	-44.607	-41.993
0.2	V_N	-0.437	-0.561	-0.335	-0.2088	-0.1765	-0.1945	-0.205	-0.2335
	V_R	0.389	0.493	0.262	0.132	0.0895	0.1165	0.134	0.1985
	NB	-385.35	-247.35	-98.47	-45.855	-31.128	-28.586	-25.825	-25.738
0.1	V_N	-0.2275	-0.2265	-0.146	-0.1105	-0.123	-0.1425	-0.1565	-0.169
	V_R	0.1955	0.1805	0.102	0.0625	0.064	0.0865	0.1095	0.147
	NB	-200.61	-99.865	-42.915	-24.360	-21.692	-20.943	-19.714	-18.628

0	V_N	0	0	0	0	0	0	0	0
	V_R	0	0	0	0	0	0	0	0
	NB	0	0	0	0	0	0	0	0
-0.1	V_N	0.2275	0.2265	0.146	0.1105	0.123	0.1425	0.1565	0.169
	V_R	-0.2255	-0.225	-0.136	-0.1005	-0.115	-0.130	-0.150	-0.157
	NB	200.613	99.8659	42.9151	24.3602	21.6927	20.9431	19.7149	18.6284
-0.2	V_N	0.437	0.561	0.144	0.168	0.177	0.195	0.205	0.234
	V_R	-0.433	-0.558	-0.316	-0.188	-0.162	-0.178	-0.193	-0.2115
	NB	385.35	247.35	42.18	37.036	31.128	28.586	25.825	25.738
-0.3	V_N	0.678	0.926	0.47642	0.3383	0.2881	0.3297	0.3541	0.38097
	V_R	-0.671	-0.92	-0.4494	-0.3083	-0.265	-0.306	-0.336	-0.3389
	NB	597.872	408.281	140.038	74.5797	50.8103	48.4559	44.6074	41.9932
-0.4	V_N	0.825	1.073	0.7295	0.4695	0.368	0.416	0.4395	0.4921
	V_R	-0.815	-1.064	-0.6955	-0.4315	-0.336	-0.386	-0.411	-0.4321
	NB	727.5	473.095	214.428	103.503	64.9018	61.1393	55.3655	54.2428
-0.5	V_N	0.979	1.2505	0.915	0.555	0.471	0.4963	0.545	0.605
	V_R	-0.966	-1.234	-0.872	-0.509	-0.43	-0.456	-0.496	-0.53
	NB	863.3	551.356	268.954	122.352	83.0672	72.9410	68.6558	66.6875
-0.6	V_N	1.129	1.455	1.0595	0.6885	0.5625	0.587	0.661	0.721
	V_R	-1.114	-1.428	-1.0035	-0.6305	-0.508	-0.531	-0.596	-0.633
	NB	995.572	641.522	311.428	151.782	99.2045	86.2712	83.2688	79.4738
-0.7	V_N	1.3185	1.684	1.2675	0.815	0.6465	0.693	0.787	0.8505
	V_R	-1.3015	-1.65	-1.2025	-0.743	-0.578	-0.618	-0.708	-0.7445
	NB	1162.677	742.490	372.568	179.6704	114.019	101.85	99.1415	93.7482
-0.8	V_N	1.535	1.865	1.446	0.9955	0.808	0.8535	0.924	0.972
	V_R	-1.516	-1.824	-1.369	-0.9115	-0.724	-0.763	-0.827	-0.853
	NB	1353.59	822.295	425.036	219.4625	142.501	125.438	116.4	107.140
-0.9	V_N	1.758	2.1135	1.614	1.0955	0.903	0.943	0.991	1.075
	V_R	-1.735	-2.064	-1.531	-1.0025	-0.809	-0.84	-0.879	-0.938
	NB	1550.23	931.861	474.418	241.507	159.256	138.592	124.840	118.494
-1	V_N	1.96	2.327	1.807	1.1695	0.999	1.06	1.094	1.19
	V_R	-1.929	-2.272	-1.717	-1.0635	-0.889	-0.941	-0.965	-1.033
	NB	1728.36	1025.99	531.148	257.821	176.187	155.787	137.815	131.170

The Nernst and Righi-Leduc voltage and thermomagnetic power for UPA sample for various temperature differences and magnetic flux densities.

B (T) \ ΔT (°C)		10	20	30	40	50	60	70	80
1	V_N	-1.3585	-1.499	-1.3495	-1.4475	-1.529	-1.556	-1.652	-1.7475
	V_R	1.2965	1.474	1.3125	1.3945	1.465	1.477	1.565	1.6395
	NB	-916.46	-545.80	-327.57	-263.52	-222.68	-188.85	-171.85	-159.07
0.9	V_N	-1.1485	-1.385	-1.1755	-1.271	-1.3325	-1.37	-1.484	-1.5495
	V_R	1.1375	1.362	1.1395	1.219	1.2725	1.305	1.411	1.4555
	NB	-836.35	-504.29	-285.34	-231.39	-194.07	-166.27	-154.38	-141.04
0.8	V_N	-1.045	-1.2045	-1.0605	-1.0465	-1.1465	-1.225	-1.3885	-1.416
	V_R	1.035	1.1835	1.0265	0.9965	1.0905	1.163	1.3195	1.324
	NB	-760.98	-438.57	-257.42	-190.52	-166.98	-148.67	-144.44	-128.89
0.7	V_N	-1.0095	-1.045	-0.8345	-0.8735	-0.953	-1.0115	-1.047	-1.1365
	V_R	1.0005	1.025	0.8015	0.8245	0.9	0.9515	0.981	1.0465
	NB	-735.13	-380.49	-202.56	-159.02	-138.79	-122.76	-108.92	-103.45
0.6	V_N	-0.8845	-0.913	-0.6905	-0.678	-0.7105	-0.7445	-0.784	-0.823
	V_R	0.8755	0.894	0.6565	0.631	0.6605	0.6865	0.721	0.735
	NB	-644.11	-332.43	-167.61	-123.43	-103.48	-90.359	-81.560	-74.915
0.5	V_N	-0.809	-0.8475	-0.633	-0.5345	-0.5965	-0.6355	-0.696	-0.754
	V_R	0.799	0.8235	0.598	0.4865	0.5465	0.5775	0.634	0.673
	NB	-589.12	-308.58	-153.65	-97.308	-86.876	-77.130	-72.405	-68.634
0.4	V_N	-0.7115	-0.7365	-0.5425	-0.381	-0.4365	-0.494	-0.5575	-0.5815
	V_R	0.7025	0.7165	0.5135	0.336	0.3905	0.441	0.5005	0.5075
	NB	-518.12	-268.16	-131.68	-69.362	-63.573	-59.956	-57.997	-52.932
0.3	V_N	-0.5515	-0.639	-0.4815	-0.348	-0.3285	-0.359	-0.395	-0.411
	V_R	0.5425	0.621	0.4565	0.309	0.2875	0.31	0.342	0.344
	NB	-401.61	-232.66	-116.87	-63.355	-47.844	-43.571	-41.092	-37.412
0.2	V_N	-0.361	-0.4605	-0.327	-0.229	-0.1965	-0.2225	-0.244	-0.264
	V_R	0.353	0.4455	0.304	0.195	0.1615	0.1785	0.195	0.204
	NB	-262.88	-167.67	-79.375	-41.690	-28.619	-27.004	-25.383	-24.031
0.1	V_N	-0.302	-0.3855	-0.215	-0.1315	-0.1505	-0.165	-0.188	-0.2
	V_R	0.295	0.3695	0.194	0.1025	0.1225	0.136	0.161	0.159
	NB	-219.92	-140.36	-52.189	-23.940	-21.919	-20.026	-19.557	-18.205

0	V_N	0	0	0	0	0	0	0	0
	V_R	0	0	0	0	0	0	0	0
	NB	0	0	0	0	0	0	0	0
-0.1	V_N	0.302	0.3855	0.215	0.1315	0.1505	0.165	0.188	0.2
	V_R	-0.299	-0.381	-0.208	-0.122	-0.128	-0.133	-0.148	-0.165
	NB	219.92	140.36	52.189	23.940	21.919	20.026	19.557	18.205
-0.2	V_N	0.361	0.4605	0.327	0.229	0.1965	0.2225	0.244	0.264
	V_R	-0.354	-0.454	-0.316	-0.216	-0.169	-0.185	-0.194	-0.214
	NB	262.88	167.67	79.375	41.690	28.619	27.004	25.383	24.031
-0.3	V_N	0.5515	0.639	0.4815	0.348	0.3285	0.359	0.395	0.411
	V_R	-0.5465	-0.63	-0.4665	-0.328	-0.298	-0.316	-0.336	-0.344
	NB	401.61	232.66	116.87	63.355	47.844	43.571	41.092	37.412
-0.4	V_N	0.7115	0.7365	0.5425	0.381	0.4365	0.494	0.5575	0.5815
	V_R	-0.7055	-0.726	-0.5255	-0.359	-0.403	-0.448	-0.492	-0.506
	NB	518.12	268.16	131.68	69.362	63.573	59.956	57.997	52.932
-0.5	V_N	0.809	0.8475	0.633	0.5345	0.5965	0.6355	0.696	0.754
	V_R	-0.803	-0.836	-0.613	-0.509	-0.559	-0.584	-0.626	-0.673
	NB	589.12	308.58	153.65	97.308	86.876	77.130	72.405	68.634
-0.6	V_N	0.8845	0.913	0.6905	0.678	0.7105	0.7445	0.784	0.823
	V_R	-0.8785	-0.903	-0.6725	-0.653	-0.670	-0.689	-0.709	-0.739
	NB	644.11	332.43	167.61	123.43	103.48	90.359	81.560	74.915
-0.7	V_N	1.0095	1.045	0.8345	0.8735	0.953	1.0115	1.047	1.1365
	V_R	-1.0035	-1.032	-0.8115	-0.843	-0.908	-0.951	-0.967	-1.046
	NB	735.137	380.49	202.56	159.02	138.79	122.76	108.92	103.45
-0.8	V_N	1.045	1.2045	1.0605	1.0465	1.1465	1.225	1.3885	1.416
	V_R	-1.036	-1.188	-1.0335	-1.011	-1.093	-1.156	-1.298	-1.316
	NB	760.989	438.57	257.425	190.52	166.98	148.678	144.447	128.894
-0.9	V_N	1.1485	1.385	1.1755	1.271	1.3325	1.37	1.484	1.5495
	V_R	-1.1395	-1.367	-1.1475	-1.233	-1.273	-1.291	-1.382	-1.437
	NB	836.359	504.29	285.340	231.39	194.07	166.276	154.382	141.046
-1	V_N	1.3585	1.499	1.3495	1.4475	1.529	1.556	1.652	1.7475
	V_R	-1.2975	-1.477	-1.3145	-1.400	-1.461	-1.471	-1.538	-1.616
	NB	916.463	545.80	327.57	263.52	222.68	188.851	171.859	159.070

The Nernst and Righi-Leduc voltage and thermomagnetic power for DP0.1% sample for various temperature differences and magnetic flux densities.

ΔT (°C) / B (T)		10	20	30	40	50	60	70	80
1	V_N	-2.529	-2.6385	-1.9655	-1.929	-1.9335	-1.9395	-1.9405	-1.9505
	V_R	2.506	2.5925	1.8875	1.841	1.8345	1.8185	1.7935	1.7945
	NB	-3225.7	-1682.7	-835.67	-615.11	-493.23	-412.30	-353.58	-310.98
0.9	V_N	-2.303	-2.4895	-1.731	-1.639	-1.6505	-1.6835	-1.7049	-1.7115
	V_R	2.282	2.4495	1.676	1.567	1.5575	1.5705	1.5789	1.5795
	NB	-2937.5	-1587.6	-735.96	-522.64	-421.04	-357.88	-310.65	-272.87
0.8	V_N	-1.92	-2.155	-1.3105	-1.3534	-1.3861	-1.4086	-1.4591	-1.4955
	V_R	1.901	2.121	1.2595	1.28745	1.3041	1.3096	1.3391	1.3695
	NB	-2448.9	-1374.3	-557.18	-431.58	-353.59	-299.44	-265.87	-238.44
0.7	V_N	-1.285	-1.553	-1.0756	-1.1008	-1.1253	-1.1574	-1.1787	-1.2031
	V_R	1.269	1.523	1.0336	1.0478	1.0593	1.0814	1.0867	1.1061
	NB	-1639.0	-990.43	-457.31	-351.02	-287.06	-246.04	-214.77	-191.82
0.6	V_N	-1.2	-1.48	-0.845	-0.8665	-0.913	-0.942	-0.975	-1.0125
	V_R	1.187	1.454	0.81	0.8225	0.856	0.877	0.892	0.9325
	NB	-1530.6	-943.87	-359.26	-276.30	-232.90	-200.25	-177.66	-161.43
0.5	V_N	-1.088	-1.151	-0.7305	-0.7525	-0.769	-0.785	-0.8105	-0.8325
	V_R	1.076	1.13	0.6975	0.7155	0.72	0.739	0.7465	0.7725
	NB	-1387.7	-734.05	-310.58	-239.95	-196.17	-166.87	-147.68	-132.73
0.4	V_N	-0.8785	-0.967	-0.6165	-0.531	-0.564	-0.58	-0.6145	-0.6305
	V_R	0.8695	0.951	0.5945	0.504	0.532	0.545	0.5645	0.5895
	NB	-1120.5	-616.70	-262.11	-169.32	-143.87	-123.29	-111.97	-100.52
0.3	V_N	-0.4845	-0.606	-0.447	-0.3535	-0.37	-0.396	-0.4415	-0.481
	V_R	0.4775	0.591	0.428	0.3305	0.343	0.37	0.4095	0.454
	NB	-617.98	-386.48	-190.05	-112.72	-94.387	-84.183	-80.448	-76.690
0.2	V_N	-0.344	-0.4165	-0.2989	-0.1746	-0.2183	-0.2477	-0.2704	-0.2771
	V_R	0.339	0.4105	0.28795	0.1646	0.2053	0.2367	0.2564	0.2681
	NB	-438.77	-265.62	-127.10	-55.676	-55.688	-52.657	-49.271	-44.180
0.1	V_N	-0.134	-0.1585	-0.1103	-0.1010	-0.1053	-0.1178	-0.1278	-0.1308
	V_R	0.133	0.1575	0.10533	0.10207	0.1073	0.12588	0.13387	0.1438
	NB	-170.91	-101.08	-46.909	-32.228	-26.862	-25.059	-23.299	-20.854

0	V_N	0	0	0	0	0	0	0	0
	V_R	0	0	0	0	0	0	0	0
	NB	0	0	0	0	0	0	0	0
-0.1	V_N	0.134	0.1585	0.11033	0.10107	0.1053	0.1178	0.12787	0.1308
	V_R	-0.131	-0.151	-0.099	-0.084	-0.0823	-0.087	-0.0858	-0.0798
	NB	170.918	101.084	46.9090	32.228	26.8622	25.059	23.2999	20.8545
-0.2	V_N	0.344	0.4165	0.2989	0.1746	0.2183	0.2477	0.2704	0.2771
	V_R	-0.34	-0.405	-0.279	-0.148	-0.1733	-0.202	-0.2174	-0.1991
	NB	438.77	265.62	127.10	55.676	55.688	52.657	49.271	44.180
-0.3	V_N	0.4845	0.606	0.447	0.3535	0.37	0.396	0.4415	0.481
	V_R	-0.478	-0.591	-0.42	-0.315	-0.318	-0.328	-0.3645	-0.38
	NB	617.98	386.48	190.05	112.72	94.387	84.183	80.448	76.690
-0.4	V_N	0.8785	0.967	0.6165	0.531	0.564	0.58	0.6145	0.6305
	V_R	-0.869	-0.947	-0.582	-0.483	-0.503	-0.505	-0.5235	-0.5065
	NB	1120.5	616.70	262.11	169.32	143.87	123.29	111.97	100.52
-0.5	V_N	1.088	1.151	0.7305	0.7525	0.769	0.785	0.8105	0.8325
	V_R	-1.088	-1.151	-0.730	-0.752	-0.769	-0.785	-0.8105	-0.8325
	NB	1387.7	734.05	310.58	239.95	196.17	166.87	147.68	132.73
-0.6	V_N	1.2	1.48	0.845	0.8665	0.913	0.942	0.975	1.0125
	V_R	-1.189	-1.453	-0.799	-0.802	-0.828	-0.837	-0.85	-0.8555
	NB	1530.6	943.87	359.26	276.30	232.90	200.25	177.66	161.43
-0.7	V_N	1.285	1.553	1.0756	1.1008	1.1253	1.1574	1.1787	1.2031
	V_R	-1.272	-1.522	-1.025	-1.029	-1.0333	-1.039	-1.0427	-1.0331
	NB	1639.0	990.43	457.31	351.02	287.06	246.04	214.77	191.82
-0.8	V_N	1.92	2.155	1.3105	1.3534	1.3861	1.4086	1.4591	1.4955
	V_R	-1.906	-2.121	-1.255	-1.275	-1.2851	-1.281	-1.3121	-1.3175
	NB	2448.9	1374.3	557.18	431.58	353.59	299.44	265.87	238.44
-0.9	V_N	2.303	2.4895	1.731	1.639	1.6505	1.6835	1.7049	1.7115
	V_R	-2.287	-2.458	-1.681	-1.56	-1.5485	-1.549	-1.5429	-1.5115
	NB	2937.5	1587.6	735.96	522.64	421.04	357.88	310.65	272.87
-1	V_N	2.529	2.6385	1.9655	1.929	1.9335	1.9395	1.9405	1.9505
	V_R	-2.511	-2.605	-1.913	-1.847	-1.8285	-1.802	-1.7735	-1.7475
	NB	3225.7	1682.7	835.67	615.11	493.23	412.30	353.58	310.98

The Nernst and Righi-Leduc voltage and thermomagnetic power for DP0.25% sample for various temperature differences and magnetic flux densities.

ΔT (°C) / B (T)		10	20	30	40	50	60	70	80
1	V_N	-3.3345	-3.352	-3.1285	-3.055	-3.38	-3.466	-3.457	-3.4775
	V_R	3.3225	3.325	3.0845	2.996	3.304	3.371	3.343	3.3445
	NB	-2853.3	-1434.1	-892.34	-653.53	-578.45	-494.30	-422.59	-371.96
0.9	V_N	-2.801	-2.8165	-2.606	-2.871	-2.921	-3.05	-2.9645	-3.032
	V_R	2.792	2.7935	2.567	2.819	2.853	2.965	2.8625	2.915
	NB	-2396.8	-1205.0	-743.31	-614.17	-499.89	-434.97	-362.38	-324.30
0.8	V_N	-2.199	-2.349	-2.0515	-2.285	-2.5215	-2.6	-2.5875	-2.5565
	V_R	2.191	2.327	2.0155	2.239	2.4625	2.525	2.4995	2.4525
	NB	-1881.6	-1005.0	-585.15	-488.81	-431.52	-370.80	-316.30	-273.44
0.7	V_N	-1.72	-1.8515	-1.8065	-2.0305	-2.1205	-2.075	-2.052	-2.1435
	V_R	1.713	1.8335	1.7755	1.9905	2.0685	2.011	1.975	2.0495
	NB	-1471.7	-792.16	-515.27	-434.37	-362.90	-295.92	-250.84	-229.27
0.6	V_N	-1.374	-1.4895	-1.478	-1.544	-1.729	-1.6795	-1.7355	-1.711
	V_R	1.368	1.4745	1.452	1.511	1.684	1.6245	1.6685	1.632
	NB	-1175.7	-637.27	-421.57	-330.29	-295.89	-239.52	-212.15	-183.01
0.5	V_N	-1.2225	-1.254	-1.2275	-1.388	-1.4355	-1.468	-1.496	-1.582
	V_R	1.2165	1.241	1.2045	1.359	1.3965	1.418	1.436	1.514
	NB	-1046.0	-536.52	-350.12	-296.92	-245.67	-209.36	-182.87	-169.21
0.4	V_N	-0.766	-0.85	-0.7715	-0.8175	-0.8765	-0.9635	-1.0285	-1.0705
	V_R	0.761	0.839	0.7525	0.7935	0.8455	0.9235	0.9815	1.0175
	NB	-655.46	-363.67	-220.05	-174.88	-150.00	-137.41	-125.72	-114.50
0.3	V_N	-0.493	-0.63	-0.6465	-0.679	-0.684	-0.708	-0.7405	-0.793
	V_R	0.49	0.624	0.6345	0.664	0.664	0.683	0.7095	0.755
	NB	-421.85	-269.54	-184.40	-145.25	-117.05	-100.97	-90.520	-84.820
0.2	V_N	-0.448	-0.465	-0.436	-0.4365	-0.4625	-0.467	-0.5045	-0.548
	V_R	0.446	0.461	0.427	0.4255	0.4475	0.448	0.4825	0.523
	NB	-383.35	-198.94	-124.36	-93.377	-79.151	-66.601	-61.671	-58.615
0.1	V_N	-0.132	-0.146	-0.1235	-0.151	-0.179	-0.1965	-0.229	-0.2345
	V_R	0.132	0.145	0.1185	0.147	0.172	0.1855	0.217	0.2205
	NB	-112.95	-62.465	-35.226	-32.302	-30.633	-28.024	-27.993	-25.082

0	V_N	0	0	0	0	0	0	0	0
	V_R	0	0	0	0	0	0	0	0
	NB	0	0	0	0	0	0	0	0
-0.1	V_N	0.132	0.146	0.1235	0.151	0.179	0.1965	0.229	0.2345
	V_R	-0.129	-0.14	-0.1185	-0.142	-0.17	-0.1885	-0.219	-0.2245
	NB	112.951	62.4658	35.2261	32.3025	30.6339	28.0240	27.9934	25.0825
-0.2	V_N	0.448	0.465	0.436	0.4365	0.4625	0.467	0.5045	0.548
	V_R	-0.447	-0.462	-0.435	-0.4345	-0.4615	-0.467	-0.5045	-0.549
	NB	383.351	198.949	124.361	93.3778	79.1518	66.6016	61.6712	58.6151
-0.3	V_N	0.493	0.63	0.6465	0.679	0.684	0.708	0.7405	0.793
	V_R	-0.492	-0.629	-0.6485	-0.681	-0.688	-0.714	-0.7495	-0.807
	NB	421.858	269.544	184.402	145.254	117.059	100.972	90.5204	84.8208
-0.4	V_N	0.766	0.85	0.7715	0.8175	0.8765	0.9635	1.0285	1.0705
	V_R	-0.768	-0.854	-0.7805	-0.8285	-0.8915	-0.9845	-1.0535	-1.0995
	NB	655.463	363.670	220.056	174.882	150.003	137.410	125.726	114.502
-0.5	V_N	1.2225	1.254	1.2275	1.388	1.4355	1.468	1.496	1.582
	V_R	-1.2255	-1.26	-1.2405	-1.404	-1.4585	-1.499	-1.534	-1.626
	NB	1046.08	536.521	350.122	296.926	245.670	209.360	182.874	169.213
-0.6	V_N	1.374	1.4895	1.478	1.544	1.729	1.6795	1.7355	1.711
	V_R	-1.377	-1.4975	-1.494	-1.564	-1.758	-1.7155	-1.7805	-1.766
	NB	1175.72	637.279	421.572	330.298	295.899	239.523	212.151	183.012
-0.7	V_N	1.72	1.8515	1.8065	2.0305	2.1205	2.075	2.052	2.1435
	V_R	-1.726	-1.8625	-1.8275	-2.0575	-2.1565	-2.12	-2.107	-2.2135
	NB	1471.79	792.160	515.271	434.372	362.900	295.928	250.841	229.273
-0.8	V_N	2.199	2.349	2.0515	2.285	2.5215	2.6	2.5875	2.5565
	V_R	-2.205	-2.364	-2.0775	-2.318	-2.5645	-2.656	-2.6535	-2.6365
	NB	1881.67	1005.01	585.153	488.816	431.527	370.801	316.301	273.448
-0.9	V_N	2.801	2.8165	2.606	2.871	2.921	3.05	2.9645	3.032
	V_R	-2.807	-2.8325	-2.635	-2.91	-2.973	-3.116	-3.0445	-3.125
	NB	2396.80	1205.03	743.314	614.175	499.897	434.978	362.387	324.308
-1	V_N	3.3345	3.352	3.1285	3.055	3.38	3.466	3.457	3.4775
	V_R	-3.3435	-3.372	-3.1625	-3.101	-3.44	-3.542	-3.549	-3.5795
	NB	2853.31	1434.14	892.348	653.537	578.450	494.307	422.591	371.960

Appendex 10:

Variation of the Nernst voltage with temperature difference at various DC magnetic field density for USR sample.

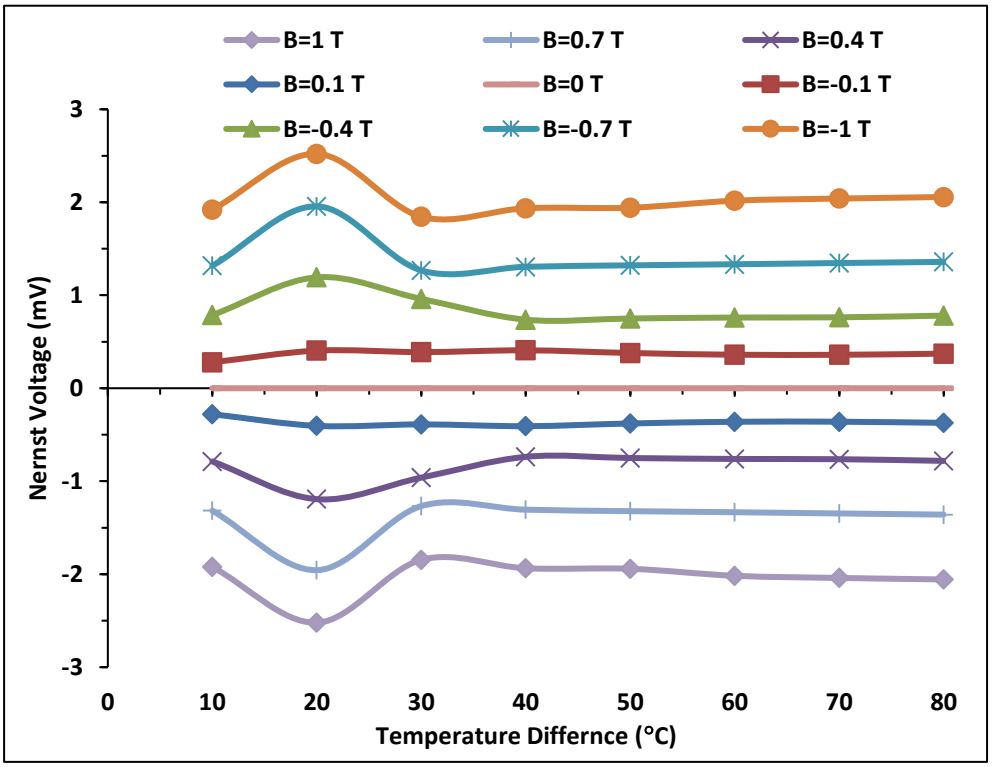

Variation of the Nernst voltage with temperature difference at various DC magnetic field density for UPB sample.

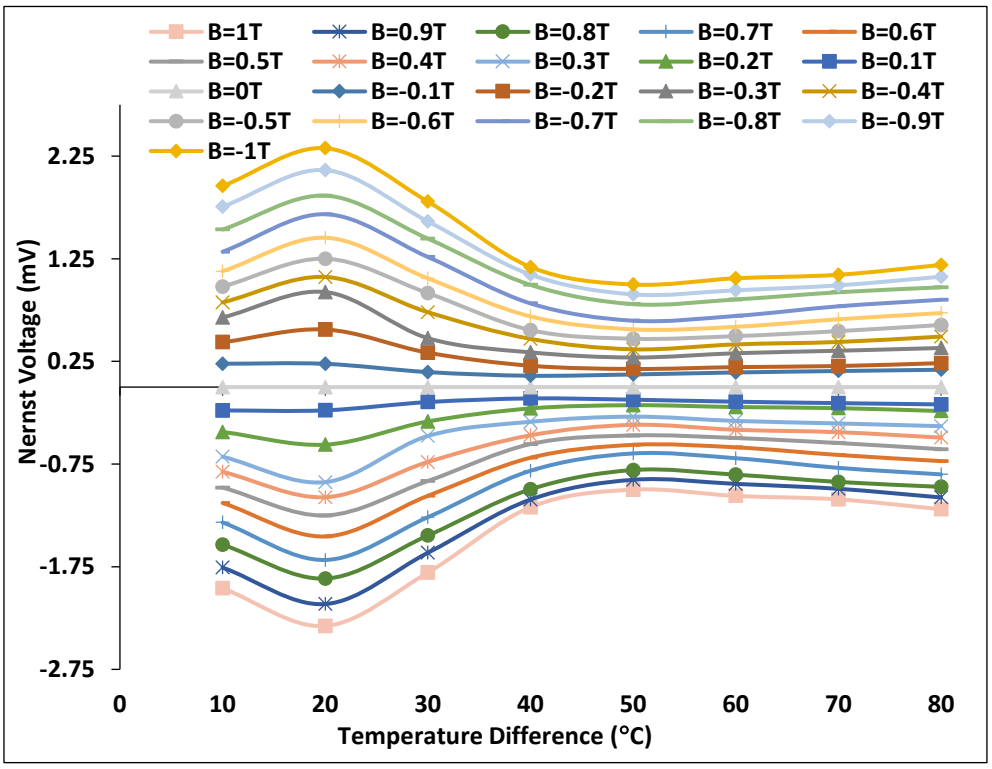

Variation of the Nernst voltage with temperature difference at various DC magnetic field density for UPA sample.

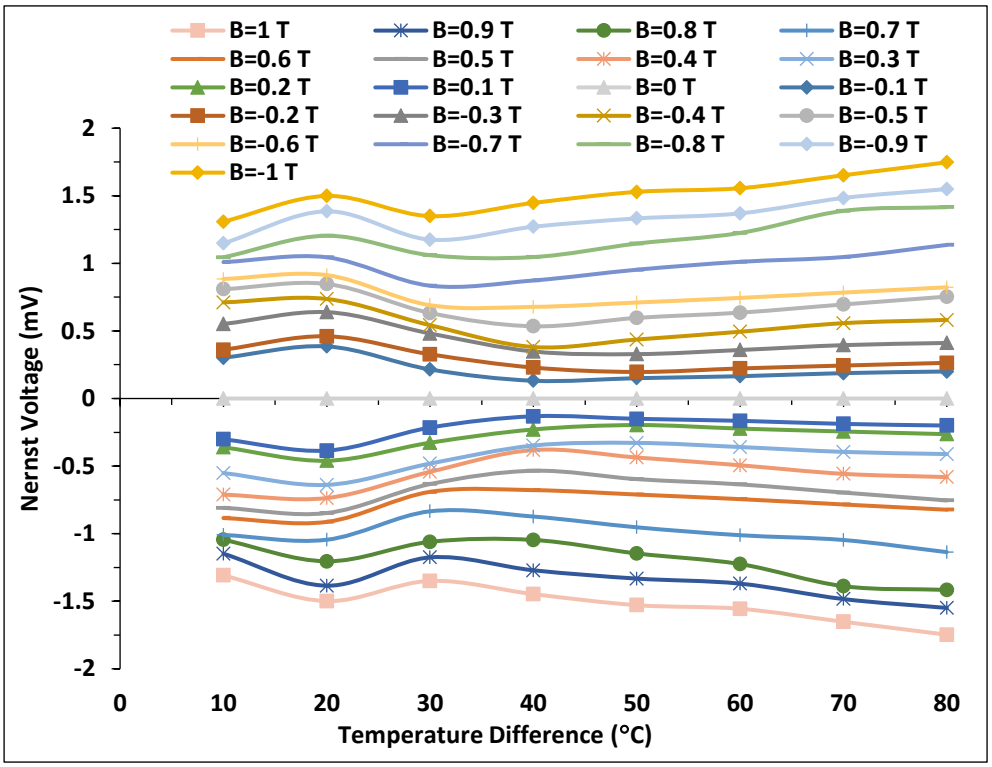

Variation of the Nernst voltage with temperature difference at various DC magnetic field density for DP0.1% sample.

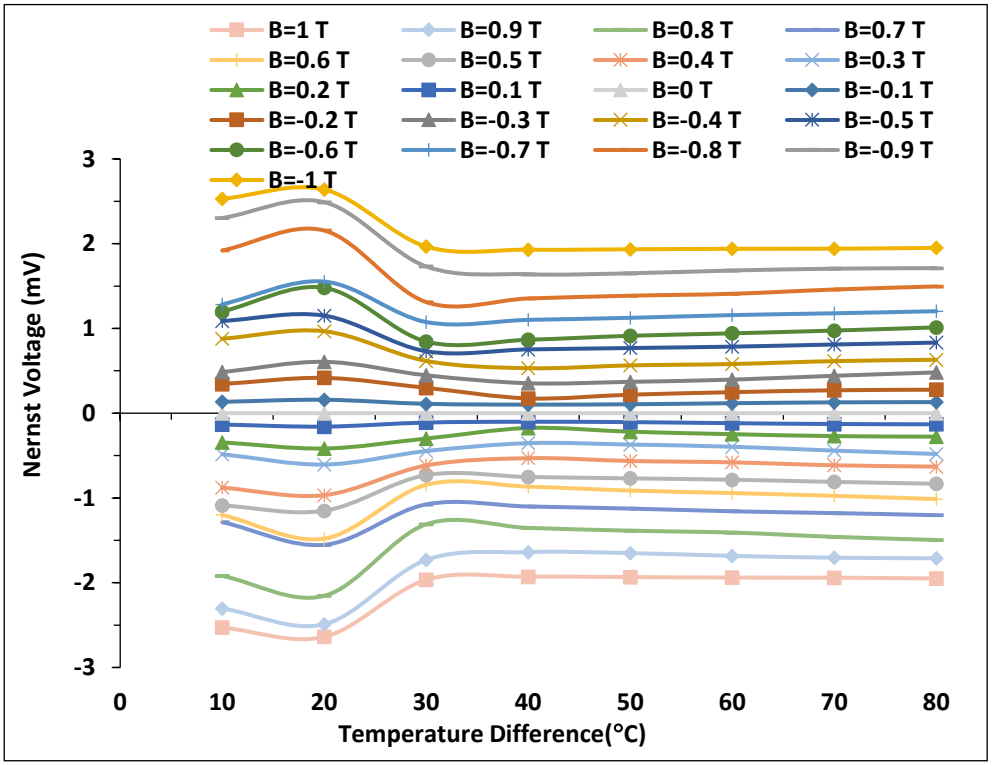

Variation of the Nernst voltage with temperature difference at various DC magnetic field density for DP0.25% sample.

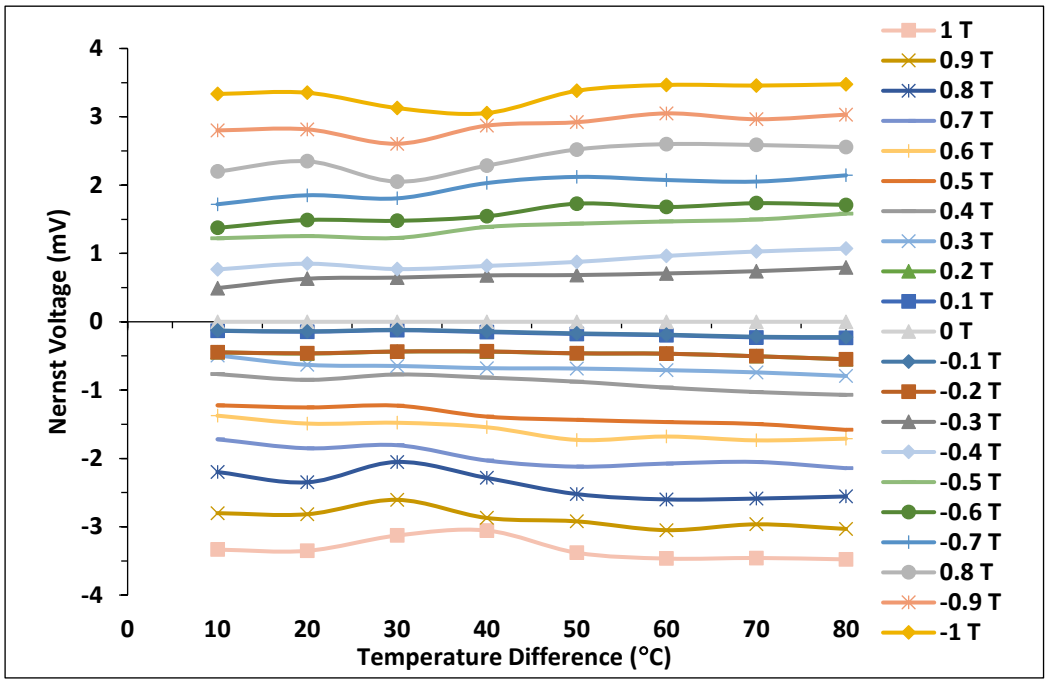

Comparison the Nernst voltage with temperature difference at various DC magnetic field density for all samples.

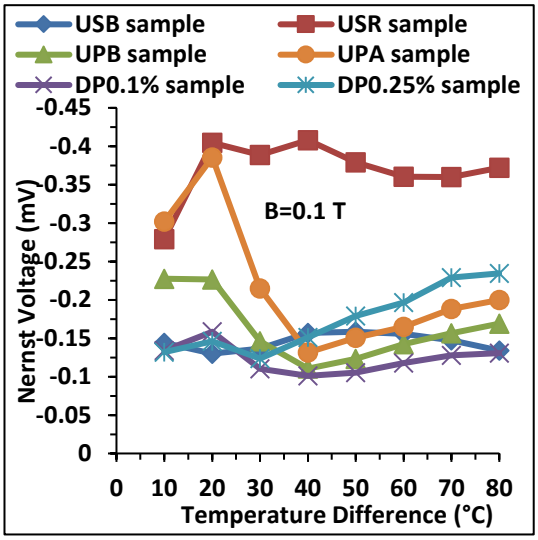

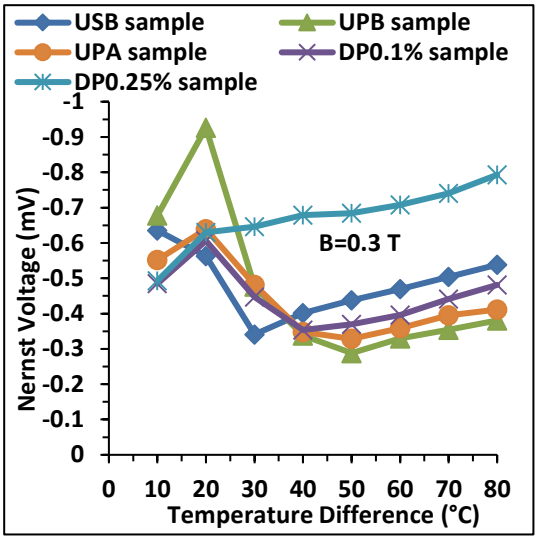

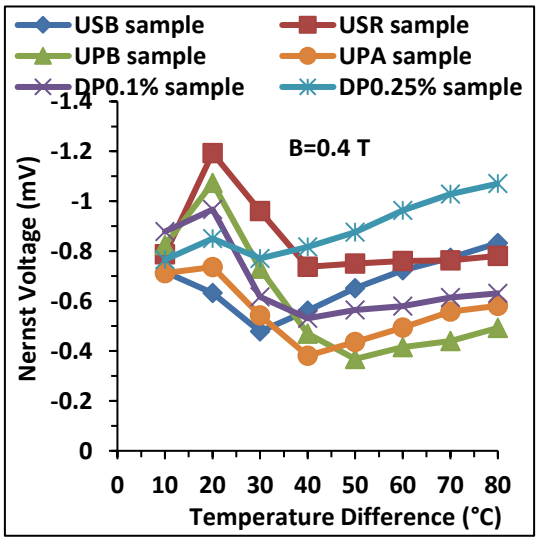

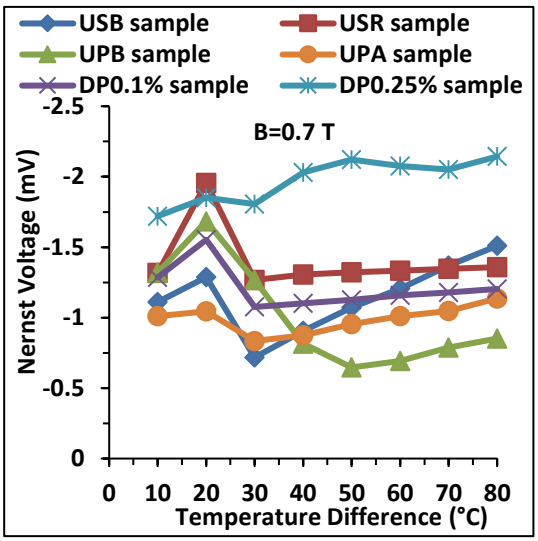

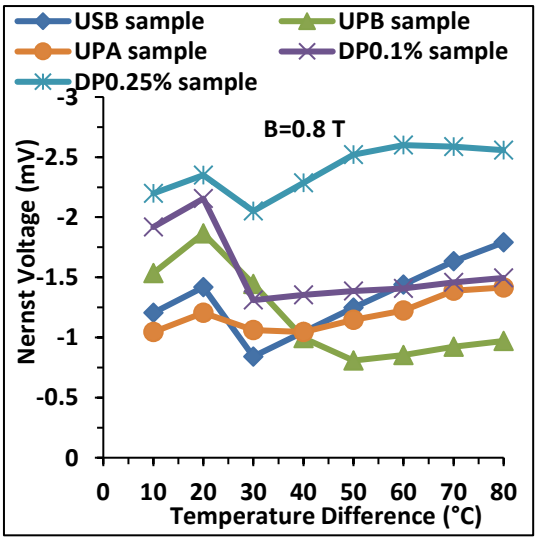

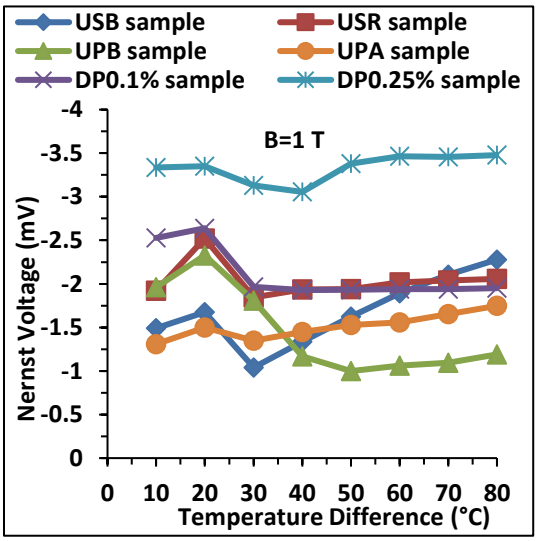

Appendix 11:

Variation of the Righi-Leduc voltage with temperature difference at various DC magnetic field density for USR sample.

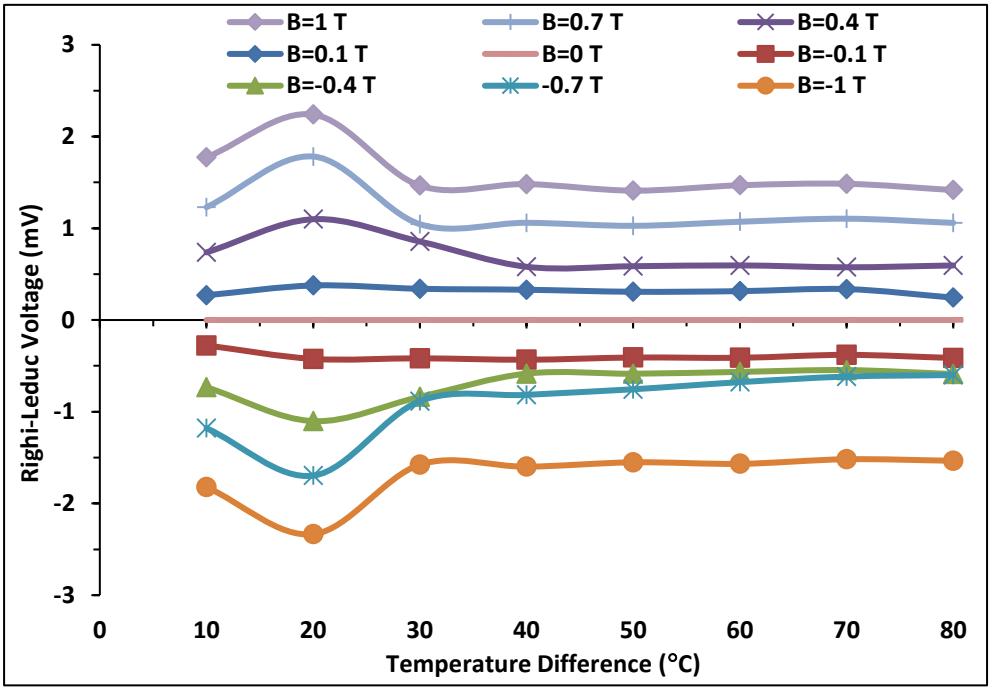

Variation of the Righi-Leduc voltage with temperature difference at various DC magnetic field density for UPB sample.

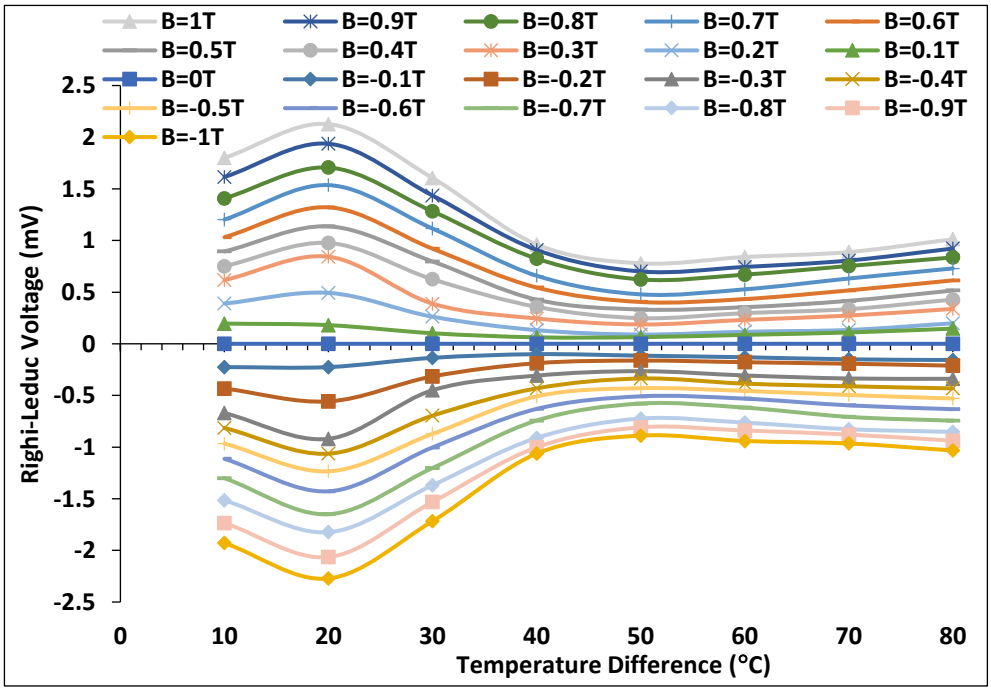

Variation of the Righi-Leduc voltage with temperature difference at various DC magnetic field density for UPA sample.

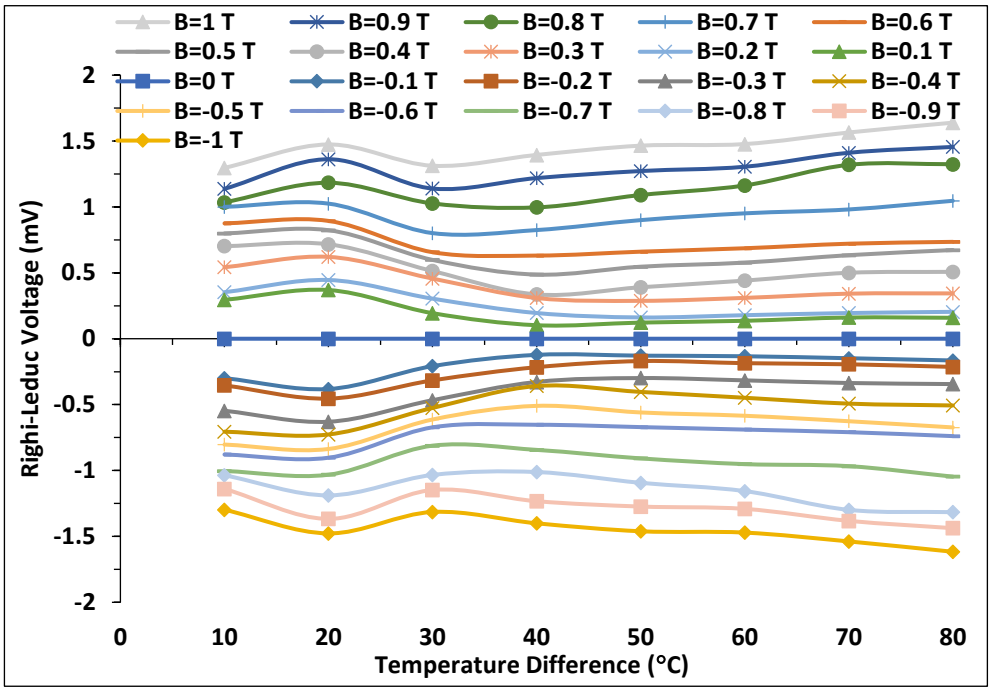

Variation of the Righi-Leduc voltage with temperature difference at various DC magnetic field density for DP0.1% sample.

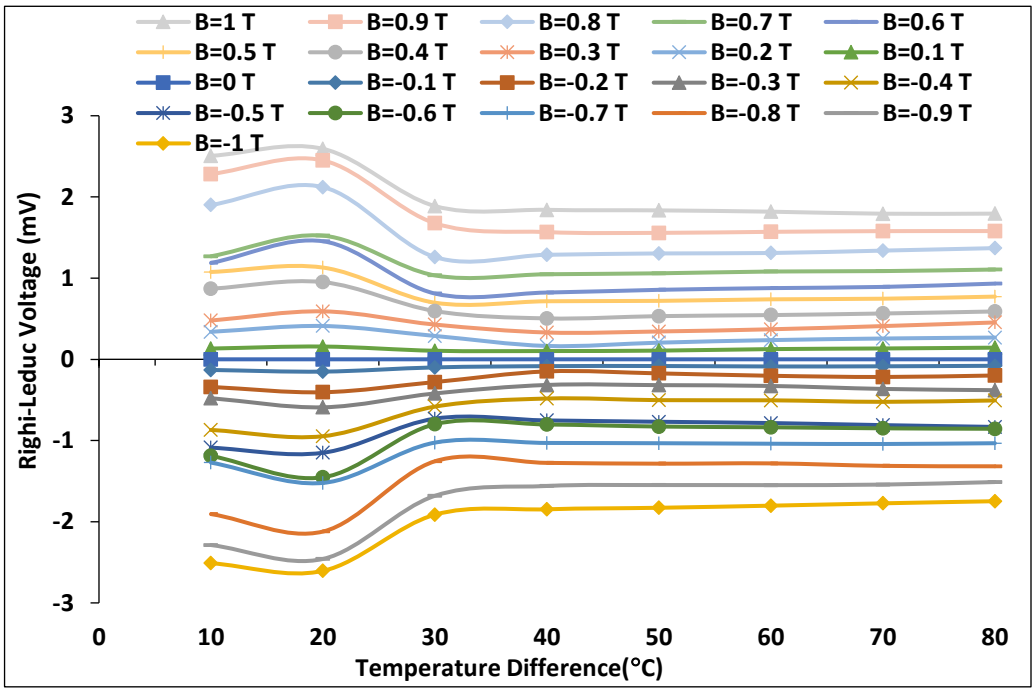

Variation of the Righi-Leduc voltage with temperature difference at various DC magnetic field density for DP0.25% sample.

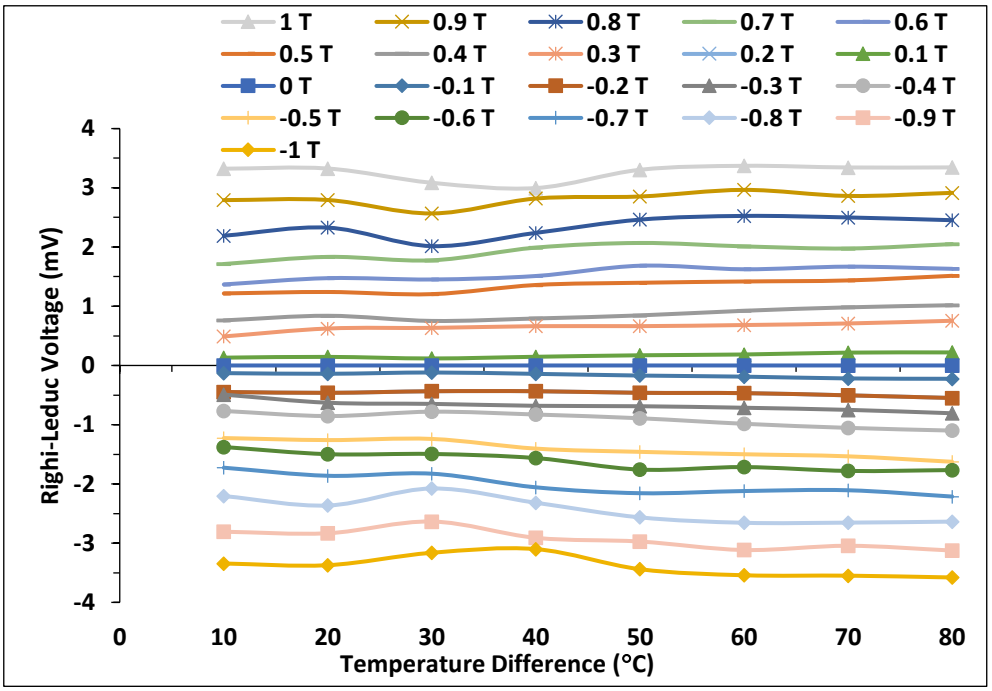

Comparison the Righi-Leduc voltage with temperature difference at various DC magnetic field density for all samples.

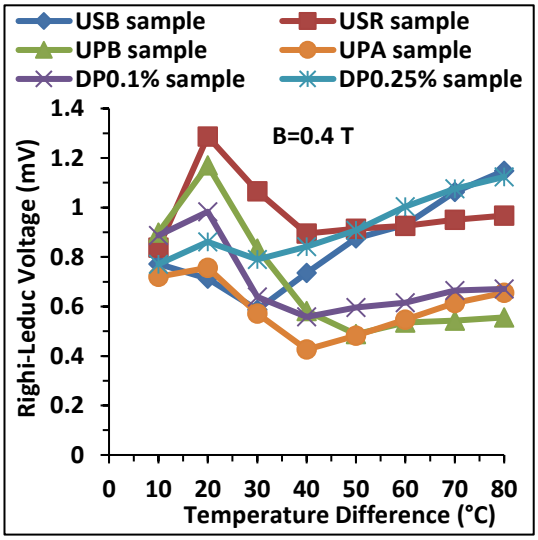

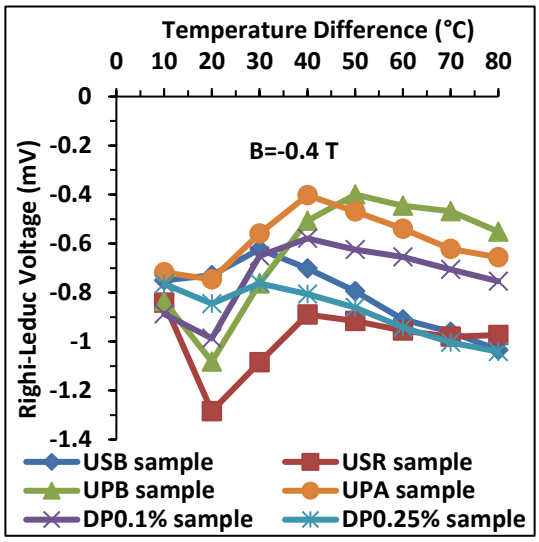

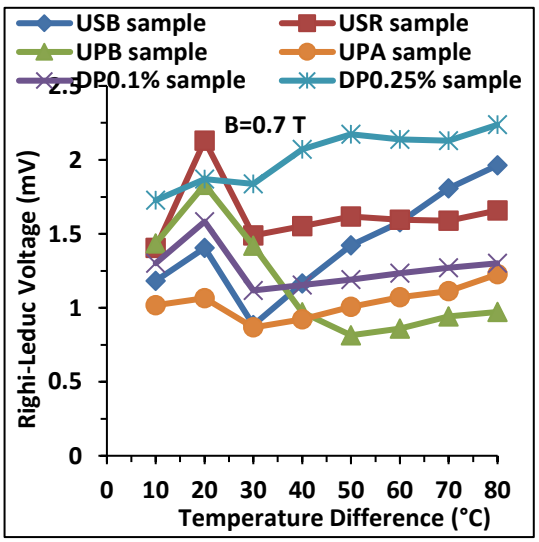

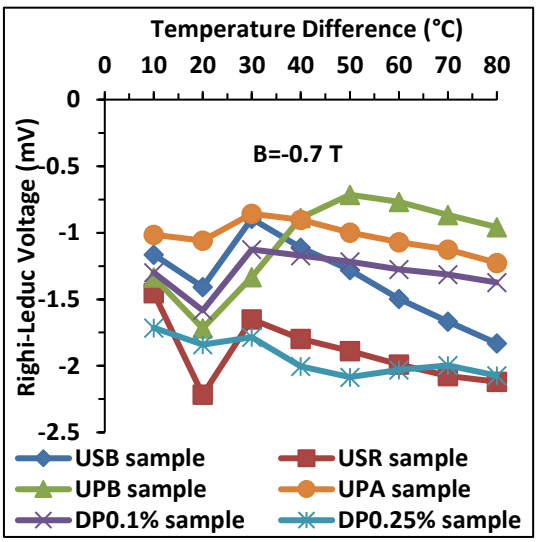

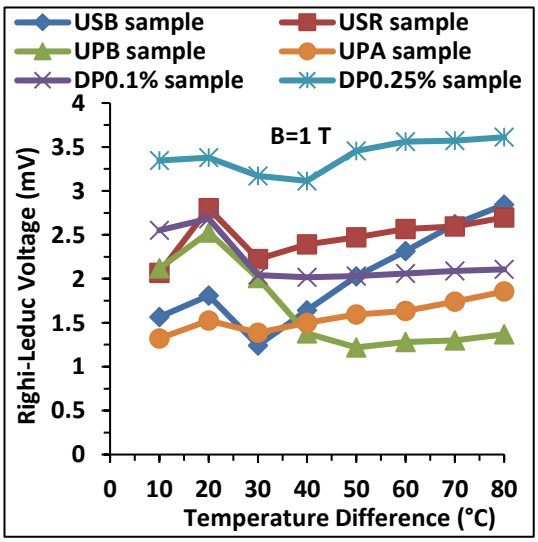

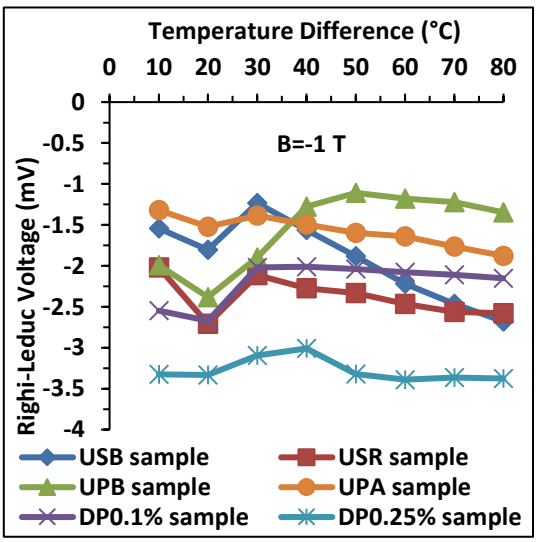

Appendex 12:

Variation of the misalignment voltage with temperature difference for:

a) USR sample

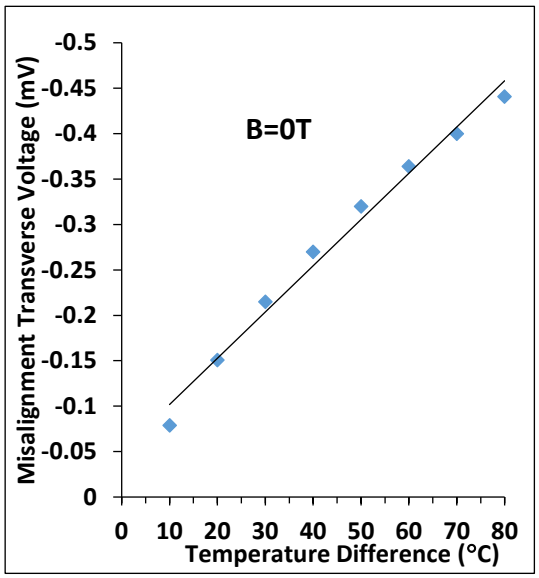

b) UPB sample

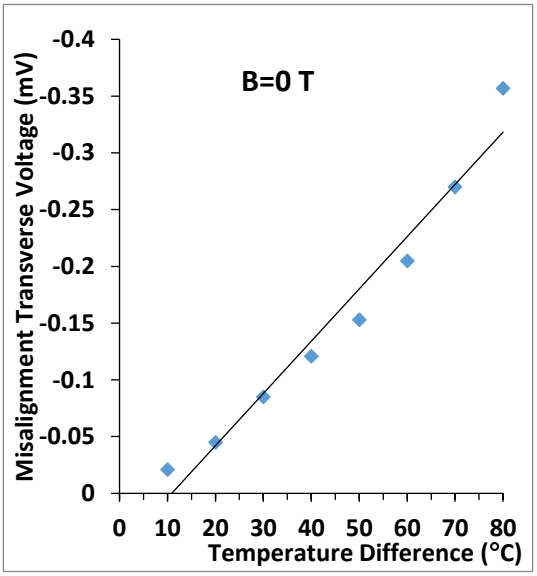

c) UPA sample

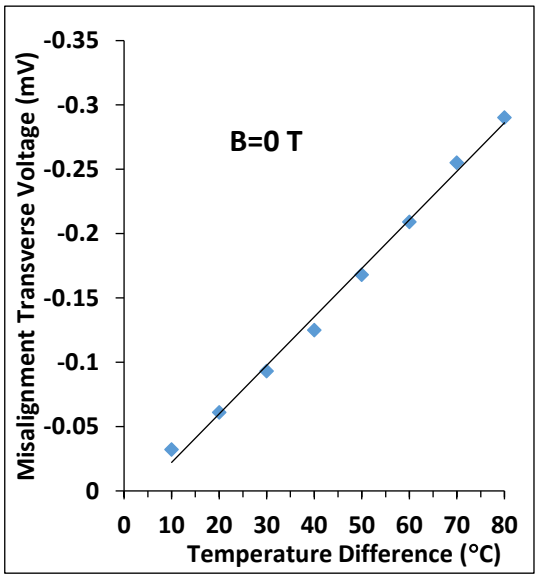

d) DP0.1% sample

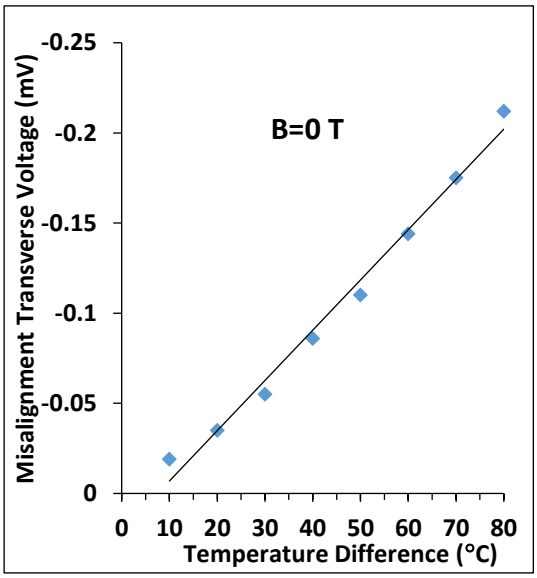

e) DP0.25% sample

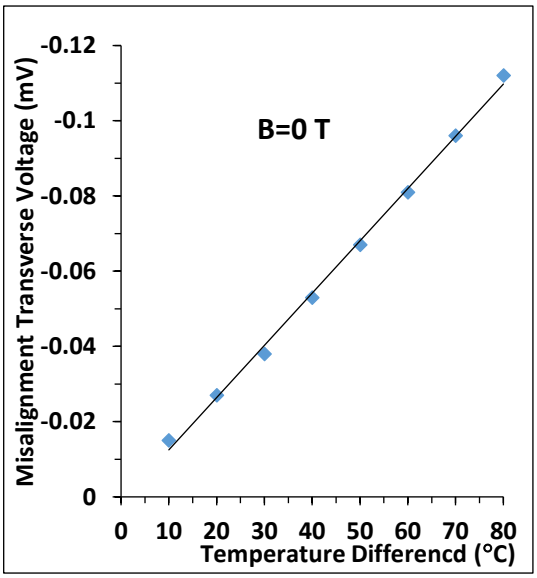

Comparison the misalignment voltage with temperature difference for all samples.

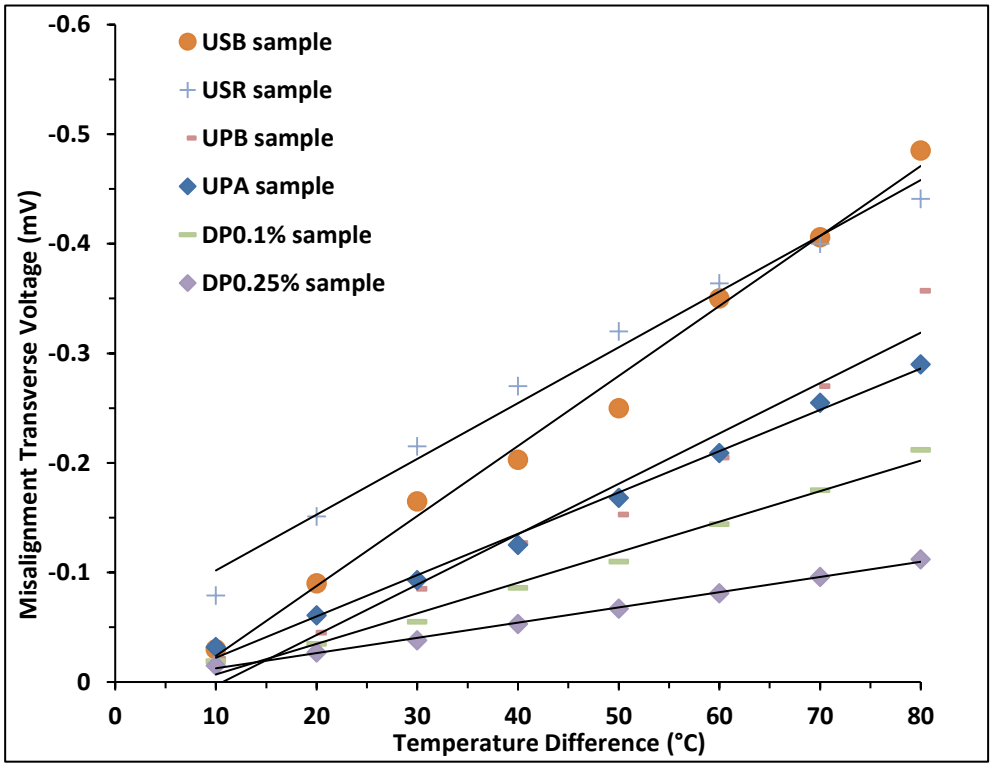

Appendex 13:

Variation of the Nernst coefficient with temperature difference at various DC magnetic field density for USR sample.

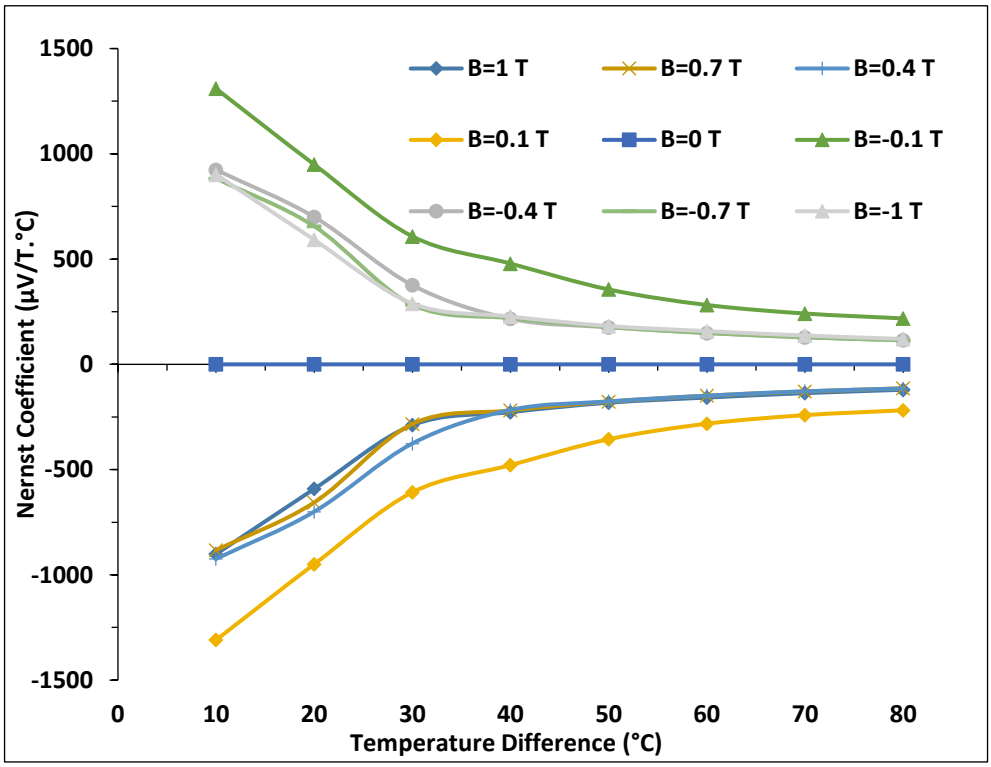

Variation of the Nernst coefficient with temperature difference at various DC magnetic field density for UPB sample.

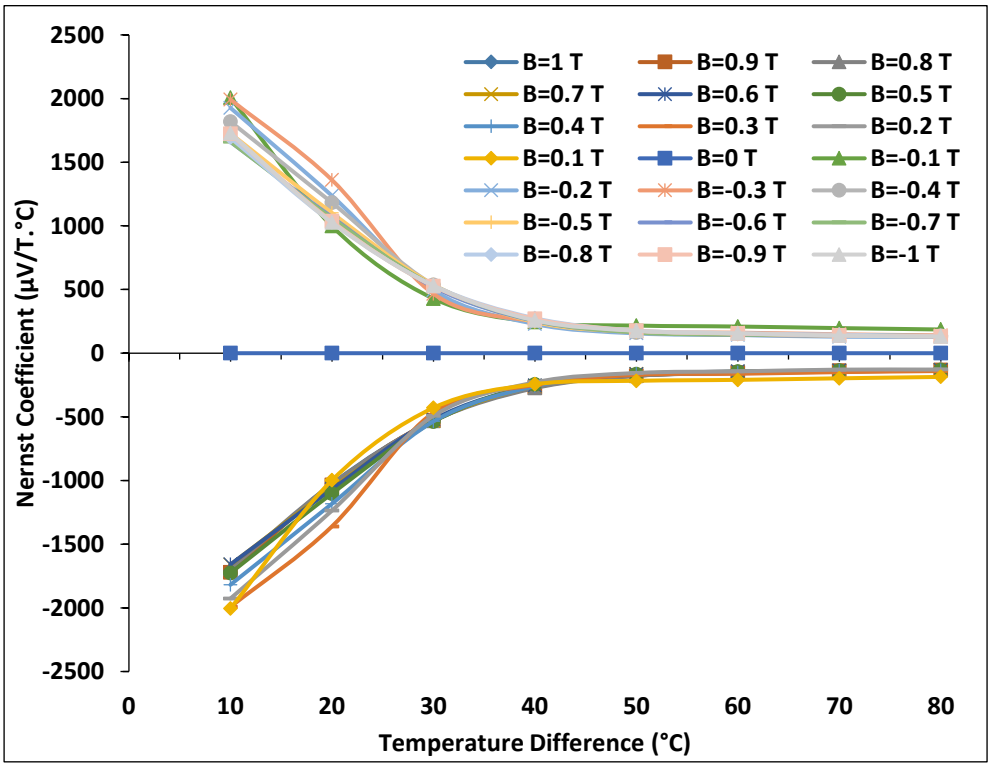

Variation of the Nernst coefficient with temperature difference at various DC magnetic field density for UPA sample.

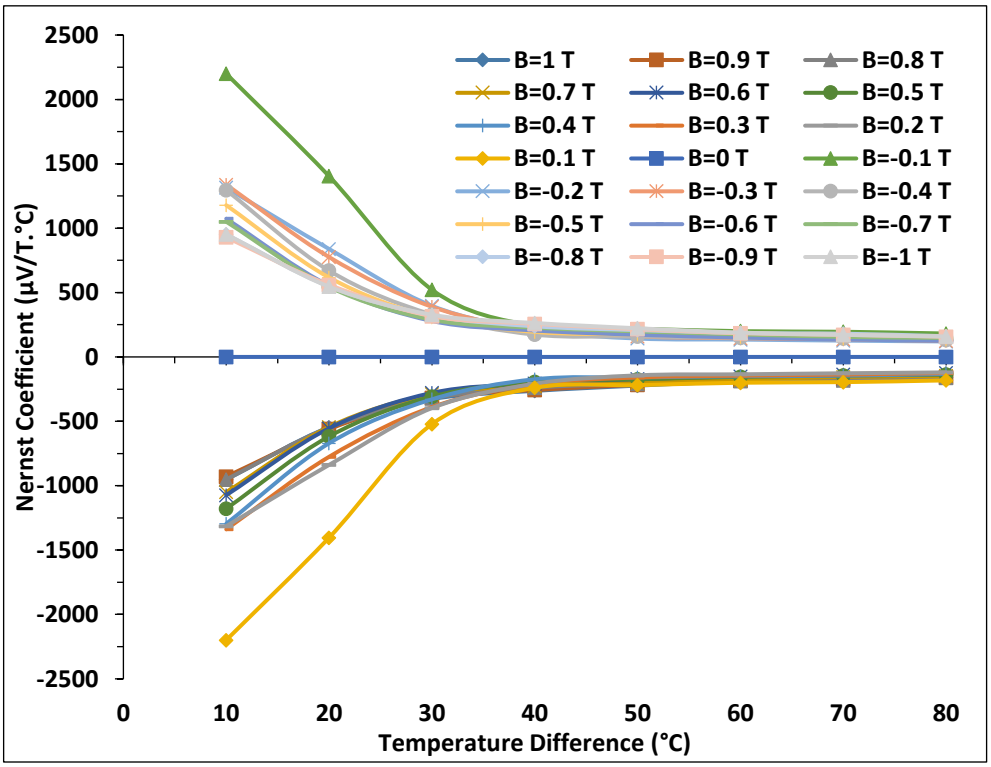

Variation of the Nernst coefficient with temperature difference at various DC magnetic field density for DP0.1% sample.

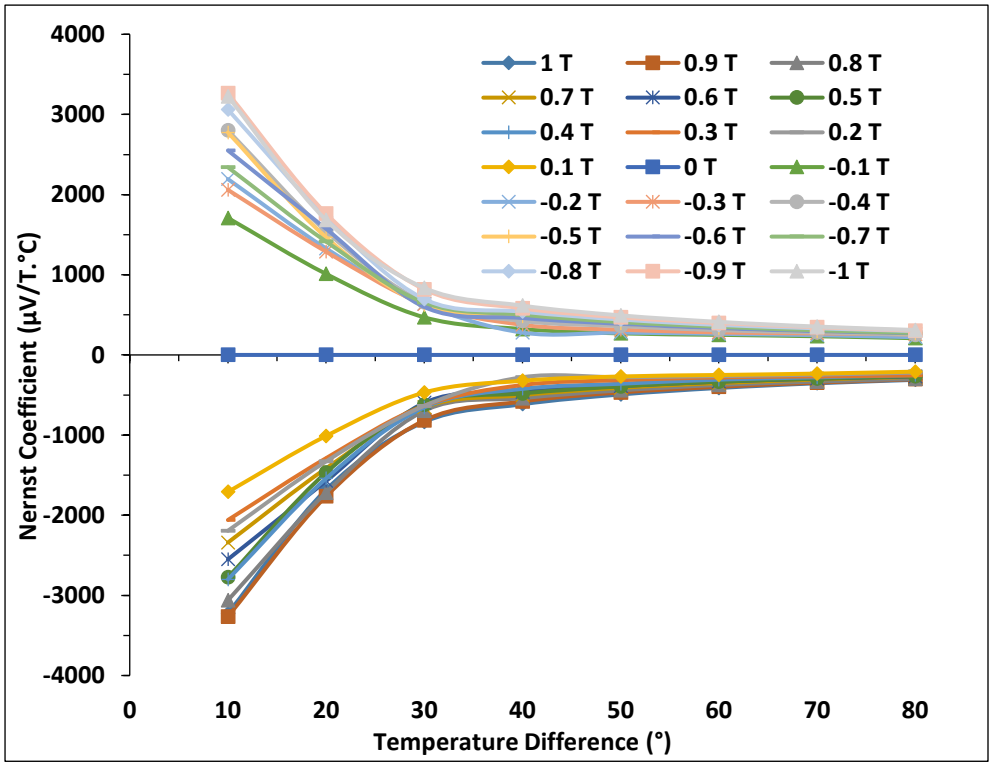

Variation of the Nernst coefficient with temperature difference at various DC magnetic field density for DP0.25% sample.

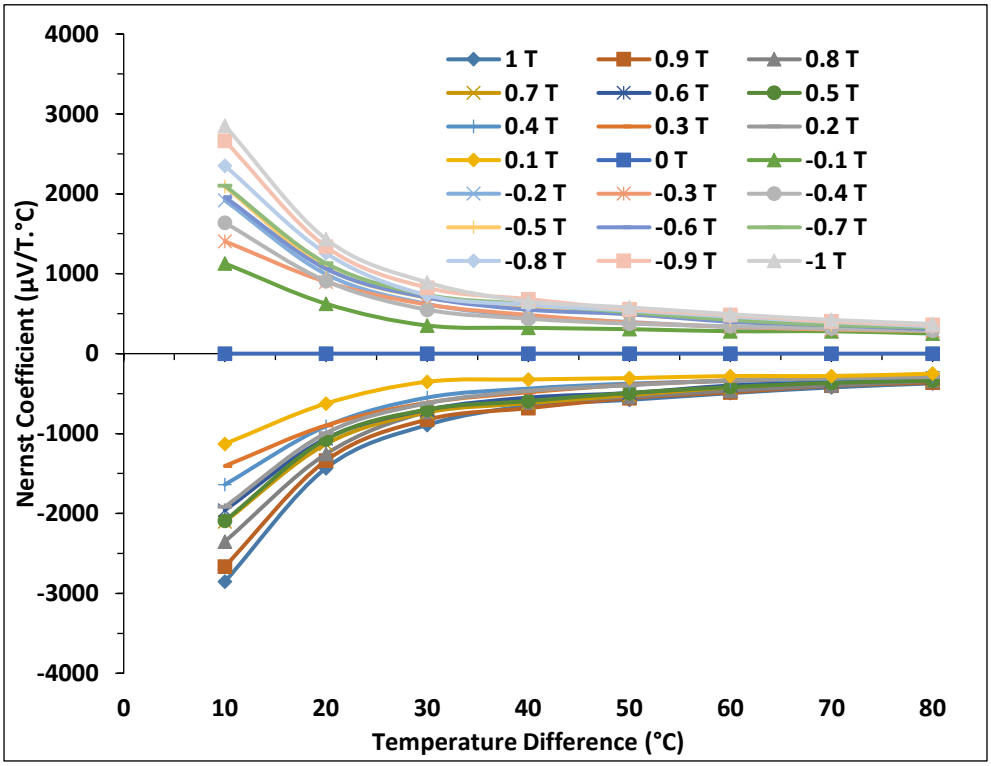

Comparison among the Nernst coefficient with temperature difference at various DC magnetic field density for all samples.

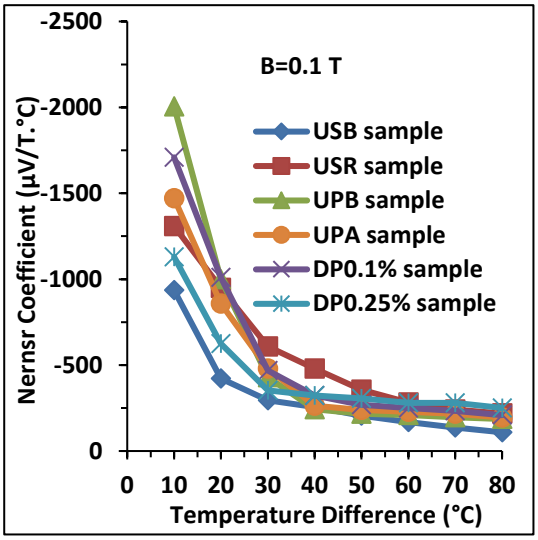

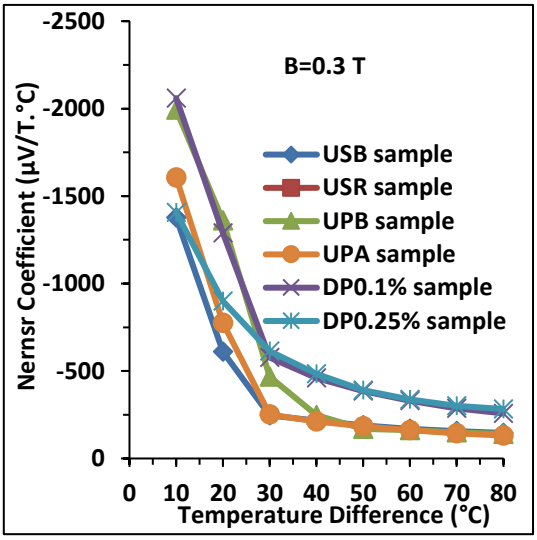

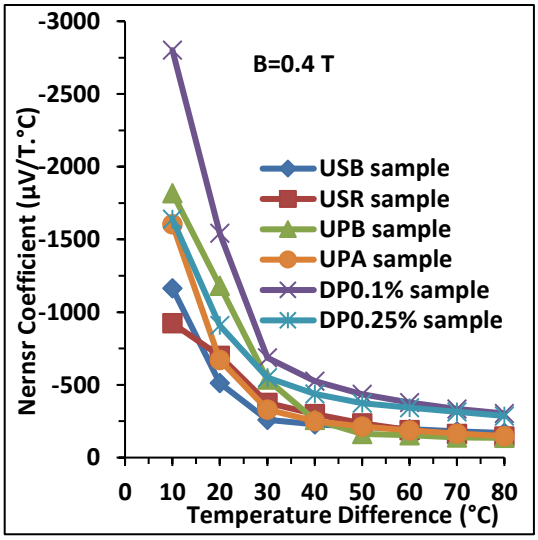

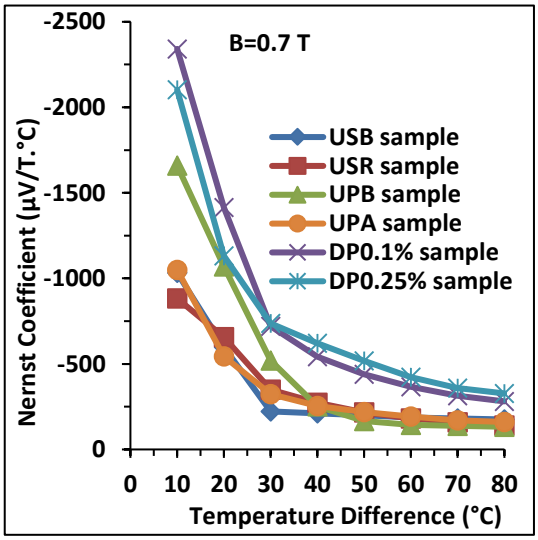

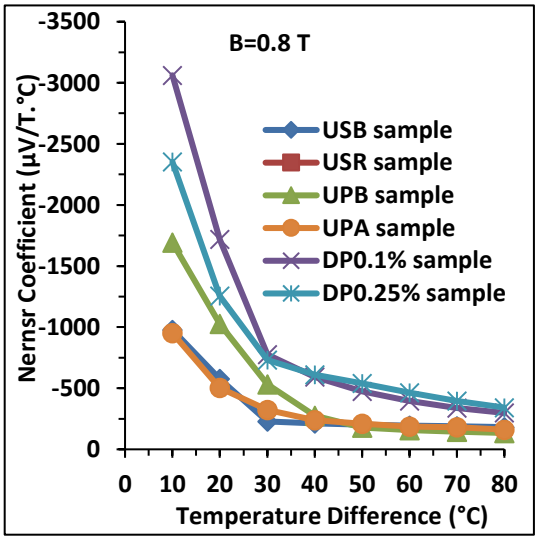

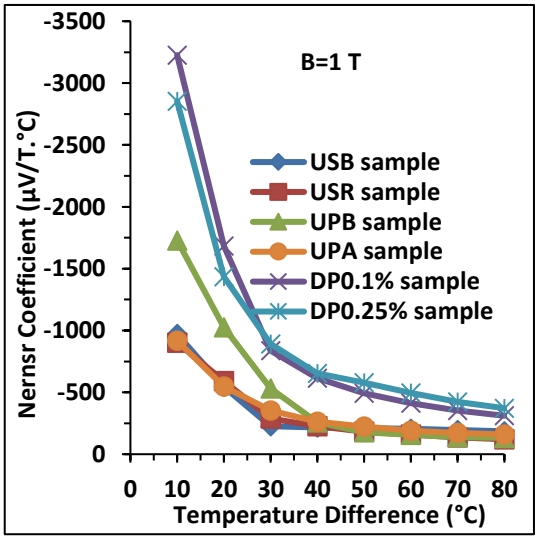

Appendex 14:

Variation of the thermomagnetic power with temperature difference at various DC magnetic field density for USR sample.

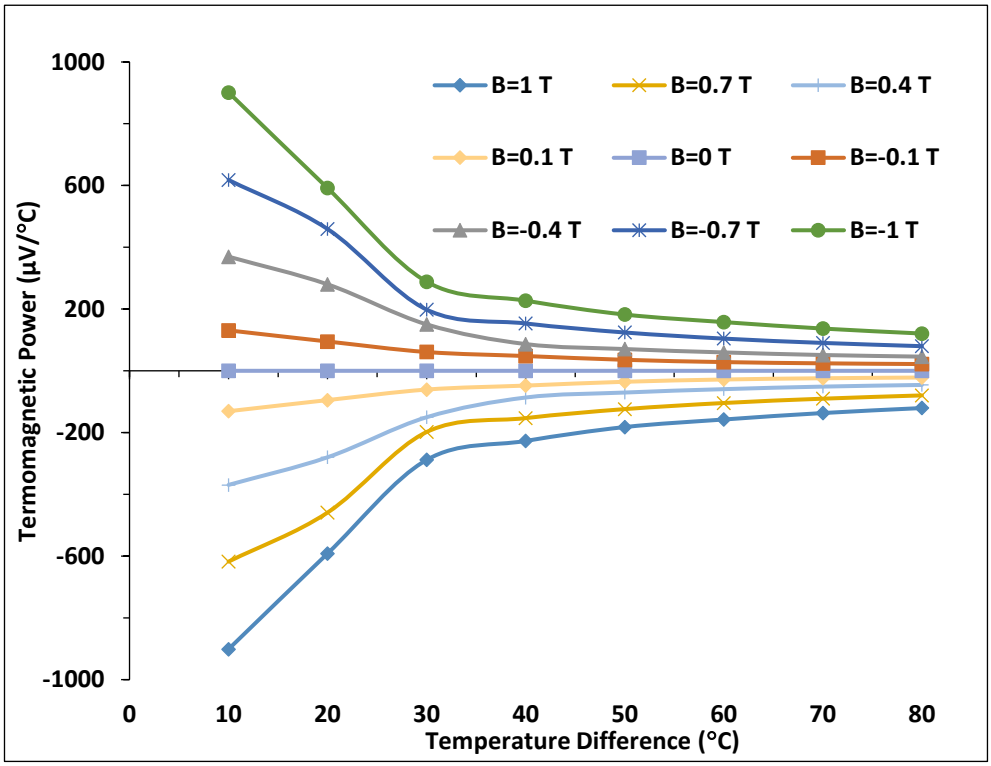

Variation of the thermomagnetic power with temperature difference at various DC magnetic field density for UPB sample.

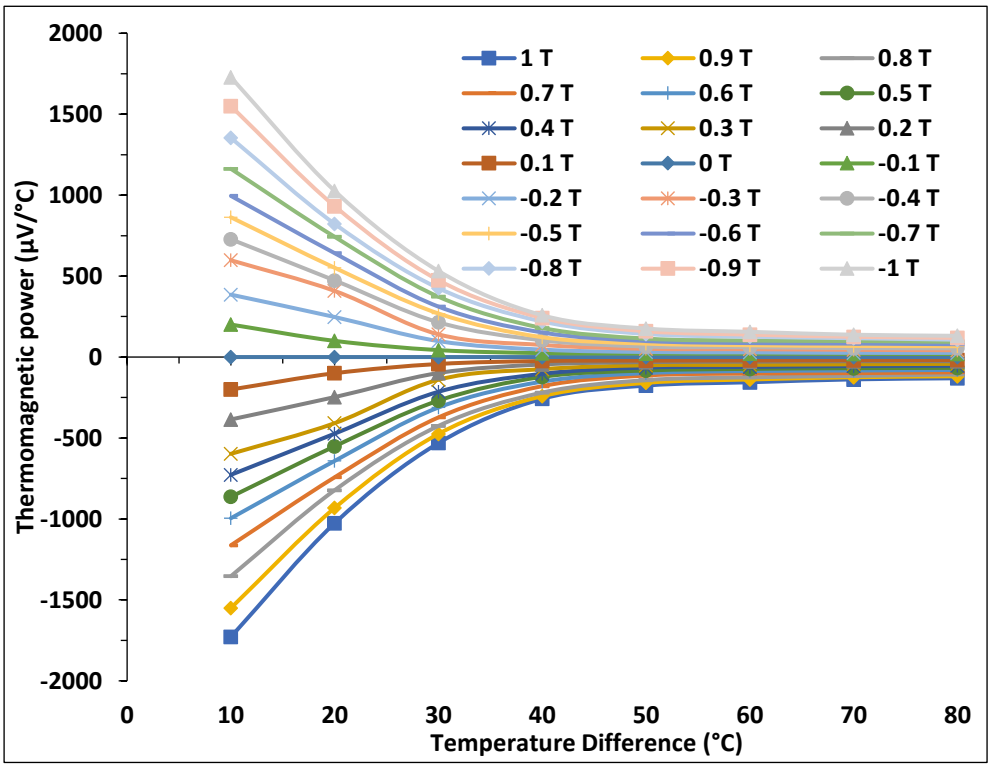

Variation of the thermomagnetic power with temperature difference at various DC magnetic field density for UPA sample.

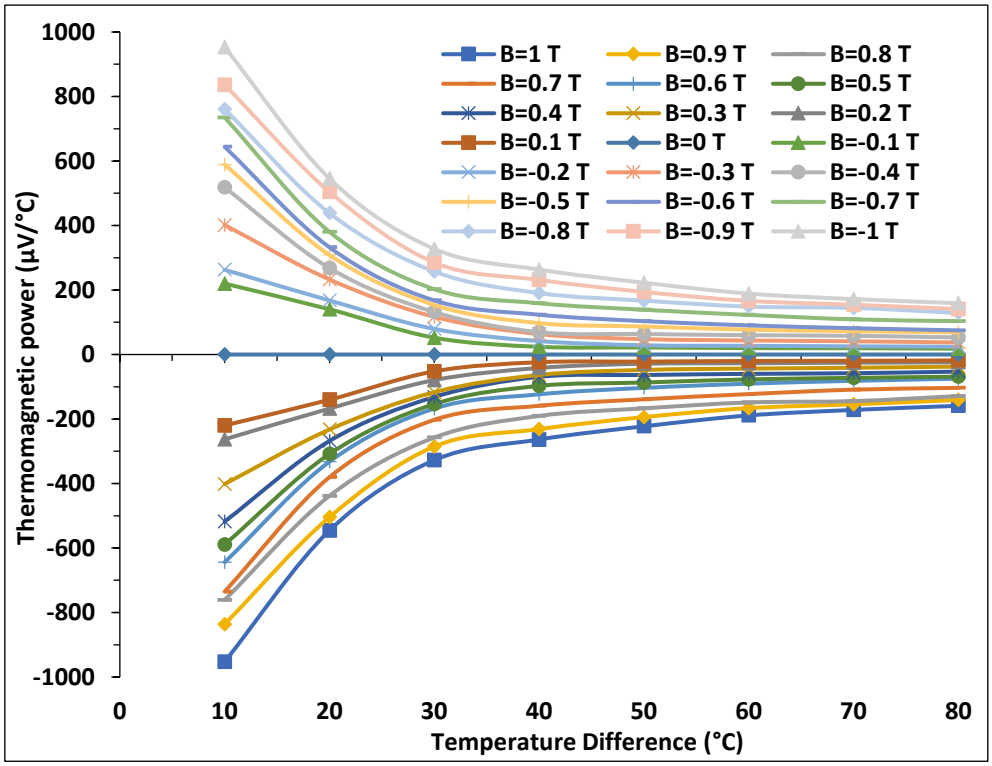

Variation of the thermomagnetic power with temperature difference at various DC magnetic field density for DP0.1% sample.

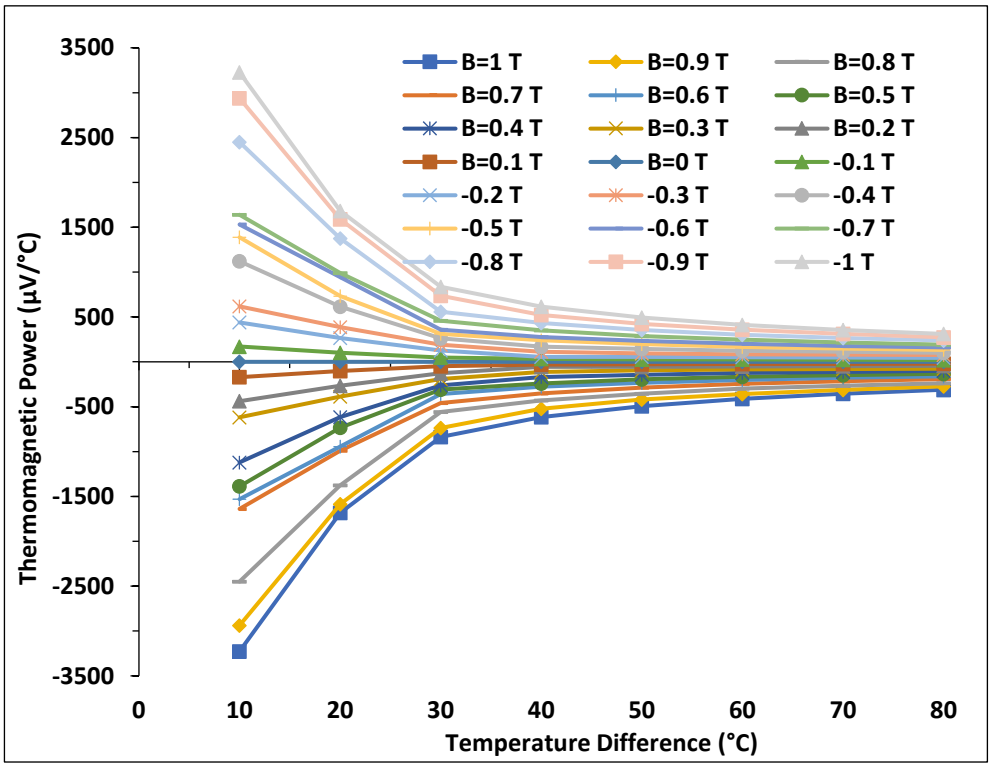

Variation of the thermomagnetic power with temperature difference at various DC magnetic field density for DP0.25% sample.

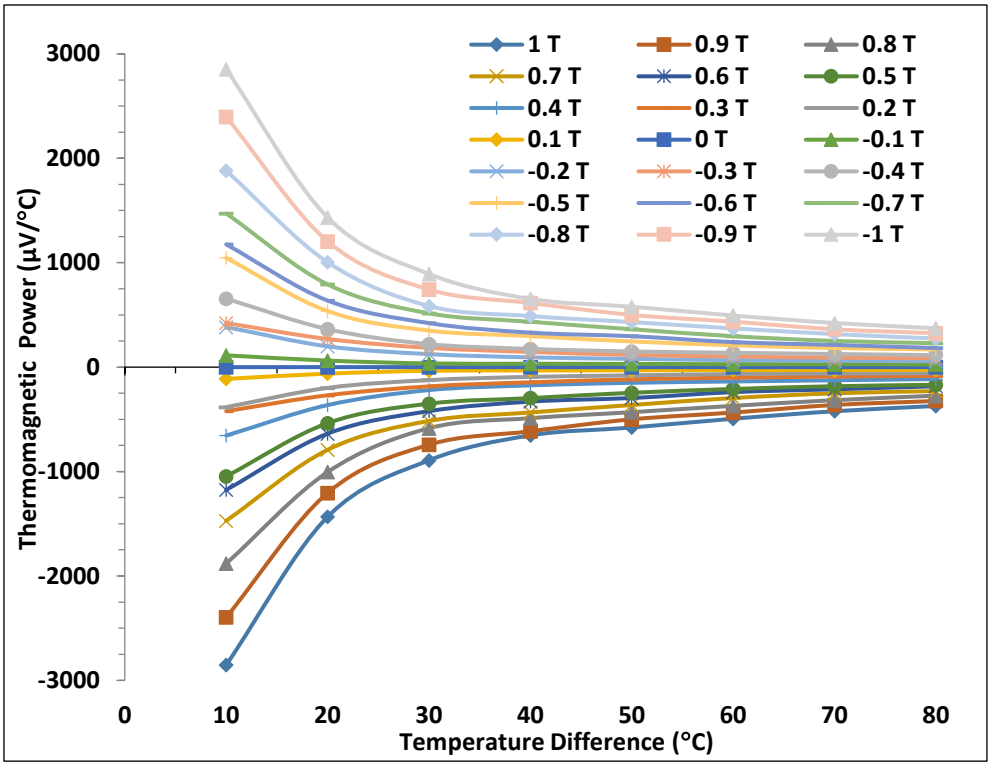

Comparison among the thermomagnetic power with temperature difference at various DC magnetic field density for all samples.

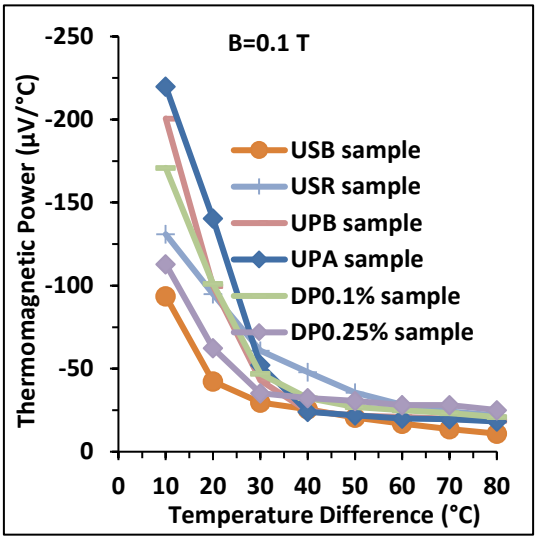

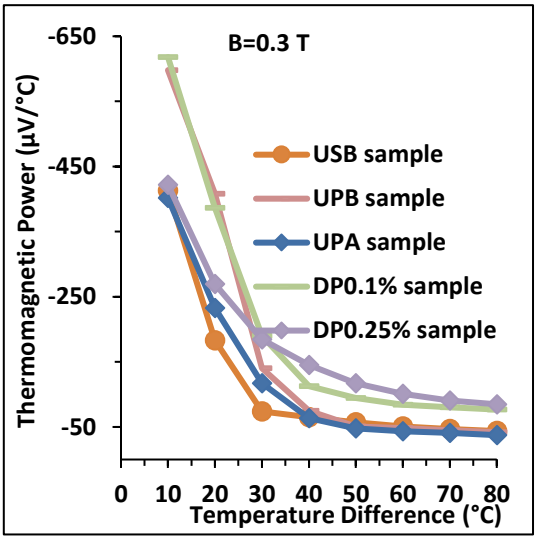

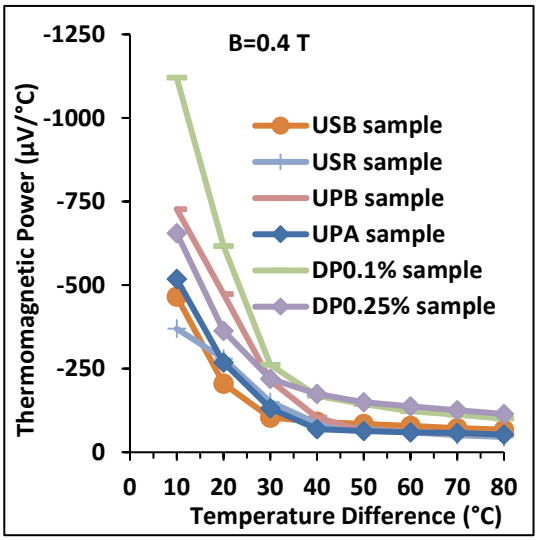

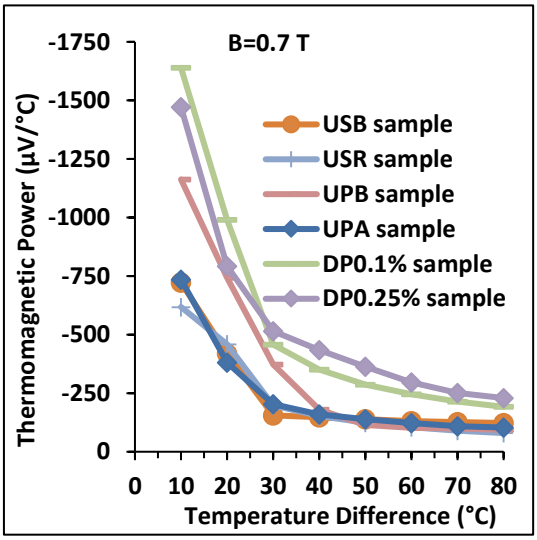

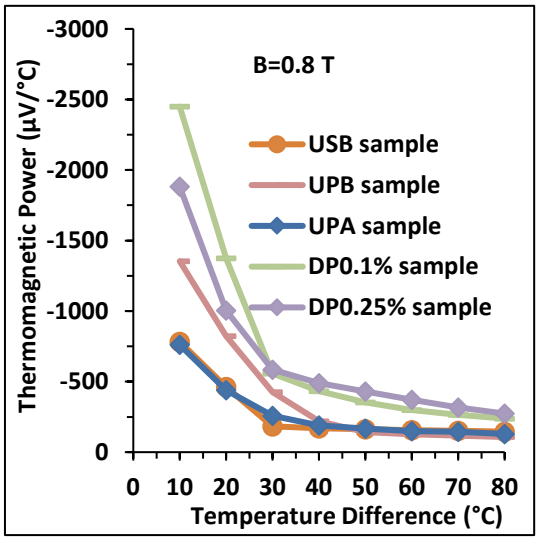

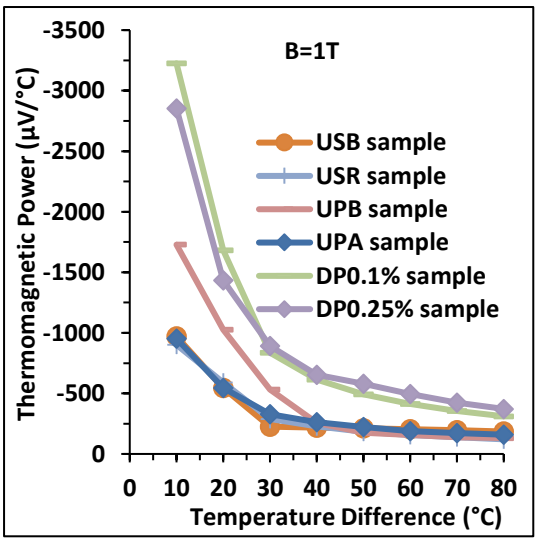

Appendex 15:

Variation of the thermomagnetic power with DC magnetic field density at various temperature differences for USR sample.

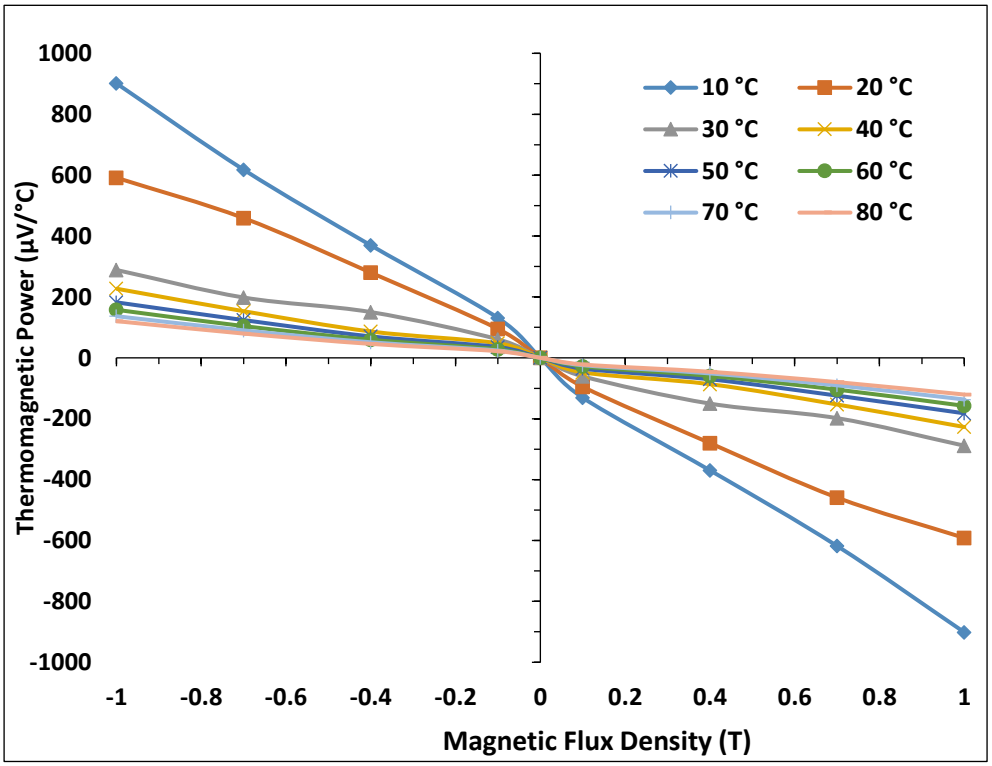

Variation of the thermomagnetic power with DC magnetic field density at various temperature differences for UPB sample.

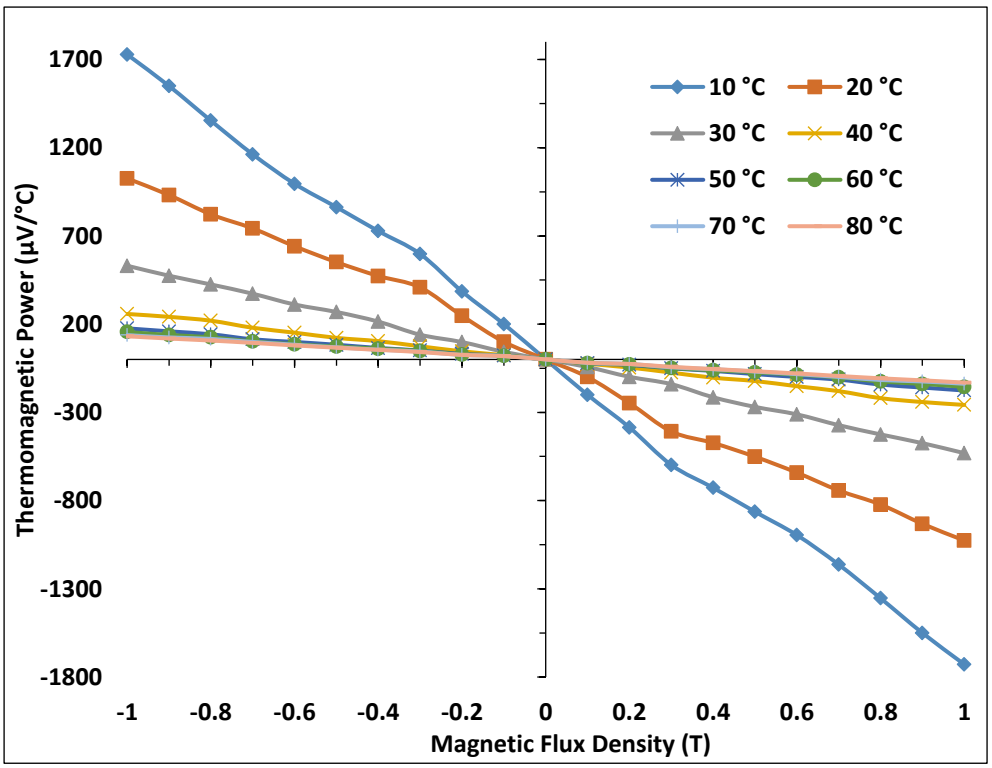

Variation of the thermomagnetic power with DC magnetic field density at various temperature differences for UPA sample.

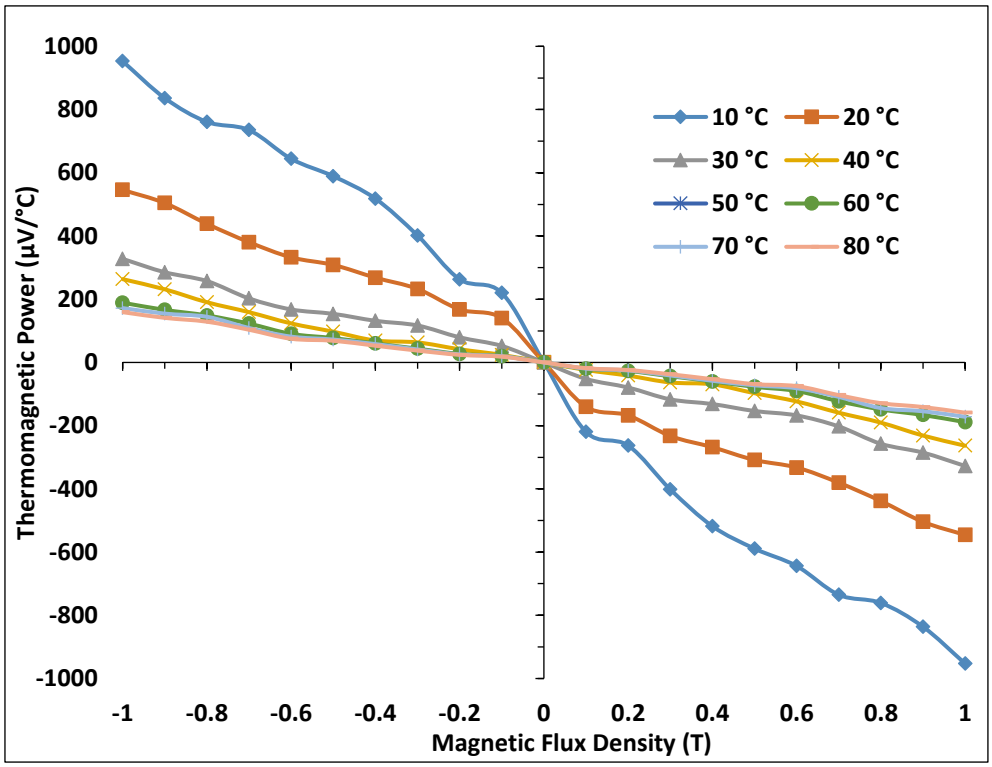

Variation of the thermomagnetic power with DC magnetic field density at various temperature differences for DP0.1% sample.

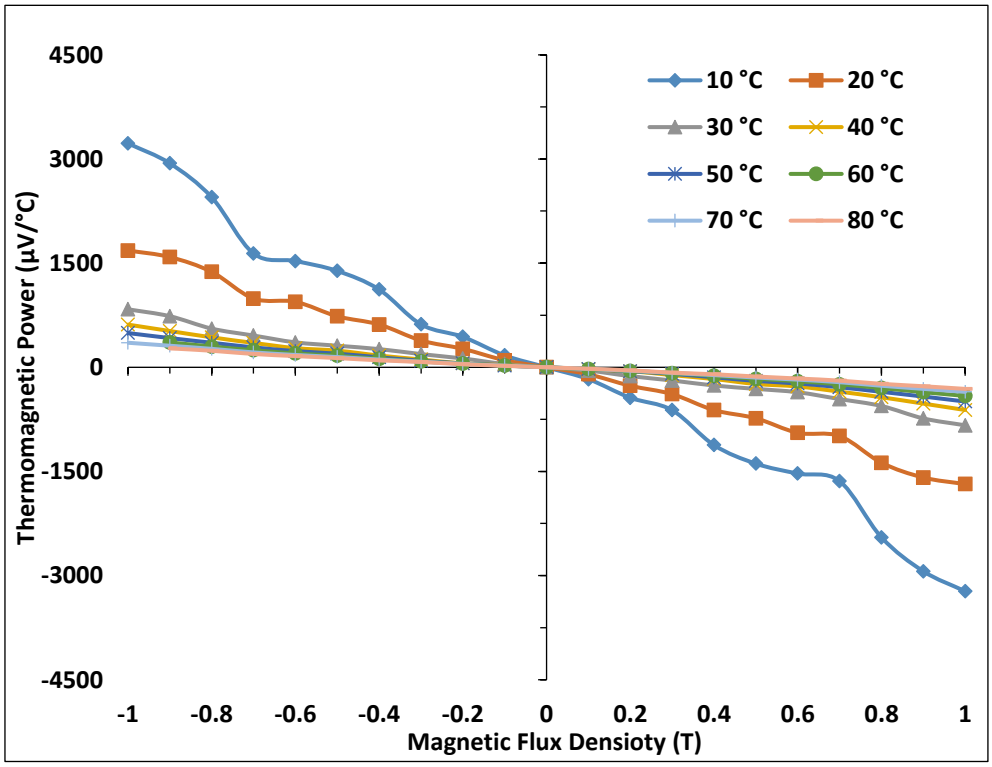

Variation of the thermomagnetic power with Dc magnetic field density at various temperature differences for DP0.25% sample.

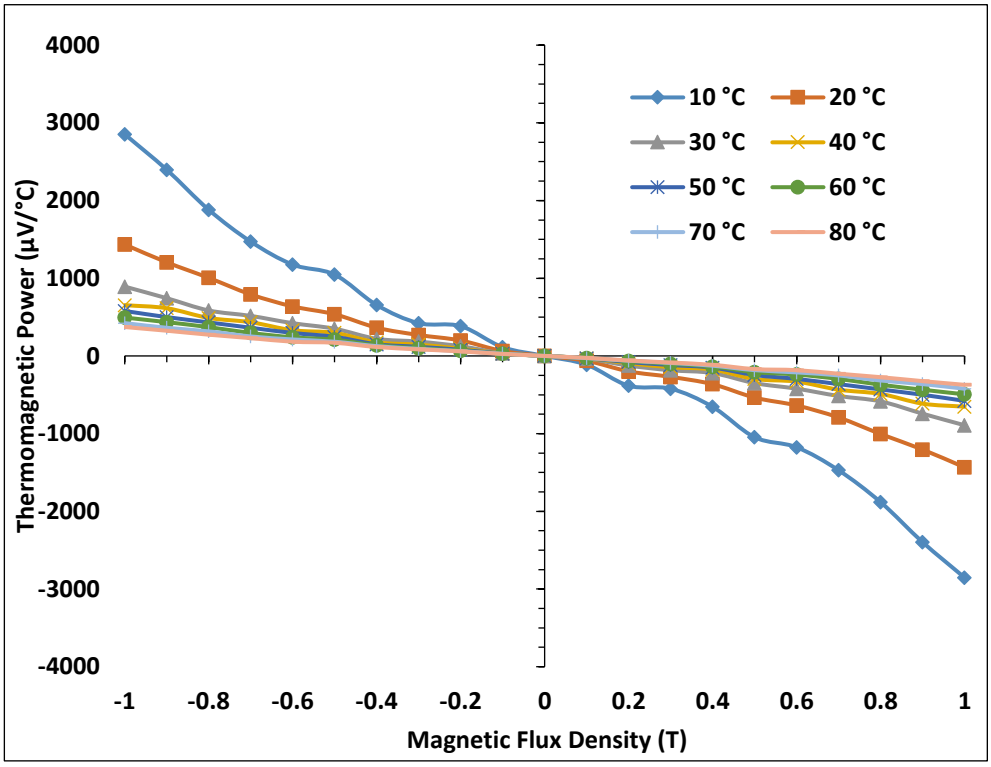

Comparison among the thermomagnetic power with Dc magnetic field density at various temperature differences for all samples.

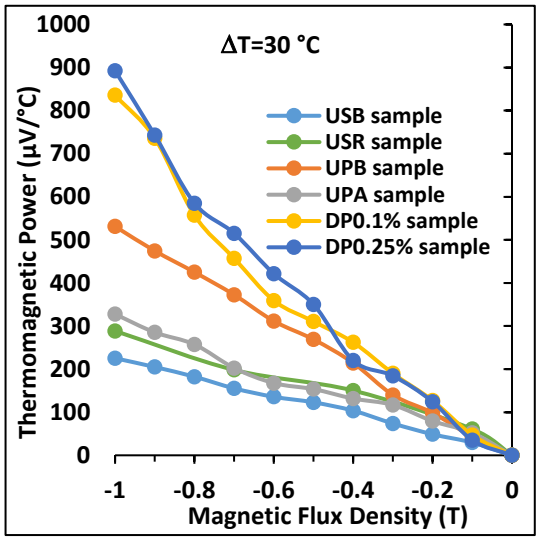

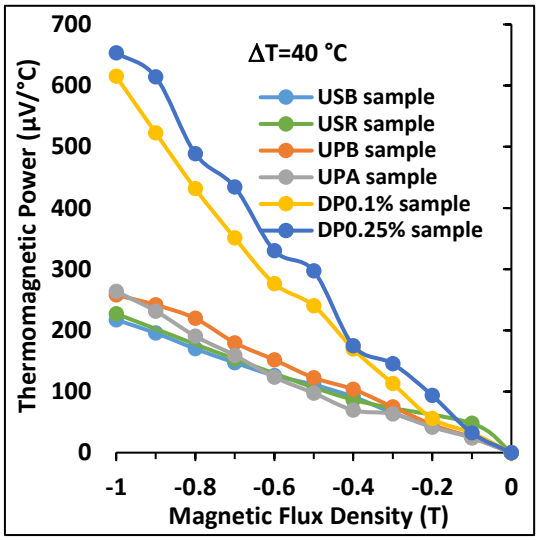

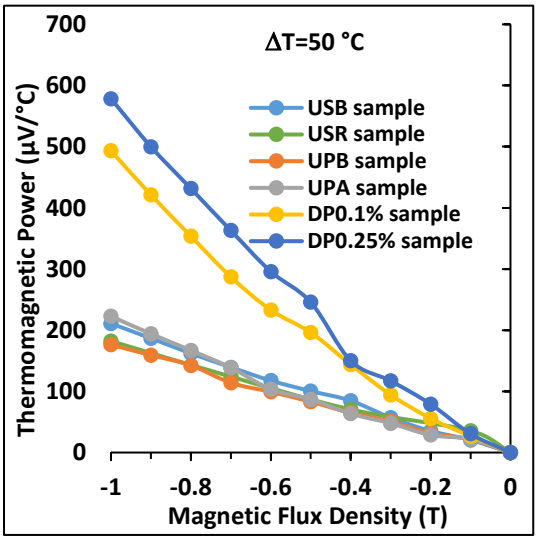

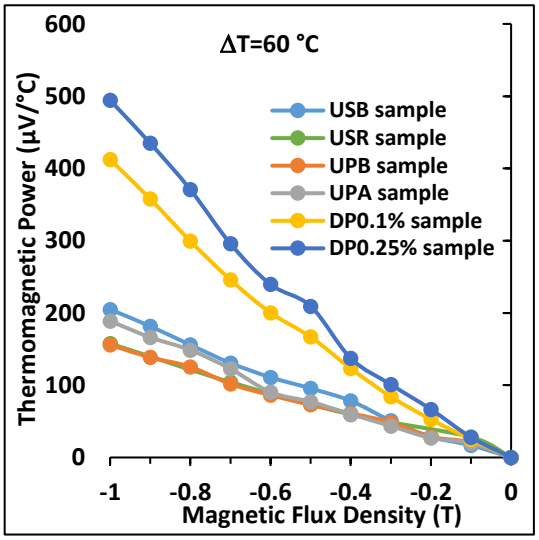

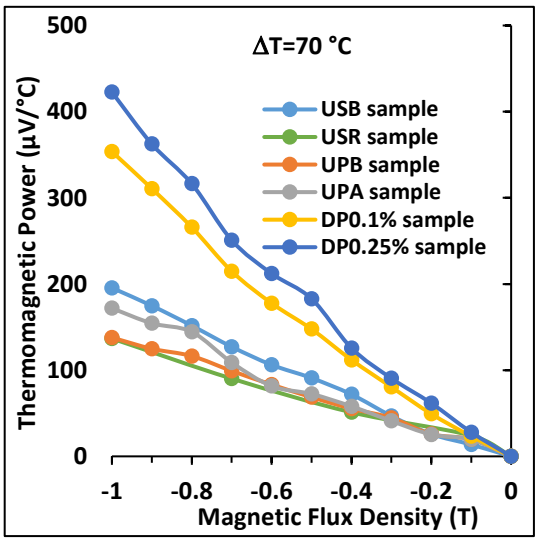

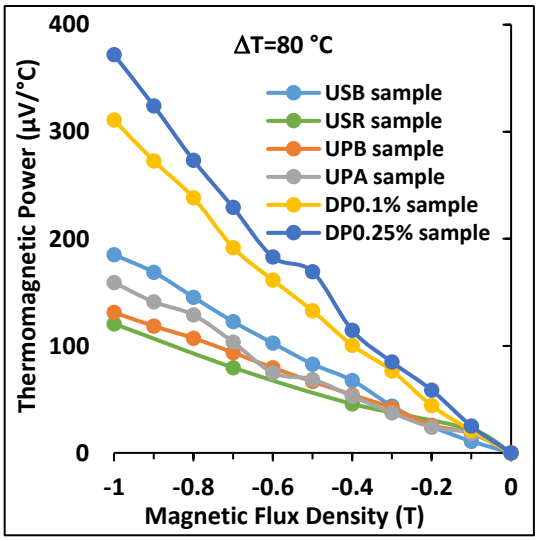

Appendex 16:

Variation of the hybrid transverse voltage with temperature difference at various DC magnetic field density for USR sample.

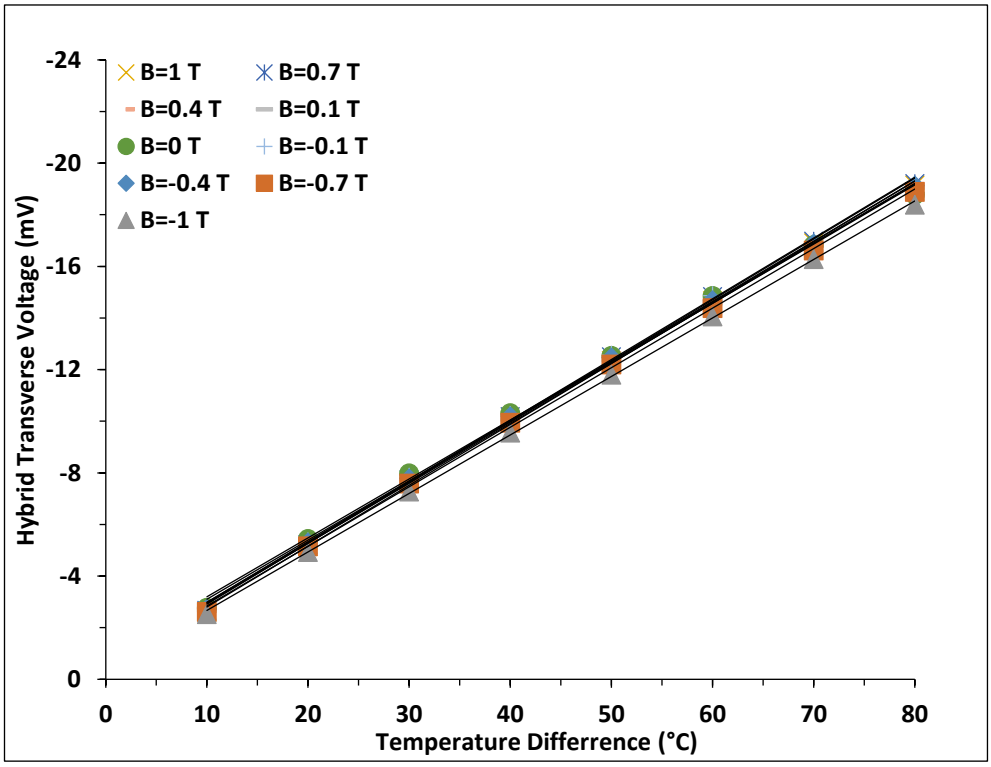

Variation of the hybrid transverse voltage with temperature difference at various DC magnetic field density for UPB sample.

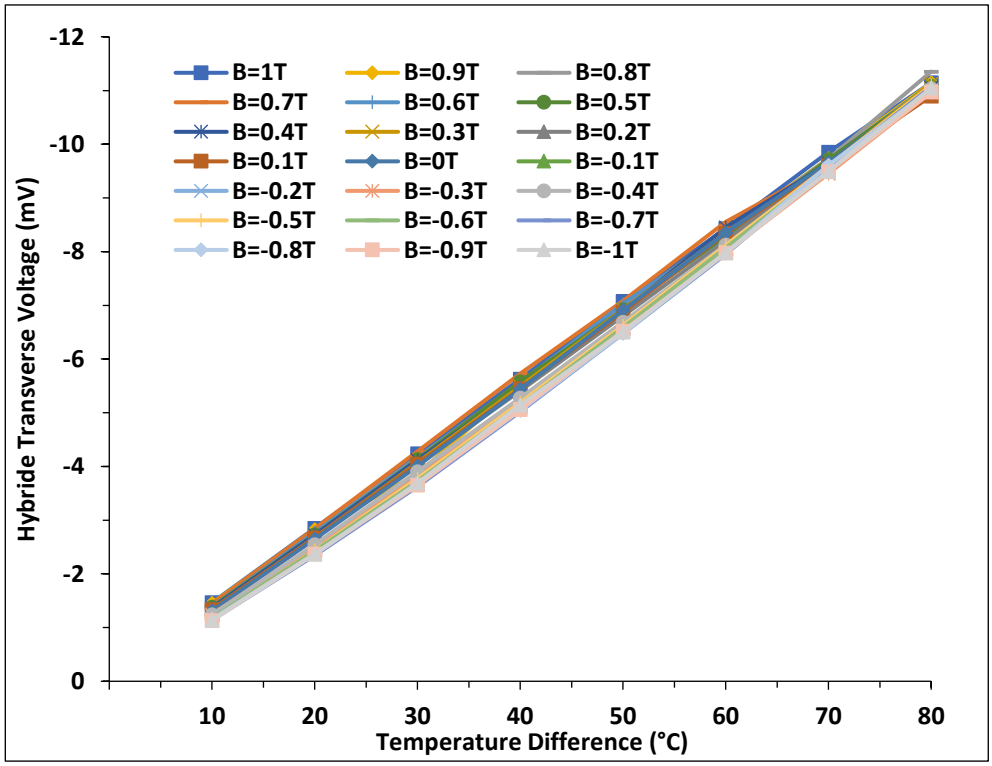

Variation of the hybrid transverse voltage with temperature difference at various DC magnetic field density for UPA sample.

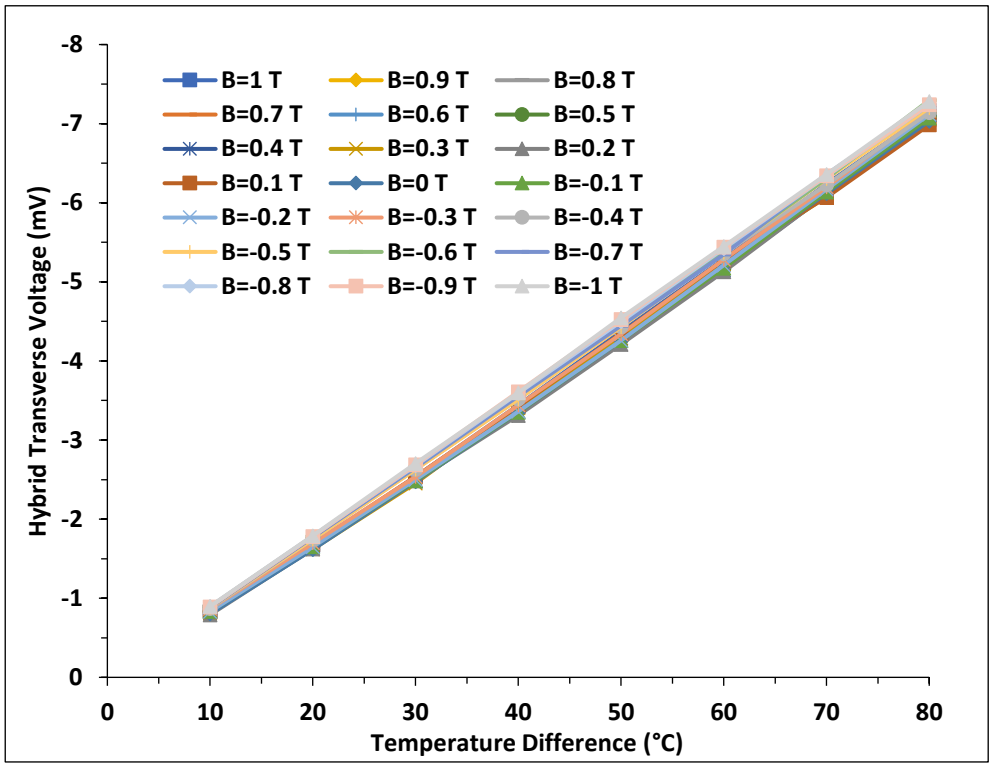

Variation of the hybrid transverse voltage with temperature difference at various DC magnetic field density for DP0.1% sample.

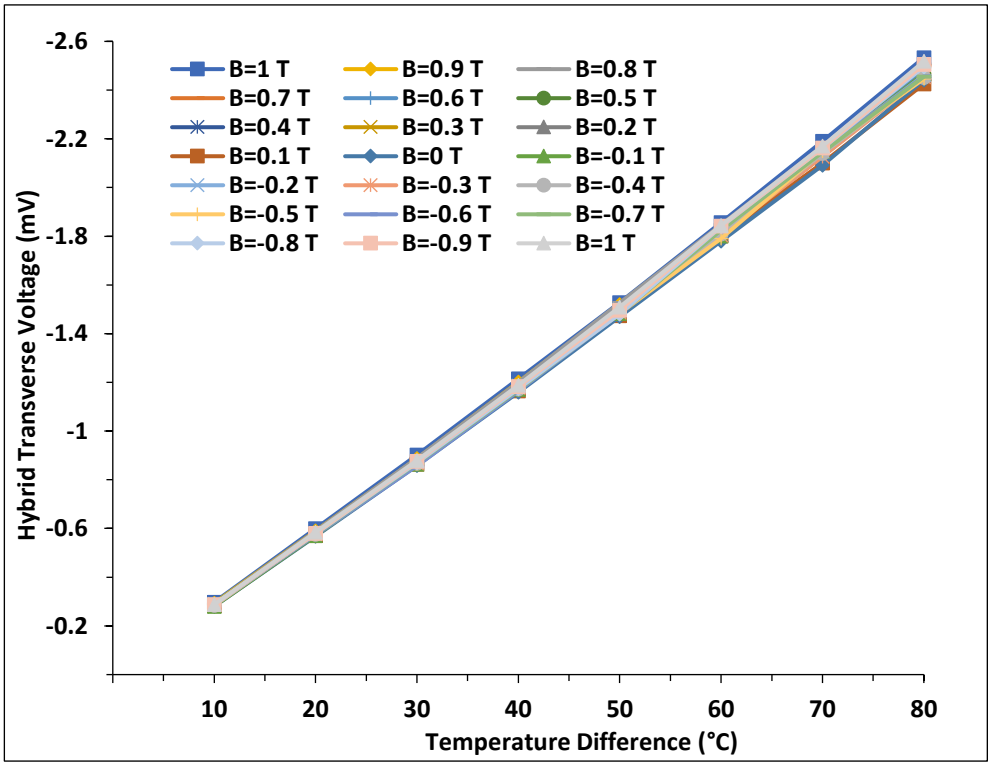

Variation of the hybrid transverse voltage with temperature difference at various DC magnetic field density for DP0.25% sample.

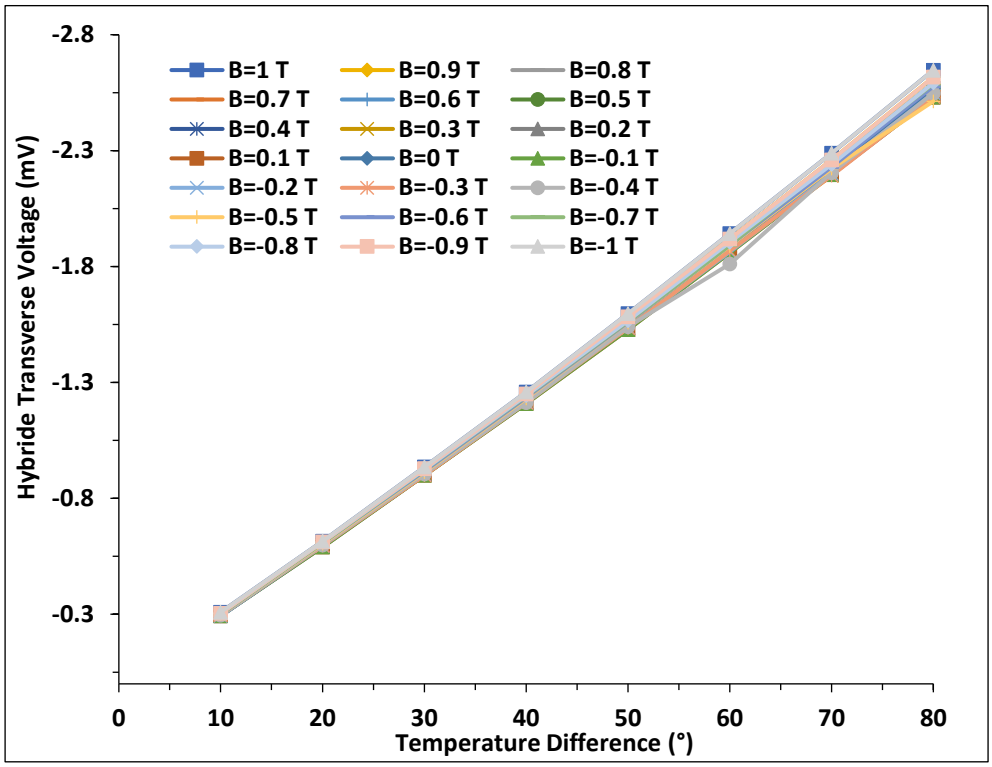

Comparison among the hybrid transverse voltage with temperature difference at various DC magnetic field density for all samples.

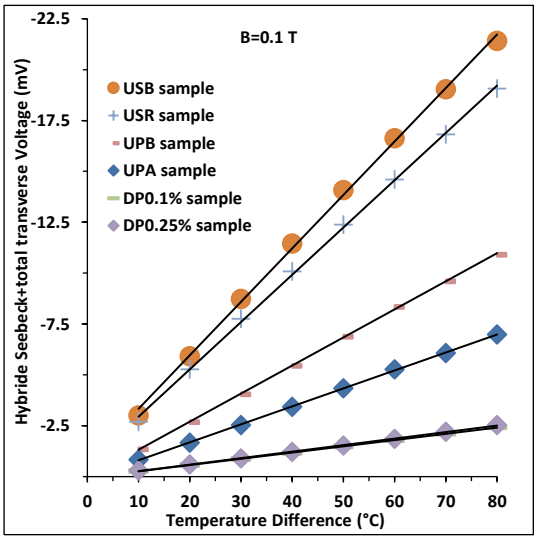

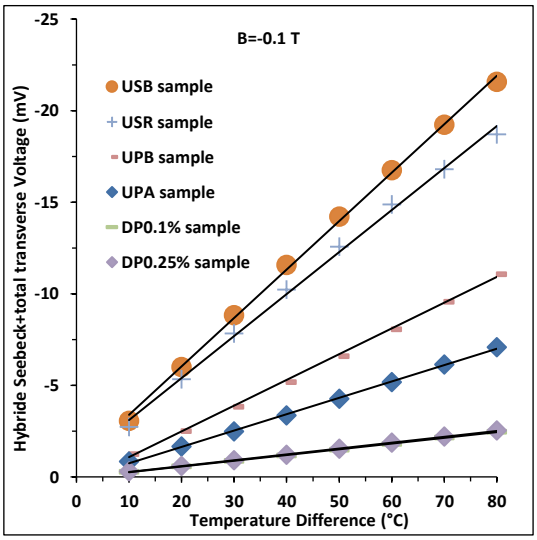

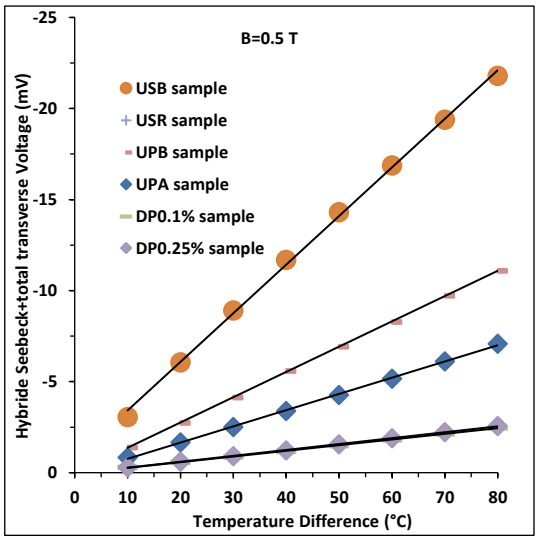

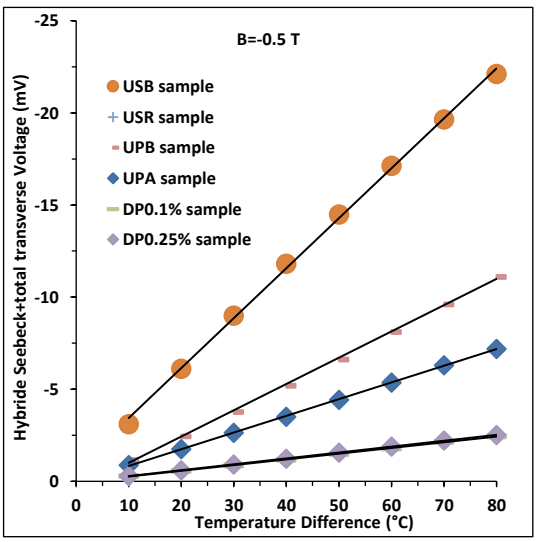

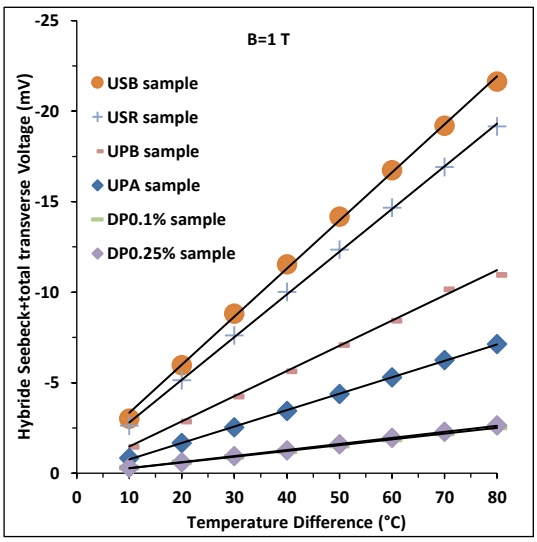

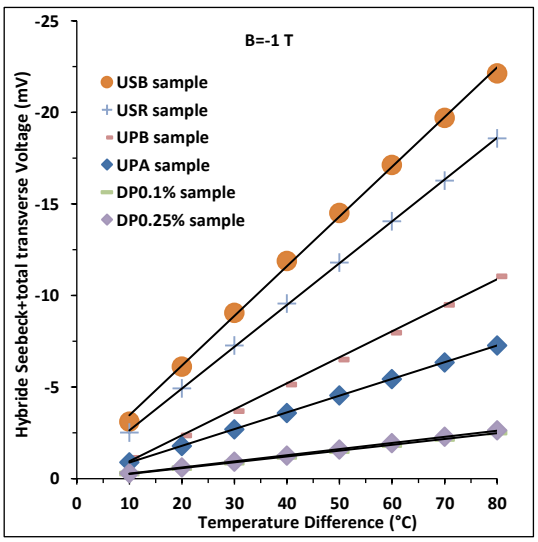

Appendex 17:

Variation of the all three parameters: Seebeck, total transverse, hybrid transverse voltage with temperature difference under various DC magnetic field density for USB sample.

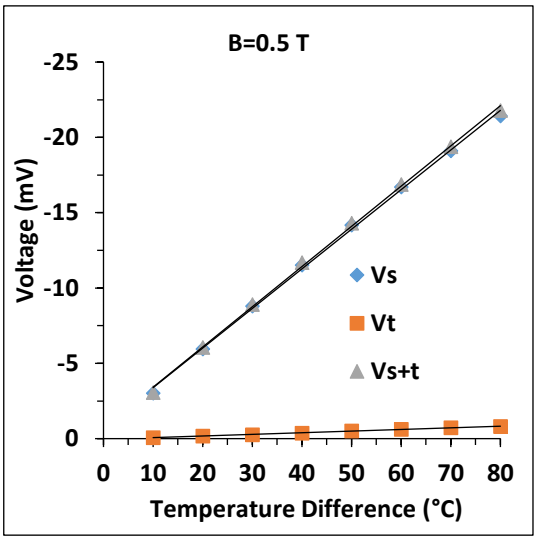

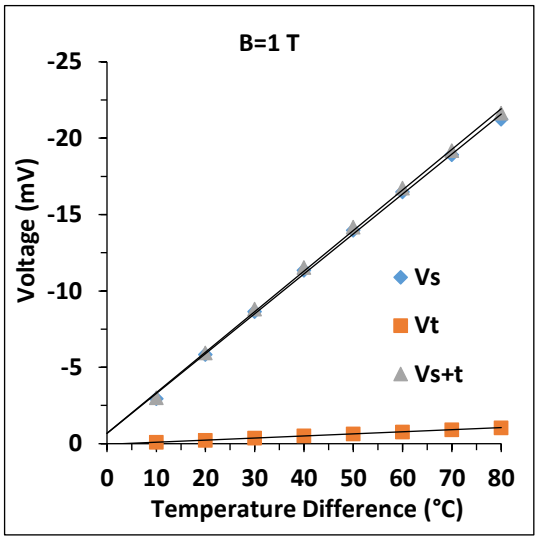

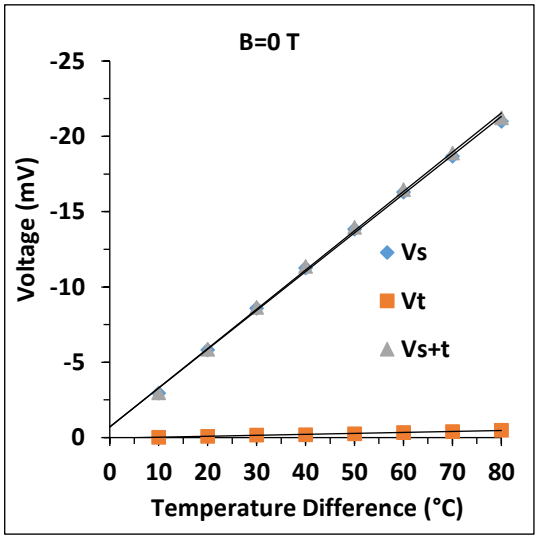

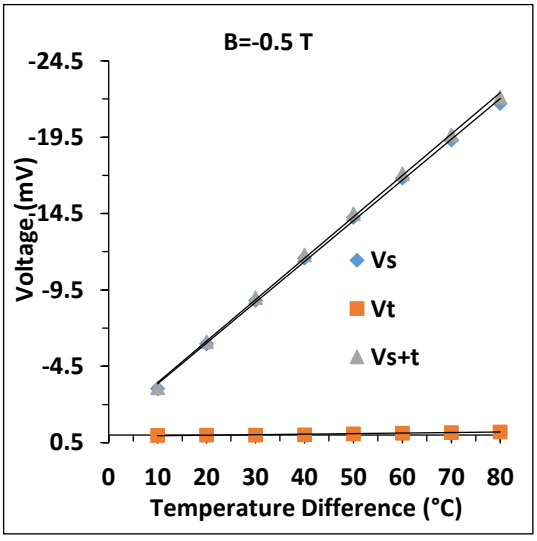

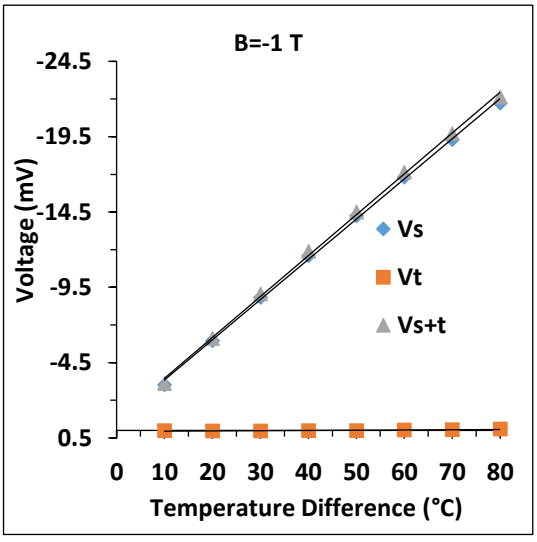

Variation of the all three parameters: Seebeck, total transverse, hybrid transverse voltage with temperature difference under various DC magnetic field density for USR sample.

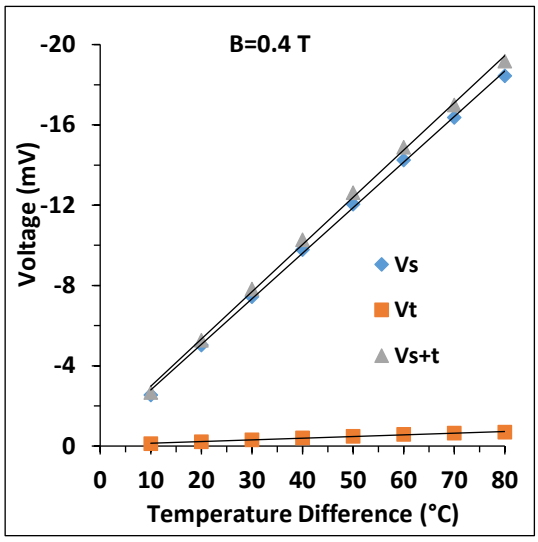

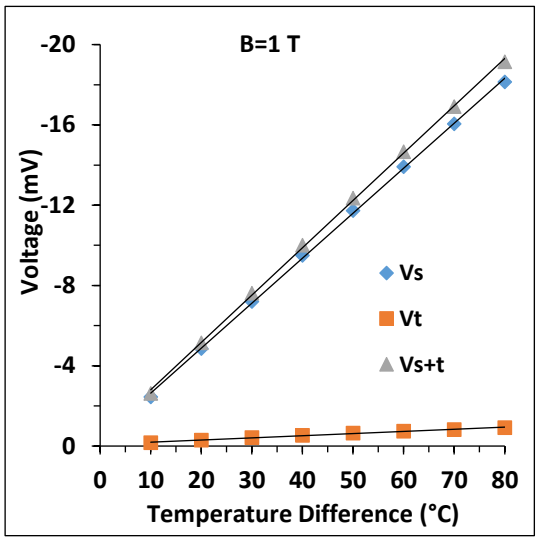

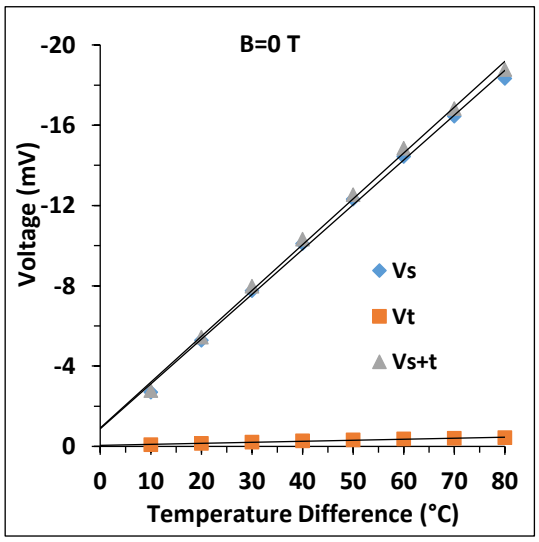

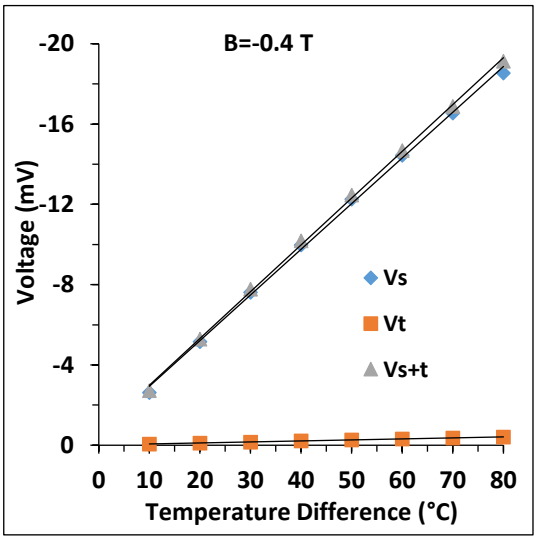

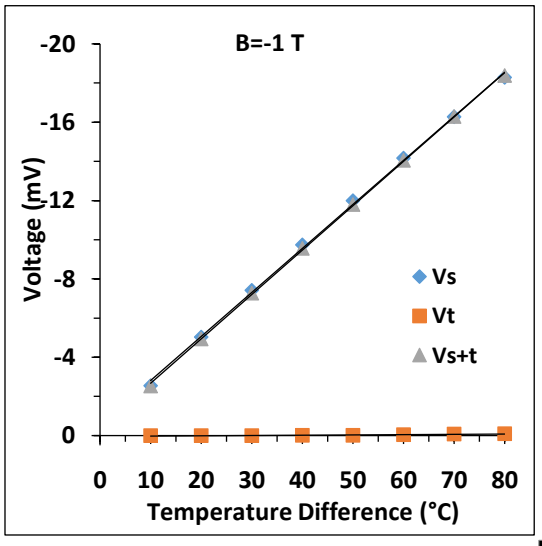

Variation of the all three parameters: Seebeck, total transverse, hybrid transverse voltage with temperature difference under various DC magnetic field density for UPB sample.

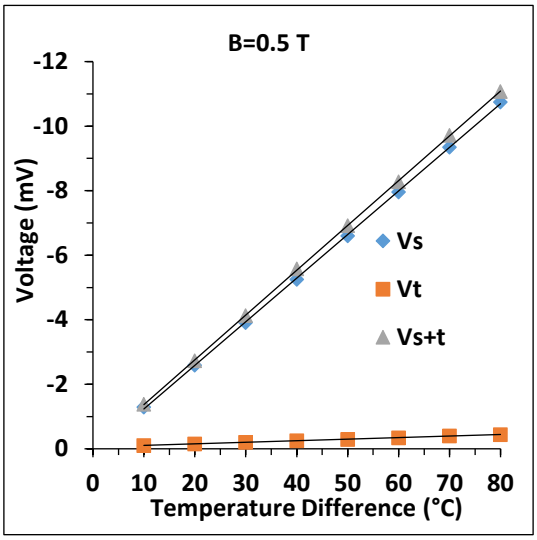

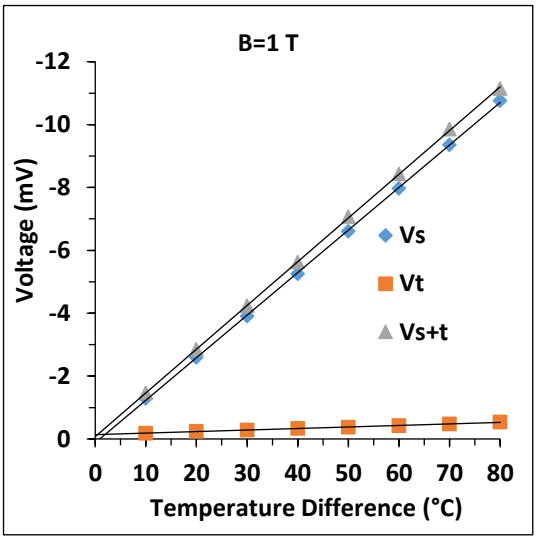

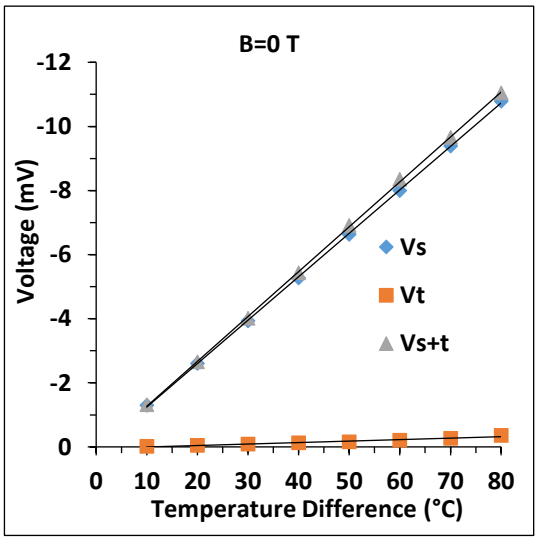

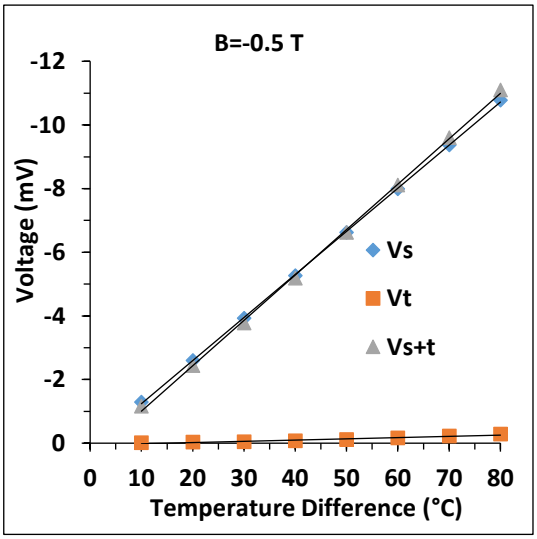

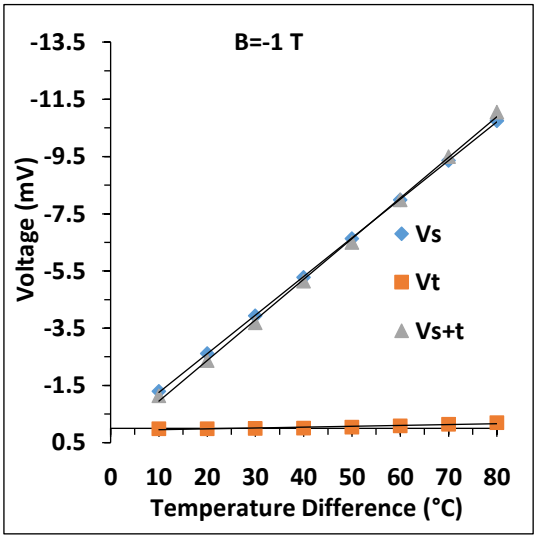

Variation of the all three parameters: Seebeck, total transverse, hybrid transverse voltage with temperature difference under various DC magnetic field density for UPA sample.

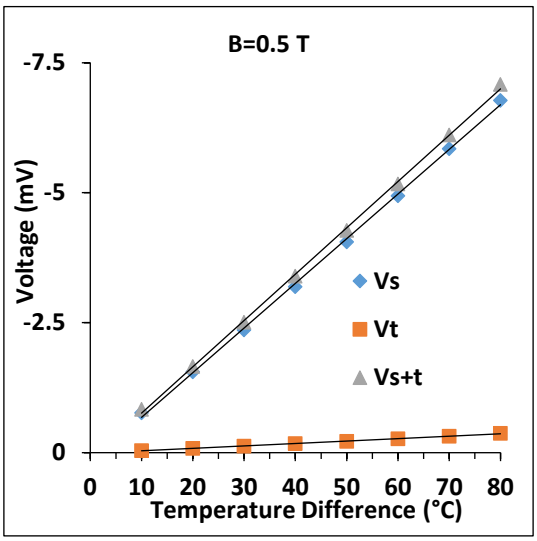

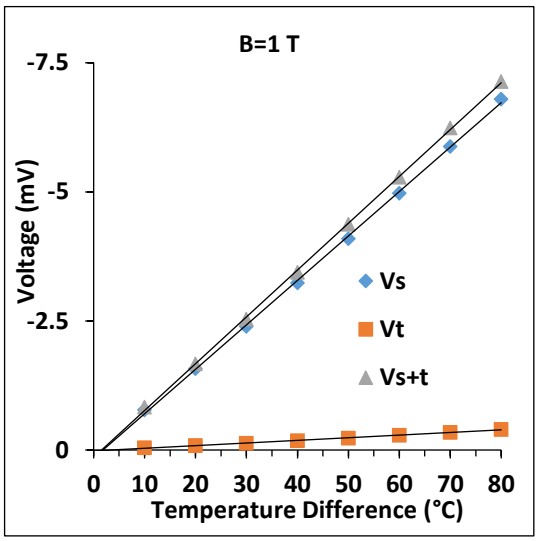

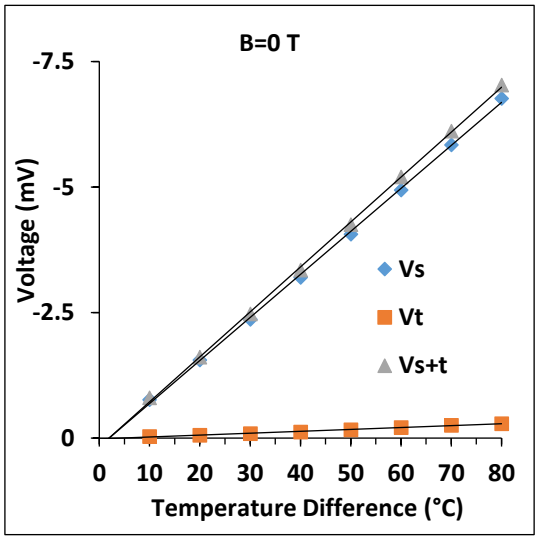

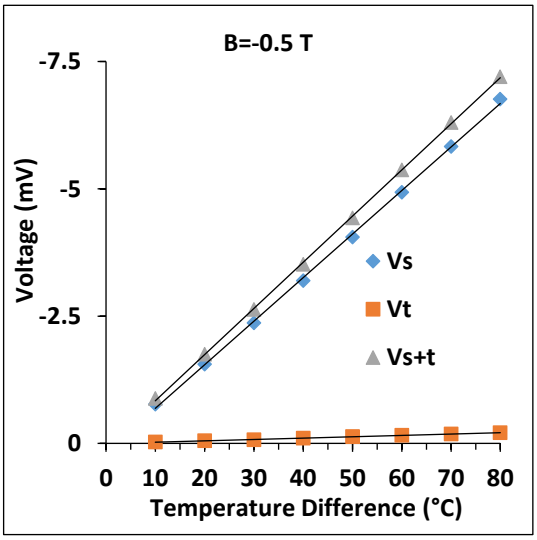

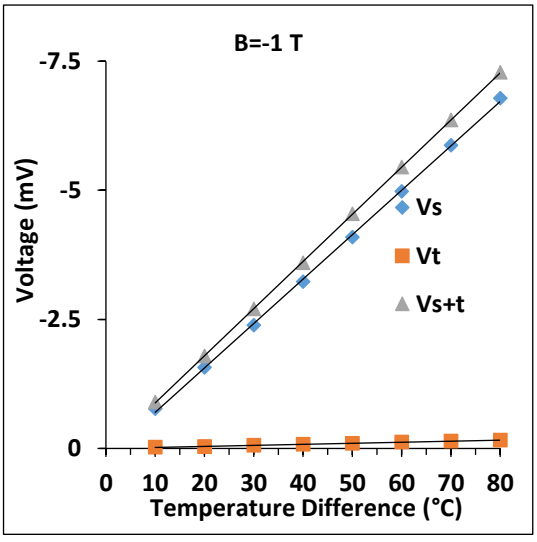

Variation of the all three parameters: Seebeck, total transverse, hybrid transverse voltage with temperature difference under various DC magnetic field density for DP0.1% sample.

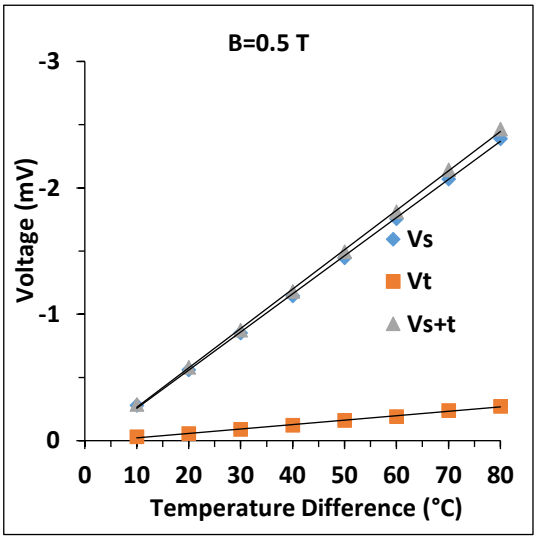

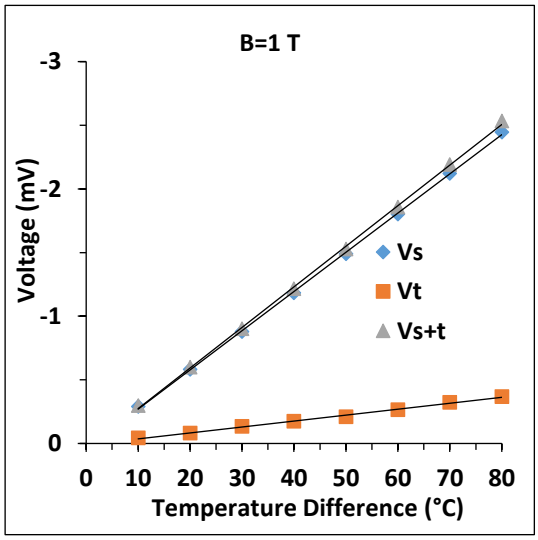

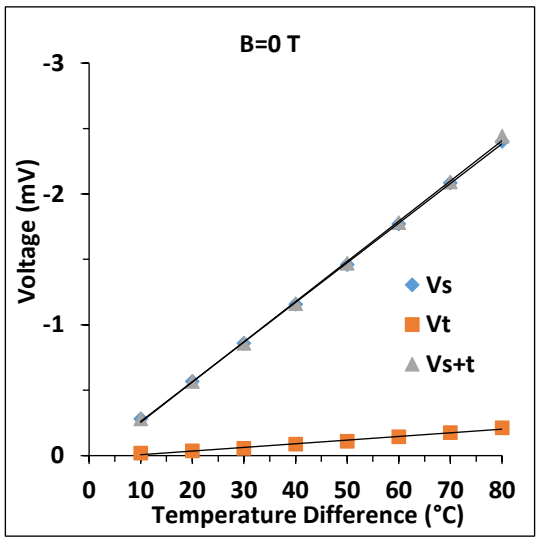

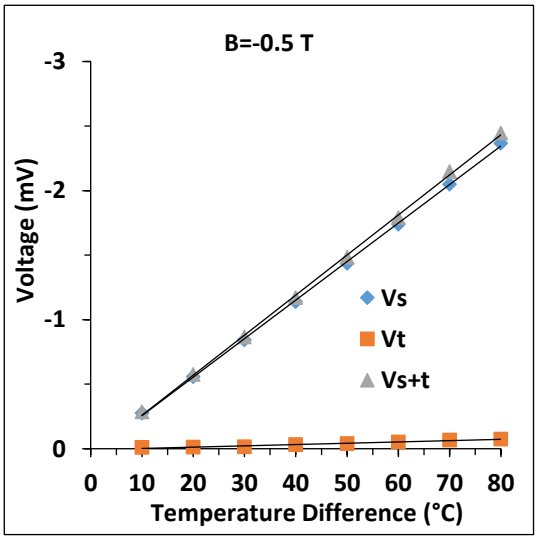

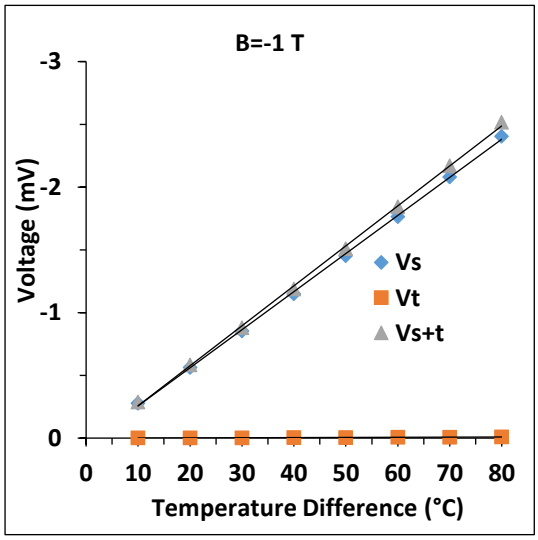

Variation of the all three parameters: Seebeck, total transverse, hybrid transverse voltage with temperature difference under various Dc magnetic field density for DP0.25% sample.

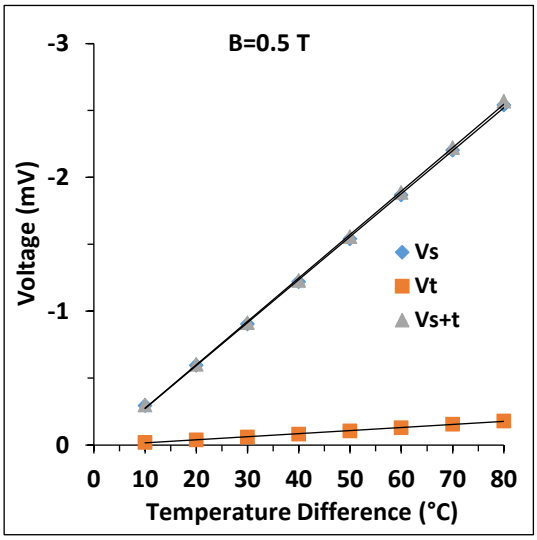

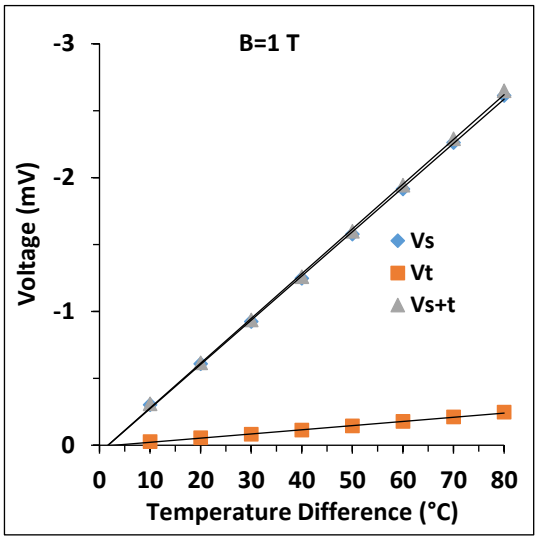

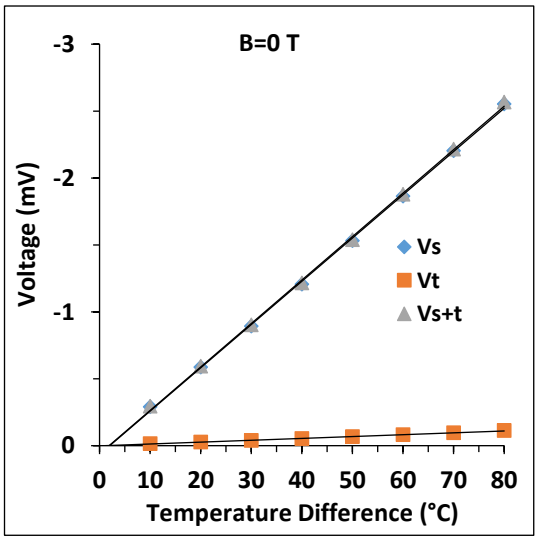

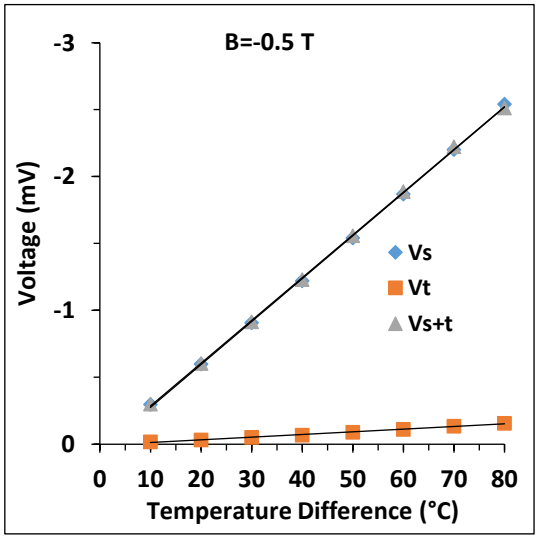

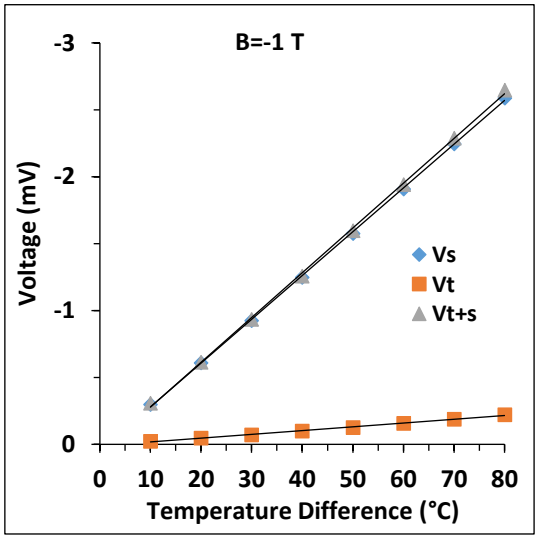

Appendex 18:

Variation of the Seebeck coefficient with AC magnetic field density for UPB sample.

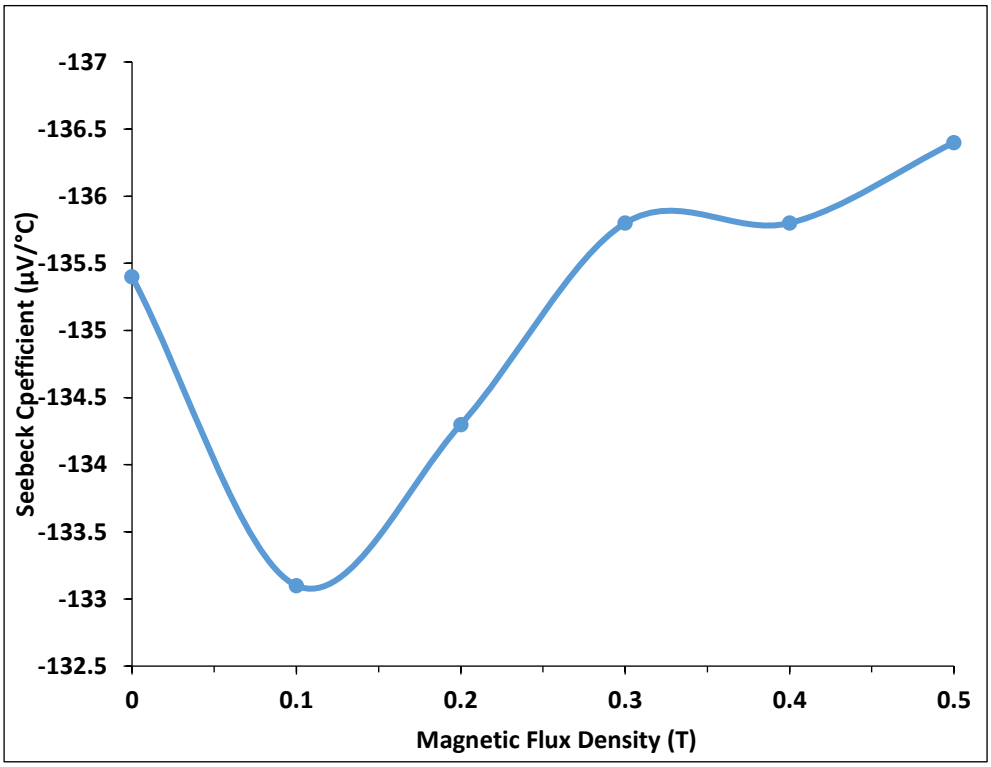

Variation of the Seebeck coefficient with AC magnetic field density for UPA sample.

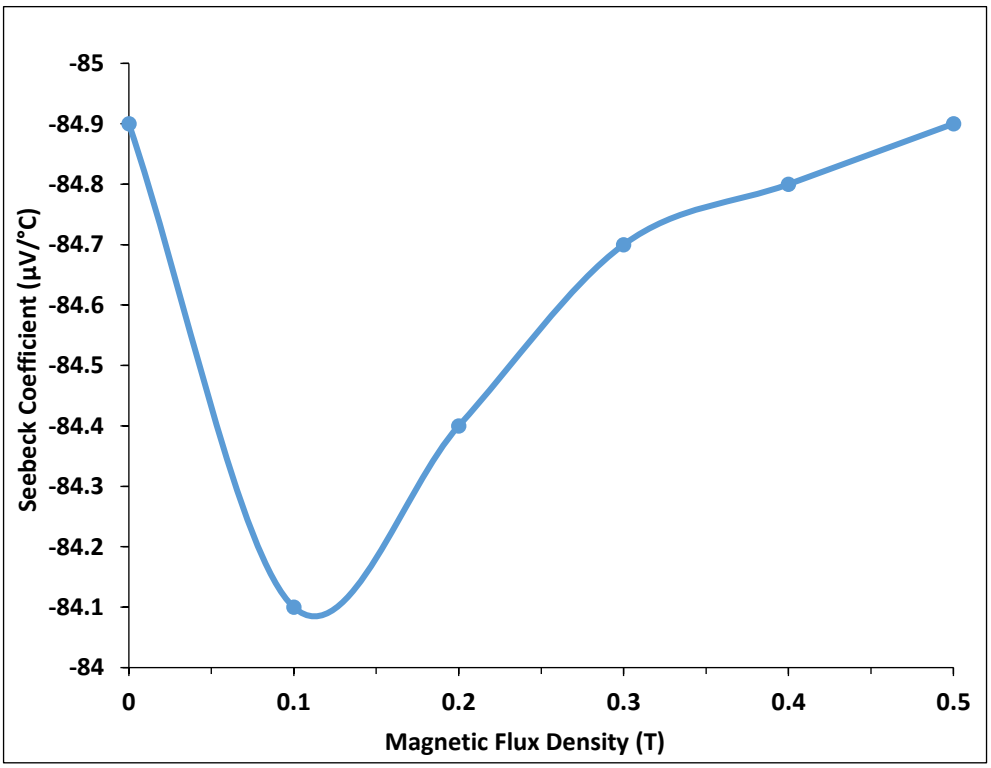

Variation of the Seebeck coefficient with AC magnetic field density for DP0.1% sample.

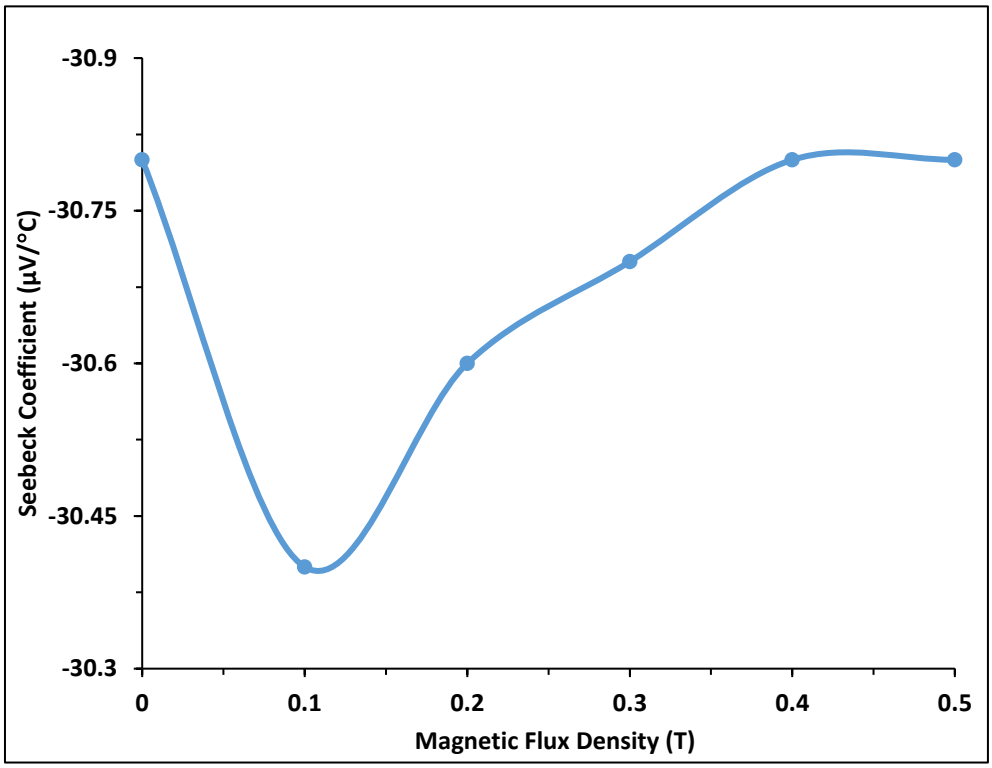

Variation of the Seebeck coefficient with AC magnetic field density for DP0.25% sample.

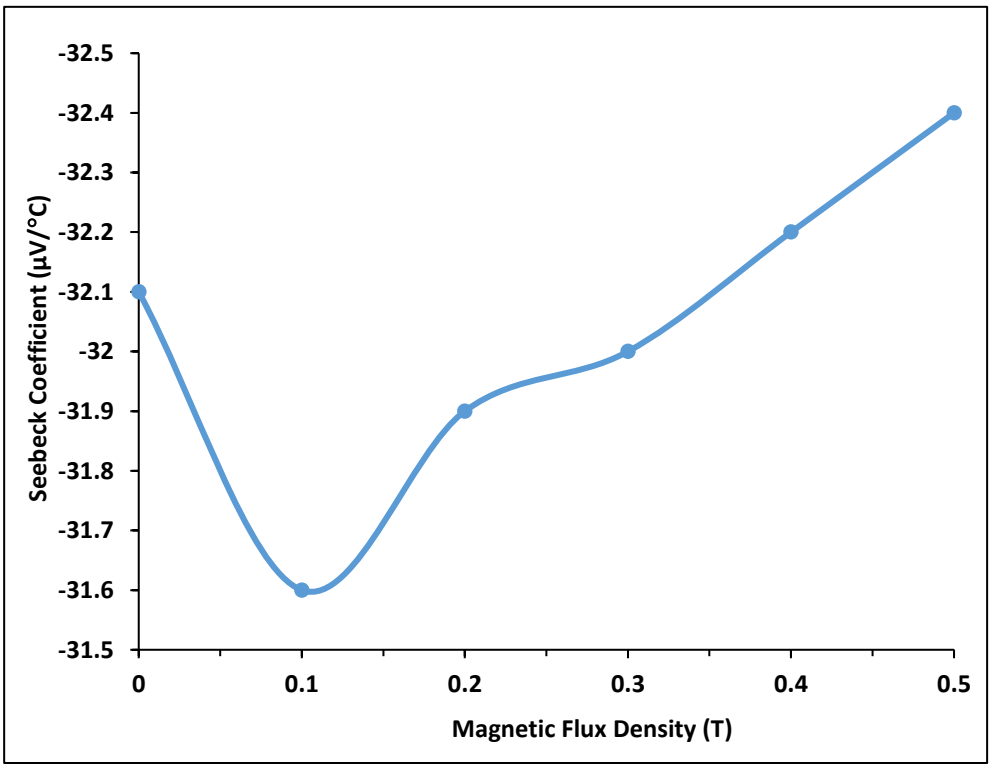

Comparison among the Seebeck coefficient with AC magnetic field density for all samples.

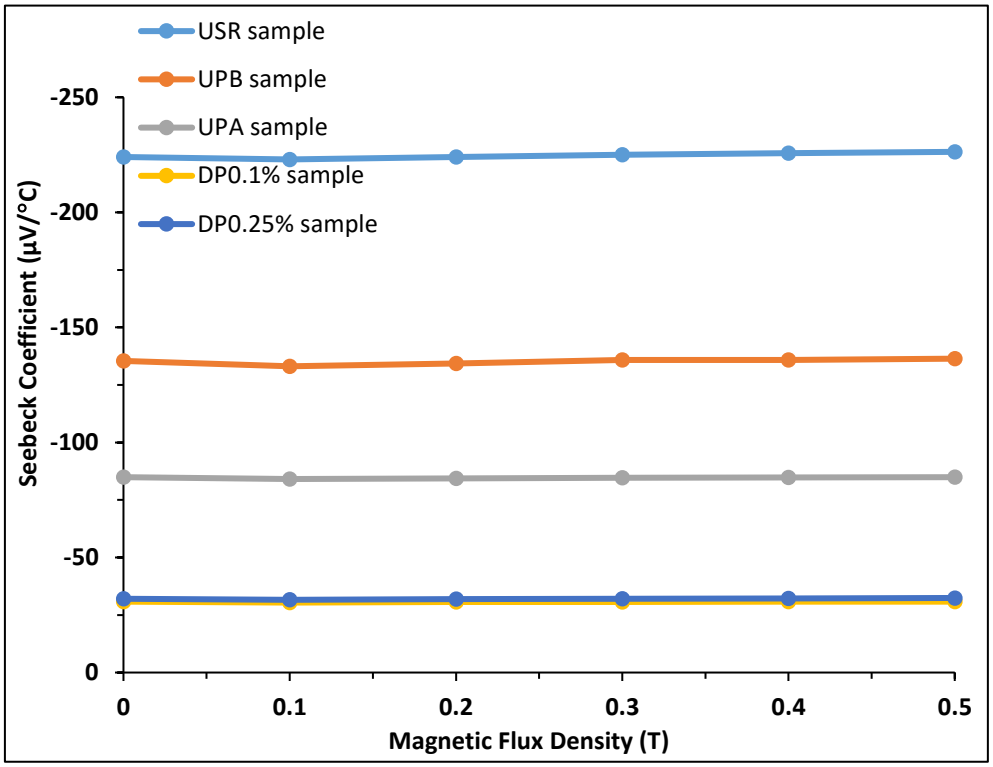

Appendex 19:

Variation of the voltage measured transversely with time at different magnetic field density for UPB sample.

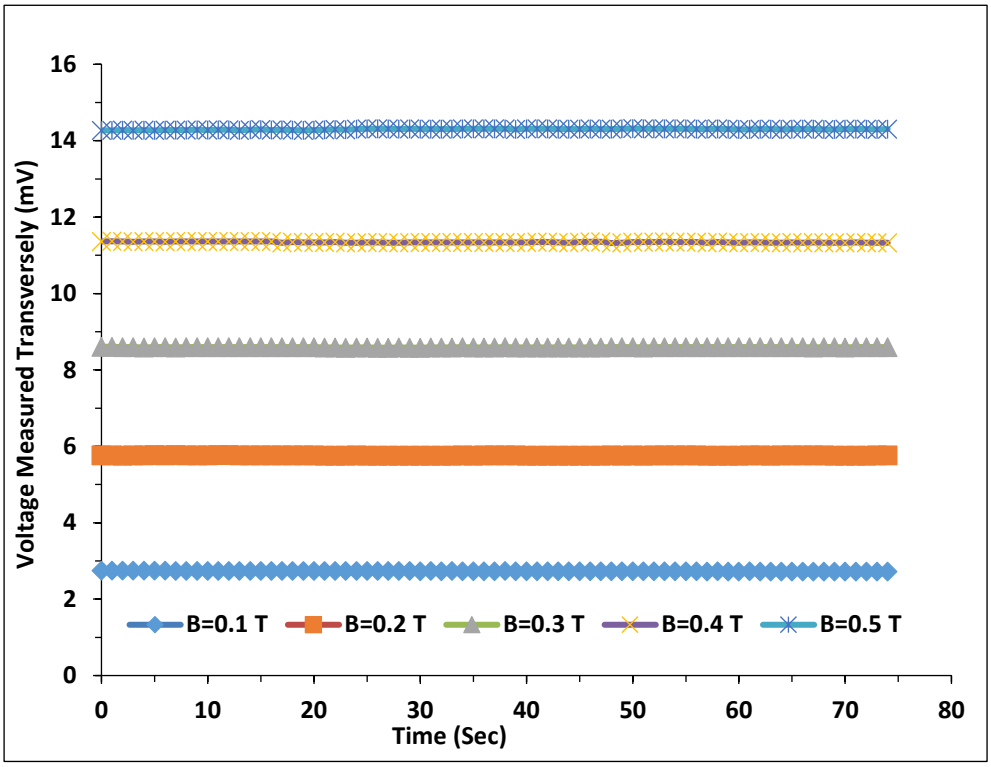

Variation of the voltage measured transversely with time at different magnetic field density for UPA sample.

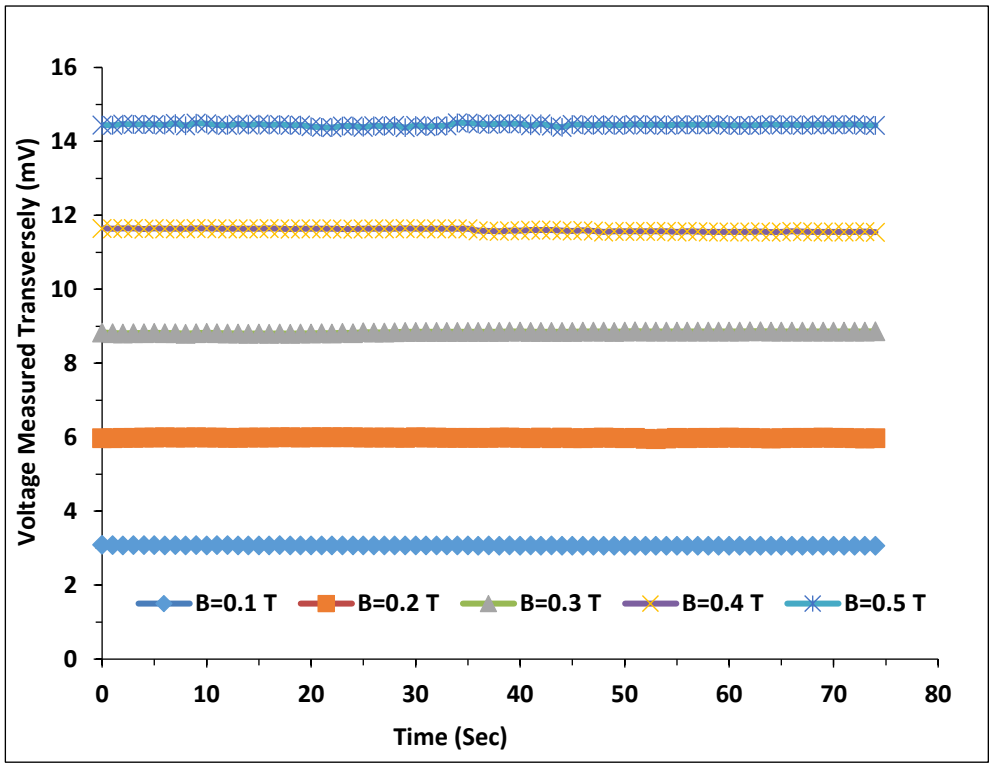

Variation of the voltage measured transversely with time at different magnetic field density for DP0.1% sample.

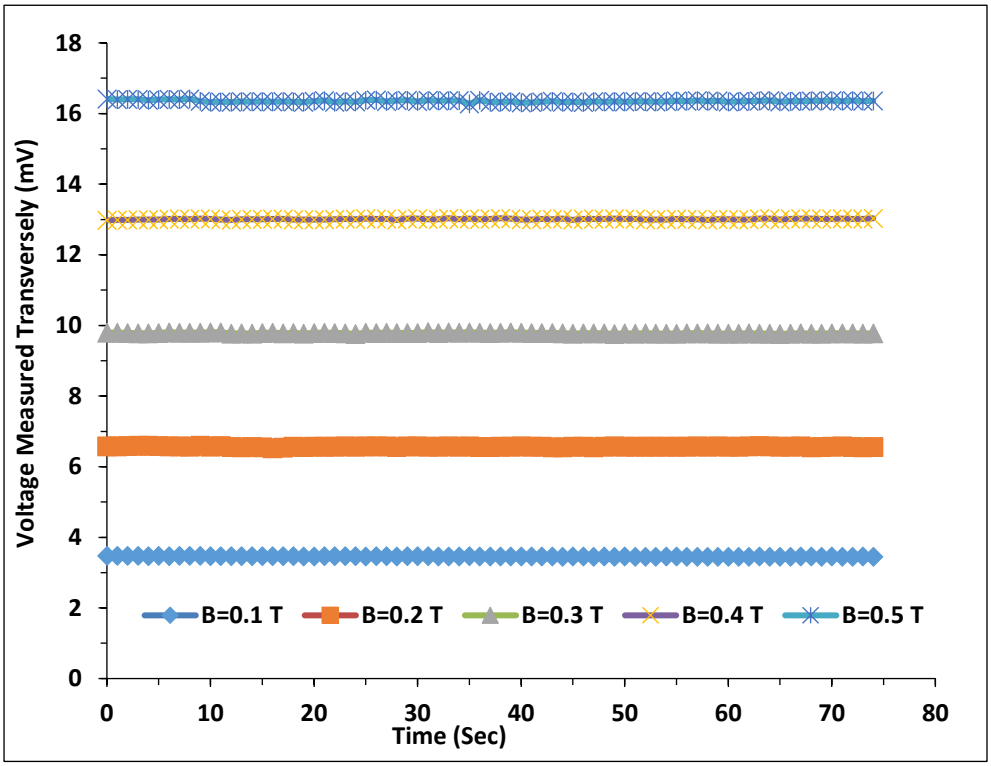

Variation of the voltage measured transversely with time at different magnetic field density for DP0.25% sample.